CHARLES PANKOW
FOUNDATION
Building Innovation through Research

Acceptable Elongations and Low-Cycle Fatigue Performance for High-Strength Reinforcing Bars

Final Report

The University of Texas at San Antonio

Drit Sokoli
Graham Hogsett
Albert A. Limantono
Ariel Suselo
Dhiaa Al-Tarafany
Wassim M. Ghannoum

Acceptable Elongations and Low-Cycle Fatigue Performance

for High-Strength Reinforcing Bars

CPF Research Grant Agreement #03-16

Funded by
CHARLES PANKOW FOUNDATION
P.O. Box 820631
Vancouver, Washington 98682

Co-funded by
The Concrete Reinforcing Steel Institute, and
The American Concrete Institute Foundation Strategic Development Council

Principal Investigator: Wassim M. Ghannoum, Ph.D., P.E., F.SEI

Research Assistants: Drit Sokoli
Graham Hogsett
Albert A. Limantono
Ariel Suselo
Dhiaa Al-Tarafany

<u>Industry Support:</u>

Industry Champion: Mike Mota, VP Engineering, CRSI

Advisory Panel: Dominic Kelly, SGH
Conrad Paulson, WJE
Andrew Taylor, KPFF
Loring Wyllie, Degenkolb

Metallurgy and steel production: Erik Nissen, NUCOR
Jacob Seltzer, CMC
William Peppler, Gerdau
Jeffrey Kramer, Cascade Steel
Salem Faza, MMFX

Acknowledgements

Abstract

High-strength reinforcing bars (HSRB) with varying mechanical properties and performance under low-cycle fatigue are being introduced to the U.S. market driven by constructability and economic incentives. The project described in this report is part of a larger national effort aimed at quantifying changes in the seismic collapse risk of concrete structures associated with switching from conventional grade 60 reinforcing bars to HSRB. Correlations between seismic collapse risk and bar properties are crucial for code bodies to set acceptable properties for HSRB, especially fracture elongations and low-cycle fatigue performance. However, in order to objectively and reliably evaluate the seismic collapse risk of concrete buildings, the effects of the varying mechanical properties of HSRB on the deformation capacity of seismically detailed concrete members must be quantified. The objective of this project in particular is to provide the necessary experimental data and behavioral models to identify when longitudinal bars in seismically detailed frame members reach fracture during seismic events across all types of bars and grades in production or under development in the U.S. Three tasks were undertaken to achieve project objectives: 1) a low-cycle fatigue-capacity model was calibrated to cyclic tests conducted on bars of different grades and mechanical properties; 2) a mechanics-based model was developed and calibrated to experimental data from the literature to correlate member global deformations with strain demands that govern the fatigue behavior of longitudinal bars in concrete members; and 3) based outcomes from tasks 1) and 2), a methodology was proposed to estimate the point during a seismic loading history at which longitudinal bars fracture in seismically detailed concrete frame members. Cyclic tests

were performed on reinforcing bars to bolster available fatigue data. Additional tests included bars of varying grades of steel, manufacturing techniques, clear lateral bracing spans, and strain amplitudes.

Table of Contents

List of Figures

xiv

xvi

List of Tables

List of Equations

1 INTRODUCTION

1.1 Motivation

In an effort to meet the increasing challenges of structural designs, high-strength reinforcing steel bars are becoming increasingly necessary. Higher strength reinforcing bars allow for measurable reductions in the amount of steel required in design, thus providing benefits in constructability, as well as economic and environmental benefits derived from reduced material quantities.

High-strength reinforcing bars (HSRB) are defined in this report as bars having a yield strength of 80ksi or higher. For simplicity, this report also uses the term grade to refer to the approximate yield strength provided by the manufacturer in kips per square inch (ksi). For example, grade 60 bars refer to bars that have a nominal yield strength of 60ksi and have an actual yield strength that slightly exceeds 60ksi. Code provisions as laid out in ACI 318-14, set the reinforcement strength limit for longitudinal reinforcement in gravity systems at 80ksi, but for seismic applications, the maximum reinforcement strength is limited to 60ksi. This limitation is in part due to well-known changes in the mechanical behavior of steel as its strength increases, namely, higher strength steel has a greater strain at yield and a lower strain at fracture. Additionally, uncertainties about the toughness and low-cycle fatigue performance of newly developed HSRB have also contributed to maintaining the status quo in the ACI 318 design code (ATC-115, 2015).

Recent tests have demonstrated significantly lower low-cycle fatigue life for certain higher grades of steel bars compared to grade 60 bars (Ghannoum and Slavin, 2016).

Additionally, much larger scatter was observed in the low-cycle fatigue performance of HSRB compared with grade 60 bars, which indicates that current production methods cannot yet achieve consistent low-cycle fatigue performance for HSRB. On the other hand, experimental evidence has shown that high-strength reinforcing bars in concrete members can experience much larger strains than regular grade 60 bars at any given member deformation level (Aoyama, 2001, Macchi et al, 1996, Sokoli, 2014, Sokoli and Ghannoum, 2016, Sokoli et al., 2017, Sokoli, 2018). In recent column tests by Sokoli and Ghannoum (2016), grade 100 bars experienced as much as 100% larger strain demands than their grade 60 counterparts. The tensile-to-yield strength (T/Y) ratio of the reinforcing bars was suspected to play a major role in driving the strain demands; with the lower T/Y ratios of higher steel grades generating higher strain concentrations and demands. Other tests conducted by Sokoli et al. (2017) and To et. Al. (2018), have indicated that grade 100 longitudinal bars having a T/Y ratio at the lower end of current production capabilities (~1.15) can experience in excess of 50% higher strain demands than those with a T/Y ratio at the high-end of current production methods (~1.27). These tests have confirmed the relation between the T/Y ratio and bar strain demands and are helping uncover other influential parameters on the strain demands of longitudinal bars. Since higher grade bars tend to have significantly lower T/Y ratios than grade 60 bars, it is expected that HSRB will sustain significantly larger strain demands than grade 60 bars in concrete members. This is especially concerning given that the low-cycle fatigue life of bars reduces exponentially with strain demands (Slavin and Ghannoum, 2016). For example, a 100%

increase in strain amplitude can lead to an order of magnitude reduction in the number of inelastic strain cycles to fracture of reinforcing bars, regardless of grade.

Given these findings, concerns have been raised about longitudinal HSRB possibly suffering premature fracture during seismic events, which can increase the collapse risk of buildings reinforced with HSRB. Thus, as HSRB are increasingly introduced in the U.S. market, methods for estimating their performance under seismically induced low-cycle fatigue are crucial for assessing any potential increase or decrease in collapse risk associated with their usage.

1.2 Objectives and Scope

This project is part of a larger national effort aimed at quantifying changes in the seismic collapse risk of concrete structures associated with switching from conventional grade 60 reinforcing bars to high-strength reinforcing bars (HSRB). Correlations between seismic collapse risk and bar properties are crucial for code bodies to set acceptable properties for HSRB, especially fracture elongations and low-cycle fatigue performance. However, in order to objectively and reliably evaluate the seismic collapse risk of concrete buildings, the effects of the varying mechanical properties of HSRB on the deformation capacity of seismically detailed concrete members must be quantified. The objective of this project, in particular, is to provide the necessary experimental data and behavioral models to identify when longitudinal bars in seismically detailed frame members reach fracture during seismic events across all types of bars and grades in production or under development in the U.S. Three tasks were undertaken to achieve project objectives:

Task 1: Low-cycle fatigue capacity models

Task 1a: Low-cycle fatigue testing

Low-cycle fatigue testing was carried within the scope of this project to bolster available fatigue data in the literature. The tests were conducted in a uniaxial testing machine on reinforcing bars to quantify the fatigue life of HSRB and compare it with that of conventional grade 60 seismic bars. Bars produced using the main three manufacturing processes in the U.S. for producing HSRB were tested. By covering the range of production techniques, the test matrix covered the ranges of bar mechanical properties, particularly for the HSRB. Other parameters that were investigated were bar grades, bar sizes, unsupported length between machine grips, and strain amplitudes.

Task 1b: Fatigue-capacity models

Fatigue-capacity models were developed for current production of grade 60 and HSRB. These models are based on the extensive low-cycle fatigue testing conducted in this study as well as tests compiled from previous studies conducted by the authors. The proposed models estimate the number of half cycles to fracture for reinforcing bars depending on manufacturing process and other bar properties.

Task 2: Strain-demands governing fatigue life in concrete frame members

Mechanics-based models were developed and calibrated to experimental data to correlate member global deformations with strain demands that govern the fatigue behavior of longitudinal bars in concrete frame members. A computational framework based on fiber-section elements and mechanics-based behavioral models is proposed to accurately estimate both member-level deformations and strain demands in longitudinal bars and the concrete surrounding them within the plastic hinge regions of

23

frame members. Particularly, the effects of the mechanical properties and steel grade of reinforcing bars on these strain demands are quantified by the proposed framework.

Prior to buckling, strain demands in longitudinal bars accumulate differently than in the post-buckling loading range. A model for predicting longitudinal bar buckling initiation and post-buckling strain demands in seismically detailed frame members is proposed. The model is based on estimates of local strain demands in longitudinal bars of members, the mechanical properties of the reinforcing bars, as well as the loading history the bars and surrounding concrete experience prior to buckling.

Task 3: Bar fracture estimation in frame members

Finally, a methodology combining the material-specific bar fatigue models with the strain-demand estimation models is proposed to determine the point in a seismic loading history at which longitudinal bars are expected to fracture. The proposed methodology was validated based on test results of several frame members tested in reversed cyclic loading.

1.3 Organization

This report is organized based on the tasks listed in the Objectives and Scope section. In Chapter 2 the test matrix of tests conducted within this project as well as those conducted as part of other projects is presented. In Chapter 3, a summary of the fatigue-life results is presented as well the proposed fatigue-life models. Chapter 4 describes the pre-buckling strain demand model developed within Task 2, while the buckling trigger, post-buckling strain-demand estimation and fracture point estimation are described in Chapter 5. Chapter 6 summarizes findings and conclusions.

2 LOW-CYCLE FATIGUE TESTING

Recent low-cycle fatigue testing of high-strength reinforcing bars (HSRB) have revealed a high variability in the number of half-cycles to fracture of HSRB being developed in the U.S., with some exhibiting much higher and others much lower fatigue lives than the benchmark grade 60 bars (Ghannoum and Slavin, 2016). These results spurred the reinforcing bar industry to seek further improvements in production methods and chemical compositions to improve the ductility and toughness of high-strength reinforcing bars, as well as an effort to better quantify the fatigue life of bars currently in production in the U.S. The authors of this report conducted several series of low-cycle fatigue tests on reinforcing bars in production is the U.S. within those broader objectives. In this report, the low-cycle fatigue tests and results from tests conducted as part of this study and other studies are compiled to arrive at comprehensive low-cycle fatigue models for steel reinforcing bars produced in the U.S. In this Chapter, the test methodology and test matrices are summarized, while the test results and fatigue models are presented in the subsequent Chapter.

2.1 Experimental Program

Results from three Series of tests conducted by the authors are included in this report.

Series 1: this test Series was conducted by Ghannoum and Slavin (2016), Slavin and Ghannoum (2015) and funded by the Charles Pankow Foundation as part of a previous

project. This was the original test series that raised concerns descried in Chapter 1 and spurred subsequent test series.

Series 2: Tests were conducted as part of Series 2 by the authors to quantify the mechanical properties of experimental batches of bars and aid in the development process of those bars. This test Series was therefore partially aimed at aiding certain steel mills in quantifying and improving the low-cycle fatigue performance of their HSRB. Additional tests were also conducted within this Series and within the scope of this project to fill in gaps in the test matrix, particularly with respect to manufacturing process, strain protocols, and unbraced length of bars.

Series 3: this test Series, conducted outside of the scope of this project, looked in more detail into the low-cycle fatigue performance of bars of various sizes from one manufacturing process and explored a wider range of strain protocols.

2.2 Test Matrix of Controlled Parameters

Parameters known to have a substantial impact on fatigue life were varied explicitly in the experimental programs. These primary parameters were manufacturer or manufacturing process, steel grade and ASTM designation, bar size, unbraced or clear span, and strain protocol. Other potentially influential parameters such as monotonic tension-test properties, chemical composition, and bar deformations were recorded but could not be varied deliberately by the research team.

Manufacturing process: Low-cycle fatigue tests were conducted on bars generated from three different manufacturing processes representative of the current production methods for HSRB in the United States. Manufacturing process 1 utilizes micro-alloying

to increase bar strength while limiting reductions in ductility with increasing bar strength. Manufacturing process 2 uses a quenching and tempering approach with minimal micro-alloying, while Manufacturing process 3 produces high-strength reinforcing bars satisfying the ASTM A1035 specifications using a patented micro-structure manipulation process. Additional detail about these three processes are described in Slavin and Ghannoum, 2015.

Steel grade and ASTM designation: a broad range of grades and ASTM designations were tested to aid in uncovering influential parameters on the fatigue-life of bars. Grade 60 and Grade 80 bars satisfying the ASTM A615 and A706 designations were tested. Grade 100 bars satisfying the ASTM A615 and A1035 specifications were also tested. Some of the grade 100 bars were tested prior to the introduction of grade 100 into the ASTM A615 standard but were manufactured with the intent to satisfy it and a possible grade 100 A706 specification that is being debated in the ASTM A706 committee at the time this report was written.

Bar size: a wide range of bar sizes used as longitudinal reinforcement and transverse reinforcement in concrete building structures were tested. The sizes tested are listed in Table 2-1, and ranged from #5 to #11.

Unbraced or clear span of bars: to simulate the effects of bar buckling on bar strain demands and fatigue-life of steel bars, the clear span between grips of the uni-axial testing machine was varied. The clear spans used ranged from $3.3d_b$ (d_b = bar diameter) to $8d_b$. At the higher end of the clear span significant buckling could be observed in the tests, while at the lower end, virtually no buckling was observed.

Strain protocols: to aid in developing comprehensive low-cycle fatigue models, a wide range of inelastic strain protocols were applied to bars until they fractured. The protocols used are listed in Table 2-1. The majority of tests were conducted in protocols with a relatively small compression strain (-0.5% or -1.0% strain) and larger tension strains (+2.0% to +6.0% strains). These protocols are representative of the strains experienced in longitudinal bars of concrete frame members (Sokoli and Ghannoum, 2015).

The nomenclature used to identify tests of all three series in this report is as follows:

Series# – Manufacturing Process# – Batch Number# – Grade# – ASTM Specification# – Bar Size# – Strain Protocol# – Clear Unbraced Length#

Example:

S02M3_1_100E08_P00P40_40db

Series# 01, 02, 03
Manufacturing Process# 1, 2, 3
Batch Number# 1, 2, 3, 4, 5
Grade# 60, 80, 100
ASTM Specification# A=A615, B=A706, C=Dual A615/706, E=A1035
Bar Size# #5, #8, #9, #10, #11
Strain Protocol# (ex: Negative 0.0% Positive 4.0%) N40P10, N30P10, N20P20, N10P30, N10P60, N10P50, N10P40, N05P10, N05P20, P00P40, P00P60
Clear unbraced length# $3.3d_b$, $3.6d_b$, $4d_b$, $4.5d_b$, $5d_b$, $6d_b$, $8d_b$

Table 2-1: TEST MATRIX INCLUDING NUMBER OF TESTS

		Manufacturing Process			Grade/ASTM Designation								Bar Size					Strain Protocols											Clear Unbraced Length (d_b)						
		M1	M2	M3	60 A615	60 A706	60 Dual	80 A615	80 A706	80 Dual	100 A615	100 A1035	#5	#8	#9	#10	#11	-0.5% to 1%	-0.5% to 2%	-3% to 1%	-2% to 2%	-1% to 3%	0% to 4%	-4% to 1%	-1% to 4%	-2% to 4%	0% to 6%	-1% to 6%	3.3	3.6	4	4.5	5	6	8
Manufacturing Process	M1	**231**	0	0	120	10	10	105	0	0	52	0	39	93	29	25	45	79	3	2	48	2	35	1	60	0	0	1	25	25	62	10	28	81	0
	M2	0	**225**	0	123	2	2	80	0	0	45	0	40	169	0	0	16	0	0	0	56	0	68	0	63	8	30	0	0	0	74	0	23	95	33
	M3	0	0	**70**	0	0	0	0	0	0	0	0	0	60	0	10	0	0	0	0	22	0	14	0	12	8	14	0	0	0	8	0	0	38	24
Grade/ASTM Designation	60-A615	120	123	0	**243**	0	0	0	0	0	0	0	44	178	0	0	21	79	3	2	57	0	49	0	34	0	12	0	25	25	69	10	23	101	20
	60-A706	10	2	0	0	**12**	0	0	0	0	0	0	0	2	0	0	10	0	0	0	0	0	0	0	12	0	0	0	0	0	5	0	0	5	2
	60-Dual	10	2	0	0	0	**12**	0	0	0	0	0	0	2	0	0	10	0	0	0	0	0	0	0	12	0	0	0	0	0	5	0	0	5	2
	80-A615	105	80	0	0	0	0	**185**	0	0	0	0	35	120	0	0	21	0	0	0	57	0	49	0	63	0	8	0	50	0	23	101	11	97	0
	80-A706	0	0	0	0	0	0	0	**0**	0	0	0	0	0	0	0	0	0	0	0	0	0	0	0	0	0	0	0	0	0	0	0	0	0	0
	80-Dual	0	0	0	0	0	0	0	0	**0**	0	0	0	0	0	0	0	0	0	0	0	0	0	0	0	0	0	0	0	0	0	0	0	0	0
	100-A615	52	45	0	0	0	0	0	0	0	**97**	0	35	52	0	0	10	10	2	0	19	0	36	0	34	0	8	0	0	0	18	0	23	45	11
	100-A1035	0	0	0	0	0	0	0	0	0	0	**0**	79	0	0	0	0	25	25	19	10	0	34	0	14	70	8	0	25	25	50	10	23	101	11
Bar Size	#5	39	40	0	44	0	0	35	0	0	35	0	**79**	0	0	0	0	0	0	0	0	0	72	0	7	0	0	0	25	25	19	10	0	54	0
	#8	93	169	60	178	2	2	120	0	0	52	0	0	**322**	0	0	0	10	1	0	120	0	45	0	87	16	44	0	0	0	98	0	26	131	57
	#9	29	0	0	0	0	0	0	0	0	0	0	0	0	**29**	0	0	19	2	0	6	0	0	1	1	0	0	0	0	0	29	0	0	0	0
	#10	25	0	10	0	0	0	0	0	0	0	0	0	0	0	**35**	0	25	0	0	6	0	0	0	4	0	0	0	25	0	4	0	0	10	0
	#11	45	16	0	21	10	10	21	0	0	10	0	0	0	0	0	**61**	25	0	0	0	0	0	0	36	0	0	0	25	0	17	0	19	0	0
Strain Protocols	-0.5% to 1%	79	0	0	79	0	0	0	0	0	10	0	0	10	19	25	25	**79**	0	0	0	0	0	0	0	0	0	0	25	25	19	10	0	54	0
	-0.5% to 2%	3	0	0	3	0	0	0	0	0	2	0	0	1	2	0	0	0	**3**	0	0	0	0	0	0	0	0	0	0	0	3	0	0	0	0
	-3% to 1%	2	0	0	2	0	0	0	0	0	0	0	0	0	0	0	0	0	0	**2**	0	0	0	0	0	0	0	0	0	0	2	0	0	0	0
	-2% to 2%	48	56	22	57	0	0	19	0	0	19	0	0	120	6	0	0	0	0	0	**126**	0	0	0	0	0	0	0	25	25	19	10	36	63	15
	-1% to 3%	2	0	0	0	0	0	0	0	0	0	0	0	0	0	0	0	0	0	0	0	**2**	0	0	0	0	0	0	0	0	2	0	0	0	0
	0% to 4%	35	68	14	49	0	0	36	0	0	36	0	72	45	0	0	0	0	0	0	0	0	**117**	0	0	0	0	0	0	0	15	0	25	62	15
	-4% to 1%	1	0	0	0	0	0	0	0	0	0	0	0	0	1	0	0	0	0	0	0	0	0	**1**	0	0	0	0	0	0	1	0	0	0	0
	-1% to 4%	60	63	12	34	0	0	34	0	0	34	0	7	87	1	4	36	0	0	0	0	0	0	0	**135**	0	0	0	0	0	43	0	14	70	8
	-2% to 4%	0	8	8	0	0	0	0	0	0	0	0	0	16	0	0	0	0	0	0	0	0	0	0	0	**16**	0	0	0	0	8	0	0	4	4
	0% to 6%	0	30	14	12	0	0	8	0	0	8	0	0	44	0	0	0	0	0	0	0	0	0	0	0	0	**44**	0	0	0	14	0	0	15	15
	-1% to 6%	1	0	0	0	0	0	0	0	0	0	0	0	0	0	0	0	0	0	0	0	0	0	0	0	0	0	**1**	0	0	1	0	0	0	0
Clear Unbraced Length (d_b)	3.3	25	0	0	25	0	0	0	0	0	0	0	25	0	0	25	25	25	0	0	0	0	0	0	0	0	0	0	**25**	0	0	0	0	0	0
	3.6	25	0	0	25	0	0	0	0	0	0	0	25	0	0	25	0	25	0	0	0	0	0	0	0	0	0	0	0	**25**	0	0	0	0	0
	4	62	74	8	69	5	5	50	0	0	18	0	19	98	29	4	15	19	3	2	36	2	15	1	43	8	14	1	0	0	**144**	0	0	0	0
	4.5	10	0	0	0	0	0	0	0	0	0	0	10	0	0	0	0	10	0	0	0	0	0	0	0	0	0	0	0	0	0	**10**	0	0	0
	5	28	23	0	23	0	0	23	0	0	23	0	0	25	0	0	14	0	0	0	12	0	25	0	14	0	25	0	0	0	0	0	**51**	0	0
	6	81	95	38	101	5	5	70	4	0	34	0	54	131	0	10	19	62	0	0	63	0	62	0	70	4	15	0	0	0	0	0	0	**214**	0
	8	0	33	24	20	2	2	11	0	0	11	0	0	57	0	0	0	0	0	0	15	0	15	0	8	4	15	0	0	0	0	0	0	0	**57**

2.3 Non-Controlled Parameters

2.3.1 Geometric Properties of Deformations

Three geometric parameters of the transverse bar deformations were considered for correlation with the cyclic fatigue performance of reinforcing bars: the ratio of the smaller of the two radii at the base of the deformation (R_{min}) to the height of the deformation (H), the ratio of the larger of the two radii at the base of the deformation (R_{max}) to the height of the deformation, and the ratio of the height of the deformation to the nominal diameter of the bar (d_b). For each bar type, at least three measurements were taken and the average was reported. The severity of curvature of the transverse ribs can cause stress concentrations from which fracture can propagate. Measurements were taken using the same high-resolution monochromatic camera used in the tests. Figure 2-1 shows an example image of bar deformations and overlaid measurements.
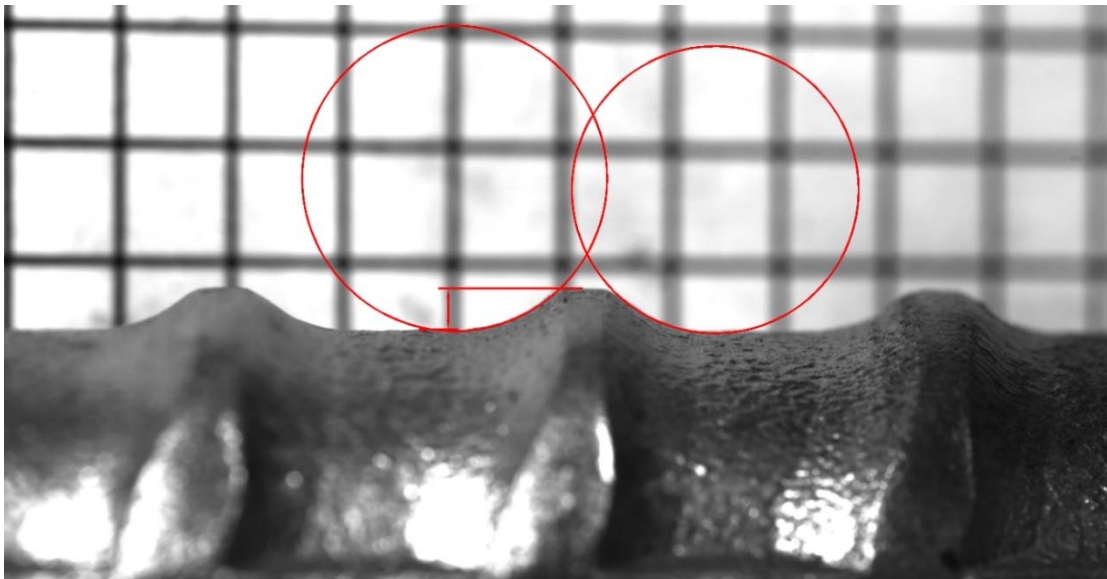
FIGURE 2-1: EXAMPLE OF GEOMETRIC DEFORMATION MEASUREMENTS FOR M1-B4-80-#8

Table 2-2 presents the ranges of bar deformation parameters for all the bars tested in the three series. One manufacturer producing bars using the Manufacturing process 2 (Quenching and Tempering) opted to soften the radius at the base of their bar deformations significantly based on results from tests of Series 1. The fatigue life of those bars improved substantially after that softening (see Section 3.2.3.1). Other manufacturers did not change their bar deformation throughout the testing programs but had relatively large deformation radii ($R_{min}/H > 1.5$ in general). All manufacturers used the same roll geometries to roll all bar grades, which resulted is similar bar deformation parameters across all grades as measured on the bars.

TABLE 2-2: BAR DEFORMATION GEOMETRIES

Bar Size	Manufacturing Process	Measured Bar Deformation					
		R_{min}/H		R_{max}/H		H/d_b	
		Min.	Max.	Min.	Max.	Min.	Max.
#5	1	1.27	2.55	1.72	3.00	0.03	0.04
	2 - Old Batch	0.63	3.22	0.86	4.94	0.04	0.05
	2 - New Batch	1.30	2.27	2.46	6.47	0.03	0.04
#8	1	0.43	3.41	0.69	3.68	0.03	0.06
	2 - Old Batch	1.32	2.27	1.81	2.31	0.05	0.06
	2 - New Batch	1.86	2.96	2.78	3.72	0.05	0.07
	3	1.54	1.68	2.44	4.87	0.05	0.06
#11	1	2.72	2.72	2.97	2.97	0.04	0.04
	2 - Old Batch	0.89	0.89	1.10	1.10	0.06	0.06

Batch 2 of the #8 bars produced using Manufacturing process 1 had surface geometry that differed significantly from any other bars. The grade 60 and grade 80 bars from M1-B2 had a single secondary longitudinal rib running along one of the longitudinal primary ribs, as can be seen in Figure 2-2 and Figure 2-3. The grade 100 bars had two

additional smaller longitudinal ribs on the same side of one of the primary longitudinal ribs. Figure 2-4 shows a front facing view of a grade 100 bar from batch 2 containing the secondary longitudinal ribs, and Figure 2-5 provides a view of the side of the same bar. The side opposite to the one seen in Figure 2-5 does not contain any additional longitudinal rib. This asymmetric cross-sectional geometry is important to note as it played an important role in determining the axis of buckling during cyclic testing. These bars sustained significantly fewer cycles to fracture than their counterparts from the same manufacturing process as is demonstrated in Section 3.2.3.2. For this reason, these bars were excluded from fatigue models and the use of bars with additional ribs such as those is strongly discouraged in seismic applications.

Figure 2-2: Front view of longitudinal geometry for M1-B2-60-#8

Figure 2-3: Front view of longitudinal geometry for M1-B2-80-#8

Figure 2-4: Front view of longitudinal geometry for M1-B2-100-#8
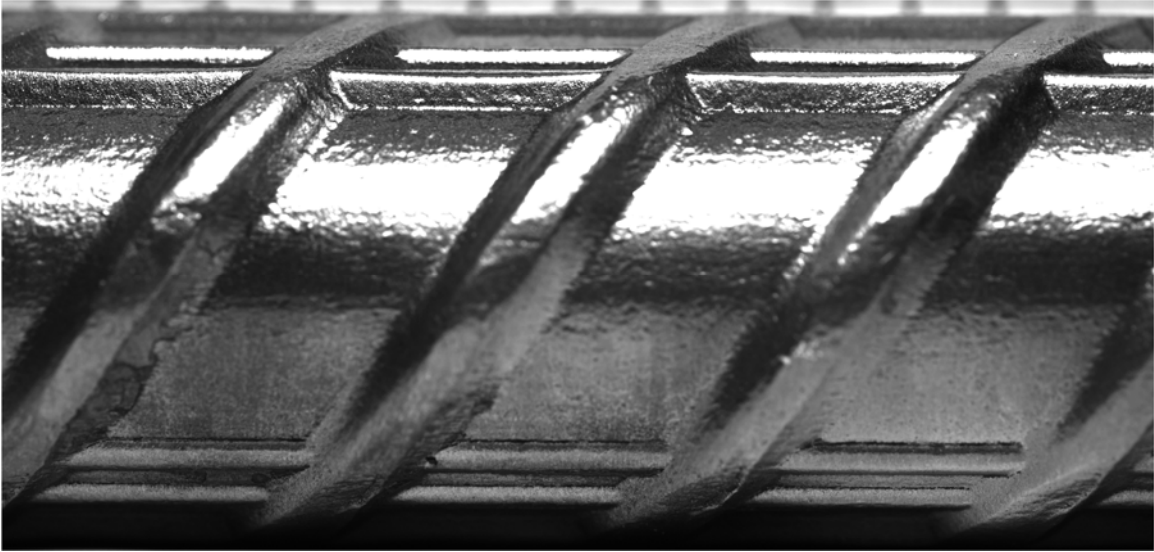
Figure 2-5: Side view of longitudinal geometry for M1-B2-100-#8

2.3.2 Chemical Composition

The chemical composition of bars tested in the three series as obtained from the manufacturer mill certifications were recorded and are summarized in Table 2-3.

TABLE 2-3: CHEMICAL COMPOSITION OF BARS TESTED IN FATIGUE

		Min.	Max.
Chemical Composition (%)	C	0.21	0.39
	Mn	0.81	1.43
	P	0.01	0.02
	S	0.02	0.05
	Si	0.16	0.33
	Cu	0.18	0.38
	Ni	0.06	0.13
	Cr	0.07	0.17
	Mo	0.01	0.053
	V	0	0.347
	Sn	0.008	0.015
	Al	0	0.003
	N	0	0.022
	Cb	0	0.04
	CEA	0.45	0.62

2.4 Monotonic Tension Tests

Tension tests were conducted for all batches of all series of steel bars to measure their tension properties and explore correlations between those properties and their fatigue life. Monotonic tension tests were conducted in conformance with procedures specified in ASTM A370 - Standard Methods and Definitions for Mechanical Testing of Steel Products and ASTM E8 - Standard Test Methods for Tension Testing of Metallic Materials for each batch of bars tested. The force-strain response of each specimen was collected during the test. Force was obtained via the load cell on the testing machine and divided by the nominal bar area as specified in ACI 318-14 to calculate stress. Strains were measured over an 8 inch gage length via digital image correlation software discussed below in the instrumentation section.

From the stress-strain response, mechanical monotonic properties were derived including yield strength, tensile strength, elastic modulus, yield strain, uniform strain and fracture strain. As not all bars had a clear yield point, the modulus of elasticity was defined as the initial elastic slope of the stress-strain curve to approximately 50% of the specified yield strength. Yield stress was extracted using the 0.2% method as detailed in ASTM E8 with yield strain defined as the strain at which yield stress first occurs. The tensile or ultimate strength represents the maximum recorded stress during a test. Uniform strain was calculated in accordance with ASTM E8, as the average of the two strains corresponding to 99.5% of the tensile strength. Fracture strain is the last strain at which force was measured in the specimen. The ratio of tensile strength to yield strength (T/Y) as well as the ratio of fracture strain to uniform strain were also evaluated from monotonic test data.

Lastly, the hardening strain was extracted as the strain at which the stress is reaches 1.01 times the yield stress, such that the difference between the hardening strain and yield strain reflects the strain length of the yield plateau.

2.5 Low-Cycle Fatigue Tests

All load-cycle fatigue tests were performed in a uni-axial test machine with two independent hydraulic gripping mechanisms. Each specimen was placed five to six inches into the gripping mechanisms to provide rotational fixity, simulating the boundary conditions that occur along longitudinal bars between transverse hoops. Both the top and bottom end sections of a bar that were to be gripped in the machine were swaged with ASTM 6063 aluminum tubing. This was necessary to distribute the applied grip pressure more evenly on the specimens and limit stress concentrations from developing at the grip interface. The swaging increased the likelihood of fracture occurring away from the grips and in the clear span. Any tests in which failure occurred at or near the gripping mechanisms was deemed to be unsuccessful and removed from subsequent analysis. Specimens were orientated such that weak axis buckling would occur perpendicular to the field of view of the monochromatic camera used in data acquisition. Specimens were cycled until fracture occurred. Two to ten successful tests per bar type and test parameters were conducted to quantify the variability in results. Figure 2-6 and Figure 2-7 show the experimental setup.

FIGURE 2-6: FRONT VIEW OF EXPERIMENTAL SETUP SHOWING TEST FRAME AND DIC CAMERA

FIGURE 2-7: SIDE VIEW OF EXPERIMENTAL SETUP SHOWING TEST FRAME AND DIC CAMERA

2.6 Instrumentation

The force applied to each of the bars was recorded from the load cell of the test machine. Due to the low strength of the aluminum swaging relative to the steel bars, the aluminum tubing experienced deformations during testing, which lead to discrepancies between actual bar deformations and the recordings of the actuator displacement. Therefore, tests were conducted via strain control measured in real time from targets attached directly to the bar surface. Bar strains were obtained using a digital image correlation (DIC) system dubbed the Ghannoum Vision System (GVIS). The system is described in detail in (Sokoli et al. 2014). A series of high-resolution images were recorded at a rate of several frames per second by a single monochromatic digital camera. A typical image obtained from the system can be seen in Figure 2-8.
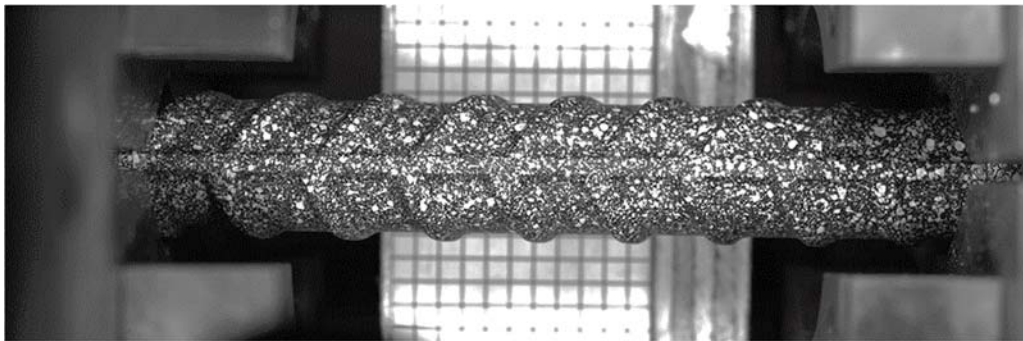
FIGURE 2-8: TYPICAL IMAGE OBTAINED FROM THE GVIS SYSTEM

The DIC software tracked the location of targets on the surface of the bars between subsequent frames. The GVIS system is able to provide strain resolutions on the order of 10^{-4} (Sokoli, et al. 2014). High-contrast surface targets were glued at each end of the bar specimens. For monotonic testing, three sets of targets were spaced eight inches apart in pairs to ensure that strains across the failure plane would be captured. For cyclic testing,

38

two targets were placed as close to the grips as allowable, to avoid regions of bar curvature which were generated during buckling. Therefore, all strains recorded in cyclic tests occurred just inside of the clear span of the grips. Figure 2-9 shows a prepared specimen before it was tested.
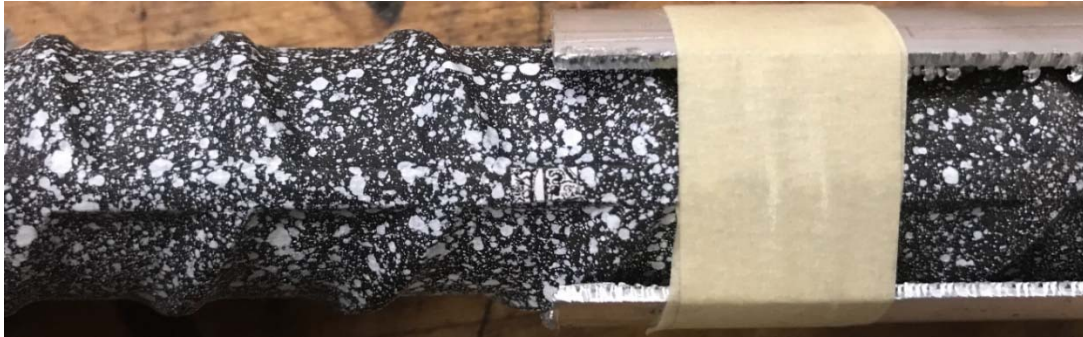
FIGURE 2-9: SPECIMEN PREPARATION WITH TARGETS AND ALUMINUM TUBING ATTACHED

Using the strain delivered by the GVIS system, a closed loop control system was implemented that allowed for automating the test procedure through strain control. For cyclic testing, the average value between sets of targets on either end of the specimen was calculated in real time and sent as feedback to the load frame control software. This automation allowed for tests to run continually from beginning to end without requiring user input. The applied strain protocol was sinusoidal with respect to time. All tests were conducted so that tension strains were imposed first prior to reversing loading direction. For cyclic tests in which the mean of the strain range of the protocol was not zero, the bars were first ramped to the mean or the bounding strains, before the sinusoidal procedure began. The rate of cyclic testing was selected to be at an average strain rate of 0.00025 in/in/s across the sinusoidal loading protocol for tests in Series 1 and Series 2. In Series 3 the loading rate was doubled as the number of cycles was large for that series.

39

3 BAR TESTING RESULTS AND LOW-CYCLE FATIGUE MODELS OF REINFORCING BARS

3.1 Monotonic Tension Test Results

A total of 144 monotonic tests were compiled in this study, consisted as 77 tests from manufacturing process 1 (M1), 55 tests from M2, and 12 tests from M3. Results of the monotonic tension tests of the bars of all three series are summarized in Table 3-1. **Error! Reference source not found.** through Figure 3-19 show the stress-strain relationship for sample batches of bars tested in this study with the different colors denoting each specimen tested and the dashed red line denoting the 0.2% offset used to calculate yield strength.
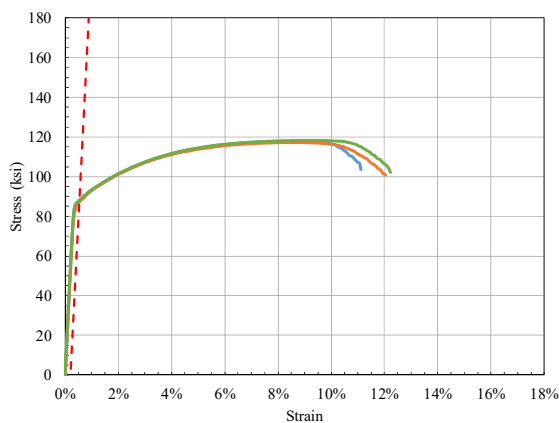
FIGURE 3-1: STRESS-STRAIN CURVES FROM MONOTONIC TENSION TESTS OF FROM M1-1-80B05
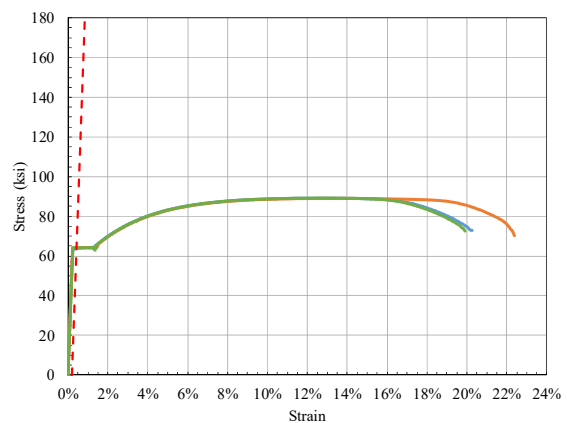
FIGURE 3-2: STRESS-STRAIN CURVES FROM MONOTONIC TENSION TESTS OF FROM M1-2-60B08

TABLE 3-1: MONOTONIC TENSION TEST RESULTS FOR ALL TEST SERIES

Monotonic Properties

Manufacturing Process	Grade	Yield Strength, ksi		Tensile Strength, ksi		T/Y ratio		Elastic Modulus, ksi		Elastic Limit Strain, %		Uniform Strain, %		Fracture Strain, %		Sample Size
		Min.	Max.	Min.	Max.	Min.	Max.	Min.	Max.	Min.	Max.	Min.	Max.	Min.	Max.	
M1	60	63.3	68.8	93.4	97.2	1.39	1.50	25,300	33,100	0.2	0.3	9.8	12.3	13.5	22.7	12
	80	78.9	88.2	106.1	118.4	1.28	1.44	25,000	37,200	0.2	0.4	8.5	12.7	11.1	19.5	53
	100	100.5	111.3	126.9	135.6	1.21	1.27	26,800	34,700	0.3	0.4	7.6	9	9.5	14	9
	120	117.7	121.6	139.3	143.3	1.18	1.19	27,800	32,600	0.4	0.4	7.5	8.3	11.4	12.2	3
M2	60	61.1	72.6	91.1	104.4	1.34	1.69	23,700	33,300	0.2	0.3	9.5	12.3	13.8	20	15
	80	83.7	100.3	103.1	119	1.19	1.29	23,500	30,500	0.3	0.4	6.3	10	10.1	15.2	19
	100	98.9	107	118.4	127.8	1.17	1.2	24,800	33,300	0.3	0.4	6.2	8.4	8.4	15	21
M3	100	113.9	125.7	159.7	165.6	1.3	1.43	27,800	35,300	0.3	0.5	4.9	5.5	11.0	12.2	12
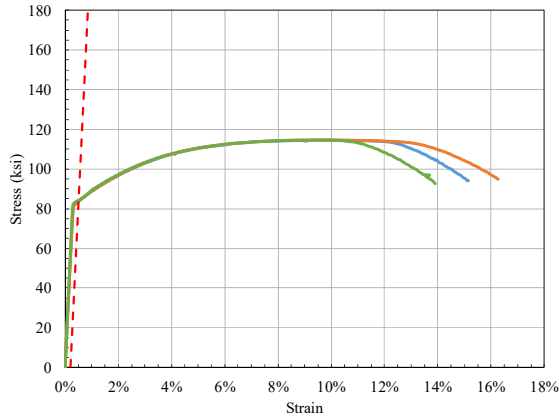
FIGURE 3-3: STRESS-STRAIN CURVES FROM MONOTONIC TENSION TESTS OF FROM M1-1-80B08
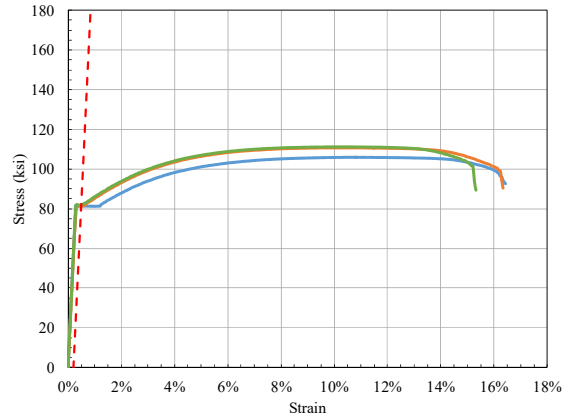
FIGURE 3-4: STRESS-STRAIN CURVES FROM MONOTONIC TENSION TESTS OF FROM M1-2-80B08
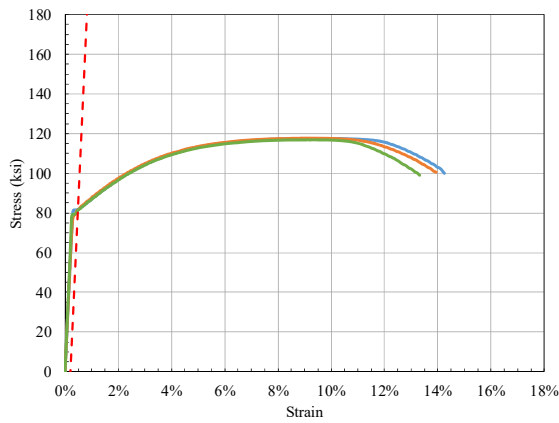
FIGURE 3-5: STRESS-STRAIN CURVES FROM MONOTONIC TENSION TESTS OF FROM M1-3-80B08
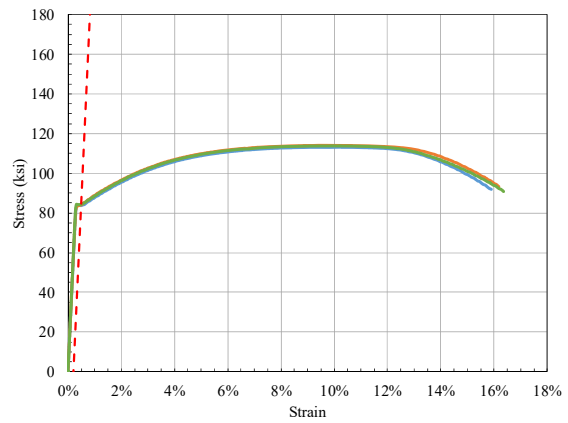
FIGURE 3-6: STRESS-STRAIN CURVES FROM MONOTONIC TENSION TESTS OF FROM M1-4-80B08
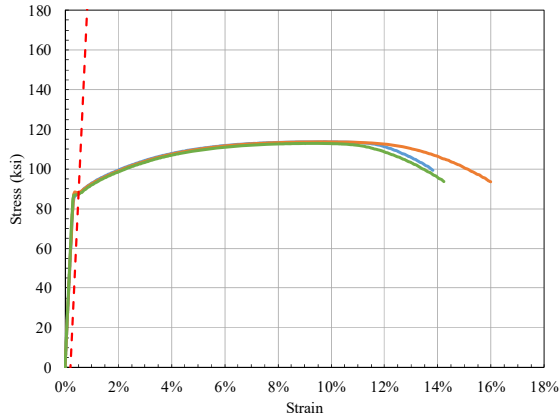
FIGURE 3-7: STRESS-STRAIN CURVES FROM MONOTONIC TENSION TESTS OF FROM M1-5-80B08
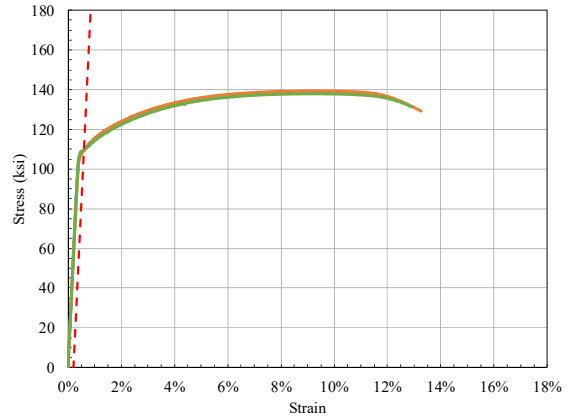
FIGURE 3-8: STRESS-STRAIN CURVES FROM MONOTONIC TENSION TESTS OF FROM M1-2-100A08
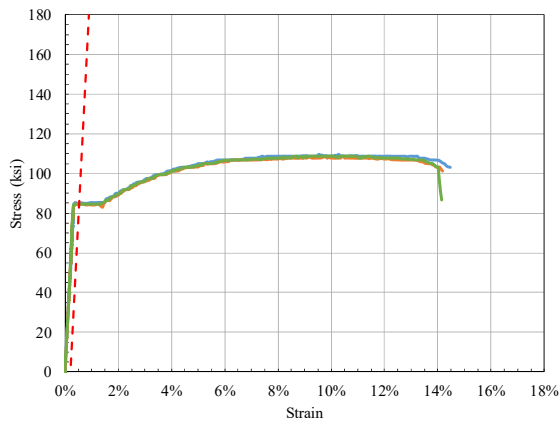
FIGURE 3-9: STRESS-STRAIN CURVES FROM MONOTONIC TENSION TESTS OF FROM M2-1-80A05
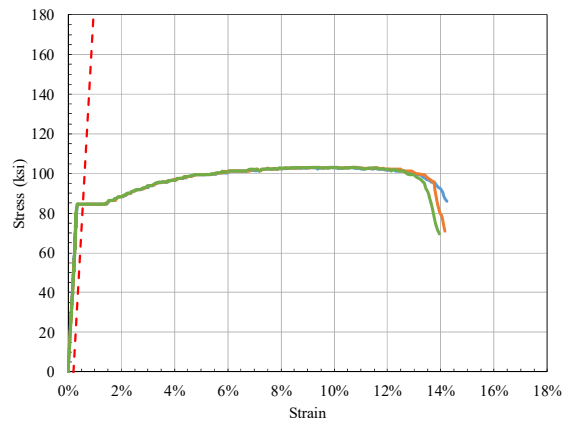
FIGURE 3-10: STRESS-STRAIN CURVES FROM MONOTONIC TENSION TESTS OF FROM M2-2-80A05
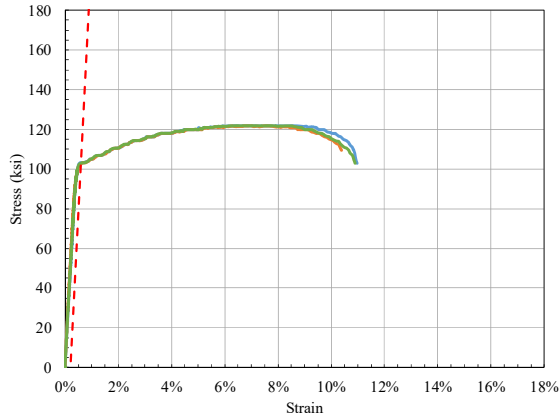
FIGURE 3-11: STRESS-STRAIN CURVES FROM MONOTONIC TENSION TESTS OF FROM M2-1-100A05
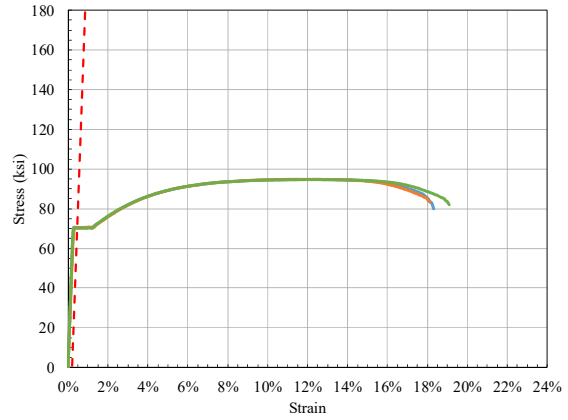
FIGURE 3-12: STRESS-STRAIN CURVES FROM MONOTONIC TENSION TESTS OF FROM M2-3-60A08
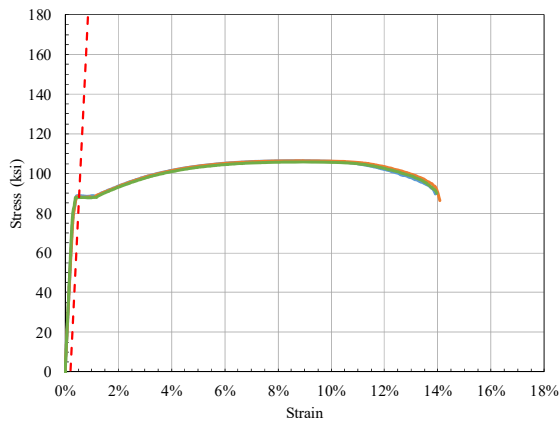
FIGURE 3-13: STRESS-STRAIN CURVES FROM MONOTONIC TENSION TESTS OF FROM M2-1-80A08
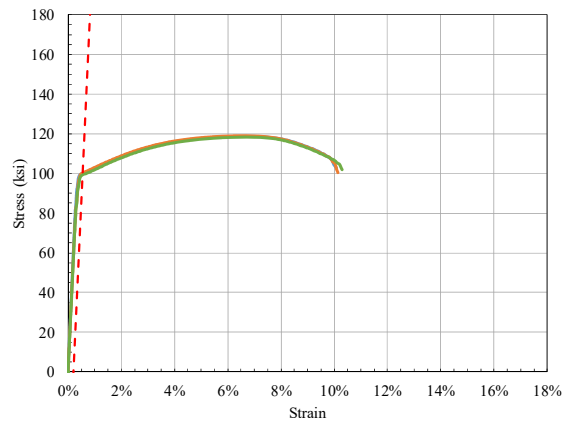
FIGURE 3-14: STRESS-STRAIN CURVES FROM MONOTONIC TENSION TESTS OF FROM M2-3-80A08
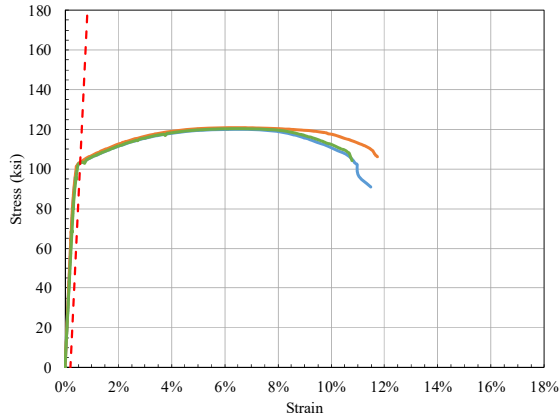
FIGURE 3-15: STRESS-STRAIN CURVES FROM MONOTONIC TENSION TESTS OF FROM M2-1-100A0#8
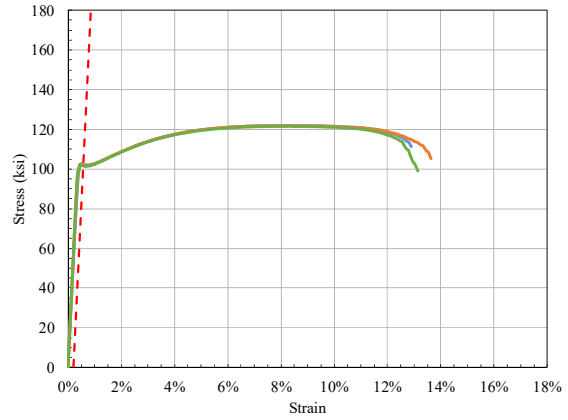
FIGURE 3-16: STRESS-STRAIN CURVES FROM MONOTONIC TENSION TESTS OF FROM M2-3-100A08
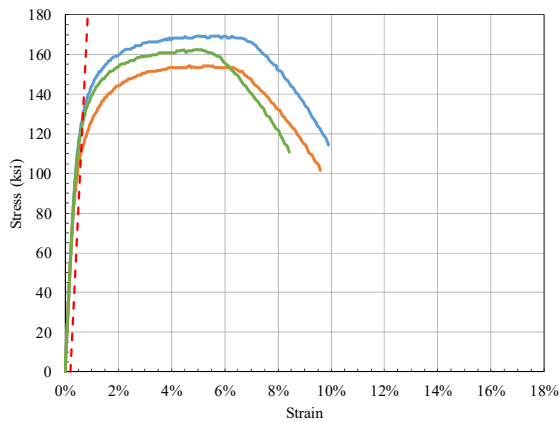
FIGURE 3-17: STRESS-STRAIN CURVES FROM MONOTONIC TENSION TESTS OF FROM M3-1-100E05
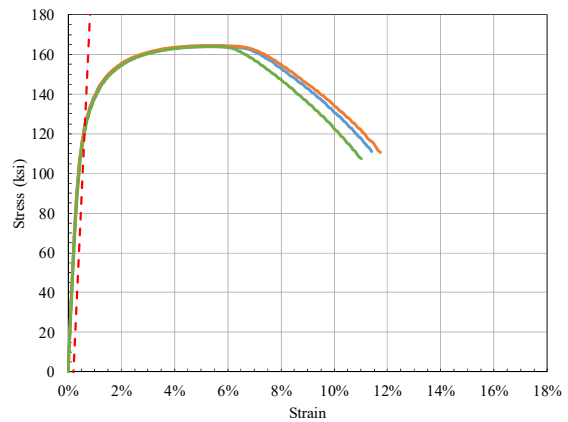
FIGURE 3-18: STRESS-STRAIN CURVES FROM MONOTONIC TENSION TESTS OF FROM M3-1-100E08

45
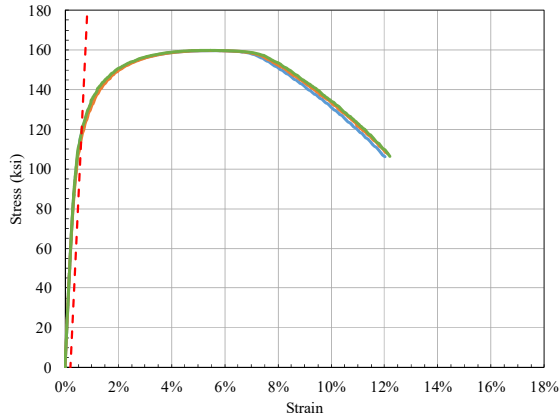
FIGURE 3-19: STRESS-STRAIN CURVES FROM
MONOTONIC TENSION TESTS OF FROM M3-2-
100E08

3.1.1 Observations from Monotonic Tests of Manufacturing Process 1 Bars

In general, M1 bars exhibited only minor variability in stress-strain relations between specimens of the same batch, size, and grade. Batch 2 grade 60 #8 M1 bars demonstrated little variability between specimens prior to reaching uniform strain but deviated from one another beyond that strain. The grade 80 #5 M1 bars exhibited a relatively long yield plateau, along with a uniform strain that is closer to the fracture strain than the yield strain, which corresponded with a smaller loss of strength before fracture. All five batches of grade 80 #8 bars from M1 tested in this study exhibited comparable monotonic properties, with a relatively short yield plateau and T/Y ratios that are approximately equivalent, with the exception of a single specimen from batch 2. Any variability between specimens of each batch occurred after uniform strain.

3.1.2 Observations from Monotonic Tests of Manufacturing Process 2 Bars

The grade 60 #8 M2 bars tested in this study showed little variation between specimens and had a yield strength that is approximately 10ksi higher than the specified 60ksi minimum. Both batches of grade 80 #5 M2 bars produced monotonic properties that are nearly equivalent with the exception of the elastic moduli and T/Y ratios. Batch 1 grade 80 #5 bars had higher elastic moduli and T/Y ratios than batch 2 grade 80 #5 bars. Batches 1 and 2 of the grade 80 #5 bars displayed a distinguished yield plateau with a length that is typical of grade 60 reinforcement. Batches 1 and 3 of the grade 80 #8 bars had significant differences in mechanical properties and stress-strain relations. Batch 3 grade 80 # 8 bars had yield strengths close to 100ksi and lower uniform and fracture elongations when compared to batch 1 bars. Batch 1 bars had a distinguished yield plateau that is similar to that found in the grade 60 bars from batch 3, while batch 3 grade 80 # 8 bars exhibited a distinct yielding point with little to no yield plateau. Batch 1 grade 100 #5 M2 bars had lower T/Y ratios and ductilities when compared to grade 80 bars. In addition, the grade 100 bars from M2 had a smaller yield plateau than bars of other grades. Batch 1 and batch 3 of the grade 100 #8 bars had nearly equivalent stress-strain properties, with the largest difference being in the length of the yield plateau.

Manufacturing process 2 could not consistently achieve the required T/Y ratio of 1.25 specified for grade 80 bars. The M2 quenching and tempering process typically produced lower T/Y ratios for grade 80 and 100 bars than the M1 micro-alloying process.

3.1.3 Observations from Monotonic Tests of Manufacturing Process 3 Bars

The grade 100 bars produced by manufacturing process 3 (M3) satisfied the ASTM A1035 specifications and lacked a clear yield point. The bars exhibited significantly higher yield and tensile strengths than other grade 100 bars tested in this study. The ratio of tensile strength to yield strength of these bars was, however, comparable to those of other grade 100 bars tested in this study. All bar sizes lost significant strength prior to fracture, up to 60ksi, after reaching uniform elongation, which corresponded with a relatively high ratio of fracture to uniform elongation and a significant reduction in cross sectional area or necking prior to fracture. The #5 bars from M3 exhibited significant variability between specimens of the same batch at all stages of the monotonic test; with yield strengths differing by 20ksi between specimens and tensile strength varying by 15ksi.

3.1.4 Relations for Fracture Strains

Fracture strain, ϵ_f is defined at the maximum tensile strain during a monotonic tension test that the bar undergoes when loss of load-carrying capacity occurred. This parameter can also be normalized to its yield (elastic limit) strain resulting in unit-less parameter called ductility ratio. Strong correlation between fracture strain and bar yield strength, f_y, and nominal diameter can be seen in Figure 3-20. Both manufacturing process 1 (M1) and M2 showed decreasing fracture strain as the yield strength increases, while M3 (all Grade 100) showed similar fracture strain values with other manufacturing and fracture strain for M1 and M2. Increasing fracture strain was observed for larger bar sizes for M1, while the reverse trend was observed for M2.

Equations based on linear regression analyses to estimate fracture strains for each manufacturing process are presented below (Equation 3-1(a), (b), and (c)). In Table 3-2 fracture strain values estimated using Equation 3-1(a), (b), and (c) for #8 bars and for $f_y = 60, 80, 100$ksi are provided. Estimated fracture strain values were within experimental limits given in Table 3-1. In Section 3.3, fracture strain was identified as an important parameter for fatigue life prediction. The fracture strain equations are used later in this report to estimate bar fatigue life.
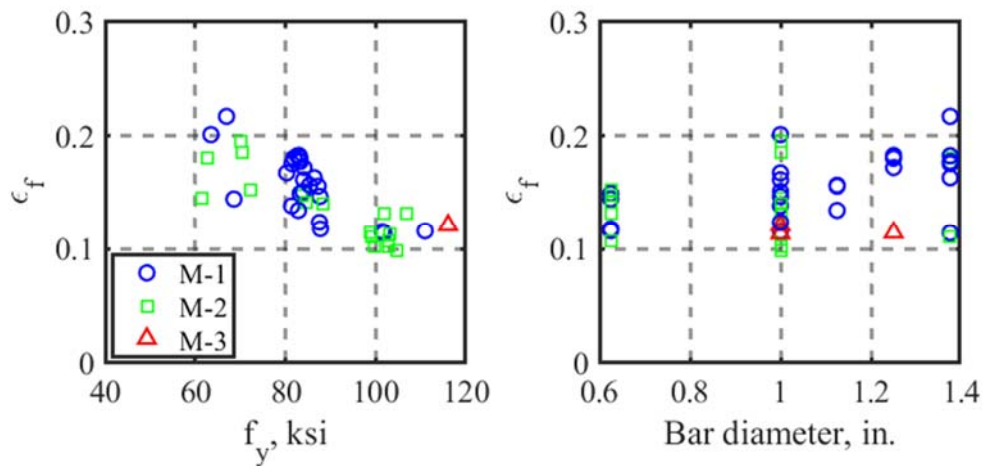
FIGURE 3-20: FRACTURE STRAIN TRENDS WITH RESPECT TO YIELD STRENGTH AND NOMINAL BAR DIAMETER

EQUATION 3-1: LINEAR RELATIONS FOR FRACTURE STRAIN

Manufacturing Process	Relations (ksi units)	Applicable Limits	Estimated / Exp. Parameters
1	$\varepsilon_f = 0.3 - 0.002f_y +$ $0.024\ dia.$ (a)	$60 \leq f_y \leq 110\ ksi$ $5/8" \leq dia. \leq 11/8"$	Mean = 1.01 Lognormal dispersion = 0.112
2	$\varepsilon_f = 0.25 - 0.001f_y -$ $0.024\ dia.$ (b)		Mean = 1.05 Lognormal dispersion = 0.13
3	$\varepsilon_f = 0.117$ (c)	$Grade\ 100$ $5/8" \leq dia. \leq 11/8"$	Mean = 1.0 Lognormal dispersion = 0.03

Note: f_y = bar yield strength (ksi), dia. = bar nominal diameter (in.)

TABLE 3-2: FRACTURE STRAIN VALUES FOR #8 BARS WITH YIELD STRENGTHS OF 60, 80, 100KSI

Manufacturing Process	Yield Strength f_y, ksi	Fracture Strain, ε_f
1	60	0.204
	80	0.164
	100	0.124
2	60	0.166
	80	0.146
	100	0.126
3	100	0.117

Nonlinear relations between fracture strain, ϵ_f, and bar yield strength could be observed in test data (Figure 3-21). In an attempt to improve estimates of fracture strain, nonlinear regression curves with their corresponding 95% confidence limits were fitted for each manufacturing process as illustrated in Figure 3-21. Power coefficients ranging from -0.5 to -1.0 were investigated. Implementation of a nonlinear relation between fracture strain and bar yield strength was found to improve the regression fit to data for manufacturing process 1 modestly over that of a linear relation (Equation 3-2). Nonlinear relations did not appreciably improve fit for the other two manufacturing processes.
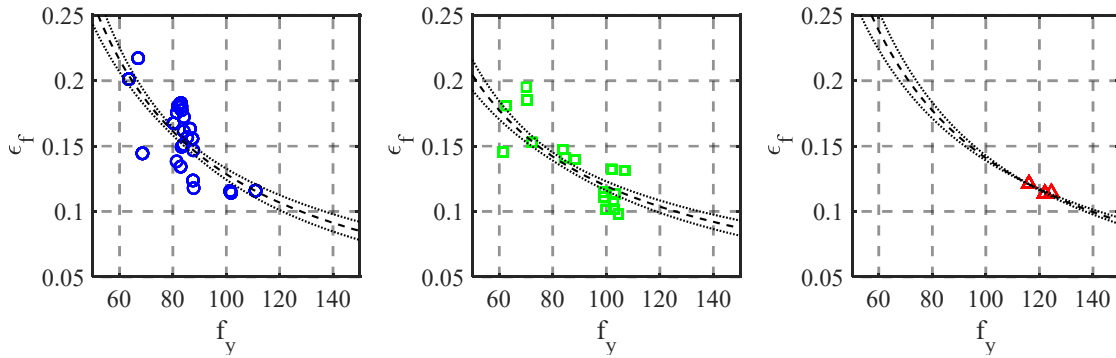
FIGURE 3-21: NONLINEAR REGRESSION FIT FOR FRACTURE STRAIN WITH RESPECT TO YIELD STRENGTH

EQUATION 3-2: NONLINEAR RELATION FOR FRACTURE STRAIN

Manufacturing Process	Relations (ksi units)	Applicable Limits	Estimated / Exp. Parameters
1	$\varepsilon_{f,nlm} = -0.05 + 12.8 f_y^{-1} + 0.048\,dia.$ (a)	$60 \le f_y \le 110\ ksi$ $5/8" \le dia. \le 11/8"$	Mean = 1.00 Lognormal dispersion = 0.105
2	$\varepsilon_{f,nlm} = -0.07 + 2.0 f_y^{-0.5} - 0.016\,dia.$ (b)		Mean = 0.98 Lognormal dispersion = 0.12

Note: f_y = bar yield strength (ksi), dia. = bar nominal diameter (in.)

3.1.5 Relations between Uniform and Fracture Strains

The uniform strain, ϵ_u, is defined as the strain reached at the bar tensile strength and immediately prior to the initiation of necking. Uniform strain was calculated according to ASTM E8 and reported in Table 3-1. The ratio of uniform to fracture strains is a unit-less measure that represents the strain range of the necking process prior to bar fracture.

Figure 3-22 shows trends of uniform strain (normalized to fracture strain) with respect to bar yield strength and nominal diameter. Overall, uniform strain magnitude was

51

found to be roughly more than half of the fracture strain. A decreasing trend between the strain ratio and bar size could be observed in the test data. This can be attributed, at least partially, to the constant 8 in. gage length used in the monotonic tests. A relatively constant ratio of uniform to fracture strain could be observed in Figure 3-22 with respect to yield strength. However, regression analyses indicated a relation with bar yield strength that improved the predictive strain-ratio relations as presented in Equation 3-3 (a), (b), (c).
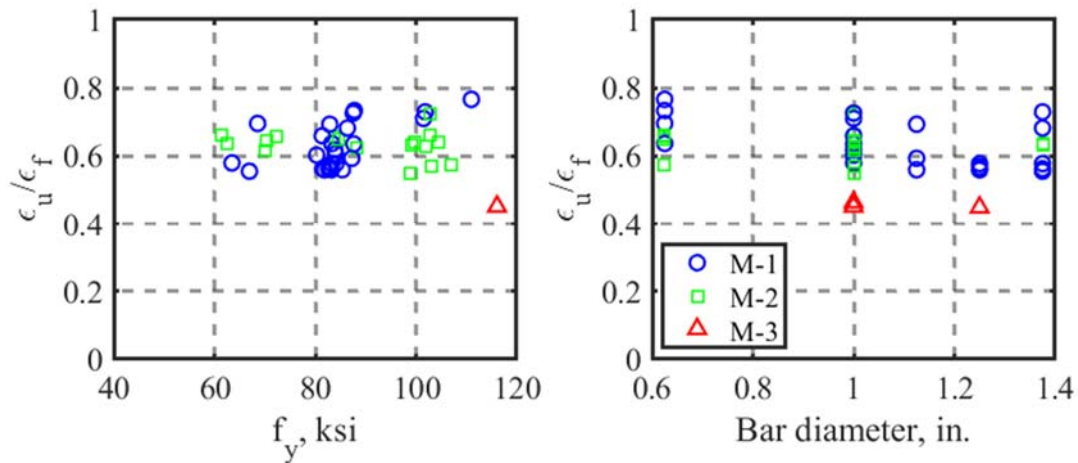
FIGURE 3-22: UNIFORM TO FRACTURE STRAIN RATIO WITH RESPECT TO YIELD STRENGTH AND NOMINAL BAR DIAMETER

EQUATION 3-3: RELATIONS OF UNIFORM TO FRACTURE STRAINS

Manufacturing Process	Relations (ksi units)	Applicable Limits	Estimated / Exp. Parameters
1	$\varepsilon_u/\varepsilon_f = 0.46 + 0.003f_y - 0.096\ dia.$ (a)	$60 \le f_y \le 110\ ksi$ $5/8" \le dia. \le 11/8"$	Mean = 0.95 Lognormal dispersion = 0.05
2	$\varepsilon_u/\varepsilon_f = 0.73 - 0.001f_y$ (b)		Mean = 1.01 Lognormal dispersion = 0.04
3	$\varepsilon_u/\varepsilon_f = 0.46$ (c)	$Grade\ 100$ $5/8" \le dia. \le 11/8"$	Mean = 1.0 Lognormal dispersion = 0.01

Note: f_y = bar yield strength (ksi), dia. = bar nominal diameter (in.)

3.1.6 Relations for T/Y Ratio

The T/Y ratio is defined as the tensile-to-yield strength ratio of the bars. Trends for the T/Y ratio for different manufacturing processes with respect to bar yield strength and diameter are shown in Figure 3-23. Decreasing T/Y magnitudes for higher yield values and relatively constant T/Y magnitudes over bar sizes were observed across manufacturing processes. Best fit equations for T/Y ratios based on linear regression are presented in Equation 3-4 (a), (b), and (c).
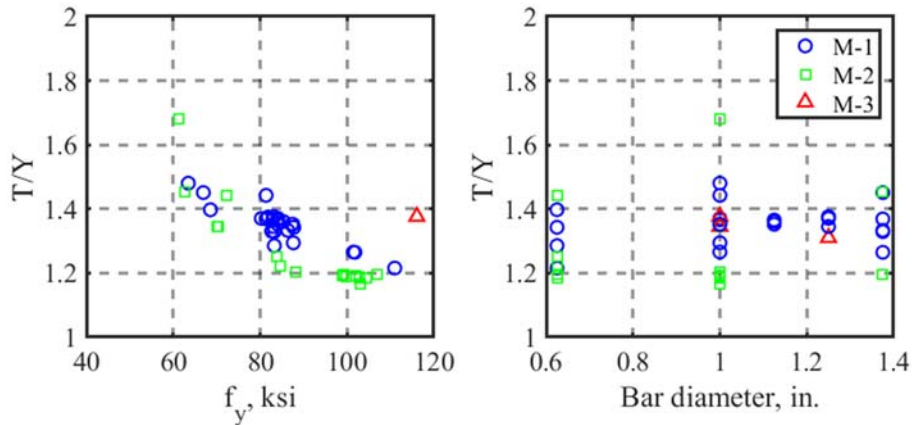
FIGURE 3-23: TENSILE TO YIELD STRENGTH RATIO TRENDS WITH RESPECT TO YIELD STRENGTH AND BAR SIZE

EQUATION 3-4: RELATIONS OF TENSILE TO YIELD STRENGTH RATIO

Manufacturing Process	Relations (ksi units)	Applicable Limits	Estimated / Exp. Parameters
1	$\frac{T}{Y} = 1.8 - 0.005f_y$ (a)	$60 \leq f_y \leq 110 \ ksi$	Mean = 1.02 Lognormal dispersion = 0.02
2	$\frac{T}{Y} = 2 - 0.008f_y$ (b)		Mean = 1.01 Lognormal dispersion = 0.05
3	$\frac{T}{Y} = 1.35$ (c)	$Grade \ 100$	Mean = 0.99 Lognormal dispersion = 0.02

Nonlinear relations between T/Y ratio and bar yield strength can be observed in Figure 3-24. To improve estimates on T/Y ratio, nonlinear regression curves with 95% confidence limits were fitted to data points. Power coefficients ranging from -0.3 to -0.6 were considered for bar yield strength in the regression analyses. Implementing nonlinear relations only improved dispersion measures for manufacturing process 2 and showed limited improvements for manufacturing process 1. Best-fit nonlinear relations for manufacturing processes 1 and 2 are shown in Equation 3-5 (a) and (b).
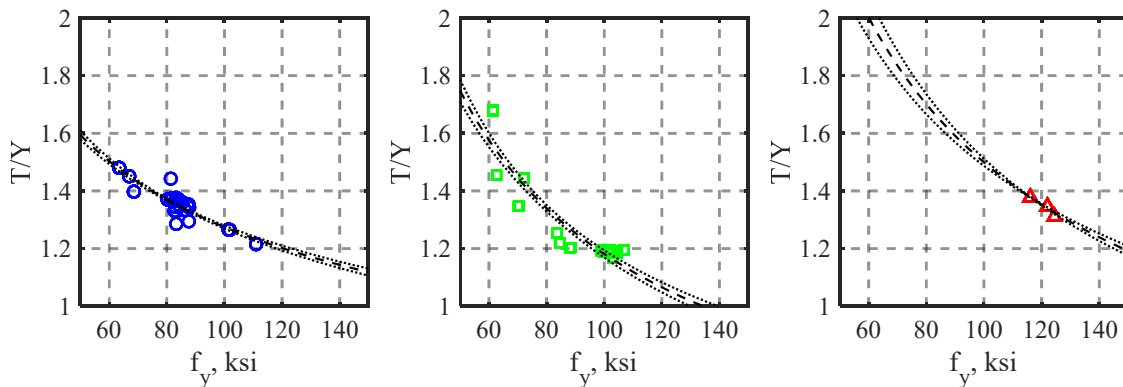
FIGURE 3-24: NONLINEAR REGRESSION FIT FOR TENSILE TO YIELD STRENGTH RATIO WITH RESPECT TO YIELD STRENGTH

EQUATION 3-5: NONLINEAR RELATION FOR TENSILE TO YIELD STRENGTH RATIO

Manufacturing Process	Relations (ksi units)	Applicable Limits	Estimated / Exp. Parameters
1	$\frac{T}{Y}, nlm = -0.1 + 5.5 f_y^{-0.3}$ (a)	$60 \leq f_y \leq 110\ ksi$	Mean = 1.01 Lognormal dispersion = 0.02
2	$\frac{T}{Y}, nlm = 0.1 + 17.3 f_y^{-0.6}$ (b)		Mean = 1.01 Lognormal dispersion = 0.04

3.2 Cyclic Test Results

3.2.1 General Behavior

A total of 526 fatigue tests were compiled in this study, consisting of 231 tests from manufacturing process 1 (M1), 225 tests from M2, and 70 tests from M3. Details of variation of controlled parameters for fatigue tests are available in Table 2-1. All tests started by pulling a bar coupon to its peak target tension strain before reversing loading direction to the opposite target bounding strain. A positive strain reported in this study implies a tensile strain measured from face to face of the clear gripping span. A negative strain indicates a compressive strain. Bars were loaded cyclically using strain control and experienced varying levels of strength degradation during the cycles resulting in compressive stresses in the bars as well as the cycles to peak tensile strains. Buckling and cracking of the bars contributed mainly to cyclic strength degradation.

Two main performance measures are used in this report to quantify fatigue life of bars. The number of half cycles to bar fracture (NHF) and the number of half-cycles until the bar stress at peak tensile strain dropped to 80% of the tensile stress measured during the first excursion to the peak tensile strain (NH80).

Cyclic strength degradation varied considerably with clear gripping span and between manufacturing processes. Typically, bars gripped at longer clear spans and sustaining greater lateral buckling amplitudes experienced more pronounced cyclic strength degradation than the equivalent bars tested at a tighter clear span. Figure 3-25, Figure 3-29, and Figure 3-34 overlay the stress-strain response for different clear spans for each manufacturer. Figure 3-26, Figure 3-30, Figure 3-35 plot the progression of tension

and compression peak stresses per cycle normalized by the first cycle peak tensile stress. It can be seen in these figures that as clear gripping span increases, the compressive strength of the bar decreases.

At a gripping span of $4d_b$, limited bar buckling was typically observed, while at $6d_b$ and $8d_b$ clear spans, significant buckling could be observed for all grades and manufacturing processes. Figure 3-27, Figure 3-28, Figure 3-31, Figure 3-32, Figure 3-33, Figure 3-36, Figure 3-37 contrast the buckling amplitude at the final compression cycle for different clear spans for each manufacturing process.
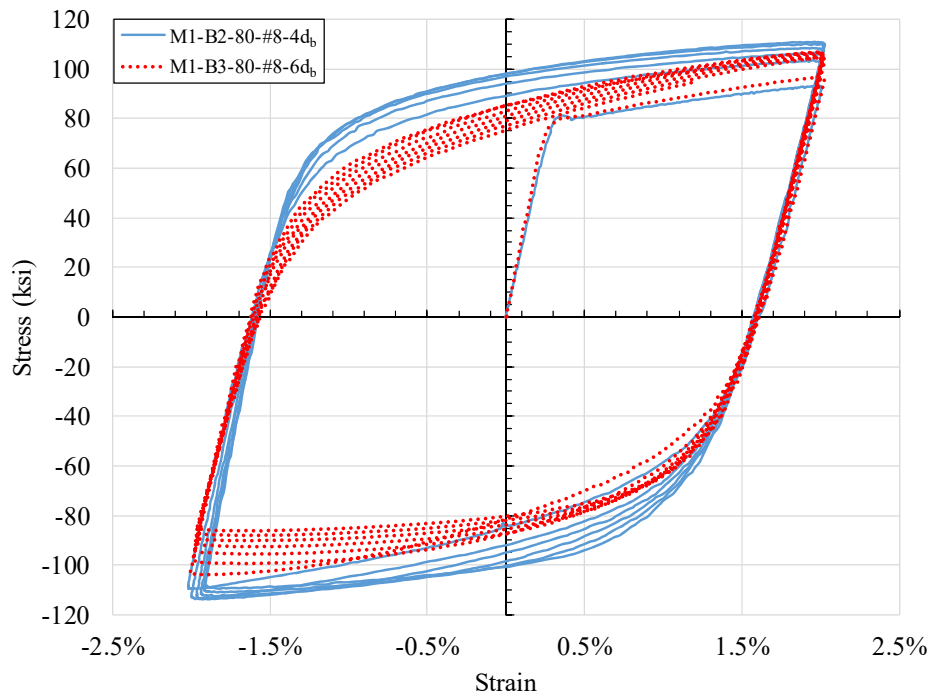
FIGURE 3-25: CYCLIC STRENGTH DEGRADATION COMPARISON FOR #8 BARS FROM MANUFACTURING PROCESS 1 TESTED AT DIFFERENT CLEAR SPANS
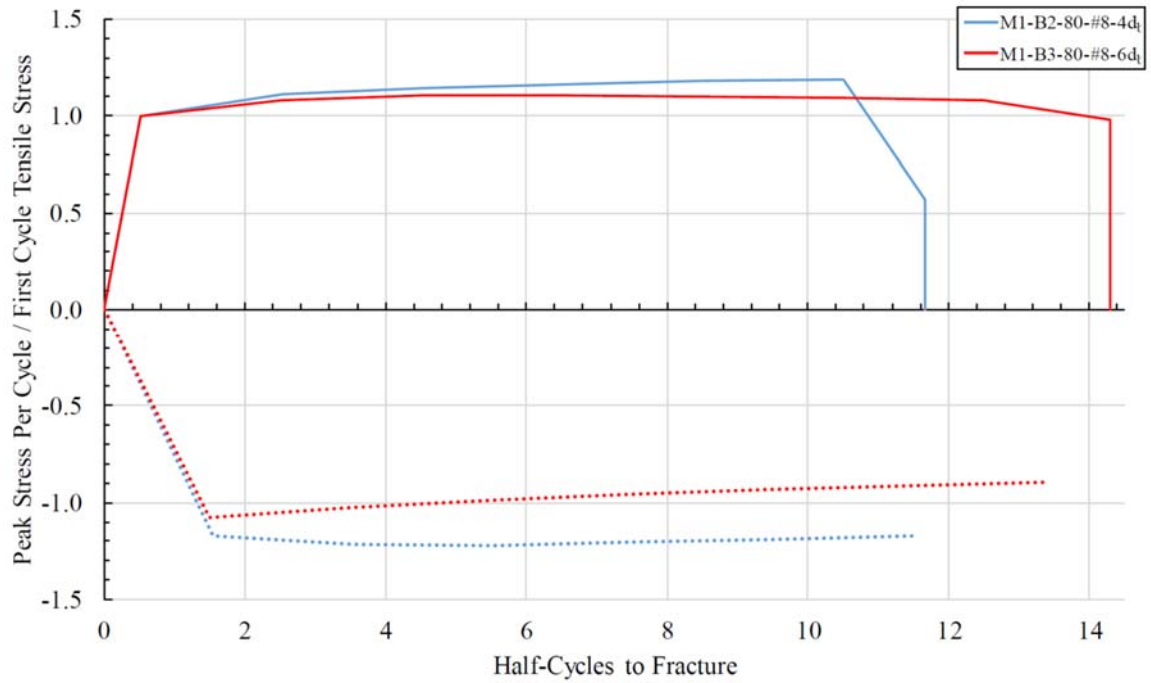
FIGURE 3-26: PROGRESSION OF PEAK STRESSES PER CYCLE FOR #8 BARS FROM MANUFACTURING PROCESS 1 TESTED AT DIFFERENT CLEAR SPANS
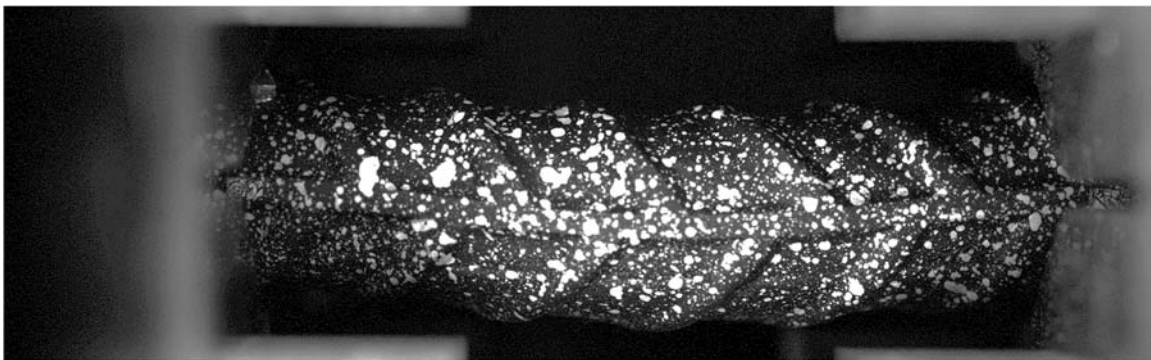
FIGURE 3-27: FINAL COMPRESSION CYCLE FOR A M1-2-80B08-4d$_B$ SPECIMEN UNDER THE +2% TO -2% STRAIN PROTOCOL
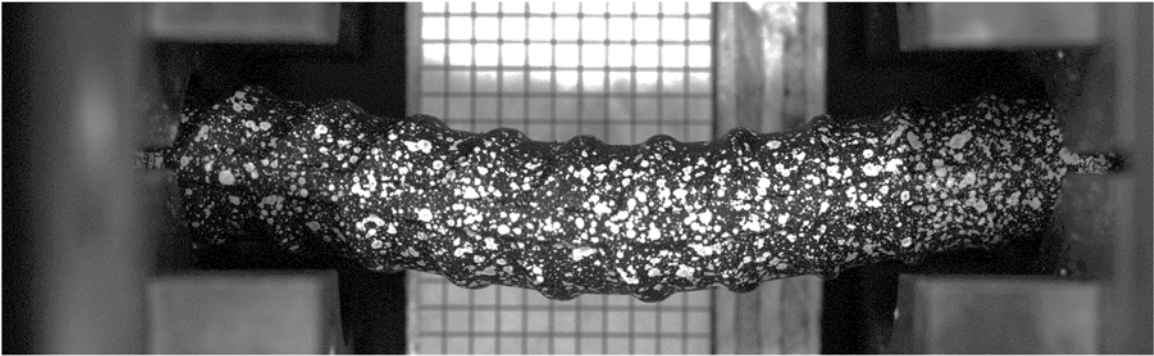
FIGURE 3-28: FINAL COMPRESSION CYCLE FOR A M1-3-80B08-6d$_B$ SPECIMEN UNDER THE +2% TO -2% STRAIN PROTOCOL
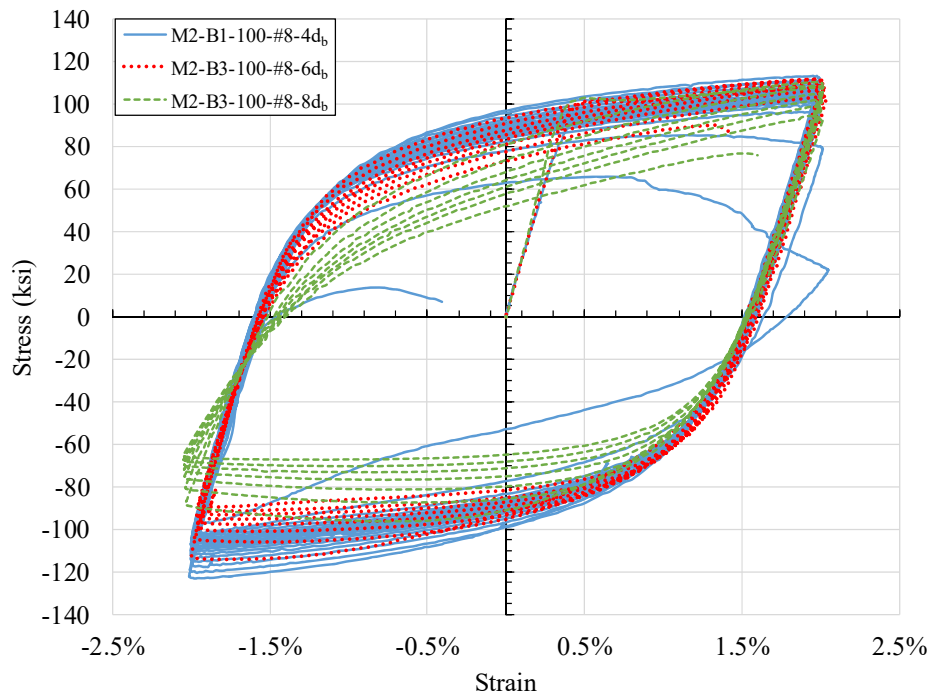
FIGURE 3-29: CYCLIC STRENGTH DEGRADATION COMPARISON FOR #8 BARS FROM MANUFACTURING PROCESS 2 TESTED AT DIFFERENT CLEAR SPANS
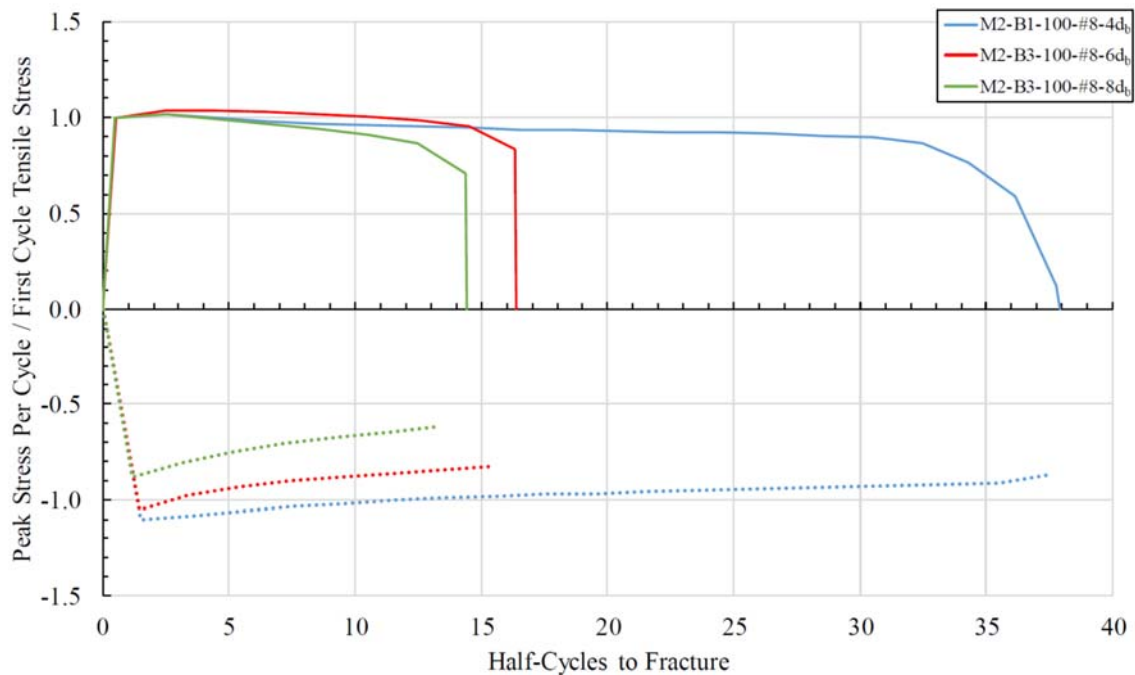
FIGURE 3-30: NORMALIZED CYCLIC ENVELOPE COMPARISON FOR #8 BARS FROM MANUFACTURING PROCESS 2 TESTED AT DIFFERENT CLEAR SPANS
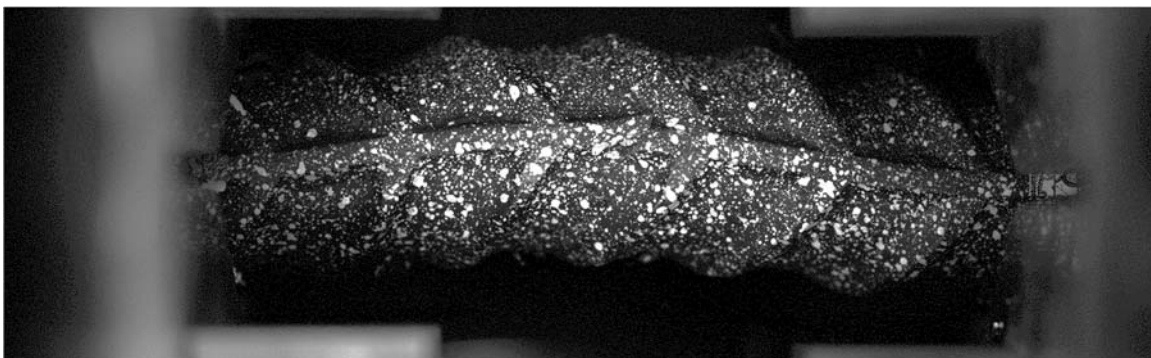
FIGURE 3-31: FINAL COMPRESSION CYCLE FOR A M2-1-100A08-4d$_B$ SPECIMEN UNDER THE +2% TO -2% STRAIN PROTOCOL
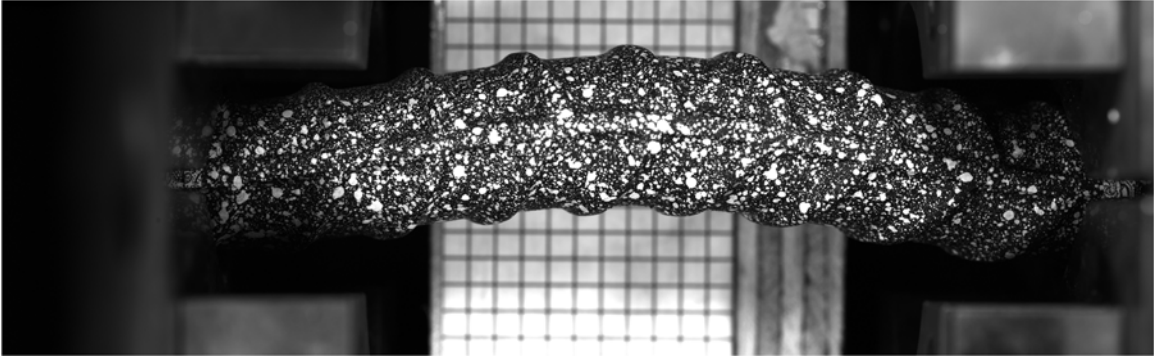
FIGURE 3-32: FINAL COMPRESSION CYCLE FOR A M2-3-100A08-6d$_B$ SPECIMEN UNDER THE +2% TO -2% STRAIN PROTOCOL
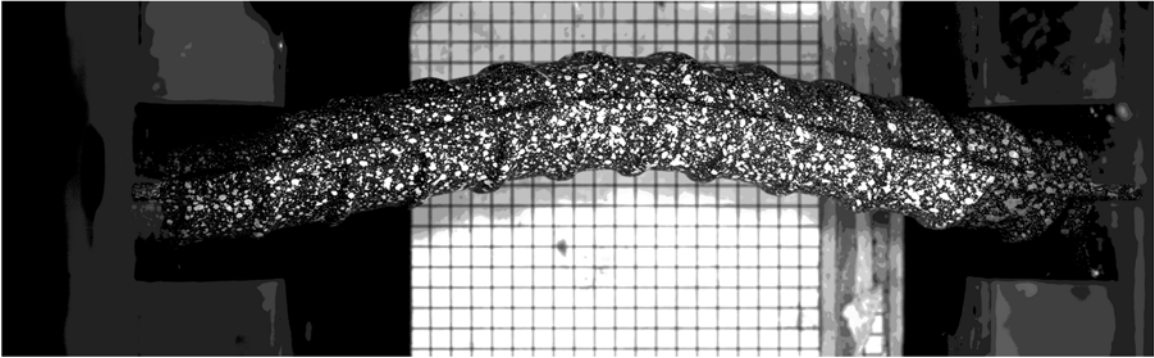
FIGURE 3-33: FINAL COMPRESSION CYCLE FOR A M2-3-100A08-8d$_B$ SPECIMEN UNDER THE +2% TO -2% STRAIN PROTOCOL
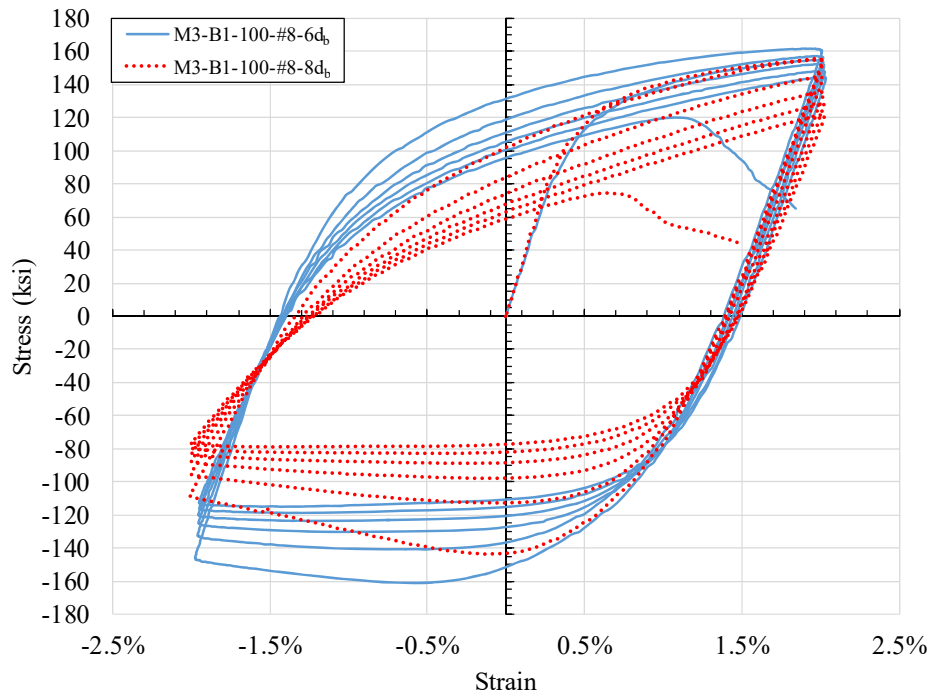
FIGURE 3-34: CYCLIC STRENGTH DEGRADATION COMPARISON FOR #8 BARS FROM MANUFACTURING PROCESS 3 TESTED AT DIFFERENT CLEAR SPANS
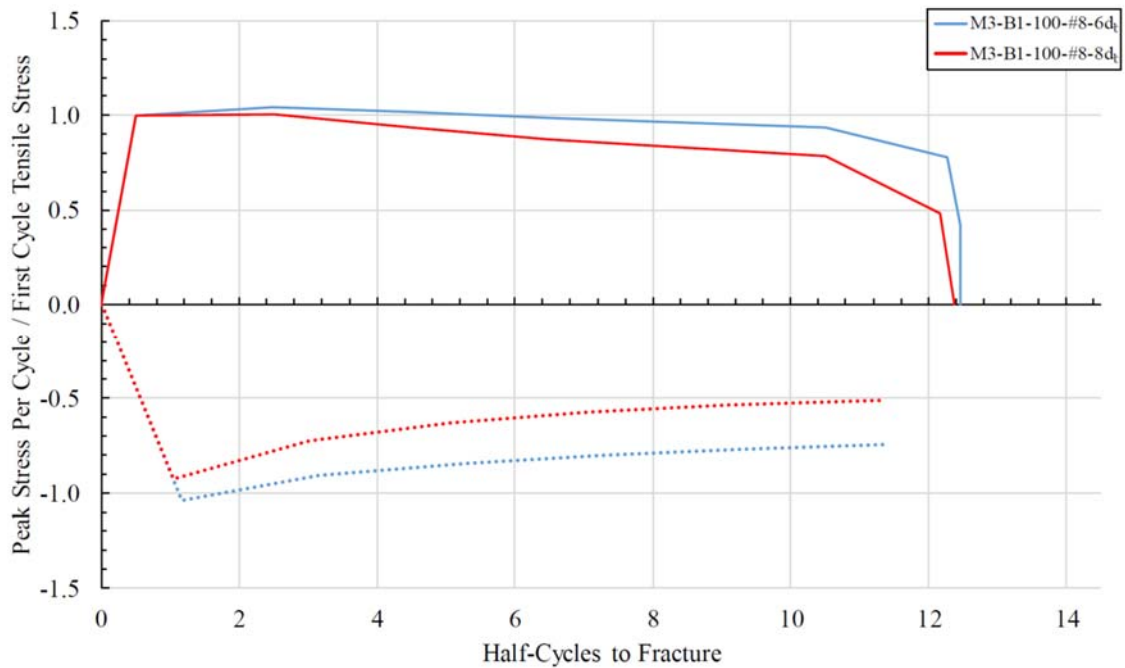
FIGURE 3-35: NORMALIZED CYCLIC ENVELOPE COMPARISON FOR #8 BARS FROM MANUFACTURING PROCESS 3 TESTED AT DIFFERENT CLEAR SPANS

61
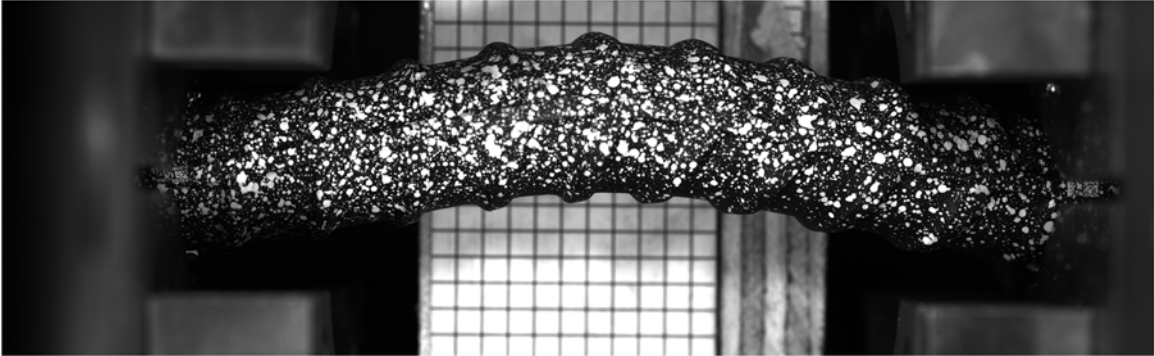
FIGURE 3-36: FINAL COMPRESSION CYCLE FOR A M3-1-100E08-6d$_B$ SPECIMEN UNDER THE +2% TO -2% STRAIN PROTOCOL
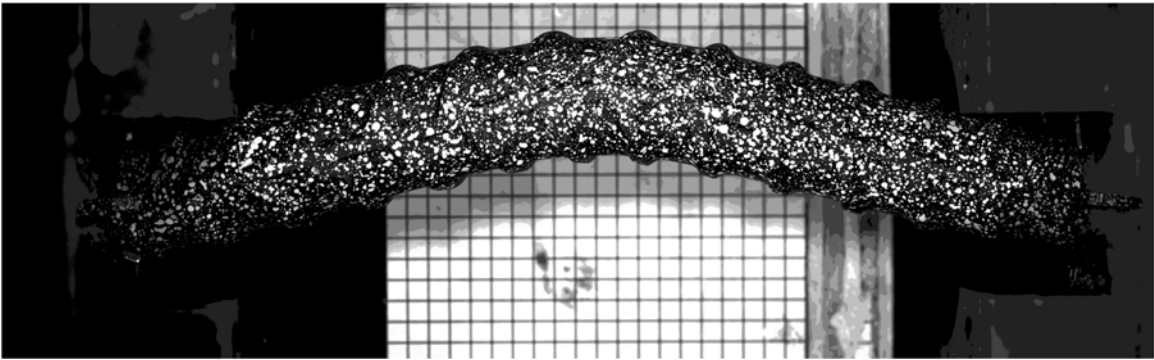
FIGURE 3-37: FINAL COMPRESSION CYCLE FOR A M3-1-100E08-8d$_B$ SPECIMEN UNDER THE +2% TO -2% STRAIN PROTOCOL

Figure 3-38, Figure 3-39, and Figure 3-40 contrast the stress-strain response of two grade 80 #8 bars from manufacturing processes1 and 2, as well as a grade 100 bar from manufacturing process 3 tested under the same clear span of 6d$_b$ and loading strain protocol of +4% to -1%. The dashed line in the figures denotes 80% of the tensile strength reached when the bars reached their peak tensile strain of +4% strain for the first time. The trends in the plots discussed herein are typical for each manufacturer and relatively insensitive to bar grade, which indicates larger dependency of the stress-strain relations on the manufacturing process. As can be seen in Figure 3-38, the grade 80 bars produced by manufacturing process 1 typically sustained relatively low cyclic strength degradation

62

before a sudden brittle fracture occurs. On the other hand, the grade 80 bars produced by manufacturing process 2 exhibited similar strength degradation as bars from manufacturing process 1 in the initial cycles but did not typically sustain a sudden fracture (Figure 3-39). M2 bars generally experienced larger numbers of cycles to fracture than M1 bars and sustained gradually widening fatigue cracks that resulted in significant strength degradation before fracture occurred. The final tensile strength just prior to fracture can be seen to drop to approximately 60% of the initial tensile strength of the M2 bar.
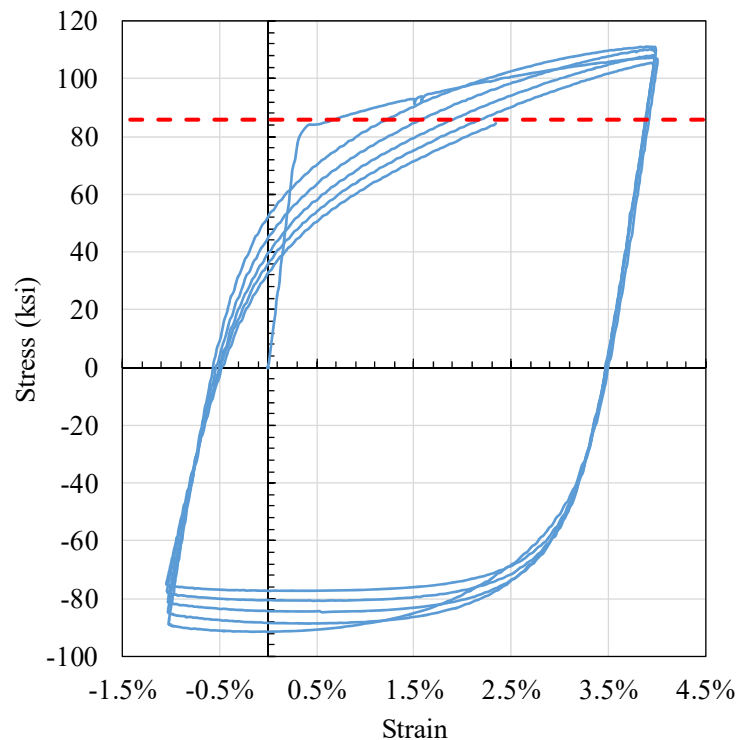
FIGURE 3-38: STRESS-STRAIN PLOT FOR A M1-1-80B08-6d$_B$ BAR UNDER THE +4% TO -1% STRAIN PROTOCOL (10.5 HALF-CYCLES TO FRACTURE)
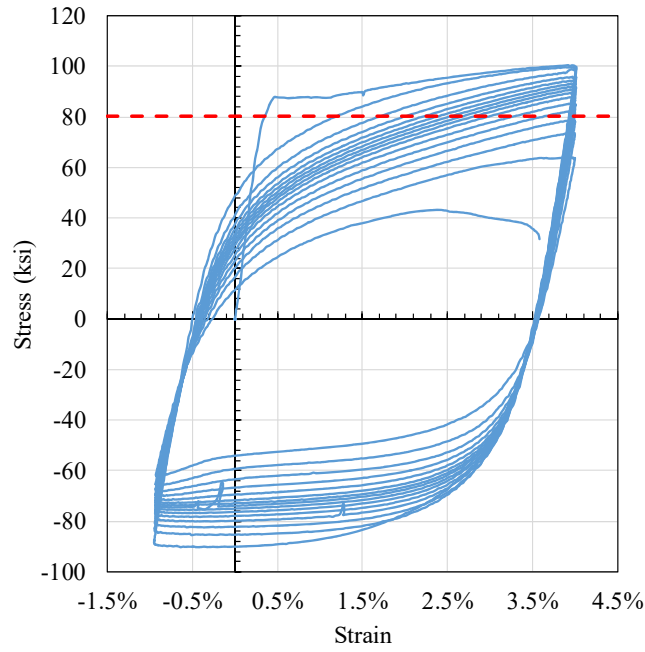
FIGURE 3-39: STRESS-STRAIN PLOT FOR A M2-1-80A08-6d$_B$ BAR UNDER THE +4% TO -1% STRAIN
PROTOCOL (30.7 HALF-CYCLES TO FRACTURE, 23.8 HALF-CYCLES TO 80% CAPACITY)
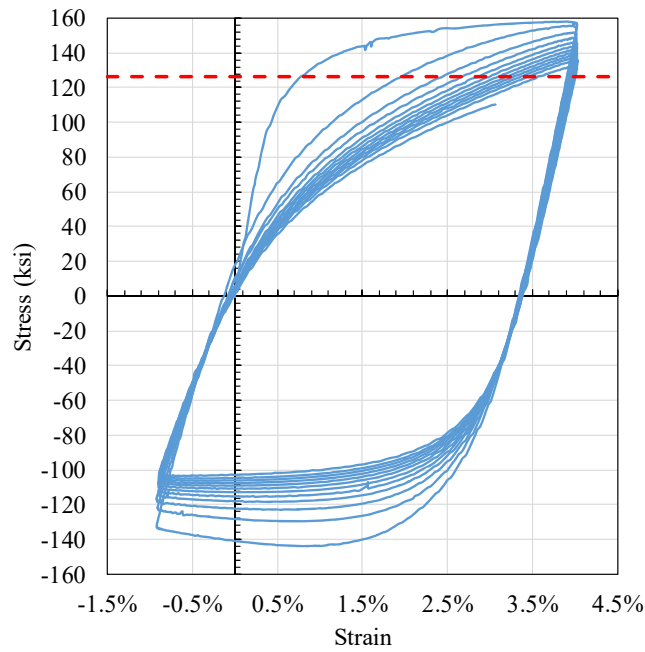
FIGURE 3-40: STRESS-STRAIN PLOT FOR A M3-2-100E08-6d$_B$ BAR UNDER THE +4% TO -1%
STRAIN PROTOCOL (24.6 HALF-CYCLES TO FRACTURE)

For M1 bars, a crack would initiate around mid-span and propagate rapidly through the cross section of the bar as seen in Figure 3-41. In contrast, bars from M2 saw cracks initiating on the compression side of buckling that ran along the transverse deformations and gradually increased in length and width until full fracture occurred. Figure 3-42 shows the fracture planes of a typical M2-1-80A08-6d$_b$ bar. A typical fracture plane of a bar from M3 can be seen in Figure 3-43.
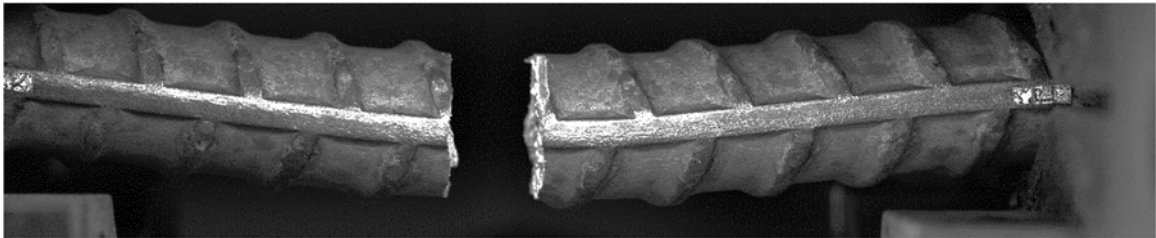
FIGURE 3-41: FRACTURE PROFILE TYPICAL OF A M1-1-80B08-6d$_B$ BAR UNDER THE +4% TO -1% STRAIN PROTOCOL
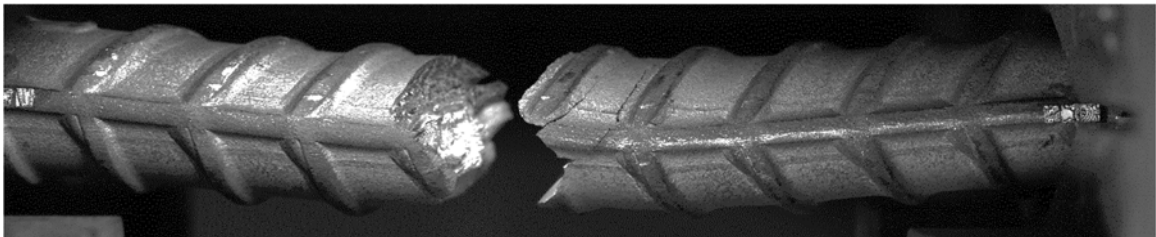
FIGURE 3-42: FRACTURE PROFILE TYPICAL OF A M2-1-80A08-6d$_B$ BAR UNDER THE +4% TO -1% STRAIN PROTOCOL
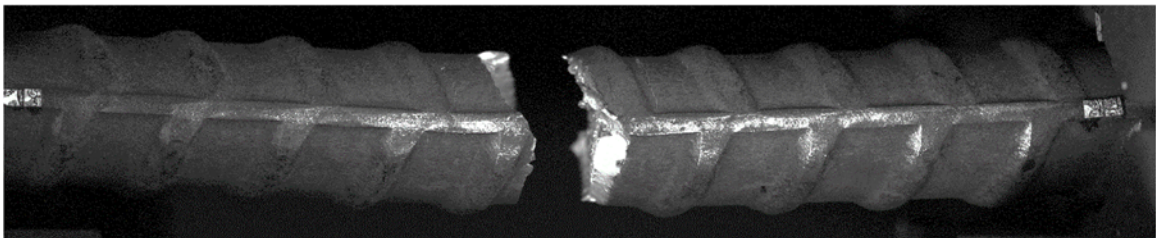
FIGURE 3-43: FRACTURE PROFILE TYPICAL OF A M3-2-100E08-6d$_B$ BAR UNDER THE +4% TO -1% STRAIN PROTOCOL

Along with a reduction in strength, bars from M2-1-80A08 typically experienced a reduction in stiffness as cracks begin to propagate through the cross section. During compression cycles, this reduction in stiffness causes the bars to reach increased buckling amplitudes. Figure 3-44 and Figure 3-45 contrast the first compression cycle and the last compression cycle before fracture for the M2-1-80A08 specimen from Figure 3-39. It can be clearly seen that the buckling amplitude in the last compression cycle is significantly greater than the amplitude experienced during the first compression cycle to the same target strain.
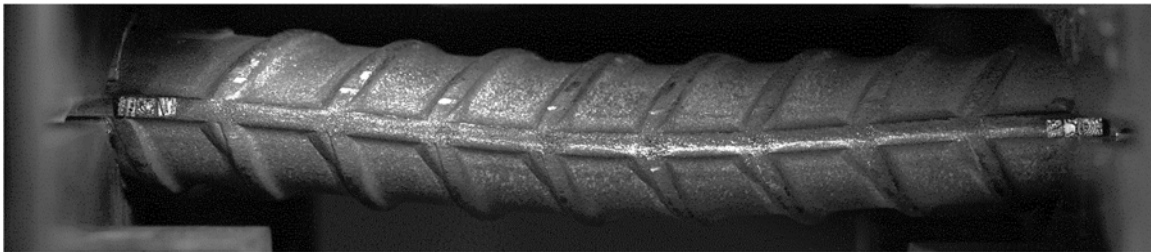
FIGURE 3-44: FIRST COMPRESSION CYCLE FOR A M2-1-80A08-6d$_B$ SPECIMEN UNDER THE +4% TO -1% STRAIN PROTOCOL
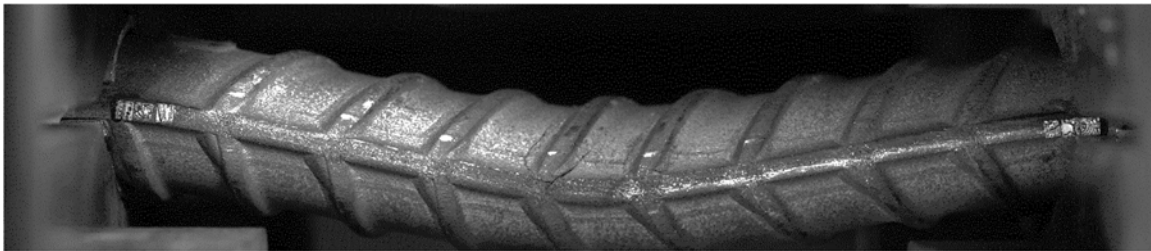
FIGURE 3-45: FINAL COMPRESSION CYCLE FOR A M2-1-80A08-6d$_B$ SPECIMEN UNDER THE +4% TO -1% STRAIN PROTOCOL

Figure 3-46 through Figure 3-51 show the crack development and growth during the peaks of the final tensile half-cycles prior to bar fracture for a typical M2-1-80A08-6d$_b$ bar. In Figure 3-46, cracks are visible, but the specimen is only experiencing a 13%

reduction in strength from its initial tensile capacity. Figure 3-47 and Figure 3-48 show the formation of additional fatigue cracks in the same direction as the transverse ribs as well as the widening of existing cracks. The tensile stress achieved by the bar at peak tensile strain is slightly above the 80% threshold at this stage. In Figure 3-49, the cracks begin to cut across the longitudinal rib. After this half-cycle, the reduction in tensile strength from cycle to cycle starts to increase. By Figure 3-50, the crack widths are substantially larger than four half-cycles prior and the bar experiences a reduction of capacity of 27%. Figure 3-51 shows the state of the bar in the final complete tensile half-cycle before fracture occurs.
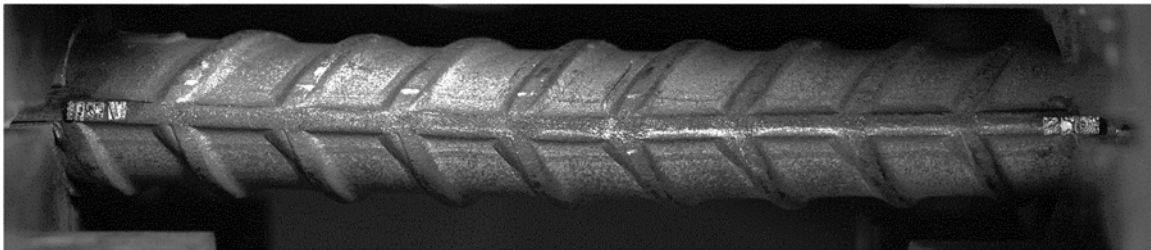
FIGURE 3-46: CRACK GROWTH FOR A M2-1-80A08-6d_B BAR UNDER THE +4% TO -1% STRAIN PROTOCOL AT HALF-CYCLE 18.8 AND 87% OF TENSILE CAPACITY (30.7 HALF-CYCLES TO FRACTURE)
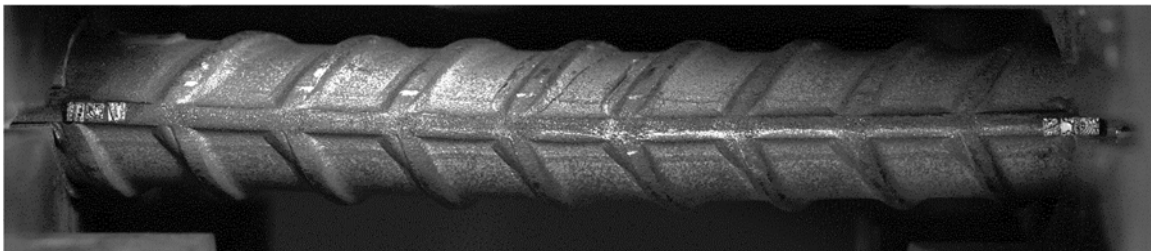
FIGURE 3-47: CRACK GROWTH FOR A M2-1-80A08-6d_B BAR UNDER THE +4% TO -1% STRAIN PROTOCOL AT HALF-CYCLE 20.8 AND 85% OF TENSILE CAPACITY (30.7 HALF-CYCLES TO FRACTURE)
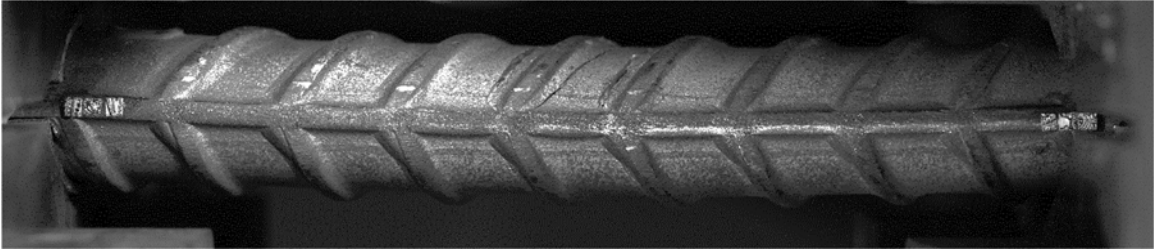
FIGURE 3-48: CRACK GROWTH FOR A M2-1-80A08-6d$_B$ BAR UNDER THE +4% TO -1% STRAIN PROTOCOL AT HALF-CYCLE 22.8 AND 82% OF TENSILE CAPACITY (30.7 HALF-CYCLES TO FRACTURE)
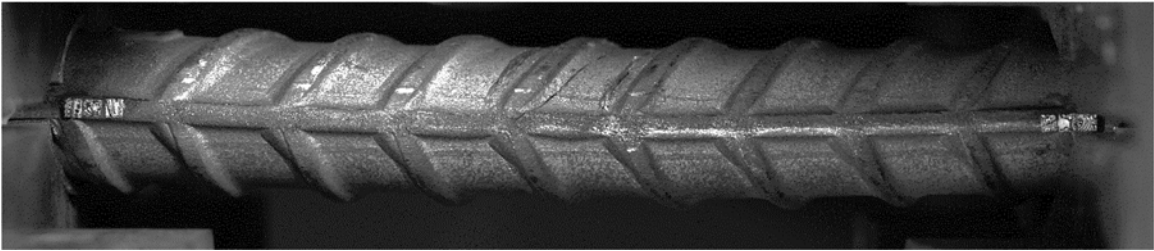
FIGURE 3-49: CRACK GROWTH FOR A M2-1-80A08-6d$_B$ BAR UNDER THE +4% TO -1% STRAIN PROTOCOL AT HALF-CYCLE 24.8 AND 78% OF TENSILE CAPACITY (30.7 HALF-CYCLES TO FRACTURE)
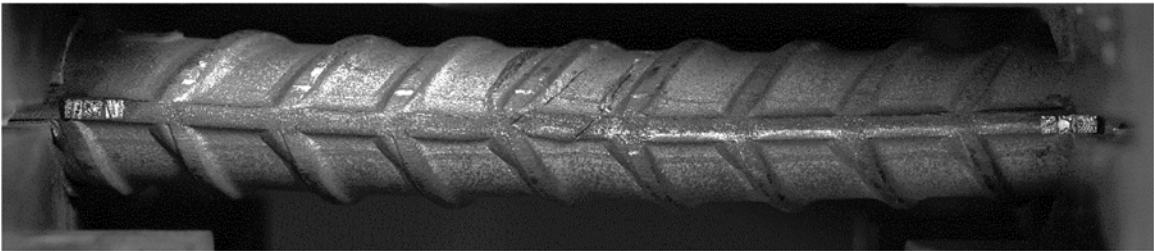
FIGURE 3-50: CRACK GROWTH FOR A M2-1-80A08-6d$_B$ BAR UNDER THE +4% TO -1% STRAIN PROTOCOL AT HALF-CYCLE 26.8 AND 73% OF TENSILE CAPACITY (30.7 HALF-CYCLES TO FRACTURE)
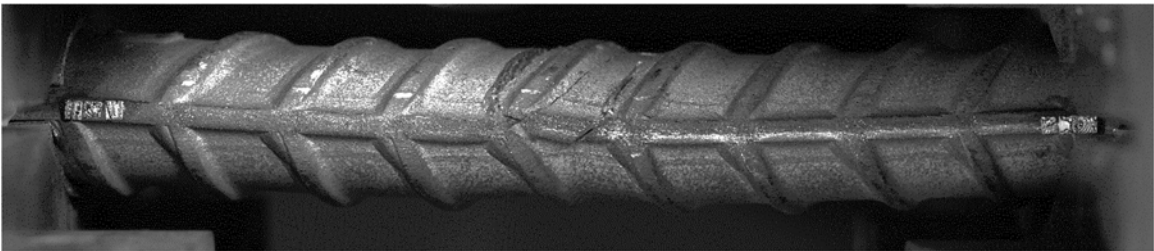
FIGURE 3-51: CRACK GROWTH FOR A M2-1-80A08-6d$_B$ BAR UNDER THE +4% TO -1% STRAIN PROTOCOL AT HALF-CYCLE 28.8 AND 63% OF TENSILE CAPACITY (30.7 HALF-CYCLES TO FRACTURE)

M1 bars tended to maintain a tensile strength larger than 80% of the initial cycle strength up to fracture. This was not typically the case for M2 and M3 bars, which generally experienced more gradual strength loss prior to fracture across all grades. Test results also indicated that the ratio of NH80 to NHF only drops slightly with increasing gripping span. This indicates that inherent bar properties such as microstructure and bar deformations may play a more prominent role than gripping span in determining this ratio of cycles to 80% of peak tensile strength with respect to cycles to fracture.

3.2.2 Effects of Controlled Parameters

The effects of the controlled parameters on fatigue life of bars are treated in a statistical manner in Section 3.3. In this Section, the effects of the controlled parameters are illustrated through isolated comparisons.

3.2.2.1 Strain amplitude

It has been demonstrated in previous studies such as Ghannoum and Slavin (2016) and Brown and Kunnath (2004), that the low-cycle fatigue life of bars measured in half-cycles to fracture is linearly related to the total strain amplitude a bar is cycled to in log-log space. This trend was also observed in this study with strain amplitude being by far the most influential parameter on fatigue life of bars (Figure 3-52).
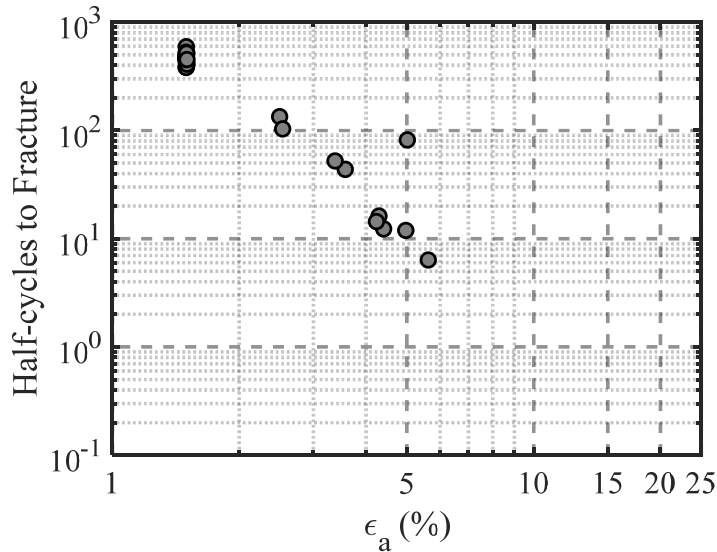
FIGURE 3-52: EFFECTS OF STRAIN AMPLITUDE ON FATIGUE LIFE (#9, 4d$_B$, GRADE 80)

3.2.2.2 Manufacturing process

Visual comparisons of the effects of manufacturing process on the fatigue life of bars are presented in this section. In these comparisons all other parameters except manufacturing process are kept the same. In Figure 3-53 the fatigue life of #8 bars gripped at 4d$_b$ cycled to a strain protocol of -2% to 2% are shown across all grades for the three manufacturing processes. As can be seen in the figure, no clear differences are evident between manufacturing processes across all grades. However, for grade 100, manufacturing process 1 appears to have an advantage over the other two processes.

In Figure 3-54, the fatigue life of #8 bars gripped at 6d$_b$ cycled to a strain protocol of -2% to 2% are shown across all grades for the three manufacturing processes. At this clear gripping span, Manufacturing Process 2 appear to produce enhanced fatigue life for

grade 80 bars but not for other grades. A more rigorous statistical evaluation of the effects

of manufacturing process is presented in Section 3.3.
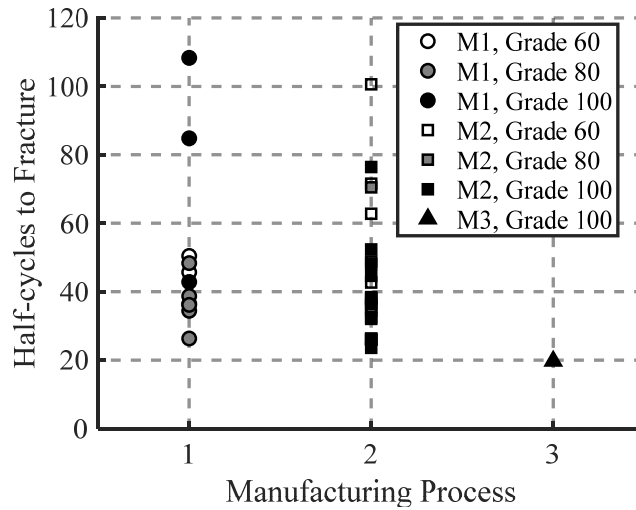
FIGURE 3-53: EFFECTS OF MANUFACTURING PROCESS ON FATIGUE LIFE (#8, STRAIN PROTOCOL OF -2% TO 2%, $4d_B$, GRADES 60, 80, 100)
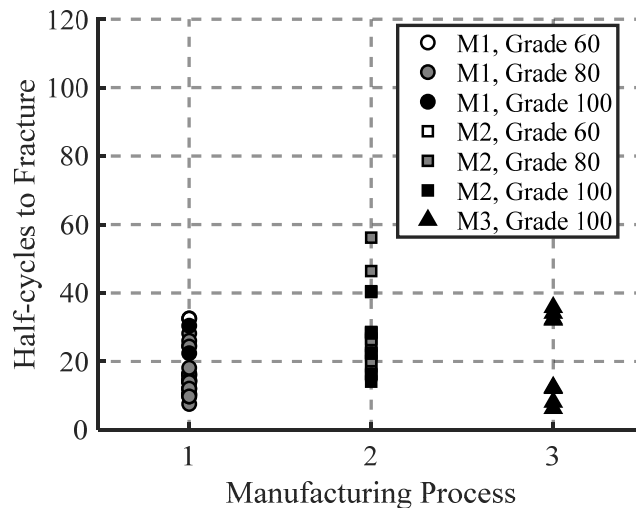
FIGURE 3-54: EFFECTS OF MANUFACTURING PROCESS ON FATIGUE LIFE (#8, STRAIN PROTOCOL OF -2% TO 2%, $6d_B$, GRADES 60, 80, 100)

3.2.2.3 Bar grade

Mixed results were obtained when looking at the effects of bar grade on fatigue life.
It appears from test data that the grade effect depends on manufacturing process. In Figure
3-55 the fatigue life of #8 bars cycled to a strain protocol of -2% to 2% are shown across
all grades for Manufacturing Process 1. As can be seen in the figure, grade 60 and 100 bars
have similar fatigue lives but grade 80 bars experienced noticeably fewer half-cycles to
fracture than bars of the other two grades. In Figure 3-56 the same the fatigue life for bars
having the same parameters as those in Figure 3-55 is presented but for Manufacturing
Process 2. As can be seen in Figure 3-56, there does not appear to be a significant
dependency of fatigue life on bar grade for Manufacturing Process 2.
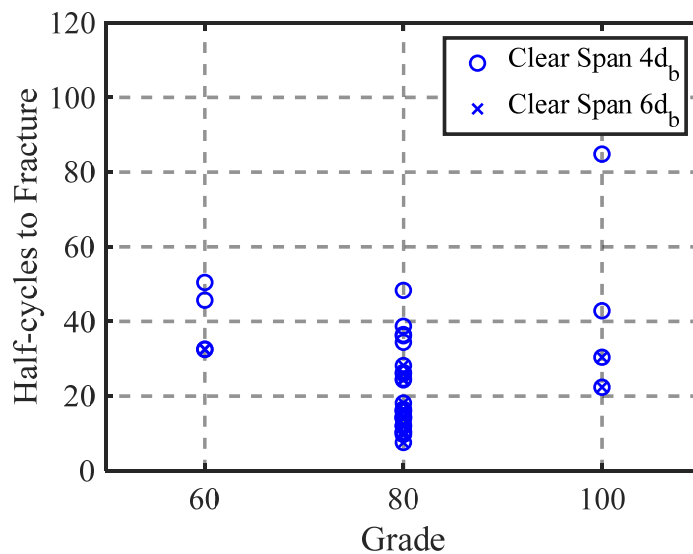
FIGURE 3-55: EFFECTS OF BAR GRADE ON FATIGUE LIFE (M1, #8, STRAIN PROTOCOL OF -2% TO
2%, GRADES 60, 80, 100)
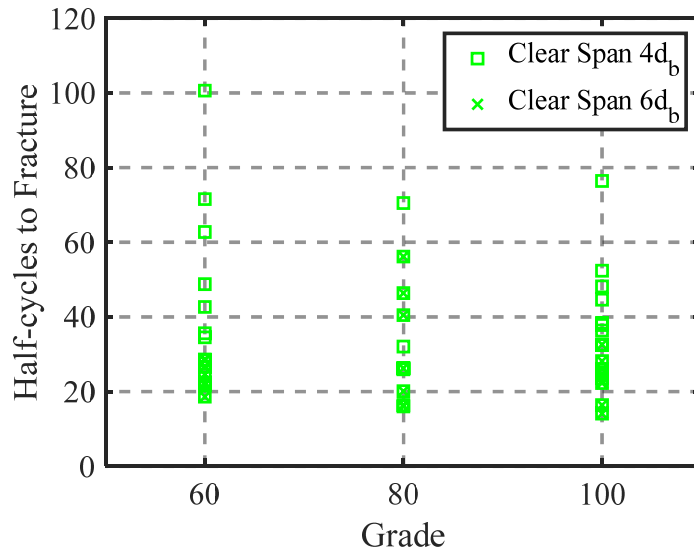
FIGURE 3-56: EFFECTS OF BAR GRADE ON FATIGUE LIFE (M2, #8, STRAIN PROTOCOL OF -2% TO 2%, GRADES 60, 80, 100)

3.2.2.4 Clear unbraced span

As discussed in Section 3.2.1, the clear unbraced span at which the bars were gripped in the testing machine governed the degree of buckling the bars experienced and therefore the maximum curvature and associated strain concentrations in the bars. At a clear span of $4d_b$ or less, essentially no buckling could be observed, while increasing the clear span increased the level of buckling.

Figure 3-57 to Figure 3-59 illustrate the effects of clear span and associated degree of bar buckling on the fatigue life of bars for all three manufacturing processes. As can be seen in the figures and for all manufacturing processes, as the clear span increased the number of half-cycles to fracture decreased substantially and appeared to level off at a clear

span of 8d$_b$. The relation between clear span and half-cycles to fracture therefore appears to follow a power law.
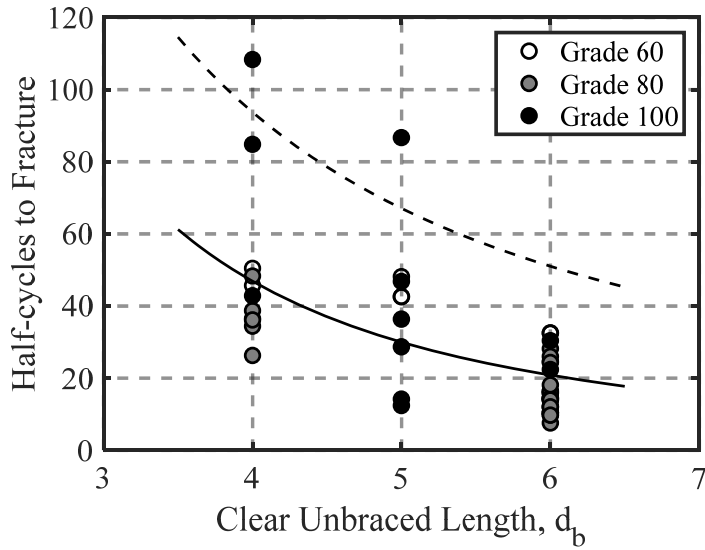
FIGURE 3-57: EFFECT OF CLEAR SPAN ON FATIGUE LIFE FOR M1 #8 BARS TESTED TO A STRAIN PROTOCOL OF -2% TO 2%
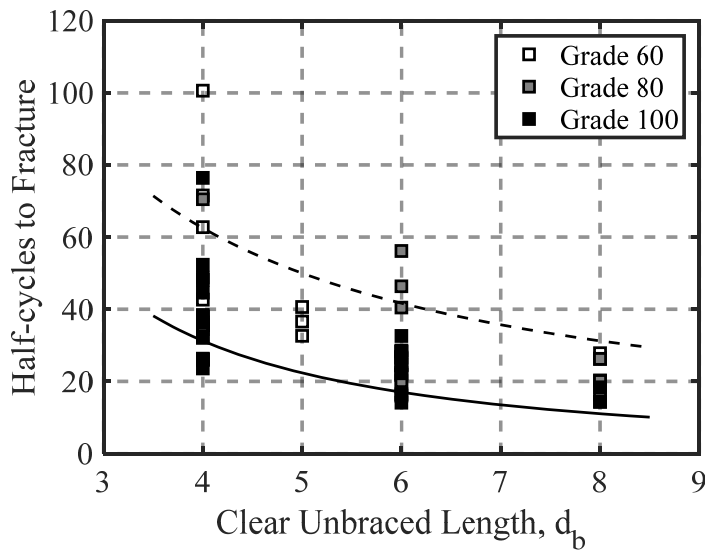
FIGURE 3-58: EFFECT OF CLEAR SPAN ON FATIGUE LIFE FOR M2 #8 BARS TESTED TO A STRAIN PROTOCOL OF -2% TO 2%
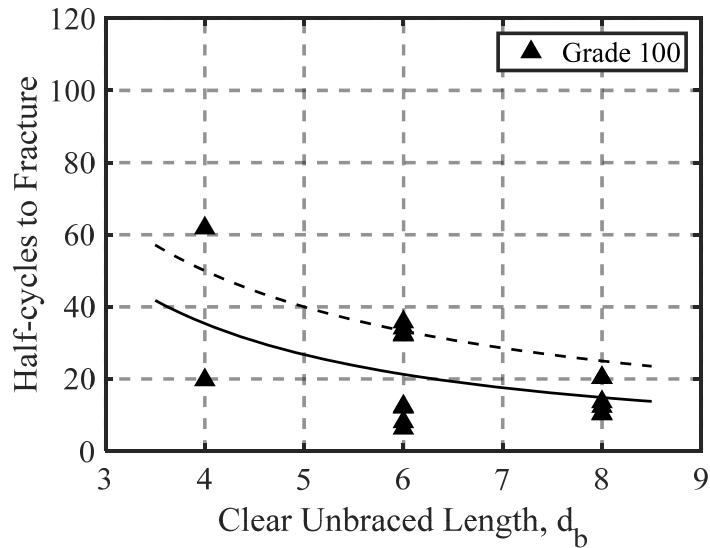
FIGURE 3-59: EFFECT OF CLEAR SPAN ON FATIGUE LIFE FOR M3 #8 BARS TESTED TO A STRAIN PROTOCOL OF -2% TO 2%

3.2.2.5 Bar size

The influence of bar size on fatigue life was less pronounced than that of other parameters such as clear unbraced length. Ghannoum and Slavin (2016) observed a modest trend between bar size and the number of half cycles to fracture (NHF) for Series 1 tests. Lower fatigue life was generally recorded for larger bars. Overall, the fatigue life of #11 bars was 27% lower than that of the #8 bars, while the fatigue life of #8 bars was about 10% lower than that of #5 bars, in that series. The effect was more pronounced for grade 100 bars than for grade 60 bars.

In Series 3, bars ranging from #8 to #11 were tested at a constant clear span of 4.5in., which lead to clear spans ranging from $3.3d_b$ for #11 bars to $4.5d_b$ for #8 bars. In Figure 3-60, the half-cycles to fracture for bars tested in Series 3 under the same strain

protocol are presented versus the bar sizes. The NHF can clearly be seen to increase significantly from #8 to #10 bars. However, #11 bars had a lower average NHF than #10 and #9 bars. It is possible that the reducing clear span with respect to bar diameter with increasing bar size may have contributed to the increase in NHF with increasing bar size up to #10. This hypothesis however does not explain why #11 bars performed worse than #10 and #9 bars.
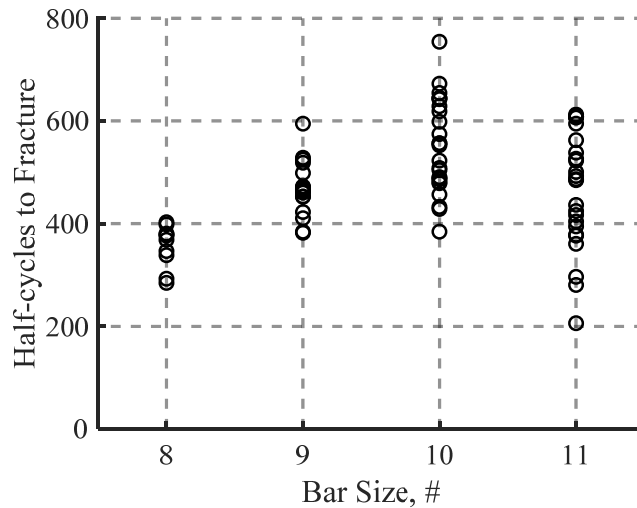
FIGURE 3-60: NHF VERSUS BAR SIZE FOR SERIES 3 TESTS WITH CONSTANT CLEAR SPAN OF 4.5 IN. CORRESPONDING TO $3.3d_B$ FOR #11 BARS TO $4.5d_B$ FOR #8 BARS

The observations from Series 3 present some inconsistencies with those of Series 1. The inconsistent results observed when exploring the effects of bars size visually therefore indicate that more complex phenomena may be at play and that the effects of bar size may have dependencies to other parameters. The effects of bar sizes are explored in a more rigorous statistical manner in the section presenting fatigue models for the bars tested (Section 3.3).

3.2.3 Effects of Non-Controlled Parameters

The effects of tension-test mechanical properties and chemical composition on fatigue life of bars are treated in a statistical manner in Section 3.3 due to the large number of parameters and the complexities of interactions that occur between them and other parameters.

In this Section, the effects of bar deformation geometry and additional ribs on fatigue life are illustrated through isolated comparisons.

3.2.3.1 *Effects of bar deformations on fatigue life*

One manufacturer using the M2 process modified bar deformation geometry from Series 1 to Series 2 to soften the radii at the base of the deformations. Clear and substantial gains in NHF were observed when minimum radii changed from a little over 1 to 2 times the deformation height (Figure 3-61). Interestingly the benefits of softer deformation radii manifested themselves in tests at a clear span of $4d_b$ but had limited effect in tests at a clear span of $6d_b$ (Figure 3-62).
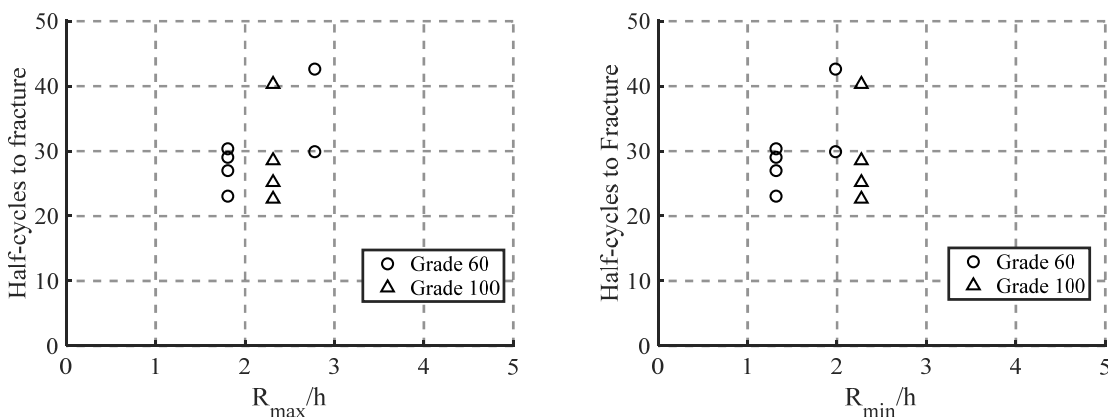
FIGURE 3-61: EFFECTS OF BAR DEFORMATION RADII AT THEIR BASE ON NHF FOR M2, #8, CLEAR SPAN OF $4d_B$, STRAIN PROTOCOL OF -1% TO 4%

M2, Grade 60, #8, clear span of 4d_b, strain protocol of -1% to 4%
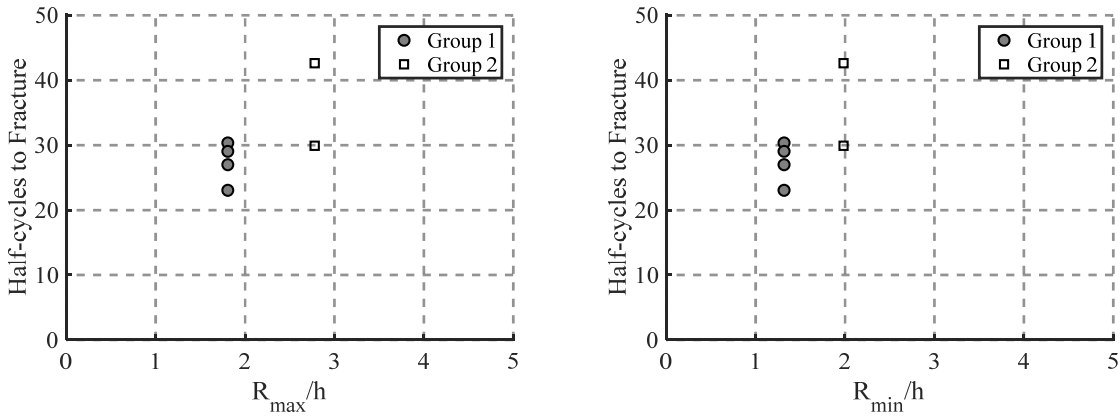
M2, Grade 60, #8, clear span of 6d_b, strain protocol of -2% to 2%
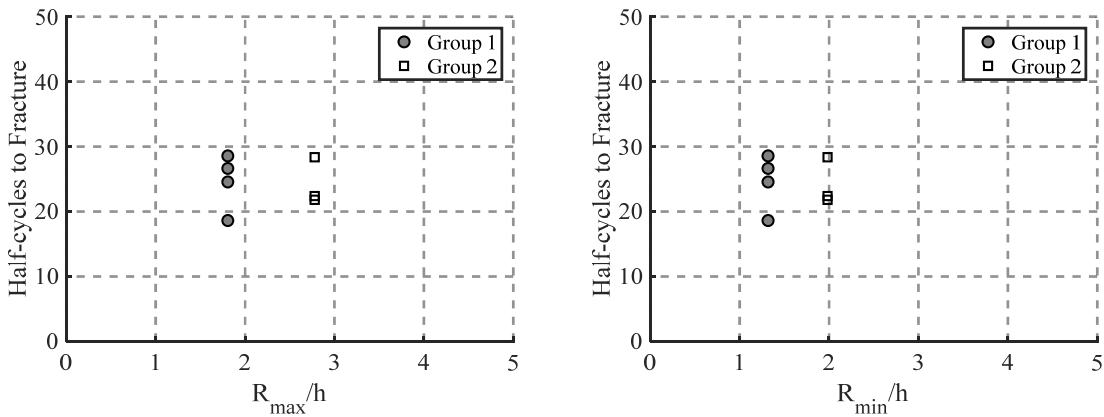
FIGURE 3-62: EFFECTS OF BAR DEFORMATION RADII AT THEIR BASE ON NHF FOR M2, #8, CLEAR SPAN OF 4d_B, AND 6d_B (GROUP 1 = OLDER BARS WITH TIGHTER DEFORMATION RADII, GROUP 2 = NEWER BARS WITH SOFTER DEFORMATION RADII)

3.2.3.2 *Effect of additional ribs on fatigue life*

As mentioned previously, some bars produced using M1 had additional ribs that designate bar grade. These were #8 and #11 bars from Batch 2. In Table 3-3, the mean NHF of the bars with additional ribs are compares to those of bars produced using M1 and having all other controlled parameters nominally identical. As can be seen in the table, the

additional ribs decreased the NHF dramatically, in some cases cutting them by a factor of

800%. The data from this batch of bars with additional ribs was therefore excluded from

the data analysis and fatigue models. It is strongly discouraged to use such bars in seismic

applications.

TABLE 3-3: NHF OF BARS WITH ADDITIONAL RIBS (M1 B2) COMPARED WITH THOSE OF BARS
WITHOUT THE ADDITIONAL RIBS AND PRODUCED USING MANUFACTURING PROCESS 1

Strain protocols	Grade	Half Cycles (mean)		No. of samples	
		Double ribs	Others	Double ribs	Others
-2% to 2%	60	28	48	3	2
	80	11	37	3	6
	100	9	79	6	3
-1% to 4%	60	15	34	3	3
	80	8	15	3	5
	100	7	22	6	5

3.3 Low-Cycle Fatigue Models for Reinforcing Bars

Ghannoum and Slavin (2016) proposed relationships between half-cycles to failure for HSRB which were derived from #8 bars with two cyclic strain ranges (4% and 5%) as a function of total strain range, ε_a in Equation 3-6. Variables used for statistical analyses were manufacturing process (M1 and M2), grade (60, 80, 100), and clear span (4d_b, 5d_b, and 6d_b).

EQUATION 3-6: RELATION BETWEEN HALF-CYCLES TO FRACTURE TO TOTAL STRAIN RANGE

$$Half-cycles\ to\ failure = a \times (\varepsilon_a)^b$$

The coefficients a and b were obtained from linear regression analyses in log spaces and summarized as follow:

TABLE 3-4: PARAMETER COEFFICIENTS FROM LINEAR REGRESSION ANALYSIS AFTER GHANNOUM AND SLAVIN (2016)

Manufacturing Process	Grade	Clear Span	a	b
M1	60	4d_b	5.14×10^{-3}	-2.87
		5d_b	5.92×10^{-3}	-2.77
		6d_b	7.92×10^{-3}	-2.59
	80	4d_b	2.48×10^{-3}	-2.97
		6d_b	6.6×10^{-3}	-2.43
	100	4d_b	2.4×10^{-5}	-4.62
		5d_b	8.14×10^{-5}	-4.06
		6d_b	1.49×10^{-4}	-3.77
M2	60	4d_b	5.14×10^{-3}	-2.87
		5d_b	5.92×10^{-3}	-2.77
		6d_b	7.92×10^{-3}	-2.59
	100	4d_b	2.4×10^{-5}	-4.62
		5d_b	8.14×10^{-5}	-4.06
		6d_b	1.49×10^{-4}	-3.77

3.3.1 Functional Form for the Proposed Fatigue Models

Strain at fracture during a monotonic test can be interpreted as the strain amplitude for one half-cycle at fracture. Figure 3-63 illustrates that this assumption is reasonable. As can be seen in the figure, for #9 bars from a single batch tested with all parameters kept nominally identical except for strain amplitude, the mean fracture strain from monotonic tests for that specific batch of bars intersected the regression and weighted regression lines for half-cycles to fracture at about 0.7 to 0.9 half-cycles.
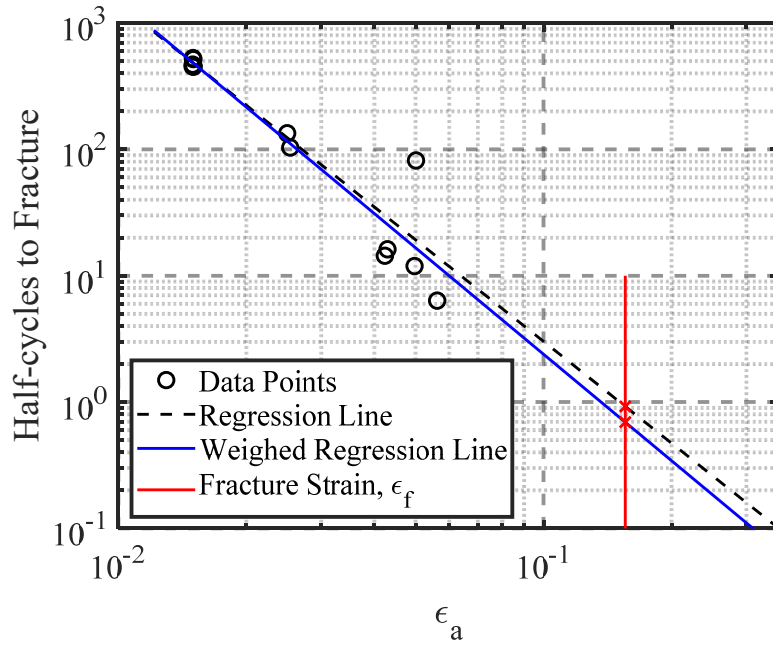
FIGURE 3-63: MONOTONIC TEST FRACTURE STRAIN RELATION TO FATIGUE LIFE FOR SERIES 3, M1, BATCH 3, #9, GRADE 80, CLEAR SPAN OF 4d$_B$

Based on the assumption that monotonic-test fracture strains correspond to the strain amplitude for one half-cycle, a modified functional form of Equation 3-6 is introduced to estimate the fatigue life of bars (Equation 3-7). The proposed equation form

forces the fatigue life to intersect the monotonic-test fracture strain at a half-cycle value of

1.0. As such, this form incorporates the fracture strain from monotonic tests into the fatigue

models.

$$Half - cycles\ to\ failure = (\varepsilon_a/\varepsilon_f)^{\beta}$$

To estimate the fatigue life of reinforcing bars using Equation 3-7, input of the

fracture strain of bars as well as a β parameter are required given an input cyclic strain

amplitude, ε_a. The fracture strain of bars can be calculated using Equation 3-1 or Equation

3-2 provided earlier in this report. The β parameter, on the other hand, was extracted for

each cyclic test by combining the fracture strain of the bar with its NHF for the strain

amplitude imposed on the bar. For the subset dataset presented in Figure 3-63, Figure 3-64

illustrates the process used of connecting a line between the fracture strain point and the

cyclic-test data point. The slope of that line represents the β parameter for a given cyclic

test. For that subset of the data, the mean beta (β) value was estimated at -2.5, which

resulted in the predictive fracture life equation for these bars presented in Equation 3-8.

Figure 3-65, illustrates how well Equation 3-8 matches the fatigue life data for the subset

of cyclic tests.
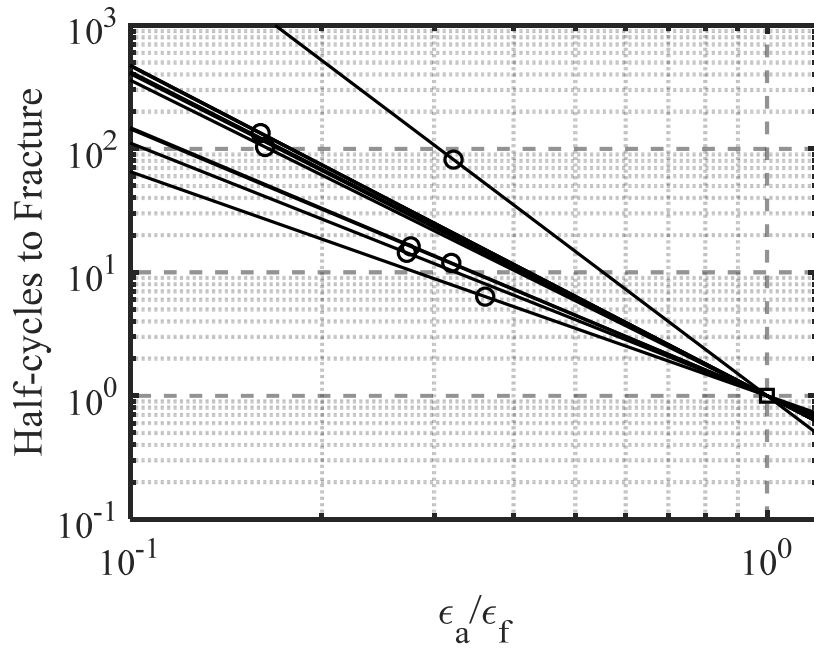
FIGURE 3-64: FITTED NONLINEAR REGRESSION FOR EACH DATA POINT OF SERIES 3, M1, BATCH 3, #9, GRADE 80, CLEAR SPAN OF 4d$_B$

EQUATION 3-8: RELATION BETWEEN HALF-CYCLES TO FRACTURE TO NORMALIZED TOTAL STRAIN RANGE FOR SERIES 3, M1, BATCH 3, #9, GRADE 80, CLEAR SPAN OF 4d$_B$

$$Half - cycles\ to\ failure = \left(\varepsilon_a/\varepsilon_f\right)^{-2.5}$$
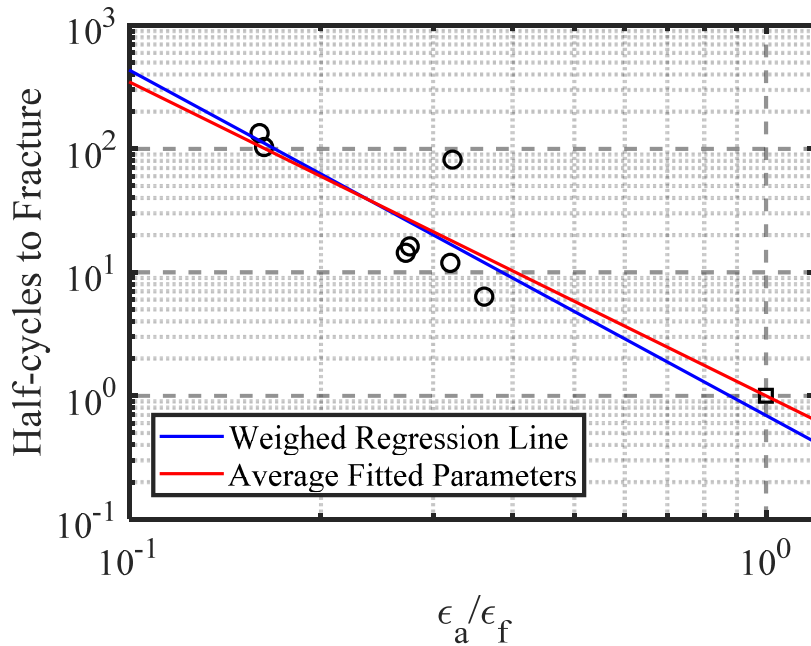
FIGURE 3-65: COMPARISON BETWEEN PREDICTED NHF AND WEIGHED REGRESSION LINE FOR SERIES 3, M1, BATCH 3, #9, GRADE 80, CLEAR SPAN OF $4d_B$

3.3.2 Fatigue Models

The process illustrated in Section 3.3.1 was used for all data series. Given the observed differences in fatigue behaviors between manufacturing processes, fatigue models for each manufacturing process were developed independently. Figure 3-66 illustrates the process used to obtain β values for all cyclic tests using the monotonic fracture strain, ε_f, specific to each of the cyclic tests.
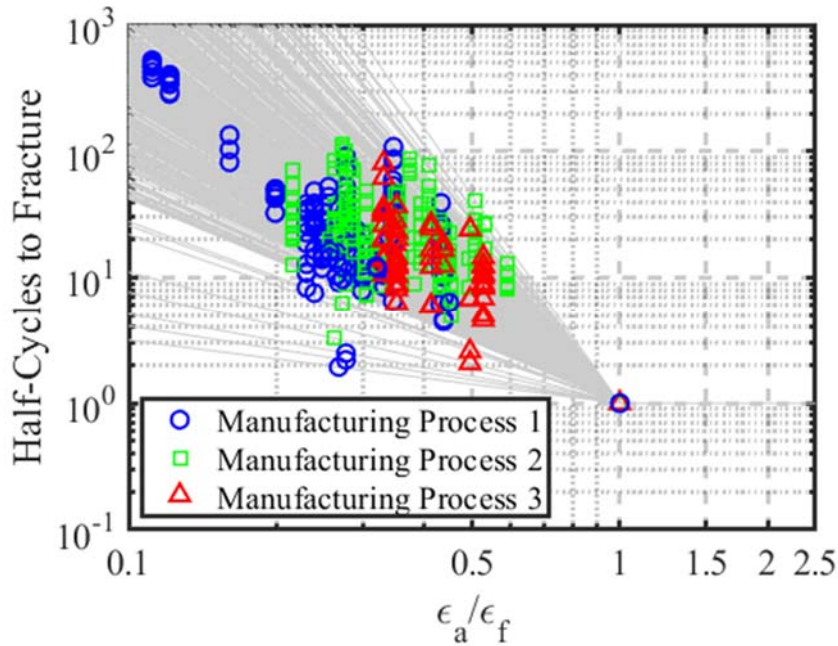
FIGURE 3-66: FITTED LINES USED TO EXTRACT THE β PARAMETER FOR EACH CYCLIC-TEST DATA POINT

Regression analyses were performed on β parameters for each manufacturing process. The parameters considered in in the analyses are shown in Table 3-5. All controlled parameters were considered, except strain amplitude, which is built into the functional form. The non-controlled parameters that were considered as well were the chemical composition parameters listed in Section 2.3.2, the bar deformation parameters discussed in Section 2.3.1, and the monotonic tension-test properties listed in Table 3-1.

TABLE 3-5: PREDICTORS CONSIDERED IN STATISTICAL STUDY

ID	Predictors	Categories	ID	Predictors	Categories
1	Grade	Bar Properties	23	C_u	Chemical Composition cont'd
2	Size (1/8")		24	N_i	
3	Span (d_b)	Fatigue Test Parameters	25	C_r	
4	ε_{min}		26	M_o	
5	ε_{max}		27	V	
6	ε_{mean}		28	S_n	
7	ε_a		29	A_l	
8	f_y (ksi)	Monotonic Properties	30	N	
9	f_u (ksi)		31	C_b	
10	T/Y		32	CEA	
11	ε_y		33	R_{min}/h	Bar Deformation
12	ε_h		34	R_{max}/h	
13	ε_p		35	h/d_b	
14	ε_u		36	$(Span)^{-0.5}$	Derived properties
15	ε_f		37	$(Span)^{-1.0}$	
16	E (ksi)		38	$(Span)^{-1.5}$	
17	E_{sh} (ksi)		39	$(Span)^{-2.0}$	
18	C	Chemical Composition	40	$\varepsilon_a/\varepsilon_f$	
19	M_n		41	$\varepsilon_a/\varepsilon_u$	
20	P		42	$Log\,(\varepsilon_a)$	
21	S		43	$Log\,(\varepsilon_a/\varepsilon_f)$	
22	S_i		44	$Log\,(\varepsilon_a/\varepsilon_u)$	

Figure 3-67 illustrates P-values from an *F*-statistic model, which were computed under a model assumption containing a constant term. P-values are commonly used for hypothesis testing in which a predictor (or combination of predictors) is considered highly correlated with respect to the observed parameter (e.g.,β) if its P-value is below a threshold value. In the figure, a black mark indicates a P-value less than 0.05, a white mark indicate that the P-values is above that threshold. Marks on the diagonal in Figure 3-67 indicate the P-values for the predictors associated with the ID number given in Table 3-5 (e.g. the diagonal at row 3 and column 3 gives the P-value mark for parameter 3, i.e., clear span in d_b units). The non-diagonal marks correspond to P-values of the cross product of two predictors associated with the row and column IDs (e.g. row 3 or 1 and column 1 or 3 associated with ID-1, grade, multiplied with ID-3, clear span in d_b unit).

Several significant predictors were identified based on P-values as observed in Figure 3-67. To simplify the predictive equations however, only the most correlated predictors (lowest P-values) that exhibited clear physical trends were included in the final fatigue models. Figure 3-68 presents the β parameter trends with respect to selected predictors. Clear nonlinear trends were observed between the fracture strain, ε_f, clear unbraced span (consistent with trends found in Section 3.2.2.4), bar yield strength and T/Y ratio, especially for manufacturing processes 1 and 2. Manufacturing process 3 data showed limited trends due to the narrow range of parameter for that data group. Higher values of fracture strain, ε_f, clear unbraced span, and T/Y ratio indicated a shallower slope (larger β values), which is indicative of a less rapid loss of fatigue life with increasing strain

amplitude, but typically a lower fatigue life at smaller strain amplitudes. This trend was opposite for bar yield strength.
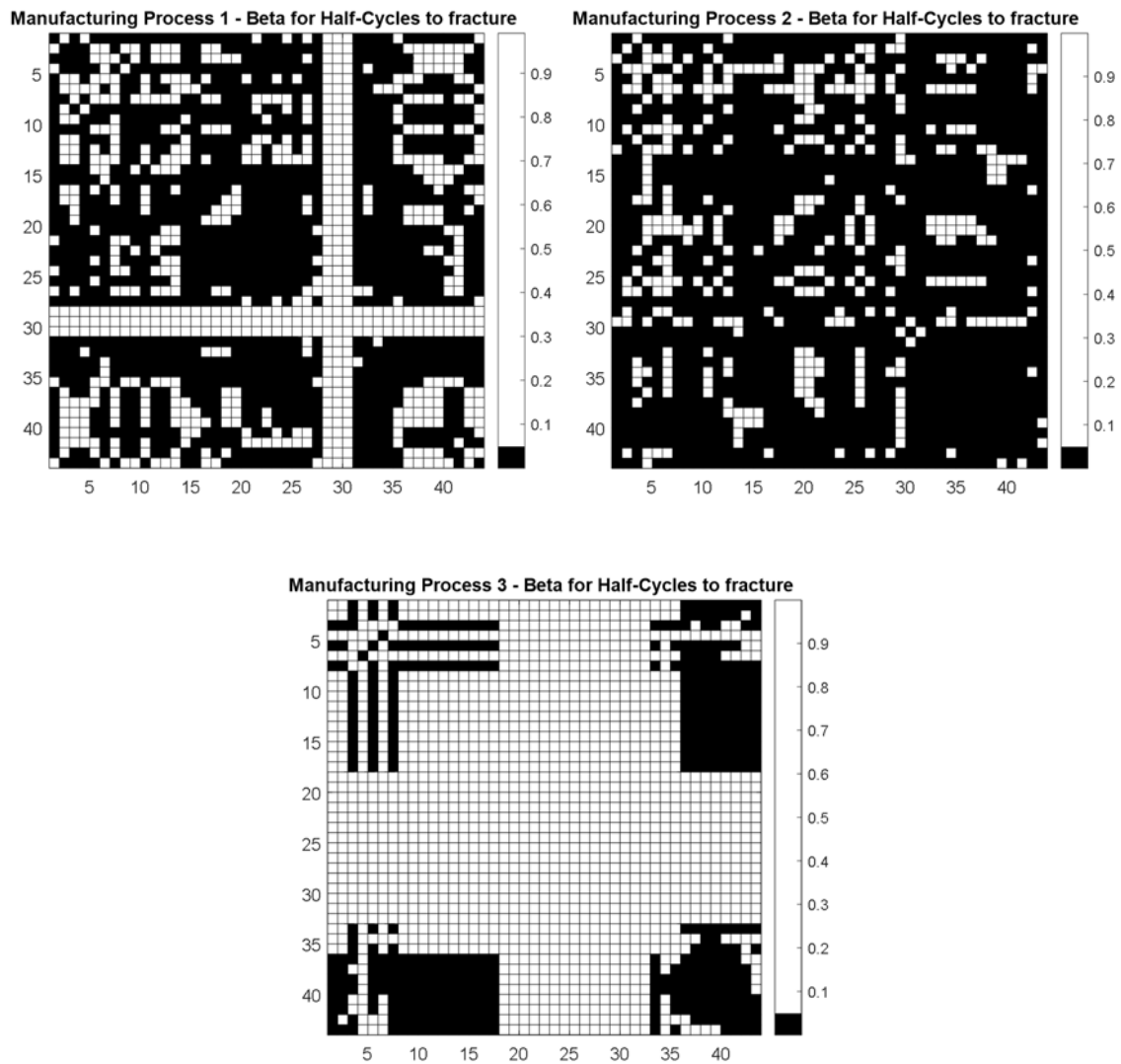
FIGURE 3-67: MAP OF FOR P-VALUES < 0.05 FOR PREDICTORS AND CROSS-PRODUCT TERMS
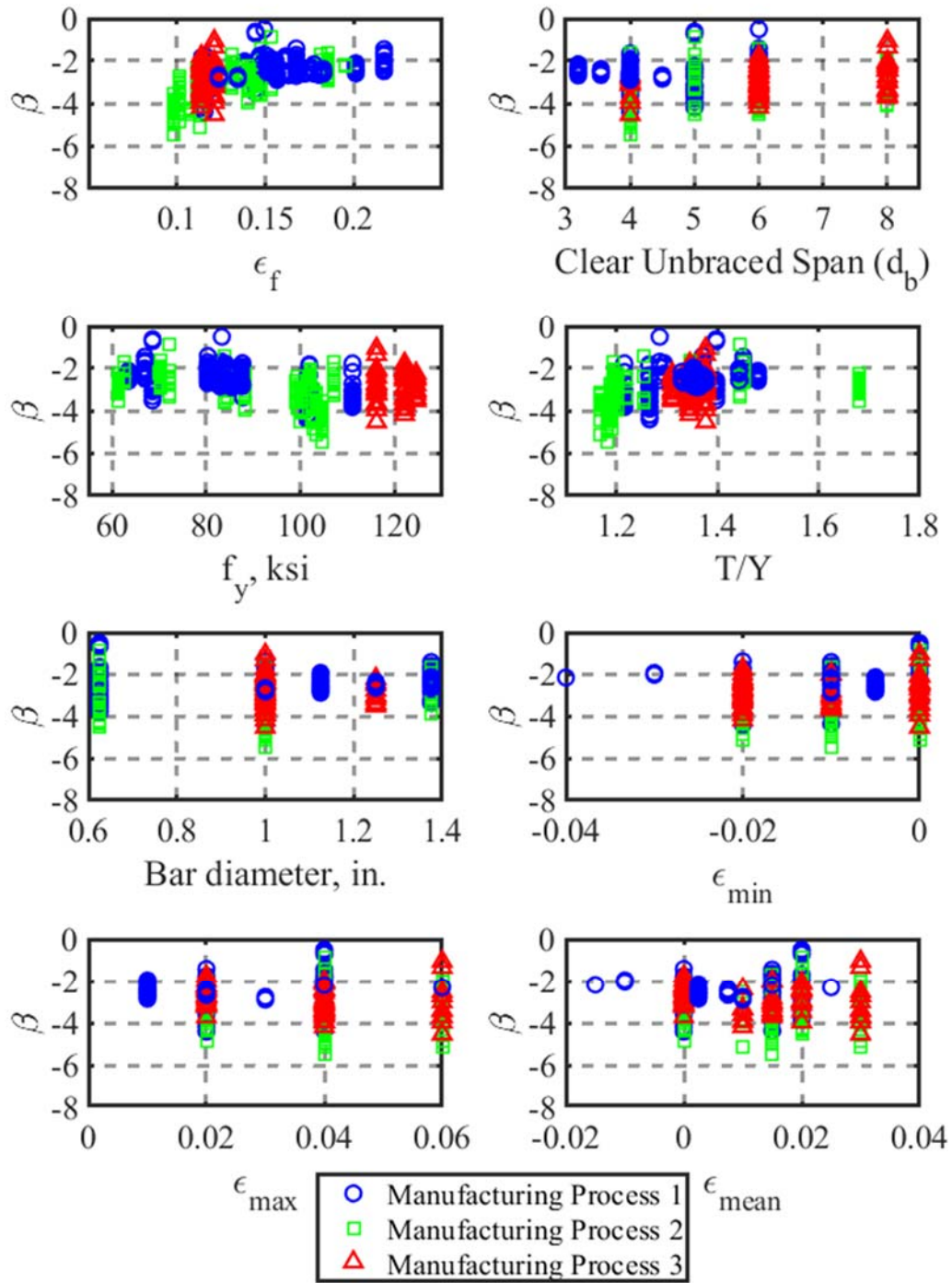
FIGURE 3-68: TRENDS OF BETA PARAMETERS WITH RESPECT TO SELECTED PREDICTORS

Based on the preliminary P-value statistical study, nonlinear regression analyses were performed for each manufacturing process to predict β based on fracture strain, ε_f, clear unbraced span, and bar yield strength. Power functions were used to improve fit wherever justified (Figure 3-69).
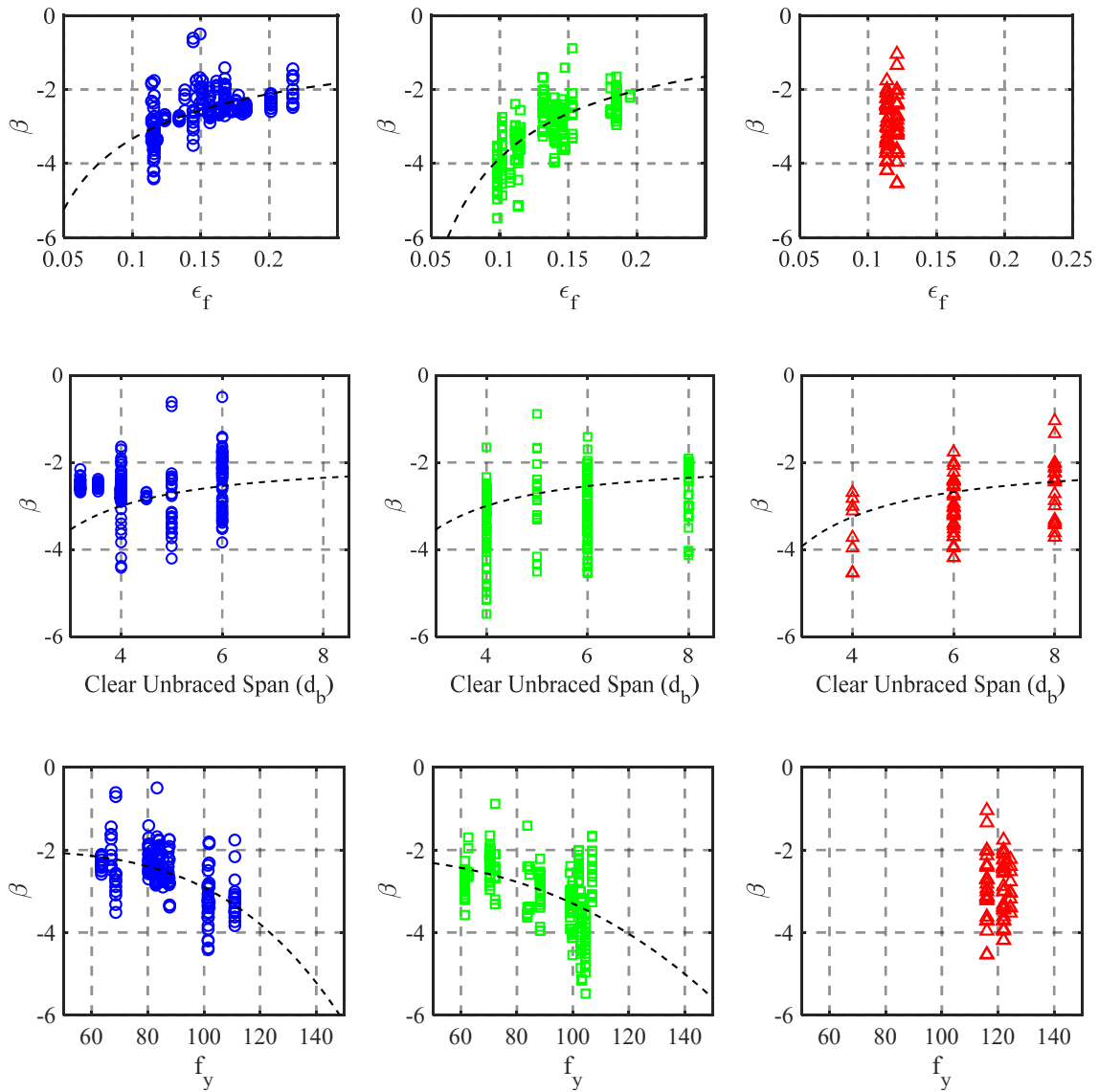
FIGURE 3-69: NONLINEAR REGRESSION ANALYSES ON FRACTURE STRAIN, ε_f, CLEAR UNBRACED SPAN (d_b), AND YIELD STRENGTH FOR EACH MANUFACTURING PROCESS

The final relations for estimating the β parameter for each manufacturing process are given in Equation 3-9 (a), (b), and (c), and do not contain the T/Y ratio, as adding that parameter did not result in improvements of fit warranting the added complexity in the relations. Moreover, the T/Y ratio is highly correlated with bar yield strength, which was introduced into the predictive models It is noted as well that the fracture strain of bars, ε_f, appears in predicting the fatigue life of bars per the functional form selected (Equation 3-7). Fracture strain can be estimated using Equation 3-1 presented in Section 3.1.4.

EQUATION 3-9: RELATIONS OF BETA, β PARAMETER

Manufacturing Process	Relations (d_b units)	Applicable Limits	Estimated / Exp. Parameters
1	$\beta = -1.4 - 2.5\,Span^{-1.0} - 9.10^{-9}\,f_y{}^4$ (a)		Mean = 1.03 Lognormal dispersion = 0.22
2	$\beta = -1.0 - 6.4\,Span^{-1.0} - 1.10^{-6}\,f_y{}^3$ (b)	$60 \leq f_y \leq 110\ ksi$ $4 \leq Span \leq 8$	Mean = 1.03 Lognormal dispersion = 0.21
3	$\beta = -1.7 - 7.7\,Span^{-1.0}$ (c)		Mean = 1.06 Lognormal dispersion = 0.25

Note: Span = clear gripping pan for bars during testing in units of bar diameter (d_b). This measure represents the unrestrained length of bars in concrete members across which they would be expected to buckle.

It is important to note that the relations in Equation 3-9 were calibrated within the range of parameter listed with the relations. Additionally, Equation 3-9 relations are applicable to the range of bar properties presented in Table 3-1 for monotonic properties, Table 2-2 for bar deformation geometries, and Table 2-3 for chemical composition. Particularly, except for a limited number of bars from earlier M2 batches, bars tested in this study had relatively smooth deformation radii generally exceeding a ratio of radius to

deformation height (R_{min}/H) of 1.5. As demonstrated in Section 3.2.3, sharper deformation radii or other deformation patterns such as additional ribs used to mark bar grade can reduce the fatigue life of bars substantially. Additional ribs and deformation radii to deformation height ratios below 1.5 are not advised for bars used in seismic applications.

Figure 3-70 illustrates the fit of the proposed fatigue relations for all three manufacturing processes. The proposed relations showed good fit among all manufacturing processes but underestimated some experimental data points for grade 60 (M1) and grade 80 (M2) with clear unbraced span of 6d_b.

Figure 3-71 compares the fatigue life predictions between the three manufacturing processes for #8 bars. As can be seen in the figure, manufacturing process 2 produced in general larger numbers of half-cycles to fracture than manufacturing processes 1 and 3. As noted in Section 3.2.1, the hardened outer shell of bars treated using quenching and tempering (M2) appeared to hinder the progress of initial fatigue cracks that formed at the base of bar deformations. This behavior may have contributed to the improved fatigue life measured in number of half cycles to fracture (NHF) for M2 bars. The fatigue life of bars produces using micro-alloying (M1) and the patented MMFX process (M3) were similar for grade 100 bars at the larger clear spans.

The fatigue life of bars produced using the quenching and tempering process (M2) appear to be more sensitive than M1 bars to clear unbraced length, which is related to buckling amplitude. Buckling tends to increase strain demands more at the outer surface of bars than within the barrel, due to curvatures associated with buckling. Since M2 bars have a hardened shell that appeared to hinder fatigue crack propagation in tests,

concentrating strains due to buckling within that layer may cause such bars to see larger

decreases in fatigue life as buckling amplitudes increase compared to bars that have more

homogenous micro-structure distributions.
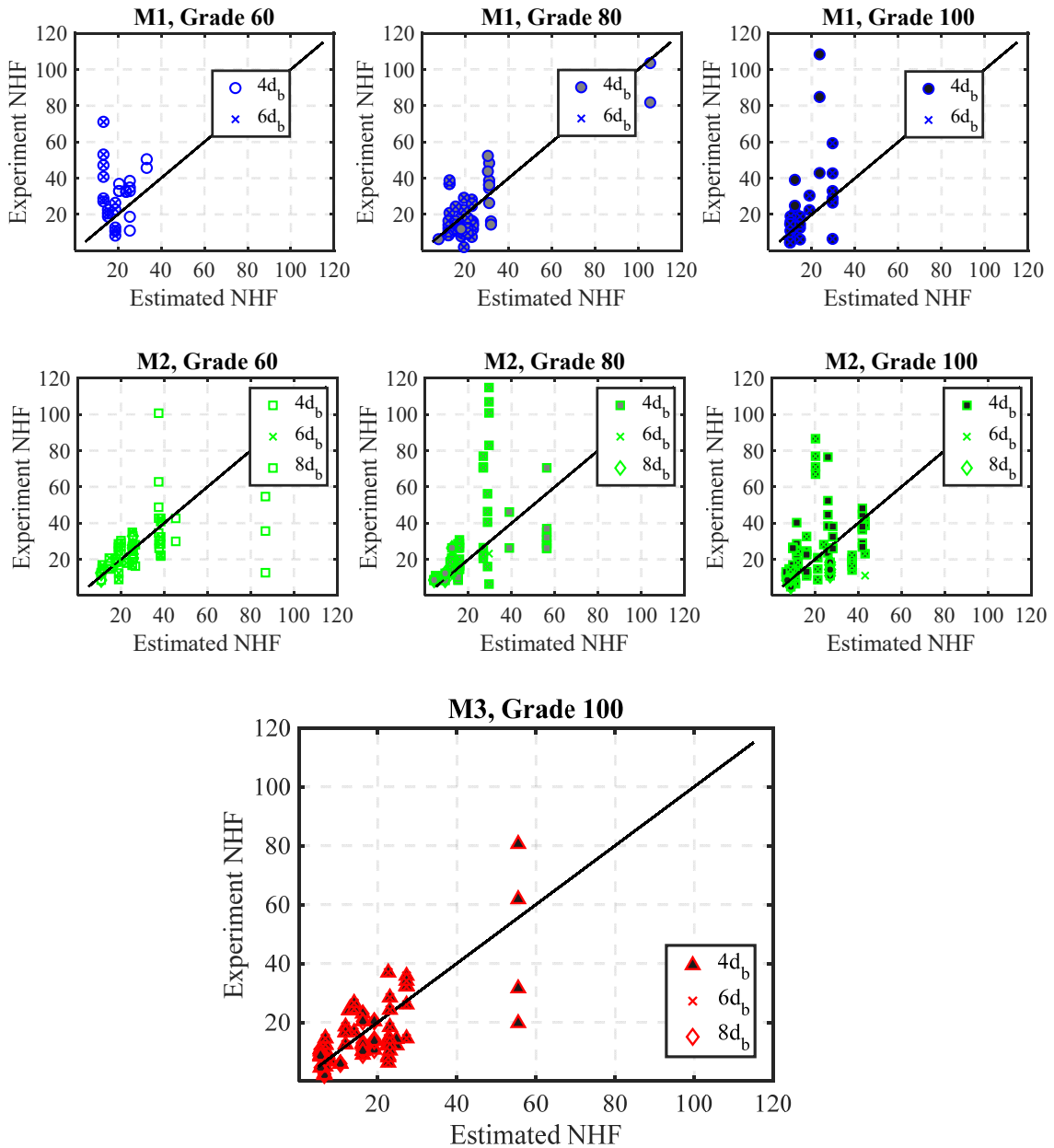
FIGURE 3-70: FIT OF PROPOSED FATIGUE RELATIONS FOR ALL MANUFACTURING PROCESSES
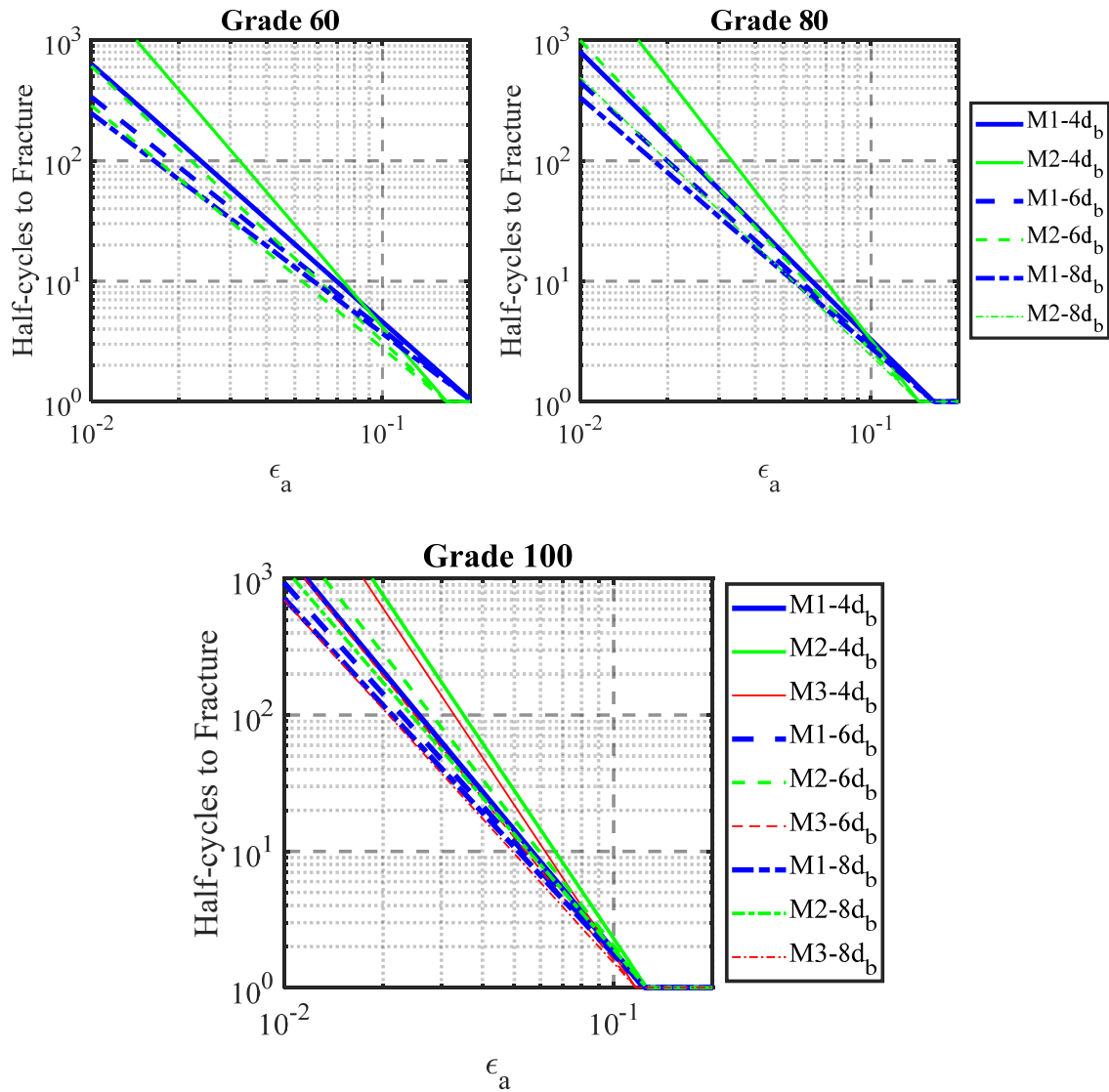
FIGURE 3-71: FATIGUE LIFE PREDICTION COMPARISON BETWEEN THREE GRADES (GRADE 60, 80, 100) FOR #8 BARS

Figure 3-72 shows fatigue life comparison for different grades per manufacturing process. For manufacturing process 2, the fatigue life between grades is estimated to be similar across the strain amplitude ranges of interest for concrete members subjected to seismic excitation (i.e., 1% to 8% strain amplitudes). For manufacturing process 1, higher

fatigue life is estimated for grade 80 and 100 bars compared with grade 60 bars at smaller strain amplitudes of 1 to 3%. However, lower fatigue life for higher strength bars is predicted at higher strain amplitudes exceeding 4%. This cross-over may be attributed in part to the smaller fracture elongations of higher strength bars and the greater representation in the test matrix of fatigue data for strain ranges of 4% and 5%, where the cross-over is observed.
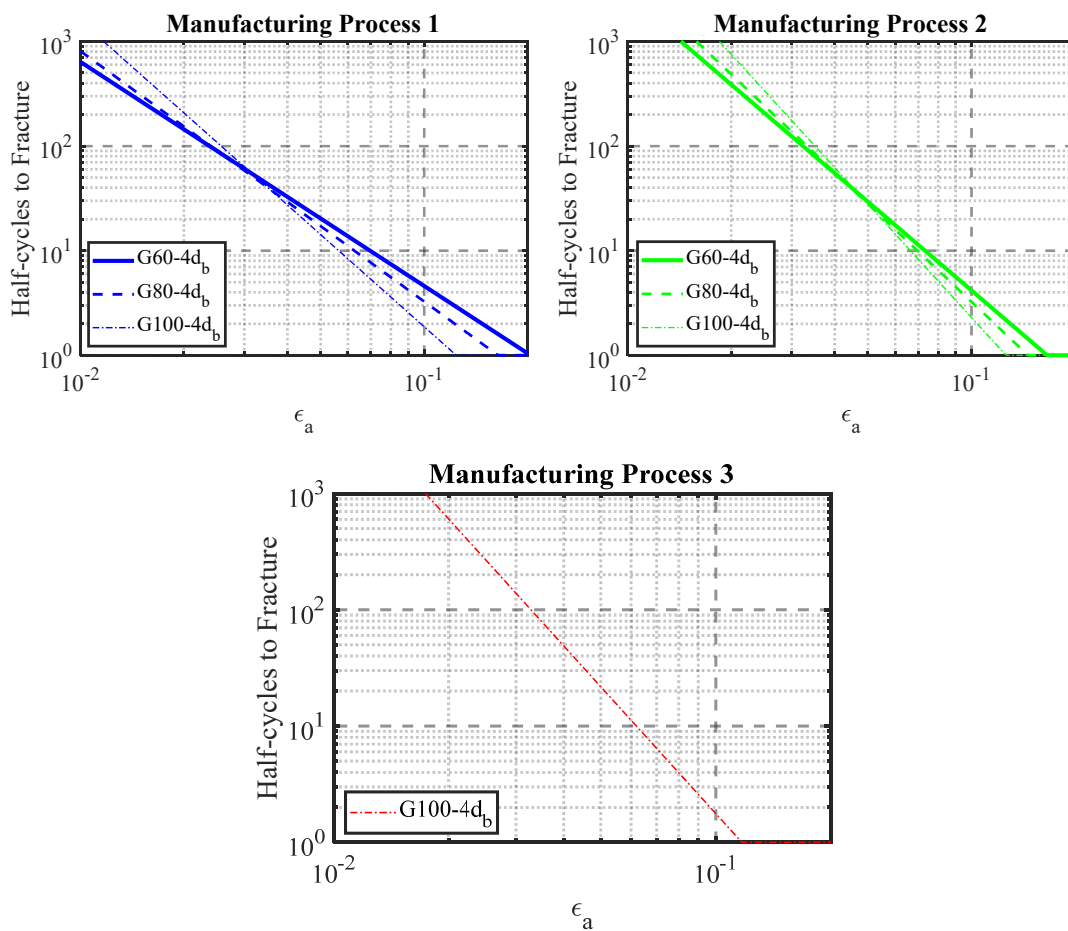
FIGURE 3-72: FATIGUE LIFE PREDICTION COMPARISON BETWEEN THREE MANUFACTURING PROCESSES FOR #8 BARS

4 FROM GLOBAL TO LOCAL DEFORMATIONS OF CONCRETE MOMENT FRAME MEMBERS

Simulating the nonlinear response of structures to seismic demands is becoming a more widespread practice with the popularization of nonlinear simulation tools and performance-based seismic design standards and guides. Performance-based documents provide modeling guidance as well as acceptance criteria, which are used to judge the adequacy of the performance of structural members. Current acceptance criteria mainly consist of deformation limits on members (e.g., plastic rotation limits), but are being converted to strain limits in many instances. The use of strain limits has the advantages of providing more reliable estimates of material damage and strength degradation, as well as improving consideration of variations in member boundary conditions (e.g., axial load). However, achieving reliable estimates of member seismic deformations and converting those member deformations to local material strains is challenging due to the paucity of physical models and test data at the local strain level.

A computational framework based on fiber-section elements and mechanics-based behavioral models is proposed to accurately estimate both member-level deformations and strain demands in longitudinal bars and the concrete surrounding them within the plastic hinge regions of frame members. Particularly, the effects of the mechanical properties and steel grade of reinforcing bars on these strain demands are quantified experimentally and estimated by the proposed framework. This work was part of a larger study investigating the fatigue fracture potential of newly introduced high-strength reinforcing bars in seismic

applications, for which accurate estimates of strain demands related to bar fracture demands were required.

4.1 Introduction

As prescriptive seismic design standards give way to more flexible and transparent performance-based standards, the need for reliable numerical simulations is increasing, as is the desire to achieve higher fidelity in the simulation tools that are the cornerstone of performance-based methodology. Performance-based documents, such as the ASCE/SEI 41 (2017) and ACI 369 (2017) standards, or the Guidelines for Performance-Based Seismic Design of Tall Buildings (Tall Building Initiative 2017) and the Guidelines for Nonlinear Structural Analysis for Design of Buildings (ATC Part I, Part IIa, and Part IIb, 2017), give nonlinear modeling guidance and acceptance criteria to judge the adequacy of performance of structural members. Current acceptance criteria mainly consist of deformation limits on members (e.g., plastic rotation limits), but are undergoing conversions to strain limits in many instances. The use of strain limits has the advantages of providing more reliable estimates of material damage and strength degradation, as well as improving consideration of variations in member boundary conditions (e.g., axial load). However, achieving reliable estimates of member seismic deformations and converting those member deformations to local material strains is challenging due to the paucity of physical models and test data at the local strain level.

A computational framework based on fiber-section elements and mechanics-based behavioral models is proposed to accurately estimate both member-level deformations and strain demands in longitudinal bars and the concrete surrounding them within the plastic

97

hinge regions of frame members. The proposed behavioral models scale strain estimates obtained using a calibrated force-formulation fiber-section computational element (Limantono 2016) to achieve the desired strain estimates.

A fiber-section computational element was selected over a lumped plasticity model, as the first one provides some estimate of strain demands in the longitudinal bars. Additionally, it was the scope of this work to produce the model using open-source software and readily available material models, such that the framework can be easily reproduced by researchers and practicing engineers in the area of Earthquake Engineering.

The framework is calibrated using 12 cyclic experimental tests conducted on concrete columns and beams that were cycled to large damage states and in some cases bar fracture. The experimental beam and column dataset contained members reinforced with regular strength, or grade 60 reinforcing bars, as well as higher strength bars of grades 80 and 100. In this work, grade refers to the specified yield strength of a reinforcing bar.

The resulting computational framework is capable of matching the global deformation behavior of reinforced concrete frame members, through the fiber-section element, and provides reliable strain demands in the longitudinal bars and surrounding concrete through the full range of expected inelastic deformations. Particularly, the effects of the mechanical properties and steel grade of reinforcing bars on their strain demands are quantified experimentally and estimated by the proposed framework.

This work was part of a larger study investigating the fatigue fracture potential of newly introduced high-strength reinforcing bars in seismic applications, for which accurate estimates of strain demands related to bar fracture were required. However, the proposed

98

framework is intended to be applicable beyond fracture fatigue problems and aid in the development of the next generation of performance-based standards.

4.2 Experimental Data

The experimental data used to calibrate the proposed framework was extracted from four series of tests carried on twelve reinforced-concrete members.

- Series 1 tests were carried to understand the fundamental behavior of moderately confined columns sustaining shear and axial failure (Leborgne, 2012). The two columns in Series 1 (2L06, 2H06) were nominally identical in design. Both were reinforced with grade 60 ASTM A615 (2016) bars. Columns were loaded under the same lateral cyclic protocol, but a different axial load was applied to each. Series 1 columns sustained significant flexural yielding prior to shear and axial failures.

- Series 2 tests (CS60, CS80, CS100) were carried to investigate the ability of high-strength transverse reinforcement in maintaining confinement integrity and the shear strength of concrete columns during inelastic demands (Sokoli 2014, Sokoli and Ghannoum 2016). These three columns were constructed using different grades of reinforcement: grade 60 ASTM A706 (2016) bars for CS60, grade 80 ASTM A706 (2016) bars for CS80, and grade 100 bars that did not have ASTM specifications at the time of testing for CS100. Series 2 columns were well confined and satisfied ACI 318-15 Special Moment Frame provisions. Columns CS60 and CS80 sustained significant flexural yielding prior to shear and axial failures. The column reinforced with grade 100 steel (CS100) sustained a bond failure mechanism, which is not beneficial for the purpose of this study. This member was not used to calibrate the proposed model.

- Series 3 tests (CH100, CL100, CM100, CH60) were conducted to investigate the effects of the different shapes of the steel stress-strain relation, the tensile-to-yield strength ratios, and fracture elongations of the longitudinal bars on the plasticity

spread and deformation capacity of concrete columns (Sokoli et al. 2017). All columns were geometrically identical, reinforced with the same bar layout and sizes. Three of these columns were reinforced with grade 100 steel sourced from different steel manufacturing processes, which led to different post-yield stress-strain curves. Column CM100 was reinforced with grade 100 ASTM A1035 (2016) bars having a rounded stress-strain relation. Columns CH100 and CM100 on the other hand were reinforced with grade 100 bars having a distinct yield point. Column CH60 was reinforced with grade 60 A706 bars (2016). All specimens sustained a flexural mode of degradation characterized by concrete crushing, varying degrees of longitudinal bar buckling, and eventually longitudinal bar fracture.

- Series 4 tests were the beam equivalent (BH100, BL100, BM100, BH60) of Series 3 columns (To and Moehle, 2017). The beams had nominally identically dimensions and concrete material properties, but were designed to maintain the same nominal moment strength across bar grades.

Relevant structural parameters for each specimen are summarized in Table 4-1. All tests were carried on large scale specimens, with sectional depth ranging from 13.5 in. to 21.75 in. Longitudinal reinforcement bar sizes varied from #6 to #10, with longitudinal reinforcement ratios ranging from 0.7% to 4.7%. Transverse reinforcement spacing was as low as 4.4 longitudinal bar diameters and as high as 6 bar diameters. The reinforcing bar grades ranged from 60 to 100. The grade 100 bars used in this study encompassed the full range of HSRB under production in the United States as of the date of this publication. Therefore, the results were able to capture the effect of different mechanical properties present in HSRB. All specimens were constructed with moderate to low concrete compressive strengths, ranging from 3.13 ksi to 5.58 ksi.

Column specimens were tested in symmetric double curvature, whereas the beam specimens were tested as cantilevers. The beams were not subjected to axial load, whereas the axial load ratio (axial load divided by the gross-sectional compressive capacity) for the column members ranged from 0.15 to 0.41 (Table 4-1). The maximum applied shear stresses varied from $3.13\sqrt{f_c'}$ to $10.55\sqrt{f_c'}$ (in psi units) (Table 4-1).

TABLE 4-1: STRUCTURAL PARAMETERS FOR EACH SPECIMEN

Member	Section Effective Depth (d)[1] (in.)	Concrete Comp. Strength (psi)	Axial Load Ratio[2]	Shear Stress[3] ($\sqrt{f_c'}$ psi)	Shear Span / Section Depth	Long. Bar Dia. (in.)	Long. Reinf. Ratio[4]	Long. Bar Yield Strength (psi)	T/Y[5] Strength Ratio	Tie Spacing / Bar Dia.
2L06	13.50	3130	0.19	4.46	4.00	1.00	0.025	65500	1.64	6.0
2H06	13.50	3340	0.41	4.74	4.00	1.00	0.025	65500	1.64	6.0
CS60	15.27	3830	0.30	10.55	2.75	1.25	0.047	67300	1.41	4.4
CS80	15.44	4290	0.27	9.86	2.72	1.13	0.037	79100	1.35	4.9
CH100	16.13	5160	0.15	4.00	3.60	0.75	0.011	84600	1.27	4.7
CL100	16.13	5210	0.15	3.93	3.60	0.75	0.011	100000	1.16	4.7
CH60	16.13	4570	0.15	3.15	3.60	0.75	0.011	68500	1.45	6.0
BH100	21.75	5000	0.00	3.13	4.31	1.00	0.007	102120	1.25	5.0
BL100	21.75	5100	0.00	2.91	4.31	1.00	0.007	105730	1.17	5.0
BH60	21.70	5340	0.00	3.69	4.31	1.13	0.011	65130	1.47	4.4
CM100	16.13	5580	0.15	4.55	3.60	0.75	0.011	124200	1.27	4.7
BM100	21.75	5470	0.00	3.82	4.31	1.00	0.007	100420	1.63	5.0

[1] *The section effective depth (d) is taken as the distance measured from the extreme compression fiber to the centroid of the outermost layer of longitudinal tension reinforcement.*

[2] *Axial load ratio is taken as the applied axial load divided by the gross sectional area and the measured concrete compressive strength at the day of column testing*

[3] *Shear stress is taken as the peak applied lateral load divided by member depth, width, and the square-root of concrete compressive strength*

Specimens were instrumented to measure strains at the point of maximum demand in the longitudinal bars, and in some instances strain demands along the length of bars. While different layouts for strain gauge placement were used in different series, the mean values recorded from multiple strain gages located at peak demand sections are reported in this paper. Tests in Series 2 and 3 were monitored with a digital image correlation (DIC) system developed by the authors (Sokoli et al. 2014, Sokoli and Ghannoum 2016). The DIC system was used to monitor surface deformations, which were useful in calibrating the propose framework.

4.2.1 Behavioral Milestones

To aid in understanding the behavior of each member and to calibrate the mechanics-based local deformation models, member behavioral milestones were extracted along with the drift ratio levels at which they occurred for tests of Series 1, 2 and 3 (Table 4-2). The information was not available for specimens in Series 4. Drift ratio is defined as the lateral drift divided by member clear span.

The reported behavioral milestones of interest are: the first flexural crack (FFC), the first inclined crack (FIC), the longitudinal bar yield (LBY), the first transverse reinforcement yield (FTBY), spalling damages state 1 (SDS1), spalling damages state 2 (SDS2), and spalling damages state 3 (SDS3).

The FFC, FIC, MLBY, and FTBY were originally reported by Leborgne 2012, Sokoli 2014, Sokoli and Ghannoum 2016 and Sokoli et al. 2017. FFC, FIC and FTBY were

102

identified by surface strains acquired from the DIC system and verified by visual inspection. LBY was identified from strain gauges installed at the interfaces of the columns and footings where the demands were expected to be the largest.

Spalling damages states (SD1, SD2, SD3) were first reported in Limantono (2016) and obtained by tracking the maximum of horizontal surface strains in the plastic hinge region at the approximate location of longitudinal bars (Figure 4-1). The milestone SD1 was defined as the first significant increase in the horizontal strain near the face of the column (i.e. Row #1 in Figure 4-1) and represented when the first hairline spalling crack occurred. SD2 was taken at the point in loading history when any horizontal strain (Row 1 – 5) jumped above a strain equal to 0.02. SD3 was taken at the point in loading history when any horizontal strain jumped above 0.04, representing severe damage in the column (Figure 4-1). A more detailed discussion can be found in Limantono (2016).
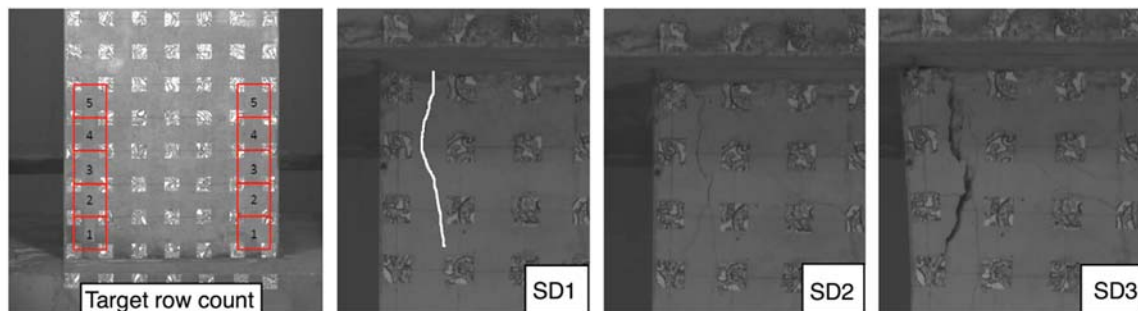
FIGURE 4-1: EXAMPLE OF SURFACE STRAIN TRACKING LOCATIONS AND DAMAGE STATES

TABLE 4-2: DRIFT RATIOS AT BEHAVIORAL MILESTONES

Specimen	FFC	FIC	LBY	FTBY	SD1	SD2	SD3
	All Values in Drift Ratio (%)						
2L06	0.69	0.92	0.90	N/A	N/A	N/A	N/A
2H06	0.65	1.62	1.30	N/A	N/A	N/A	N/A
CS60	0.30	0.60	2.00	3.00	0.60	1.32	1.67
CS80	0.40	0.60	1.05	2.00	1.00	1.41	2.00
CH100	0.20	0.60	1.01	N/A	1.50	2.87	3.00
CL100	0.20	0.60	1.00	N/A	1.50	2.70	3.12
CM100	0.20	0.60	N/A	N/A	3.00	4.00	N/A
CH60	0.20	0.60	0.60	N/A	1.00	2.68	3.99
BH100	N/A	N/A	1.25	N/A	N/A	N/A	N/A
BL100	N/A	N/A	1.25	N/A	N/A	N/A	N/A
BM100	N/A	N/A	N/A	N/A	N/A	N/A	N/A
BH60	N/A	N/A	0.90	N/A	N/A	N/A	N/A

N/A == data not available

4.2.2 Measured Strains in Longitudinal Bars

The measured longitudinal bar strains presented in this section were obtained from the strain gauge readings on bars farthest away from the flexural neutral axis and at the sections of highest moment, i.e., at both ends of the columns or the support end of the beams. Sample plot of measured strains versus drift ratios at critical sections for longitudinal bars in members CS80, CH100, BH100 and BM100 are shown in Figure 4-2.
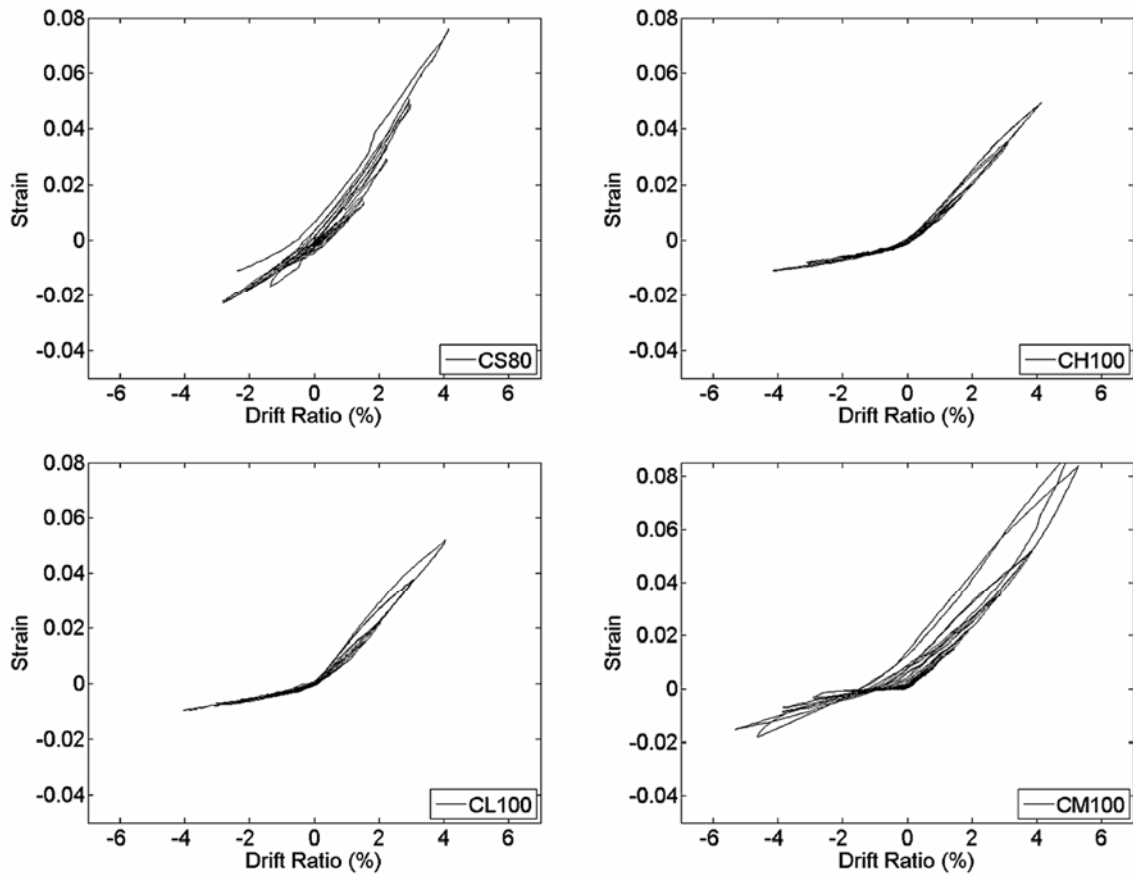
FIGURE 4-2: SAMPLE STRAIN GAUGE RECORDING FOR FOUR OF THE MEMBERS (POSITIVE STRAIN VALUES INDICATE TENSILE STRAINS)

Mean largest strains (ε_{MB}) of bars were calculated as the mean value of each reliable strain gauge measurement on corner bars at the sections of largest moments and at each drift target level, taking the average of both cycles to a certain drift target. Mean largest tension strains are plotted for all members versus drift ratio in Figure 4-3, while mean largest compression strains are shown in Figure 4-4. One of the variables that influences the value of strain in longitudinal bar is the effective depth (d) of the member section in the direction of loading. The larger the effective depth, the larger the longitudinal bar strain value is at a given lateral drift. The measured strains normalized by effective depth versus

105

the lateral drift ratios are provided for more direct comparison between all members in Figure 4-3 and Figure 4-4. The mean largest strains were only presented in Figure 4-3 and Figure 4-4 up to the drift ratios at which they were deemed to be reliable. In tests 2L06 and 2H06, the strain measurement beyond shear failure at a drift ratio of about 3.3% are not presented. Shear failure occurred in CS60 and CS80 only after drift ratios of 5.5%. Important observations can be made based on Figure 4-3 and Figure 4-4:

1- The largest inelastic tensile strain demands on longitudinal bars vary significantly from member to member at a given drift ratio. That is true even for columns that were designed to be nominally identical in dimensions and detailing, and subjected to the same axial load ratio (e.g., CH100, CL100, and CM100). In Series 2 and 3, reinforcing steel mechanical properties were found to alter inelastic strain demands in bars of nominally identical members by as much as 60%. Additional discussion on strain demands difference can be found in Sokoli and Ghannoum (2016) for Series 2, Sokoli et. al. (2017) for Series 3 and To and Moehle (2017) for Series 4.

2- Other parameters besides the reinforcing bar properties appear to alter the tensile strain demand difference between the various members, which lead to strain demands several folds different at any given drift ratio in Figure 4-3. The subsequent section discussing the strain prediction model investigates the influence of various parameters on the stain demands.

3- In columns with compressive axial loads, longitudinal bar strains did not vary significantly from cycle to cycle to the same drift target (Sokoli 2014, Sokoli and Ghannoum, 2014, Sokoli et. al 2018). On the other hand, the measured bar strains in

the beams that were not subjected to axial loads were highly dependent on the lateral loading history. After longitudinal bars yield in tension, loading reversal begins to compress residual tensile strains while flexural cracks begin to close. Depending on the magnitude of the tensile strains and member axial loads, bars can reach compressive stresses prior to cracks closing during load reversal, and prior to reaching compression strains. Therefore, it is possible for the longitudinal bars that have yielded in tension to experience only tensile strains (i.e. positive strain) during symmetrical cyclic lateral loading history. This was observed in beams specimens, where strains in longitudinal bars were seen to gradually increase in tension during cyclic loading. It is noteworthy that beams were not restrained longitudinally during testing, while such beams cast monolithically with slabs would be restrained and therefore may not experience such gradually increasing strains during cycling.
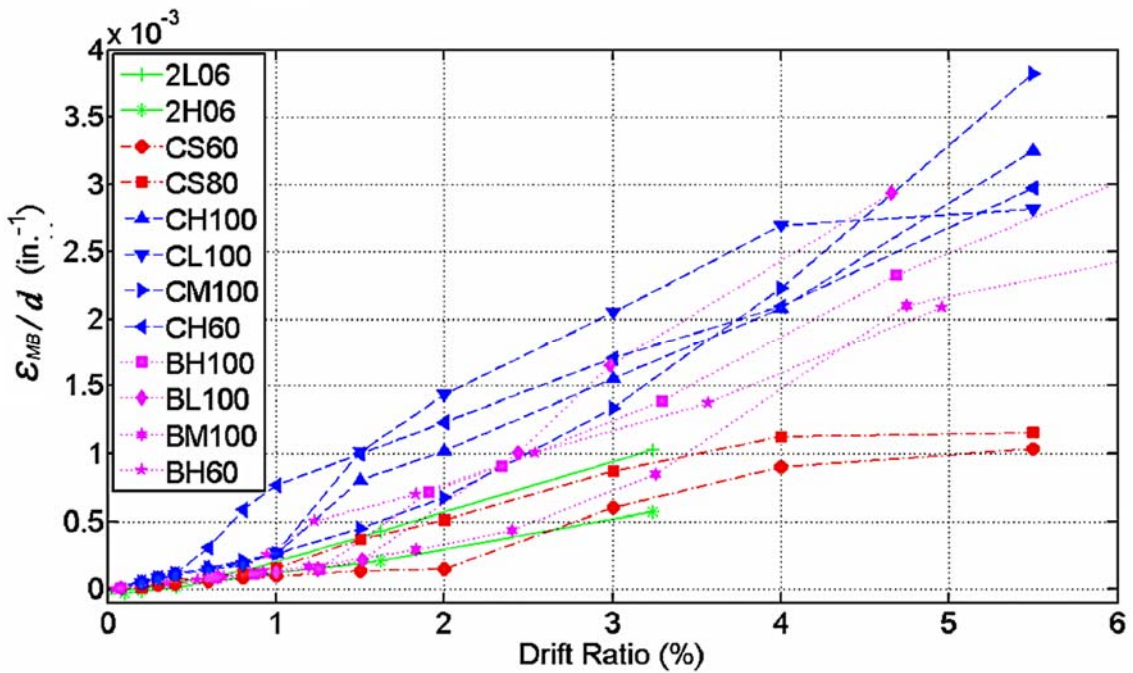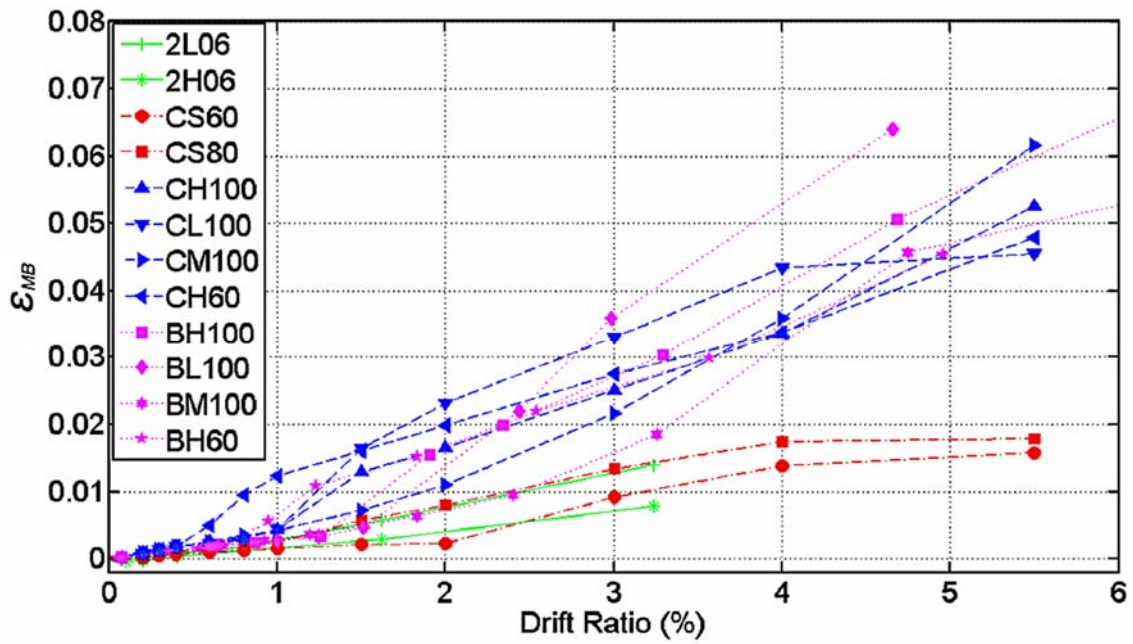
FIGURE 4-3: MEAN LARGEST TENSILE STRAIN DEMANDS (ε_M) VERSUS DRIFT RATIOS (UP), AND ε_M NORMALIZED TO SECTION DEPTH VERSUS DRIFT RATIOS (DOWN) FOR ALL SPECIMENS
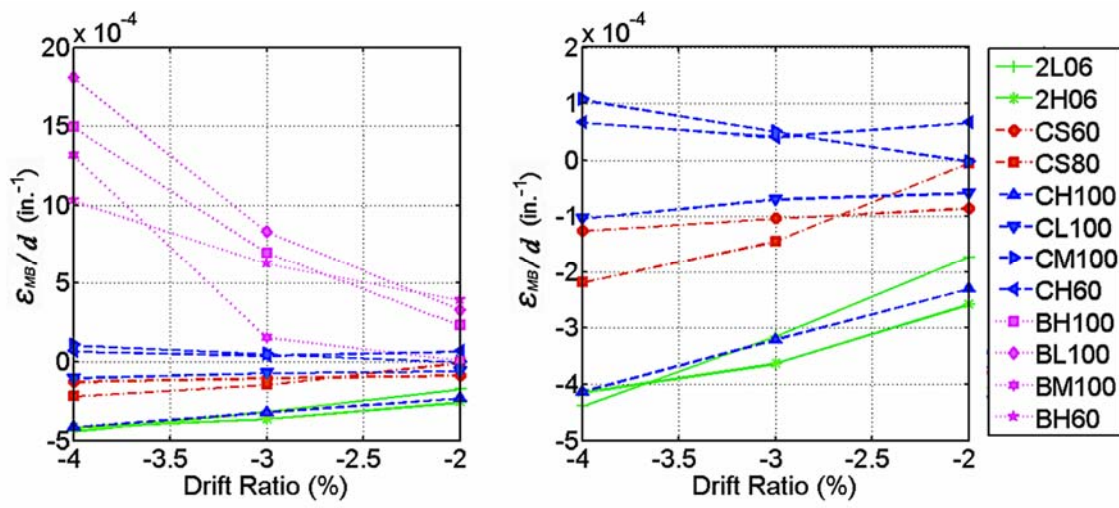
FIGURE 4-4: MEAN MEASURED STRAINS IN COMPRESSION FOR ALL MEMBERS (LEFT) AND COLUMNS ONLY (RIGHT)

4.2.3 Measured Surface Strains in Plastic Hinge Regions

Longitudinal strains on the concrete surface were monitored along the outermost longitudinal bars at column ends (Figure 4-5). This data was available for six column specimens, namely, CS60, CS80, CH100, CL100, CM100 and CH60. The strains were extracted between targets on the footings and targets 7 in. from the column/footing interface. This height represents the approximate location of the second hoop in the members. The measurements included deformations due to slip of bars from the foundations caused by strain penetration effects. Sample surface strains versus member drift ratio are presented in Figure 4-6.
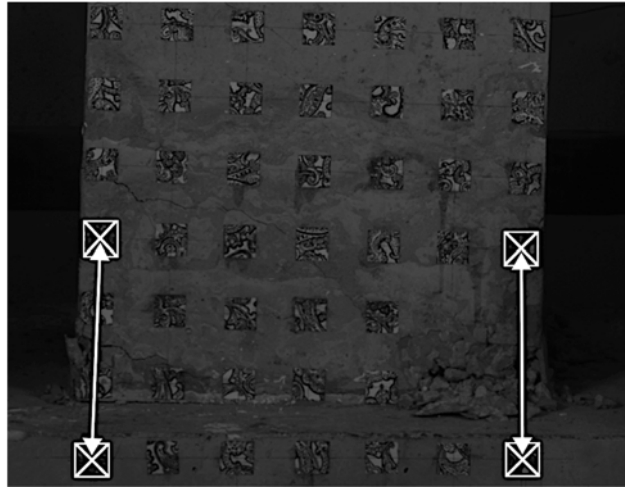
FIGURE 4-5: SCHEMATICS OF MONITORED STRAINS ON CONCRETE SURFACE
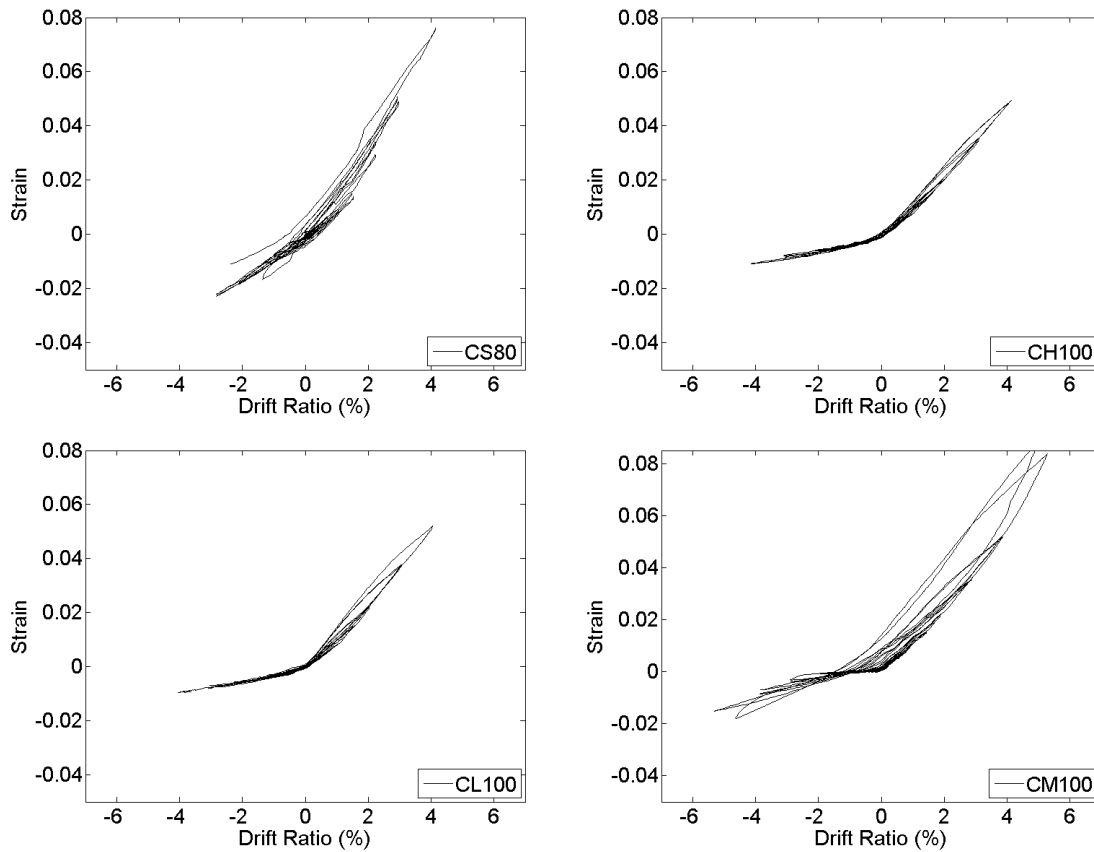
FIGURE 4-6: SAMPLE LONGITUDINAL SURFACE STRAINS IN MEMBER PLASTIC HINGE REGIONS

Measured surface longitudinal stains were fairly similar between the two consecutive half-cycle to the same drift ratio (Figure 4-6). This trend is similar to the one observed in the longitudinal-bar strains recorded in the same columns. The mean of the surface strains at each drift target (ε_{MS}) are plotted in Figure 4-7 for all specimens for which the data were available. Similar to strains in the longitudinal bars, members subjected to higher axial loads (CS60 and CS80) experienced higher compressive strains and lower tensile strains on average.
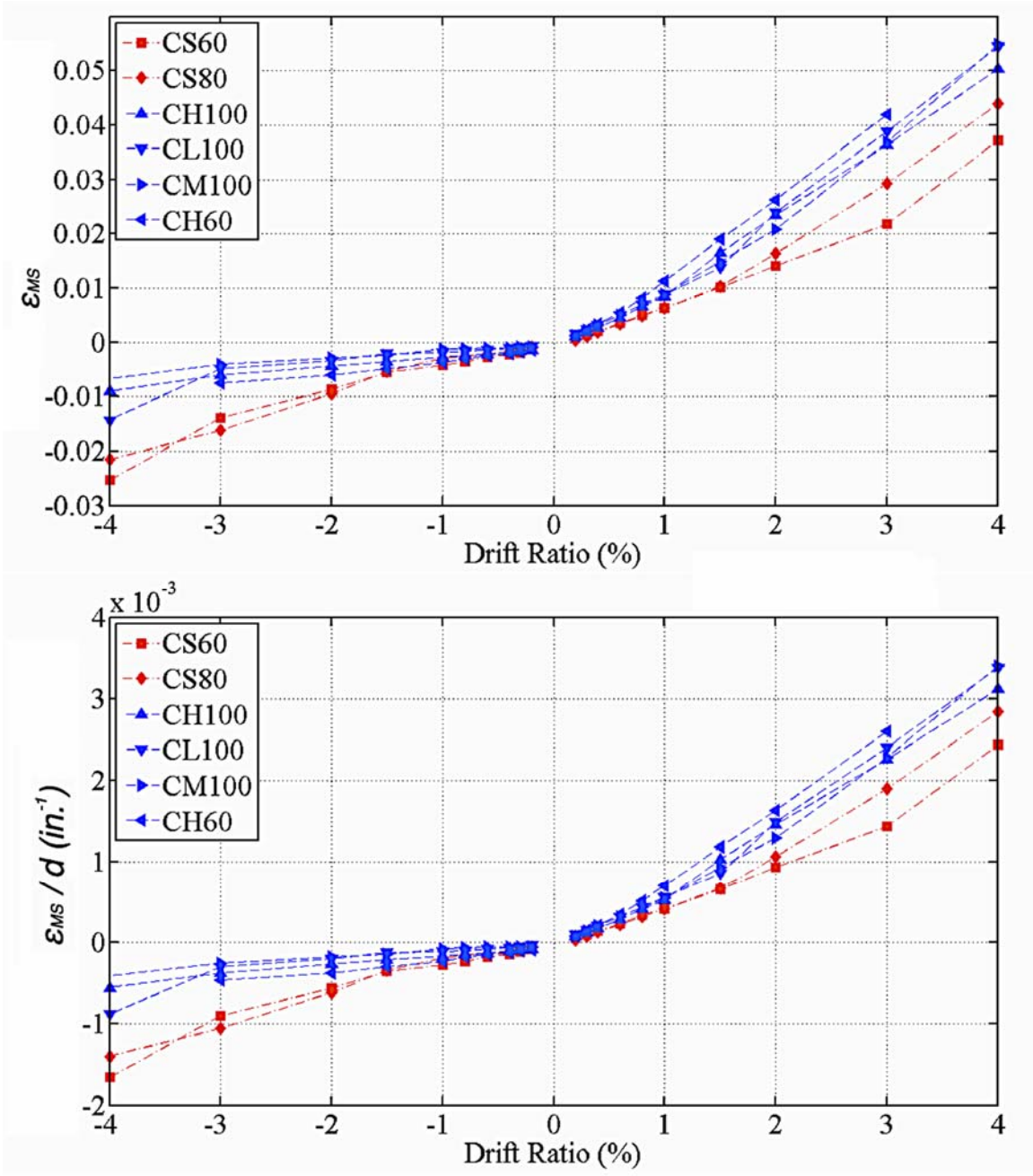
FIGURE 4-7: MEAN CONCRETE SURFACE STRAIN DEMANDS (UP) AND NORMALIZED TO SECTION
DEPTH (DOWN) FOR SIX OF THE SPECIMENS

4.3 Fiber-Section Computational Model

A fiber-section line-element computational model was calibrated to obtain reliable member-level deformations. The model also provides strain estimates for longitudinal bars and the surrounding concrete within the plastic hinge region, which reflect at least partially, the effects axial loads and material properties. Nonlinear monotonic and cyclic pushover analyses were conducted for each specimen to calibrate the computational model. Results from monotonic analyses were used for the sensitivity analyses in order to save computation time. Model parameters including the layout of the fibers in the section, number of integration points, and material constitutive models, were selected to achieve reliable member deformations for the 12 tests considered. The open source simulation software OpenSees (McKenna 2000) was used in analyses.

4.3.1 Fiber-Section Distributed Plasticity Element

A distributed plasticity fiber-section force based formulation element was used to model the column flexural behavior (Spacone et al., 1996), with the suggested changes by Coleman and Spacone (2001) (Figure 4-8). This element is formulated with constant curvature between integration points, which generates constant strains around each integration point, unlike displacement-based elements that typically have linear curvature assumptions along the element. Additionally, one force-based element is sufficient to capture the column global deformation and strain demands in the nonlinear range of behavior, as opposed to requiring several displacement-based elements to achieve the same accuracy (Neuenhofer and Filippou 1997, Scott and Fenves 2006, Addessi and Ciampi 2007). Elastic rotational springs were added at the end of the distributed plasticity line

113

element to simulate the softening effect of strain penetration of longitudinal bars in the adjacent footings. Elastic shear springs were introduced as well at the ends of the distributed plasticity element to capture shear flexibility. Nonlinear geometry effects were treated in the analyses.
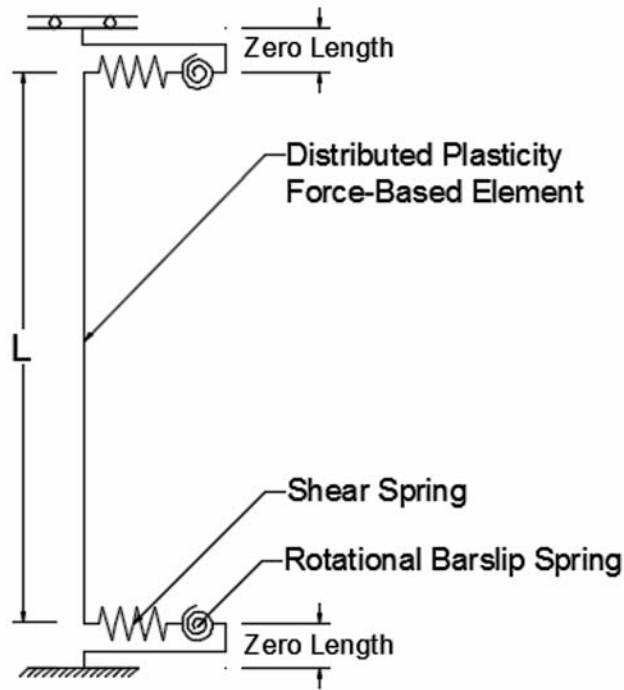
FIGURE 4-8: DISTRIBUTED PLASTICITY FIBER-SECTION MODEL

4.3.2 Fiber Discretization

The column section was discretized into fibers modeling the cover concrete, core concrete, and steel reinforcement (Figure 4-9). Considering that the number of fibers affects computational time, a sensitivity study was conducted to determine the optimal number of concrete fibers required to capture column lateral response and provide a reasonable starting point for tension strains in longitudinal bars for all type of sections investigated in this study. Details of the sensitivity study can be found in Limantono

(2016). Ten fibers in the core and side covers were selected based on the study, while two fibers were selected for the outermost covers in the direction of loading for all members (Figure 4-9).
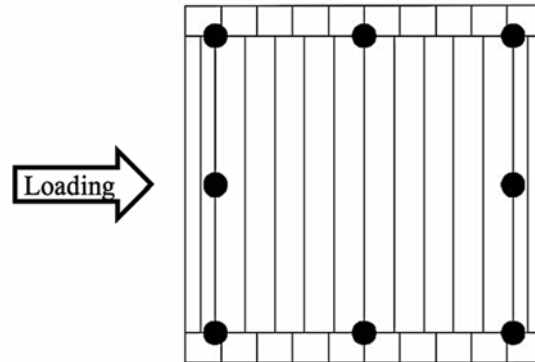
FIGURE 4-9: FIBER SECTION CONFIGURATION FOR ALL MODELED MEMBER

4.3.3   Material Models

Concrete

The stress-strain response of the cover concrete was modeled using the Concrete02 material model in OpenSees, which is based on the work by Kent and Park (1971) and utilizes linear tension degrading behavior. To avoid rapid and unrealistic softening of the member response due to localization of deformations occurring in force-based elements (Scott and Fenves 2006, Scott and Hamutcuoglu 2008), the softening branch of the concrete cover material model was regularized to adjust the strain (ε_{20}) at which the concrete stress drops to $0.2\, f'c$ in the softening branch (Coleman and Spacone, 2001) (Figure 4-10); with $f'c$ being the peak compressive stress in the model. The regularization process accounts for the length over which the curvature of the end fiber-sections are integrated. For example, that length is 5% of the length of the column element for 5 Gauss-Lobatto

115

integration points (Lp in Equation 1-1). Based on work in Colman and Spacone, 2001, ε_{20} can be estimated as:

EQUATION 4-1: STRAIN AT CONSTANT ENERGY INITIATION

$$\varepsilon_{20} = \frac{G_f^c}{0.6f'c \, Lp} - \frac{0.8 \, f'c}{E_c} + \varepsilon_0$$

where G_f^c is the material fracture energy under the material stress strain curve as illustrated in Figure 4-10; E_c is the modulus of elasticity of the concrete, ε_0 is strain at peak stress $f'c$, L_p is plastic hinge length, which is equal to the weighted length for the first integration point in the force-based element. The fracture energy of plain regular strength concrete cylinders tested under axial compression typically range from 0.11 kip/in. to 0.17 kip/in. (Coleman and Spacone 2001). The higher value of fracture energy (G_f^c) used for regularization results in higher strain ε_{20}. Higher values of ε_{20} or G_f^c reduce the softening slope in the lateral member response, or can even produce a hardening behavior (Figure 4-11). A sensitivity analysis carried for all members suggested that a value of G_f^c equal to 0.342 kip/in. would capture the post-yield slope of the lateral force versus lateral drift response of the test specimens (Figure 4-11).
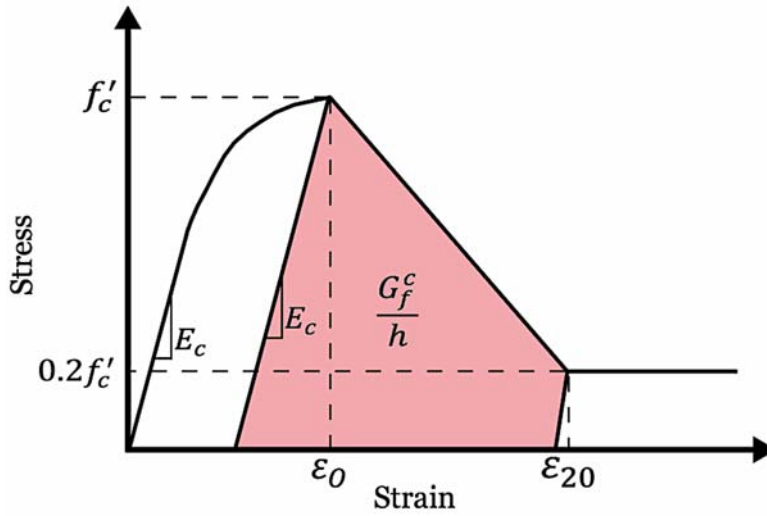
FIGURE 4-10: STRESS-STRAIN MODEL WITH FRACTURE ENERGY IN COMPRESSION AS
HIGHLIGHTED AREA (ADAPTED FROM KENT-PARK 1971)
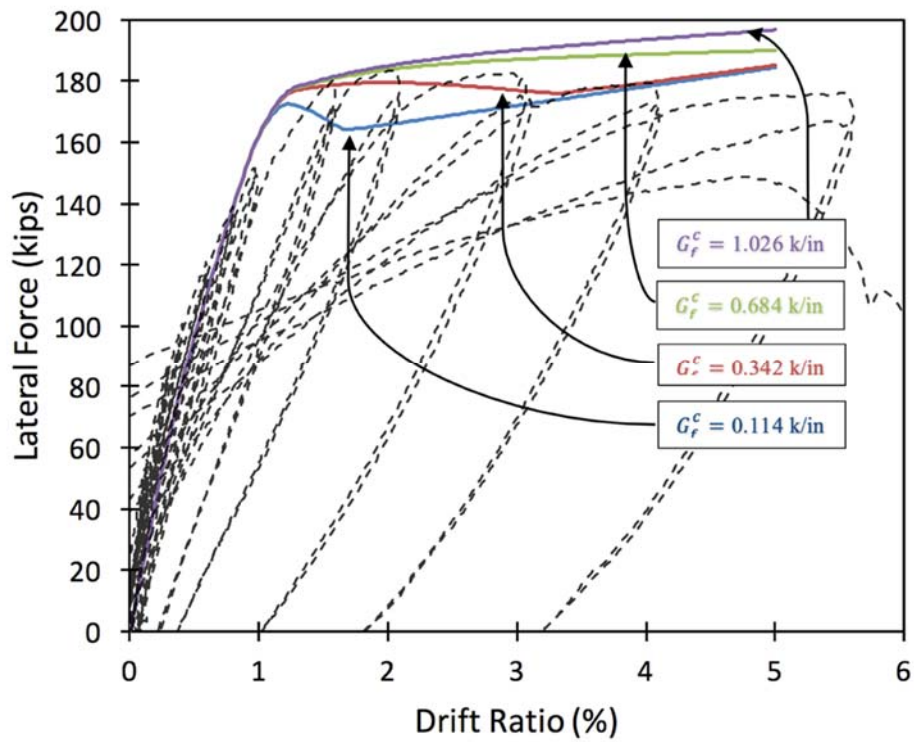
FIGURE 4-11: LATERAL RESPONSE SENSITIVITY TO G_F^C FOR CS80

To illustrate the regularization process, the adjusted concrete cover material model

in compression is plotted in Figure 4-12 for the concrete of column CL100. On the same

plot, the measured concrete compressive behaviors from three cylinder tests are shown. In regularizing the concrete model, the parameters in Equation 1-1 were taken as: $G_f^c = 0.342$ kip/in., $f_c' = 5110$ psi, $E_c = 4075$ ksi, $\varepsilon_0 = -0.0027$ (Ghannoum et al. 2008), and $L_p = 5.4$ in (for five integration points with the Gauss-Lobatto integration scheme for the force-formulation fiber element), and ε_{20} of -0.022 (compression). The difference in the pre-peak behavior between the measured cylinder response in compression and the regularized model is attributed to the single value peak strain selected ($\varepsilon_0 = -0.0027$) for all members.

The tensile response of concrete was modeled with a loading stiffness of $(2f'c/\varepsilon_0)$. The tension strength (f_t) was calculated with Eq. 19.2.3.1 in ACI 318-14. The linear softening slope (E_t) in tension was taken as 10% of the loading stiffness.
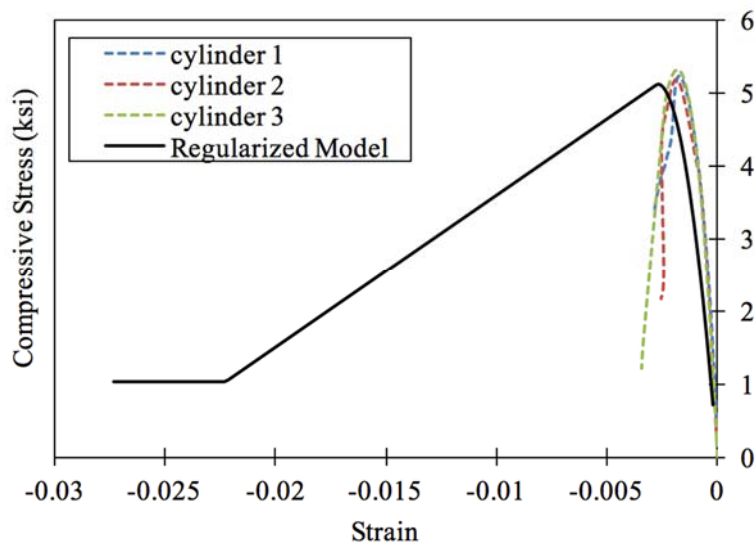
FIGURE 4-12: COMPARISON BETWEEN CYLINDER TEST AND REGULARIZED MODEL FOR CL100

The core concrete stress-strain response was modeled using the Concrete04 material model in OpenSees. This Popovics (1973) concrete material is characterized by a degraded linear unloading/reloading stiffness according to the work of Karsan-Jirsa (1969)

and tensile strength with exponential decay. The maximum stress value for the material

model was calculated in accordance with recommendations of Mander et al. (1988). The

strain at crushing was modelled using the empirical maximum strain equation suggested

by Qi and Moehle (1991). Additional details about core and cover concrete modeling can

be found in Limantono (2016). Figure 4-13 compares the cover and core concrete material

models in compression for column CS80.
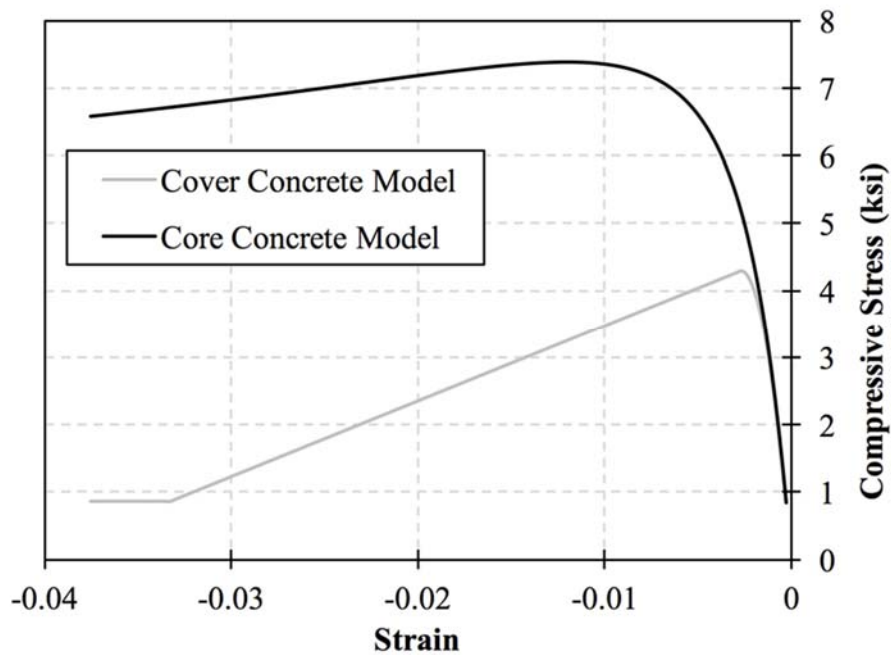
FIGURE 4-13: COVER AND CORE CONCRETE MODEL

Steel Material Model

The behavior of reinforcing bars was modeled using the Steel02 material model in

OpenSees, which is a bi-linear Giuffre-Menegotto-Pinto (1972) model that captures the

Bauschinger effect (Bauschinger, 1886). The strain hardening ratio (b), which is the ratio

between post-yield tangent stiffness and initial elastic stiffness was calculated using data from Table 4-1 in Equation 4-2:

EQUATION 4-2: CALCULATING STRAIN HARDENING RATIO

$$b = \frac{f_y\left[(T/Y) - 1\right](ksi)\Big/(\varepsilon_u - \varepsilon_y)}{29000}$$

where f_y, ε_y and ε_u are the measured yield strength, yield strain, and uniform strain, respectively, and were obtained from tension test results of the longitudinal bars.

The calculated strain hardening ratio values were found to be consistent with recommendations from previous research (Berry and Eberhard 2007), being close to 1% for grade 60 bars (Table 4-3). This value was used for specimens reinforced with grade 60 bars and for which the full stress-strain curve data was not available (i.e., 2L06 and 2H06). The hardening ratio was lower than 1% for bars having a yield strength higher than 60 ksi (420MPa) and having a distinct yield point. The ratio was higher than 1% for members reinforced with ASTM A1035 steel due to that steel's rounded stress-strain shape. Figure 4-14 compares the Steel02 monotonic stress-strain curves for longitudinal bars of CH100 and CM100, overlaid on a typical experimental stress-strain curve.

TABLE 4-3: STRAIN HARDENING RATIO

Column	2L06	2H06	CS60	CS80	CL100	CH100	CM100	CH60	BH100	BL100	BM100	BH60
b (%)	1.00*	1.00*	0.96	1.09	0.71	1.28	2.58	0.86	0.97	1.00	4.2	0.94

*Assumed values based on literature and estimated values in similar bar types
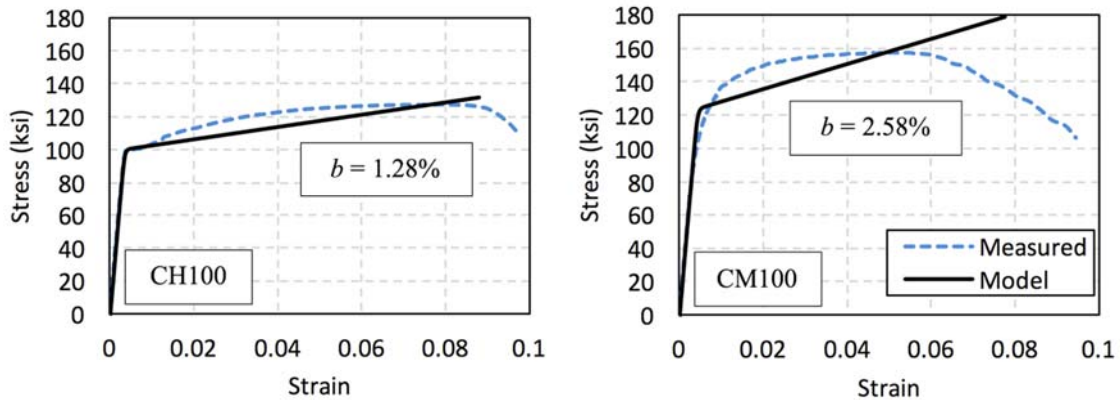
FIGURE 4-14: COMPARISON OF MEASURED AND MODELED STRESS-STRAIN CURVES FOR BARS IN CH100 AND CM100

The Reinforcing Steel material model in OpenSEES simulates the post-yield behavior of reinforcing bars much more closely than the Steel02 model. The comparison of Steel02 and Reinforcing Steel material models, however, demonstrated insignificant response differences for both high shear – high axial load columns (e.g., CS80) and low shear – low axial load columns (e.g., CL100) in (Figure 4-15). The Steel02 material model was selected in this work because similar bi-linear steel models are commonly available in most simulation software.
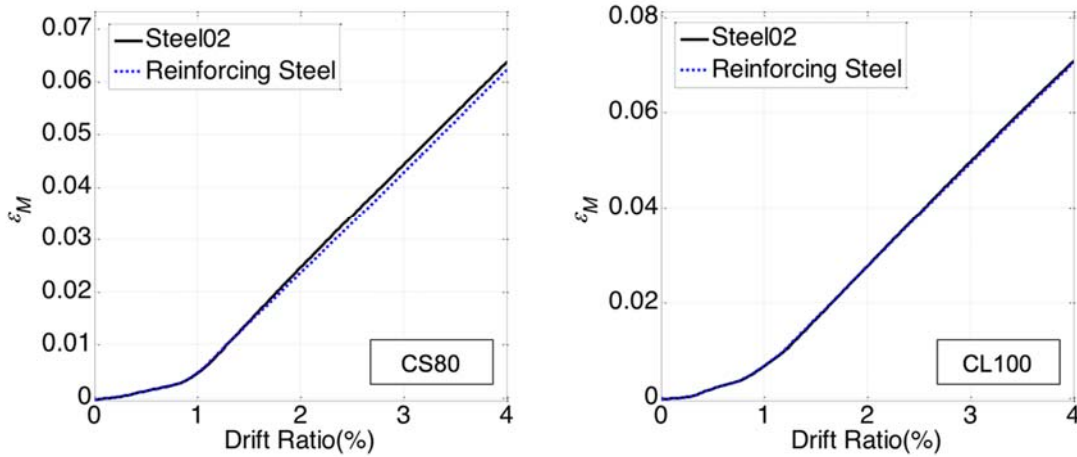
FIGURE 4-15: TENSION STRAIN COMPARISON FOR STEEL02 AND REINFORCING STEEL MATERIAL
MODELS

4.3.4 Shear Deformations

Measured shear deformations were relatively small compared with total lateral deformations for all tested specimens. Given the low impact of shear deformations on total deformation, shear deformation was modeled using a shear spring with an elastic stiffness given by:

EQUATION 4-3: SHEAR SPRING STIFFNESS

$$k_{shear} = \frac{(5/6)GA_g}{L}$$

where G is the shear modulus calculated as $G = \frac{E_c}{2(1+v)}$, A_g is gross section area, L is the column length, E_c is the concrete material elastic modulus and is calculated as $57,000\sqrt{f'c}$ psi as per ACI 318-14 provisions, v is the Poisson Ratio of concrete and was taken as 0.25.

4.3.5 Bar Slip Deformations

Slip of longitudinal bars due to strain penetration in adjacent footings, or longitudinal bar slip, accounted for around 30 to 50% of the total lateral drift of the frame

members considered (Figure 4-16) (Sokoli et al. 2017). As can be seen in Figure 4-16, bar slip deformations tend to maintain their ratio to total deformations even within the inelastic range of behavior, indicating the bar-slip deformations undergo inelastic behavior as well.
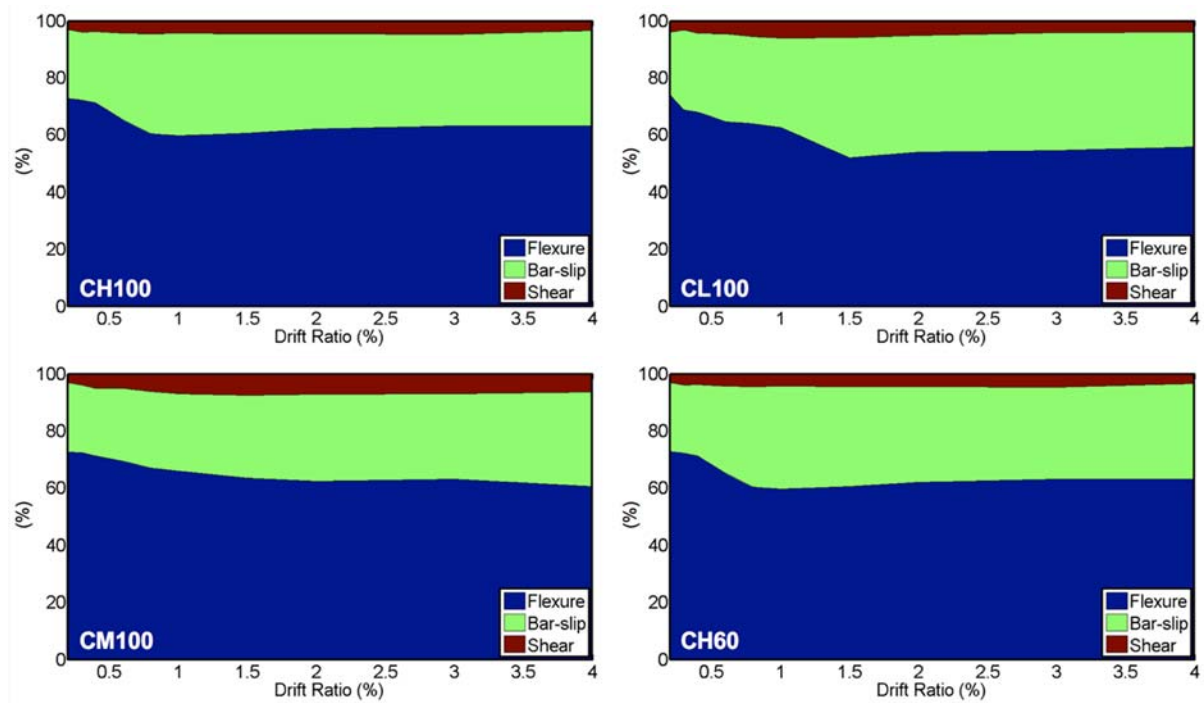
FIGURE 4-16: DEFORMATION COMPONENTS AT DRIFT TARGETS FOR COLUMNS OF SERIES 3

However, bar slip deformations were introduced through linear zero-length rotational springs at member ends. In this fashion, all nonlinear lateral drift behavior is simulated by the fiber-section element. Nonlinear bar slip behavior was not modeled to avoid numerical issues related to having two nonlinear elements in series when the fiber-section element exhibits a negative softening stiffness. This approach resulted in reasonable estimates of global member deformations as will be shown subsequently. Assuming a constant bond stress between bar and surrounding concrete in the footing (Sezen and Moehle 2004, and

Ghannoum and Moehele 2012), the rotational stiffness of the slip springs can be derived as:

EQUATION 4-4: BAR-SLIP SPRING STIFFNESS

$$k_{slip} = \frac{8u\,M_y}{d_b f_y\,\phi_y}$$

where u represents the constant bond stress between bars and adjacent concrete, M_y represents moment at first yield, ϕ_y represents the section's curvature at first yield, d_b represents longitudinal bar diameter, and f_y represents longitudinal bar stress at first yield. M_y, ϕ_y, and f_y can be estimated from moment curvature analyses, and were demonstrated experimentally to provide accurate measures using DIC data of columns tests (Sokoli et al. 2014). Recommendations for the constant bond stress parameter (u), however, vary greatly in the literature and depend on many factors, including whether the longitudinal bars are anchored in footings or in beam-column joints, and the level of damage or cracking the anchoring member.

Values of constant bond stress between bars and adjacent concrete have been reported in literature. Twelve concrete column tests carried by Lynn et. al. (1996) and Sezen and Setzler (2008), exhibited a mean u value of $11.4\sqrt{f'c}$. The same mean value for the constant bond stress ($11.4\sqrt{f'c}$) was also reported for six column tests by Melek et. al. (2003). Similar values were reported from beam tests by Sozen and Moehle (1990), where the mean u values for 35 beams tested under monotonic loading was calculated to be $10\sqrt{f'c}$.

For the column tests considered in this study, matching member lateral stiffness prior to yielding produced u values from $9\sqrt{f'c}$ to $18\sqrt{f'c}$, with a mean of $13.9\sqrt{f'c}$, and a standard deviation $2.9\sqrt{f'c}$. Limantono (2016) investigated the effect of varying the elastic bond stress parameter between the low and high end of the range identified above and found that it resulted in less than 5% difference in the inelastic strain demands in longitudinal bars produced by the fiber-section element. Therefore, the same value of bond stress (u) of $14\sqrt{f'c}$ was used in this study for column members, while a value of $11\sqrt{f'c}$ was used for beam members. It is noteworthy that the test members were connected to large footings that remained essentially undamaged during testing, which resulted in bond stresses on the higher end of the range provided in the literature. However, when considering moment frames, the lower value of $9.6\sqrt{f'c}$ recommended by Elwood and Eberhardt (2009) and Kwon (2016) may be more appropriate.

4.3.6 Flexural Deformations

The flexural deformation component was modeled using a distributed-plasticity, force-based, fiber beam-column element. The fiber beam-column element is a line element with a fiber-section assigned at each integration point, with each fiber-section defining the moment curvature response at that point. A force-based formulation always satisfies equilibrium along the length of the element. Equilibrium is satisfied by force interpolation functions. Deformations along the length of the element are obtained by weighted integration of the fiber-section deformations (Spacone et al. 1996).

Inelastic deformations in reinforced concrete columns typically occur in the end sections of the columns. In order to account for that scenario, a Gauss-Lobatto integration scheme is used in the element since it has integration points at the ends of the element, which coincide with the sections of highest inelastic deformation. The Gauss-Lobatto integration method is a numerical integration approximation of the definite integral of a function, which is evaluated as the sum of weights multiplied by function values at the integration points within the domain of integration. The Gauss-Lobatto integration method matches the exact results of polynomials of degree 2N-1 (with N being the number of integration points). Thus, the Gauss-Lobatto integration method has a specific weight and integration point locations for each number of integration points (N) to match exactly the polynomials of degree 2N-1. However, local flexural deformations along the length of reinforced concrete columns do not follow any polynomial function because of cracks, damage, and inelastic deformation that occur along the length of a column. Therefore, deformation delivered by a Gauss-Lobatto integration scheme for fiber-section curvatures can only approximate the actual distribution of flexural deformations along a column length.

The measured and modeled flexural deformations using different number of integration points were compared for all specimens at two force levels: first yield and at 80% of that value. First yield was taken as recommended by Benzoni et al. (1996) as the first point at which the tension reinforcement yielded or the maximum concrete compressive strain reached a value of 0.002. The lateral force versus drift response of column CS80 as measured from the experiment and modeled in OpenSees with different

number of integration points is plotted in Figure 4-17. Based on the results of the sensitivity analysis, five Gauss-Lobatto integration points produced reasonably small errors for all members, typically on the order of 5% across the full drift range of the tests.
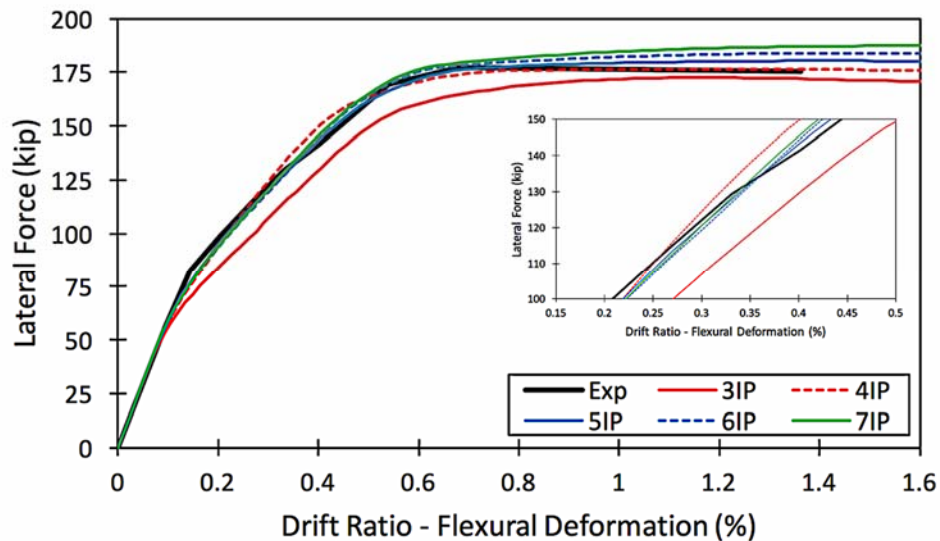
FIGURE 4-17: MEASURED AND MODELED FLEXURAL DEFORMATION COMPONENT OF CS80

It was also observed that five integration points deliver the least amount of errors in tensile strains in longitudinal bars before longitudinal bar yield (Figure 4-18). As can be seen in Figure 4-18, the strain in longitudinal bars localized significantly after yielding as the number integration points increased. The first integration point has a finite length proportional to the integration weight times the length of the element. Therefore, larger numbers of integration points generate smaller first integration weight (or length) where the plasticity is concentrated. This results in larger strains due to larger curvatures.
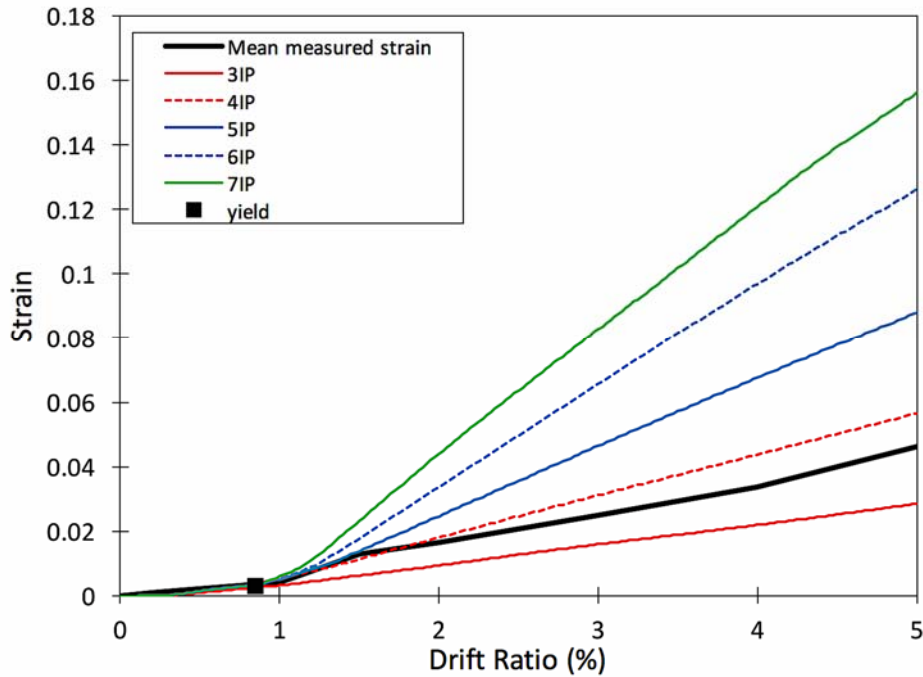
FIGURE 4-18: CH100 - INFLUENCE OF NUMBER OF INTEGRATION POINTS ON THE TENSILE STRAINS IN LONGITUDINAL BARS

Based on the above observations, five integration points are recommended per element to simulate the global column behavior and estimate the strains in longitudinal bars prior to yielding. However, when columns experience yielding, the associated fiber-section strain results become less reliable. In subsequent sections, an adjustment factor is proposed to modify the strains obtained from the five integration-point computational model after initial yielding occurs.

4.3.7 Simulated Member-Level Behavior

Due to the use of simplified elastic relations for bar slip and shear deformations, the estimated elastic stiffness before first yield was typically lower than the measured column global lateral stiffness, as shown in Figure 4-19. Nevertheless, the estimated total

drift before first yield can be considered acceptable and represents the measured stiffness after softening occurred due to cycling and past the point of first yield.

The mean measured tension strain demands at target drifts and those from fiber-section analyses are plotted for all member in Figure 4-21. In the figure, the assumed drifts at which the computational and experimental strains diverge are highlighted. This strain corresponds to the point in loading at which the bars in the analyses yield. As can be seen in Figure 4-21, the ratio between inelastic tensions strains from analyses and experiments varies greatly from member to member and can exceed a factor of 4.
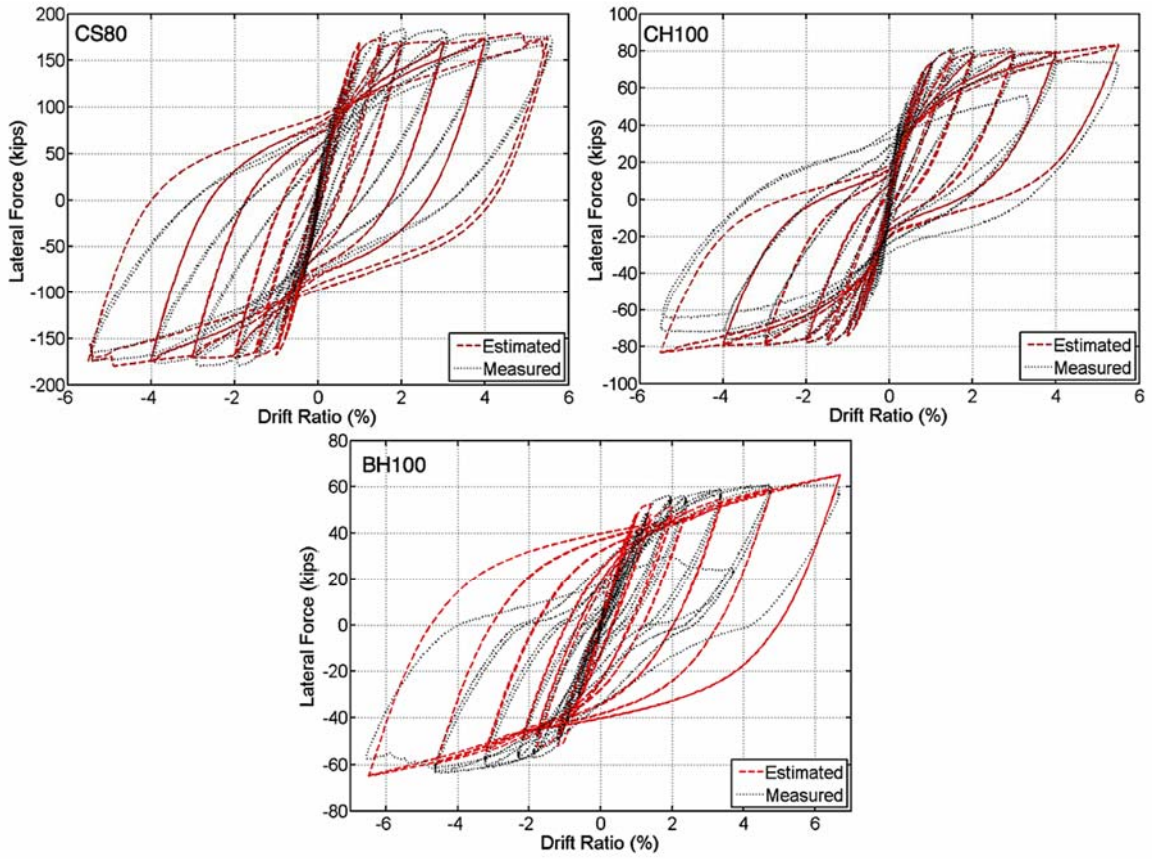
FIGURE 4-19: GLOBAL BEHAVIOR PREDICTION – CS80, CH100, BH100
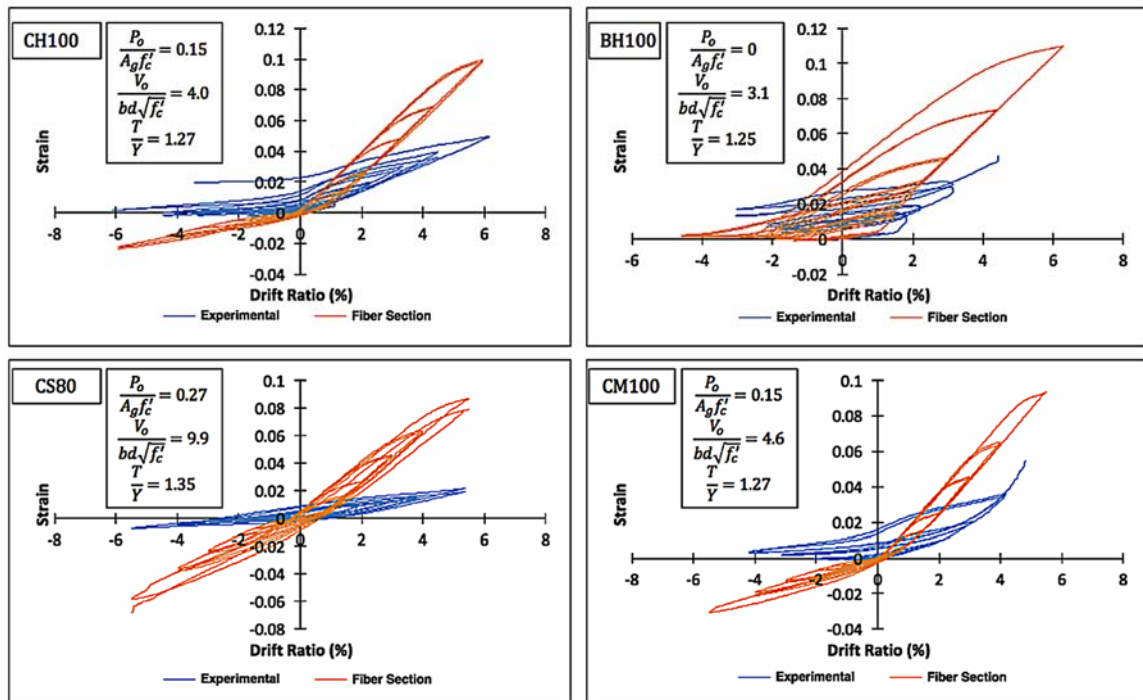
FIGURE 4-20: COMPARISON OF A TYPICAL CYCLIC STRAIN GAUGE READING AND CORRESPONDING RESULT FROM ANALYSES

The tested specimens where the only variable was the axial load ratio were columns 2L06 and 2H06 (Figure 4-21). Column 2L06 was tested with an axial load ratio of 0.19 and column 2H06 with an axial load ratio of 0.41. In these tests, higher axial loads delayed the longitudinal bar yielding to a larger drift, and produced lower strain increases with increasing drift after yielding. Even though the fiber-section model accounted partly for that effect, it did not capture the extent of the axial load influence on inelastic bar strains. Possibly, the assumption of perfect bond between steel and concrete in the fiber-section model could not capture the effects of degrading bond between longitudinal bars and concrete in the inelastic range due to concrete damage and spalling.

The tested specimens where the only variable was the strain hardening ratio (b) of the longitudinal reinforcement were columns CL100, CH100, and CH60, as well as beams

BL100, BH100, and BH60. The strain measurements from experiments indicated that the longitudinal bar strain progression after bar yielding was related to the T/Y ratio of the bars. A higher T/Y ratio produced a lower strain progression with increasing drift. Even though the strain hardening ratio was adjusted for the steel material model, the computational results showed approximately the same rate of strain progression with increasing drifts for all columns (Figure 4-21). On the other hand, the computational model captured the effects of the bar yield strength, with lower yield strengths yielding at earlier drift ratios.

FIGURE 4-21: CONTINUES INTO NEXT PAGE

133

FIGURE 4-21: CONTINUES INTO NEXT PAGE

134
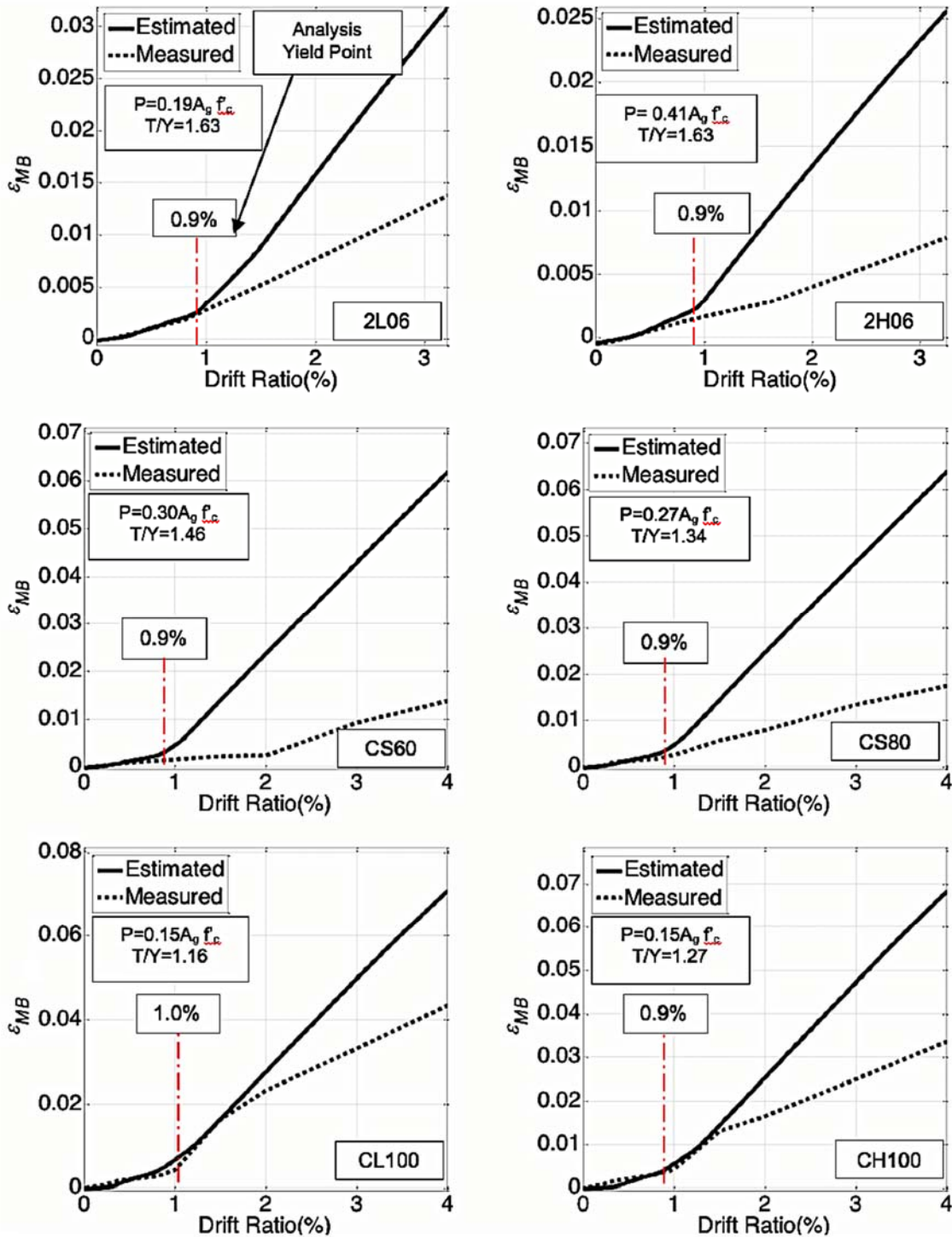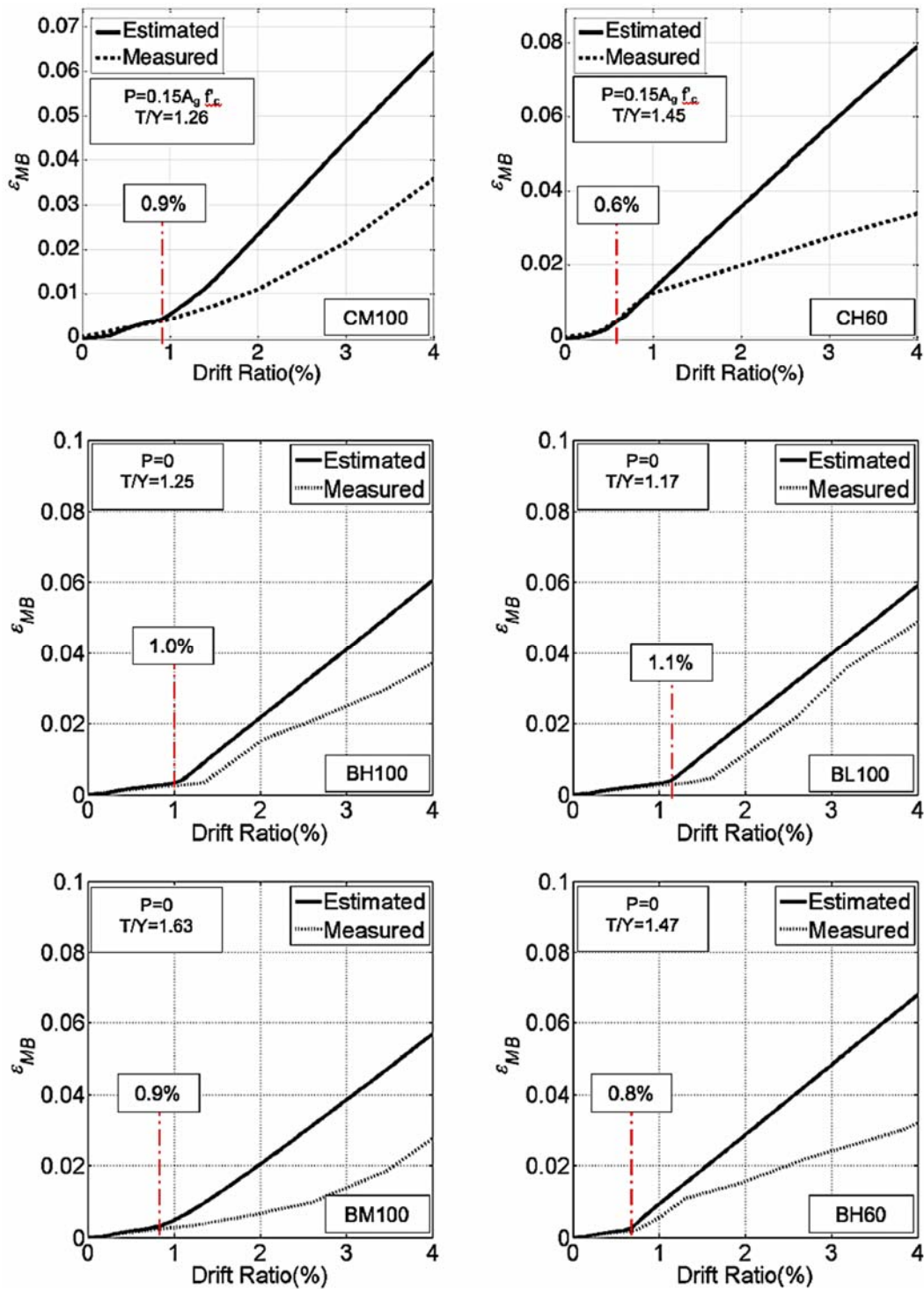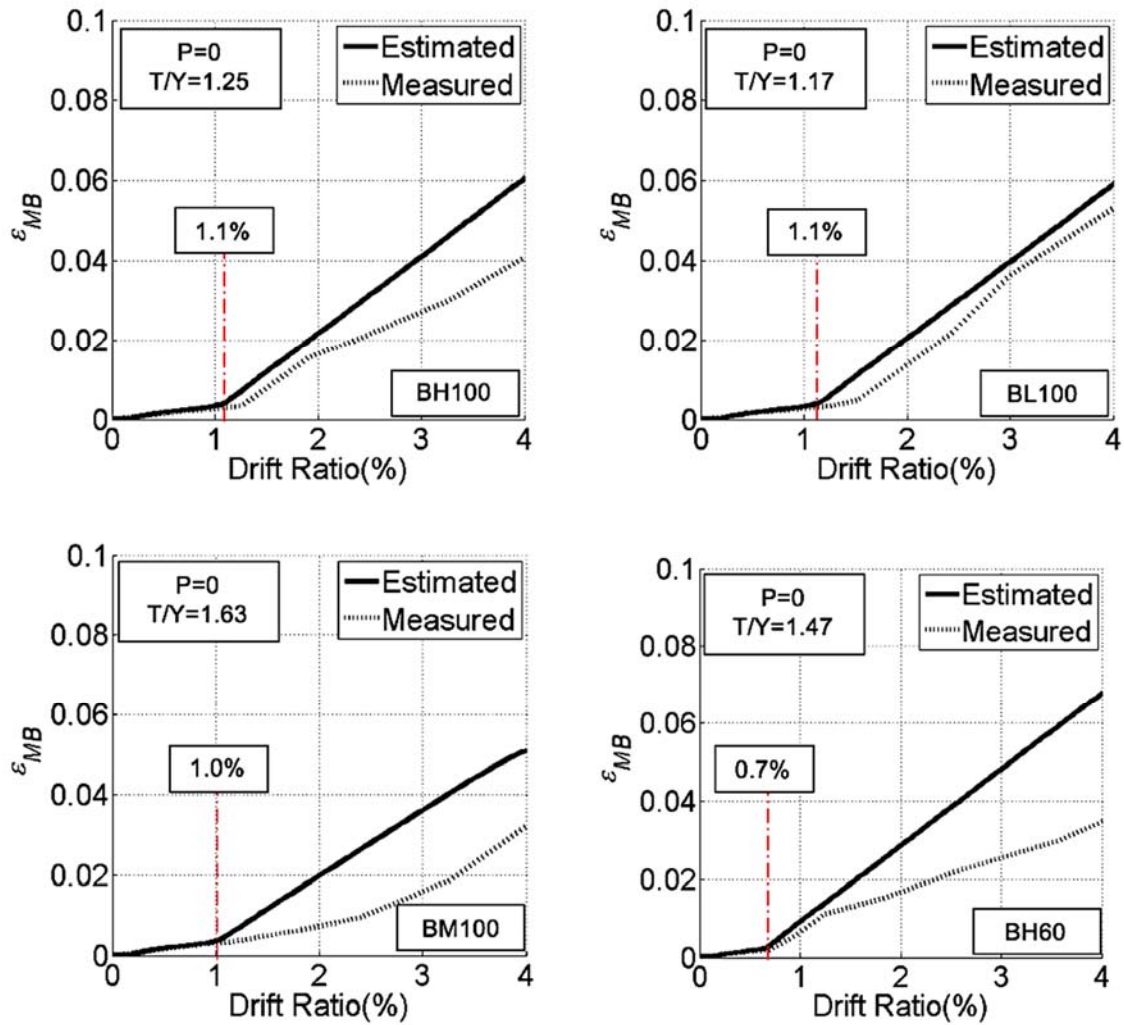
FIGURE 4-21: TENSILE STRAINS FROM ANALYSIS AND MEASURED FOR ALL MEMBERS

4.4 Estimating Strains in Reinforcing bars

4.4.1 Tensile Strains

Estimated tensile strains were always larger than the measured strains at the sections of peak flexural demand after a "divergence point". Limantono (2016) concluded that the "divergence point" closely coincide with the drifts at first yield and observed associated debonding or spalling cracks around longitudinal bars. The cracking of concrete at the longitudinal reinforcement appeared to allow for inelastic bar strains to spread over a larger length of the bar away from flexural cracks, thereby reducing the peak strain demands from those generated by a fiber-section model that assumes perfect bond. For simplicity and because strains at this level of loading are low enough to not induce damage in the longitudinal bars, the yield strain from analyses was taken as the divergence point between measured and analysis strain results.

Post-yield tension strains in longitudinal bars were scaled through a Tension Scaling Factor (*TSF*). For each test, the *TSF* factor was obtained at different lateral drift targets in accordance with Equation 4-5:

EQUATION 4-5: TENSILE STRAIN SCALING PROCEDURE

$$\varepsilon_{i-end} = \varepsilon_{i-analysis} \qquad\qquad for\ \varepsilon_{i-analysis} \leq \frac{f_y}{29000}$$

$$\varepsilon_{i-end} = \frac{f_y}{29000} + TSF\left(\varepsilon_{i-analysis} - \frac{f_y}{29000}\right) \qquad for\ \varepsilon_{i-analysis} > \frac{f_y}{29000}$$

where ε_i is the estimated strain demand at a given lateral drift ratio; $\varepsilon_{i-analysis}$ is the strain demand from the fiber-section analysis at the same lateral drift ratio for the same member, f_y is the yield strength of the longitudinal reinforcement.

The resulting *TSF* values for drift targets of 2.0%, 4.0% and 4.0% are plotted in Figure 4-22. As can be seen in Figure 4-22, the *TSF* was similar between the drift ratios of 2.0% and 4.0% for a given test, but varied greatly from test to test. The final *TSF* to be used in the scaling procedure was calibrated to achieve the highest accuracy at a drift target of 3.0%, where strain levels are also most critical for low-cycle fatigue failures. Moreover, this drift level corresponds to the drift limit specified in ASCE/SEI 7 (2016) for the Maximum Considered Earthquake scenario.
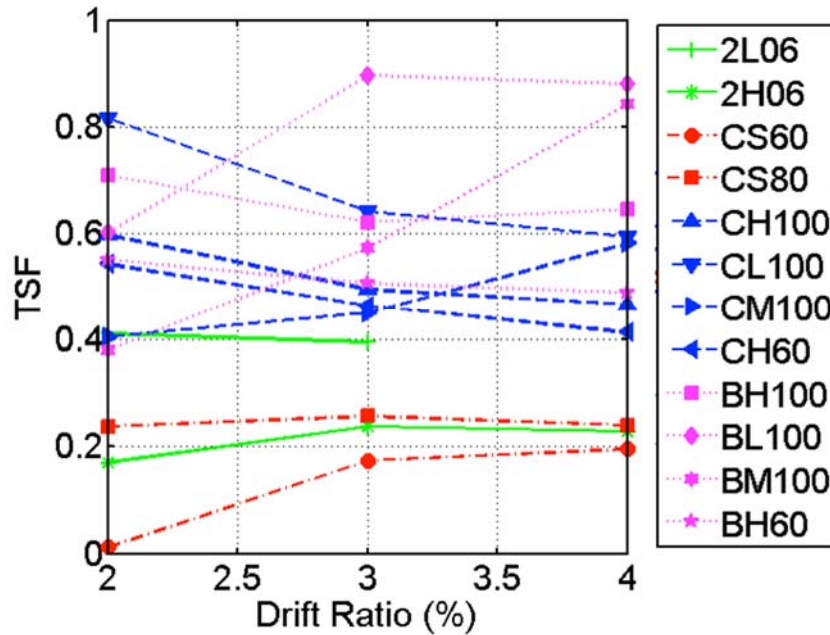
FIGURE 4-22: EXTRACTED *TSF* AT DRIFT RATIOS OF 2%, 3% AND 4%

The estimated *TSF* at 3% drift is plotted versus the most correlated test parameters in Figure 4-23. These parameters were member axial load ratio, member shears stress, and the *T/Y* ratio of the longitudinal bars. Higher axial load demands affect the strain demands

in longitudinal bars of concrete members, with a higher axial load ratio having a compressing effect on the tensile strains, and generating greater damage in concrete around the bars at any given drift level. The *TSF* was found to decrease with increasing axial load ratio, thereby reducing strain demands with increasing axial load. Higher shear stresses decrease the scaling factor, or conversely decrease bar strains. This is attributed to the increased concrete damage caused by higher shear stresses, as well as the effects of the tension shift mechanism on plasticity spread (Park and Paulay 1975). Additionally, larger values of the tensile to yield (*T/Y*) ratio of longitudinal bars reduced the scaling factor, which reduces the strain demands in the bars. This indicates that lower *T/Y* ratios concentrate strains in longitudinal bar at the critical flexural crack. This behavior is consistent with observations from laboratory tests (Macchi et al. 1996, Aoyama 2001, Sokoli 2014, Sokoli and Ghannoum 2014).
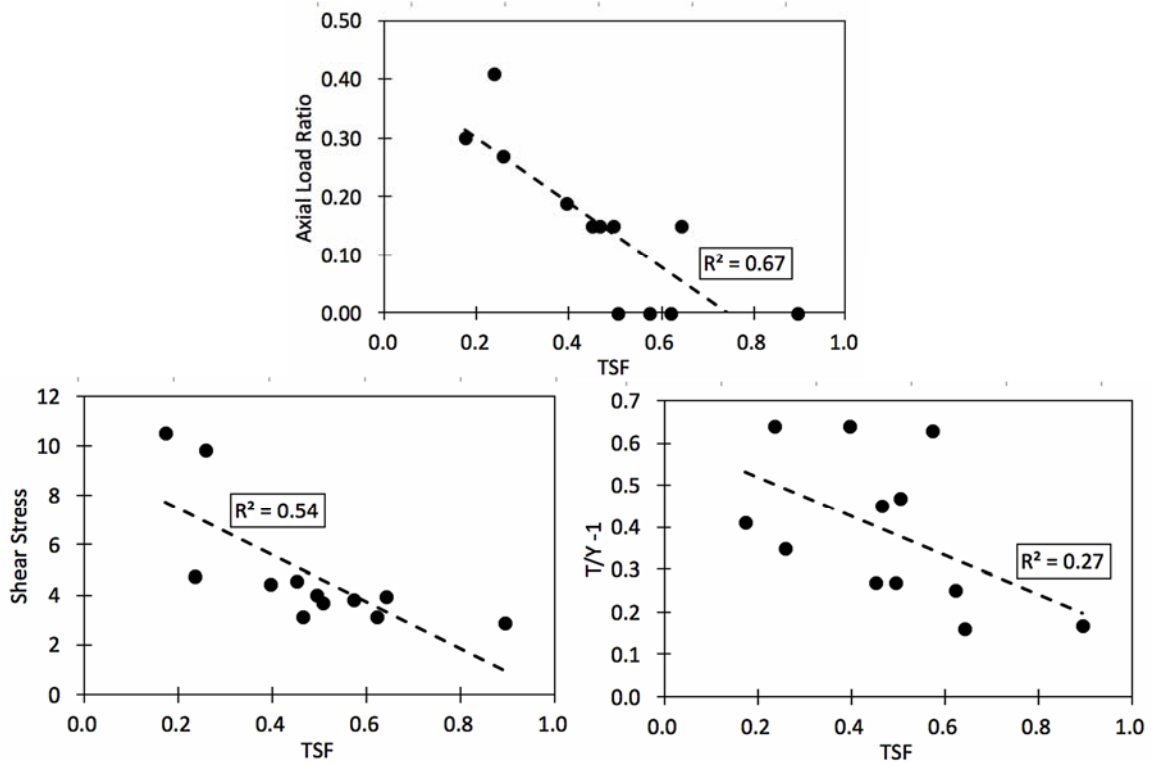
FIGURE 4-23: INFLUENTIAL PARAMETERS ON *TSF*

Equation 4-6 was produced through linear regression to calculate the *TSF* based on the three influential parameters discussed above. Results from Equation 4-6 serve as input in Equation 4-5 to scale fiber-section strains.

EQUATION 4-6: TENSILE STRAIN FACTOR

$$TSF = \frac{9}{10} - \frac{2}{3}\frac{P_o}{A_g f_c'} - \frac{1}{30}\frac{V_o}{bd\sqrt{f_c'}} - \frac{2}{5}(\frac{T}{Y} - 1)$$

where P_o is the applied axial load (in lb, positive in compression); A_g the gross sectional area (in.^{2}); f_c' is the concrete compressive strength (in psi); V_o the maximum expected shear demand and can be obtained from fiber-section analysis (in lb); b and d are the cross-sectional width and effective depth in inches, respectively; and T/Y is the tensile to yield strength ratio for the longitudinal reinforcement.

139

The extracted *TSF* at a drift ratio of 3% (as calculated from strain from analysis and mean measured strain), and the estimated *TSF* (calculated using Equation 4-6) are compared in Figure 4-24. The mean error ratio calculated as the ratio of the estimated *TSF* to matched *TSF* was 1.02. The standard deviation was 0.12. The measured and predicted tensile strains up to 4% drift ratio are compared in Sokoli (2018).
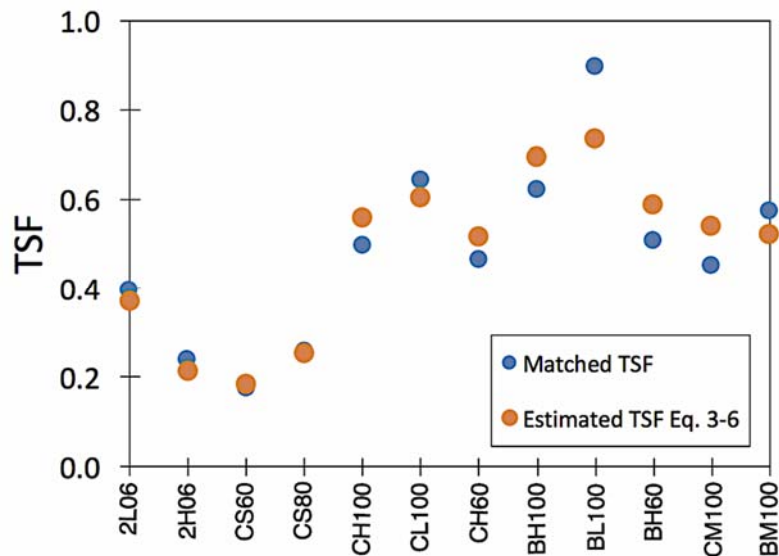
FIGURE 4-24: MATCHED VS. ESTIMATED TSF

4.4.2 Compressive Strains

A behavioral model was developed to estimate compression strains in longitudinal bars. The model is based on observed trends in the compression strains in the column tests. Longitudinal reinforcing bars in beams experienced inelastic strains when the surrounding concrete was in compression that ranged from 0 to positive 4% (i.e., tensile strains). The beams were not restrained longitudinally during testing, which allowed them to elongate as they were cycled laterally. However, beams in a moment frame are typically restrained

by a slab and columns or walls and therefore are not able to elongate to the same extent as in the laboratory tests. As such bar strains in beams may be closer to those obtained from the fiber-section analysis in structural systems. Moreover, high variability was observed in compression strains between members and even on bars of the same member, due to the highly variable distribution of concrete damage.

The best predictor of bar stains in compression was found to be axial load (Figure 4-25).
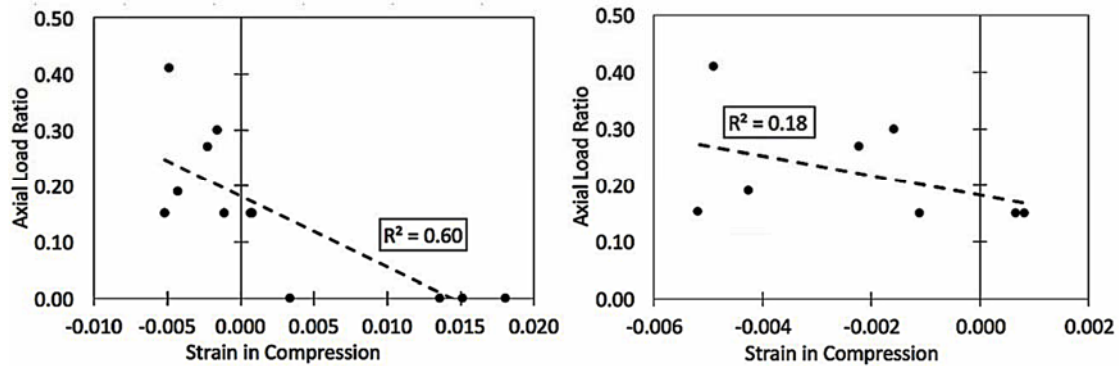
FIGURE 4-25: MEAN MEASURED STRAIN IN COMPRESSION AT 3% DRIFT RATIO VS. AXIAL LOAD RATIO (LEFT) ALL MEMBERS, (RIGHT) COLUMNS ONLY

To constrain the model, for members that are not designed to carry axial loads, the strain in bars when concrete surrounding them is in compression was taken as zero at a drift ratio of 3%. Following observed experimental trends in columns, the strain in compression at a drift ratio of 3% was taken as -0.5% for a member loaded at an axial load ratio of 50%. For axial load ratios between 0 and 50%, strain in the bars at a drift ratio of 3% can be obtained by linear interpolation as given in Equation 4-7:

EQUATION 4-7: STRAIN IN COMPRESSION AT A DRIFT RATIO OF 3%

$$\epsilon_{EC} = \frac{P_o}{100 \, A_g \, f'_c}$$

141

Scaling of the strains in the compression strain region obtained from fiber-section analyses for all drift levels can be accomplished by using a Compression Strain Factor (*CSF*) as follows:

EQUATION 4-8: COMPRESSION STRAIN SCALING PROCEDURE

$$\varepsilon_i = CSF \times \varepsilon_{i-analysis} \qquad for\ 0 > \varepsilon_{i-analysis}$$

EQUATION 4-9: COMPRESSION STRAIN SCALING FACTOR

$$CSF = \frac{\epsilon_{EC}}{\epsilon_{CA3}}$$

where ϵ_{CA3} is the compression strain from fiber-section analysis taken at a drift ratio of 3%.

4.4.3   Cyclic Strain Demands

To obtain the cyclic strain history for longitudinal bars at the critical moment sections of frame members, the Tension Scale Factor (*TSF*) and Compression Scale Factor (*CSF*) are to be applied per Equation 4-10. Scaling of bar strain is not necessary until bars exceed their yield strain for the first time as the fiber-section model is able to accurately capture those strains. In theory, after first yield all tension strains are to be scaled, but it is assumed here that strains between zero and tension yield are relatively small and therefore are not scaled (Figure 4-26).

EQUATION 4-10: SUMMARY OF SCALING PROCEDURE FOR STRAINS IN LONGITUDINAL BARS

$$\varepsilon_{i-end} = CSF \times \epsilon_{i-analysis} \qquad\qquad for\ \varepsilon_{i-analysis} < 0$$

$$\varepsilon_{i-end} = \epsilon_{i-analysis} \qquad\qquad for\ 0 \leq \varepsilon_{i-analysis} \leq \frac{f_y}{29000}$$

$$\varepsilon_{i-end} = \frac{f_y}{29000} + TSF(\varepsilon_{i-analysis} - \frac{f_y}{29000}) \quad for \; \varepsilon_{i-analysis} > \frac{f_y}{29000}$$

where:

$$CSF = \frac{\epsilon_{EC}}{\epsilon_{CA3}}; \; \epsilon_{EC} = \frac{P_o}{100 \, A_g \, f_c'}$$

$$TSF = \frac{9}{10} - \frac{2}{3}\frac{P_o}{A_g f_c'} - \frac{1}{30}\frac{V_o}{bd\sqrt{f_c'}} - \frac{2}{5}(\frac{T}{Y} - 1)$$

A comparison between scaled fiber-section strains and typical measured strains from beam and column tests is presented in Figure 4-27.
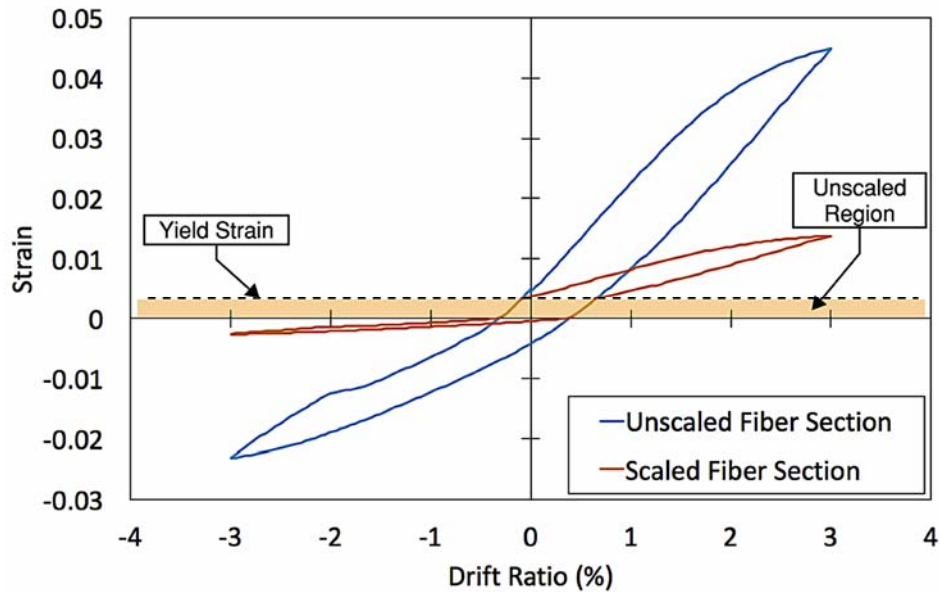
FIGURE 4-26: COMPARISON OF UNSCALED VS. SCALED STRAIN DEMANDS FROM ANALYSIS FOR A CYCLE OF LOADING IN CS80

143
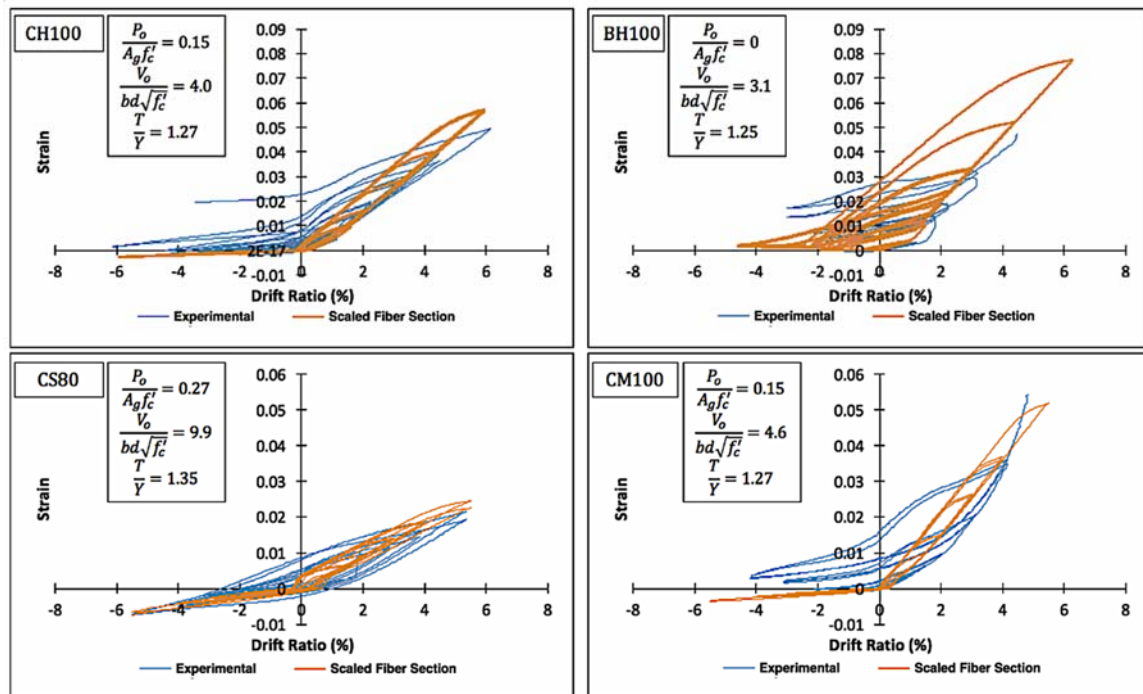
FIGURE 4-27: COMPARISON OF A TYPICAL CYCLIC STRAIN GAUGE READING AND CORRESPONDING SCALED RESULT FROM FIBER-SECTION ANALYSES

4.5 Concrete Surface Strains

In several applications, it is useful to estimate the smeared longitudinal strain in the concrete or steel bar over a member length approximating the location of peak strain concentrations. One such application consists of estimating the smeared longitudinal bar strain over it potential buckling length, from member end where moments are maximum to the location of the second hoop (for inter-hoop buckling). This could be used to identify the potential point of bar buckling initiation. Relations to estimate such strains from fiber-section bar strains extracted at the section of peak moment are presented in this section.

144

4.5.1 Tensile Strains

Tensile surface strains in the plastic hinge region versus strains from analysis in the reinforcing bars at the section of maximum demand are plotted in Figure 4-28 for six of the members for which the experimental data was available. These strains included the bar-slip crack at the interface of the member to the footing and were measured over a gage length of 7 inches, which is about 8.5% of the member length for CS60 and CS80 and 6.5% of the member length for CH100, CL100, CM100, and CH60. The analytical model included a plastic hinge of 5% of the length of each member, with deformation concentrated at the end of the member.

Because the scope of the study to obtain accurate estimates of strain demands at higher drift ratios that contribute more to the damage in the section, a similar approach to the scaling of strains in the longitudinal bars was taken assuming that estimated strains from analysis diverge at first yield from measured strains.
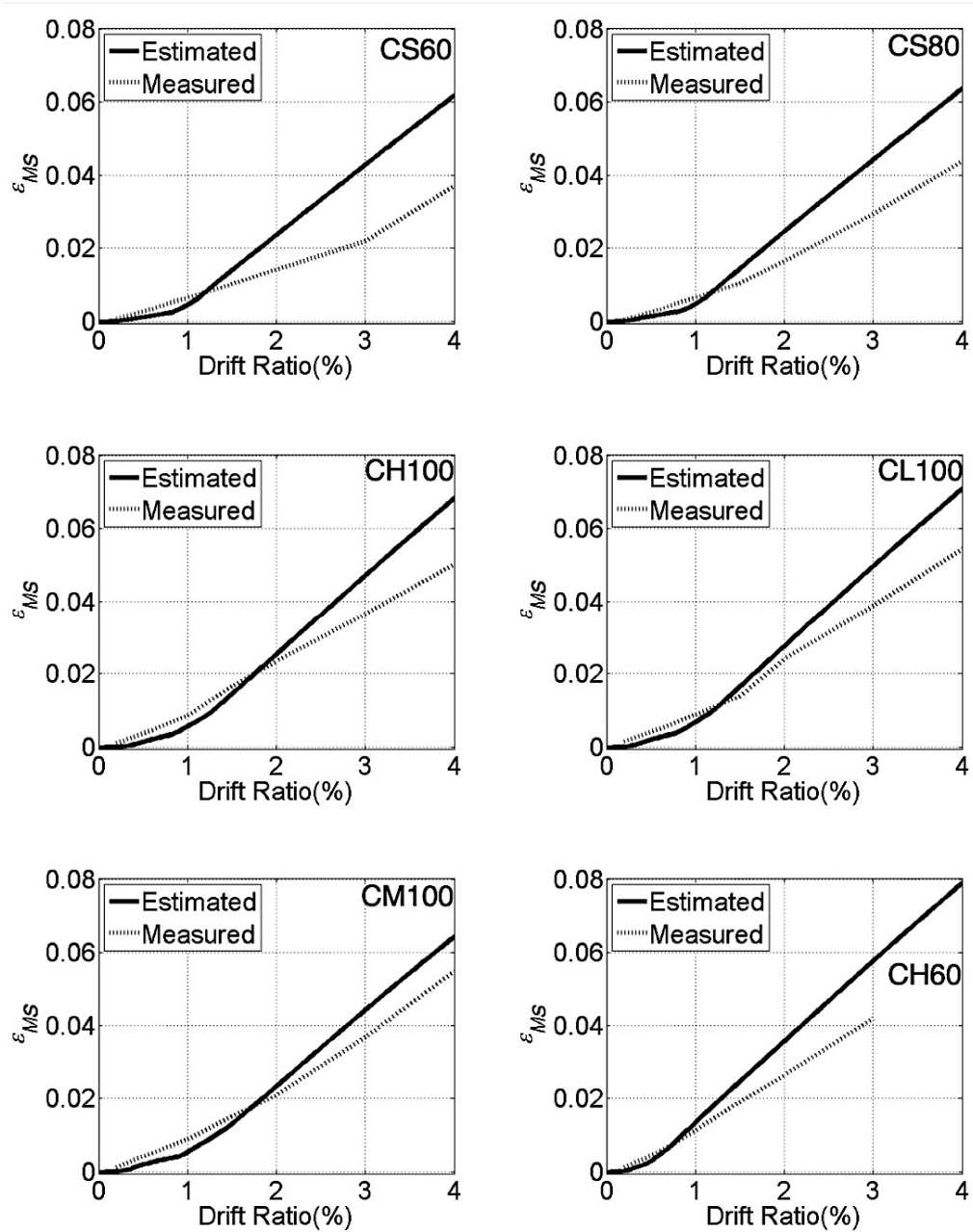
FIGURE 4-28: MEAN MEASURED TENSILE SURFACE STRAINS VS. ESTIMATED STRAINS FROM ANALYSIS

Post-yield tension strains in longitudinal bars at the critical section were scaled through a Surface Tension Scaling Factor (*STSF*). The *STSF* was obtained in accordance with Equation 4-11:

EQUATION 4-11: TENSILE STRAIN SCALING PROCEDURE

$$\varepsilon_{i-buckling} = \varepsilon_{i-analysis} \qquad\qquad for\ 0 \leq \varepsilon_{i-analysis} \leq \frac{f_y}{29000}$$

$$\varepsilon_{i-buckling} = \frac{f_y}{29000} + STSF(\varepsilon_{i-analysis} - \frac{f_y}{29000}) \qquad for\ \varepsilon_{i-analysis} > \frac{f_y}{29000}$$

where ε_i is the estimated strain demand at a given lateral drift ratio; $\varepsilon_{i-analysis}$ is the strain demand from the fiber-section analysis at the same lateral drift ratio for the same member, f_y is the yield strength of the longitudinal reinforcement.

The resulting *STSF* values for drift targets of 2.0%, 3.0%, and 4.0% are plotted in Figure 4-29. As can be seen in Figure 4-29, the S*TSF* was observed to be similar between the drift ratios of 2.0% and 4.0% for a given test, but varied from test to test. The final *STSF* was calibrated to the for higher accuracy at a lateral drift target of 3.0%.
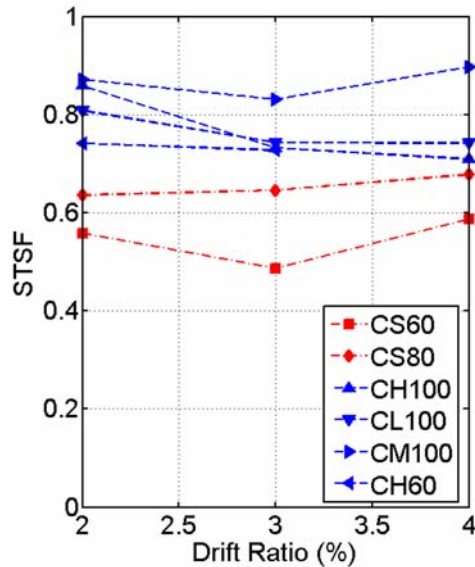
FIGURE 4-29: EXTRACTED *STSF* AT DRIFT RATIOS OF 2%, 3% AND 4%

147

The *STSF* at 3% drift was found to correlate with the axial load ratio. The *STSF* decreased with increasing axial load ratio, thereby reducing strain demands with increasing axial load.
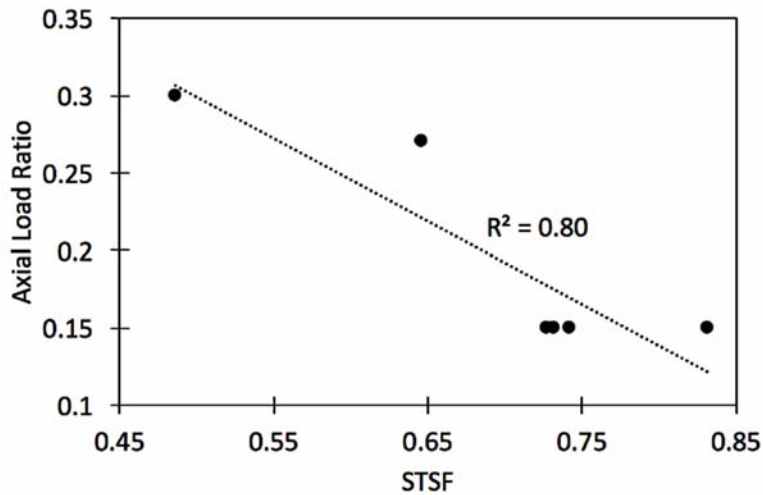
FIGURE 4-30: INFLUENTIAL PARAMETER ON *STSF*

Equation 4-12 was produced through linear regression to calculate the *STSF* based on column axial load ratio. Other terms considered, such as the longitudinal reinforcement yield strength and concrete compressive strength improved the accuracy of the relation, but the increase in accuracy did not justify the increase in complexity. The equation converges to a *STSF* of 1 for members with zero axial load.

EQUATION 4-12: TENSILE STRAIN FACTOR

$$STSF = 1 - 1.5\frac{P_o}{A_g f_c'}$$

where P_o is the applied axial load (in lb, positive in compression); A_g the gross sectional area (in.^{2}); f_c' is the concrete compressive strength (in psi);

The mean error ratio calculated as the ratio of the estimated *STSF* to matched *STSF* was 1.02. The standard deviation was 0.08. The measured and predicted tensile strains up to 4% drift ratio are compared in Sokoli (2018).

4.5.2 Compressive Strains

Compression surface strains in the plastic hinge region versus strains from analysis in the reinforcing bars at the section of maximum demand are given in Figure 4-31 for six of the members for which the experimental data was available. Measured strains were measured over a gage length of 7 inches, same as the tension surface strains.

Equation 4-13 can be used to obtain the surface compression strains from strains from analysis through the Surface Compression Strain Factor (*SCSF*).

EQUATION 4-13: TENSILE STRAIN SCALING PROCEDURE

$$\varepsilon_{si} = SCSF \times \varepsilon_{i-analysis} \qquad\qquad for\ \varepsilon_{i-analysis} < 0$$

where ε_{si} is the estimated surface strain demand at a given lateral drift ratio; $\varepsilon_{i-analysis}$ is the strain demand from the fiber-section analysis at the same lateral drift ratio for the same member.
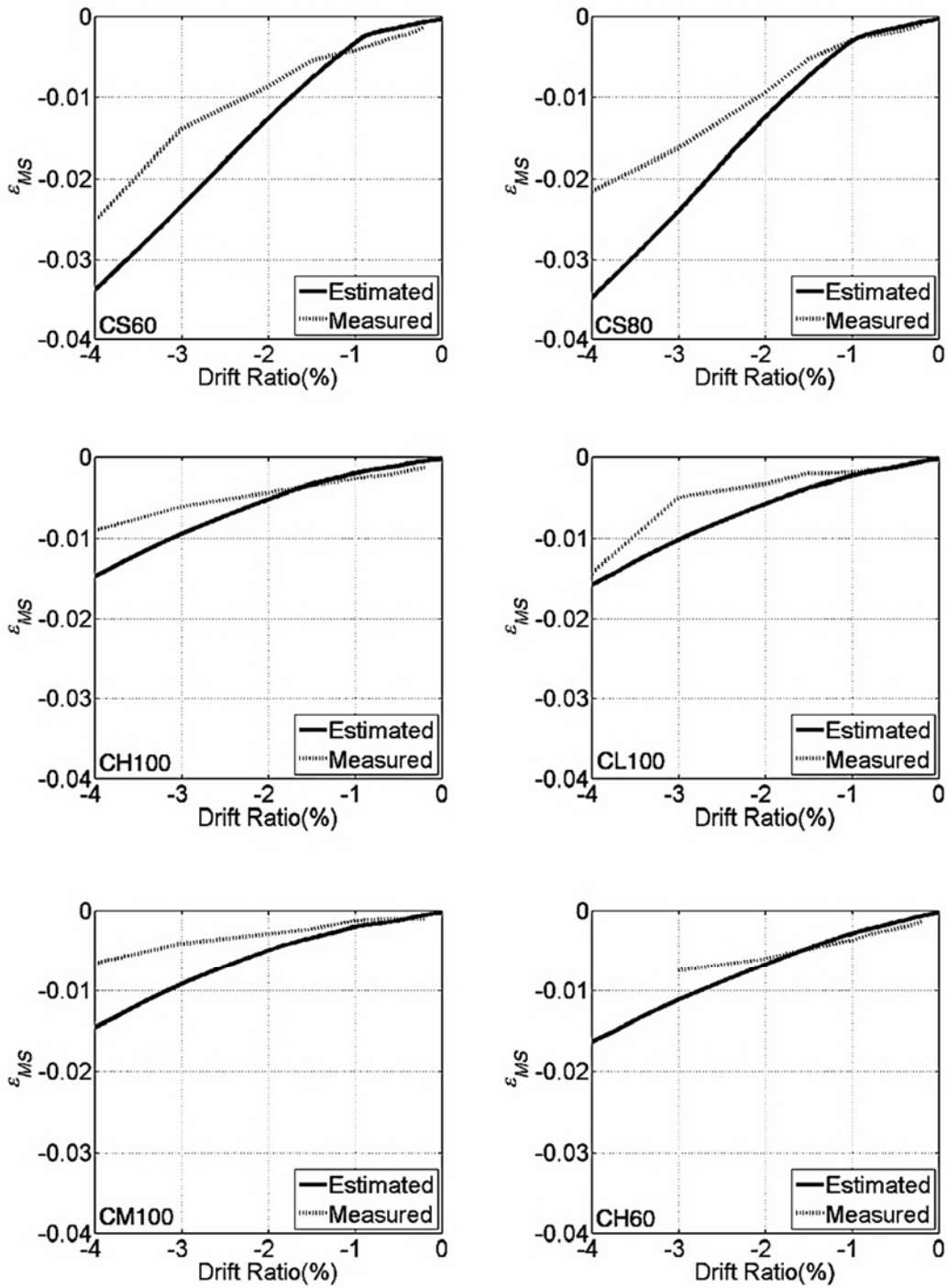
FIGURE 4-31: MEAN MEASURED COMPRESSION SURFACE STRAINS VS. ESTIMATED STRAINS FROM ANALYSIS

The resulting *SCSF* values for drift targets ranging from 2.0% to 4.0% are plotted in Figure 4-32. As observed in Figure 4-32, the S*CSF* was similar between the drift ratios of 2.0% and 4.0% for a given test. No clear correlation was found between the *SCSF* and test parameters. Therefore, the mean value of *SCSF* at 3% drift was taken between the six members, leading to a value of 0.6.
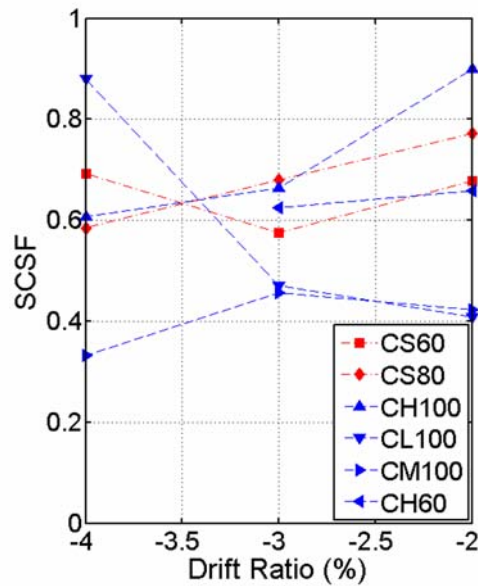
FIGURE 4-32: EXTRACTED *STSF* AT DRIFT RATIOS OF 2%, 3% AND 4%

EQUATION 4-14: COMPRESSION STRAIN FACTOR

$$SCSF = 0.6$$

The mean error ratio calculated as the ratio of the estimated *SCSF* to matched *SCSF* was 1.07. The standard deviation was 0.2.

4.5.3 Cyclic Strain Demands

To obtain the cyclic surface strain history over a height of about 7% of column length, the Surface Tension Scale Factor (*STSF*) and Surface Compression Scale Factor

(*SCSF*) are applied to scale strains from the proposed fiber-section analysis at the location of maximum moment. Scaling of bar strain is not necessary until bars exceed their yield strain for the first time as the fiber-section model is able to accurately capture strains up to that point. In theory, after first yield all tension strains are to be scaled, but it is assumed here that strains between zero and tension yield are relatively small and therefore are not scaled (Figure 4-33).

EQUATION 4-15: SUMMARY OF SCALING PROCEDURE FOR SURFACE CONCRETE STRAINS

$$\varepsilon_{si} = SCSF \times \epsilon_{i-analysis} \qquad\qquad for\ \varepsilon_{i-analysis} < 0$$

$$\varepsilon_{si} = \epsilon_{i-analysis} \qquad\qquad for\ 0 \leq \varepsilon_{i-analysis} \leq \frac{f_y}{29000}$$

$$\varepsilon_{si} = \frac{f_y}{29000} + STSF(\varepsilon_{i-analysis} - \frac{f_y}{29000}) \qquad for\ \varepsilon_{i-analysis} > \frac{f_y}{29000}$$

where:

$$SCSF = 0.6$$

$$STSF = 1 - 1.5\frac{P_o}{A_g f_c'}$$

A typical measured cyclic strain in the concrete surface of CH100 is compared to the corresponding unscaled and scaled results from fiber-section analysis in Figure 4-34.
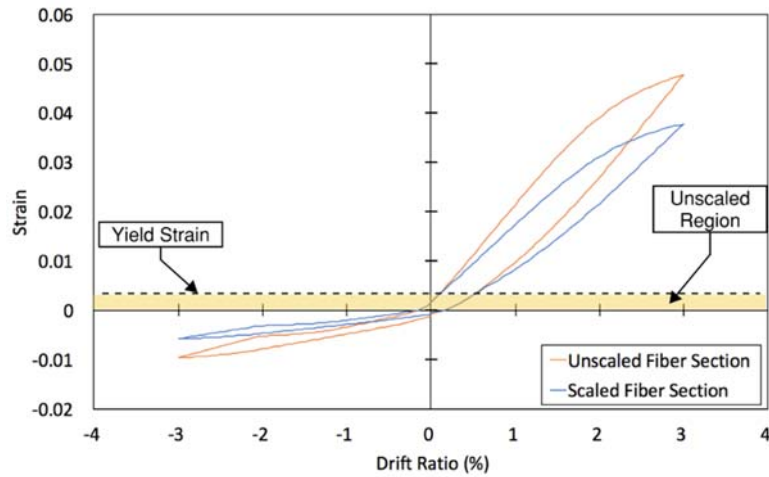
FIGURE 4-33: COMPARISON OF UNSCALED VS. SCALED STRAIN DEMANDS FROM ANALYSIS FOR A CYCLE OF LOADING IN CH100
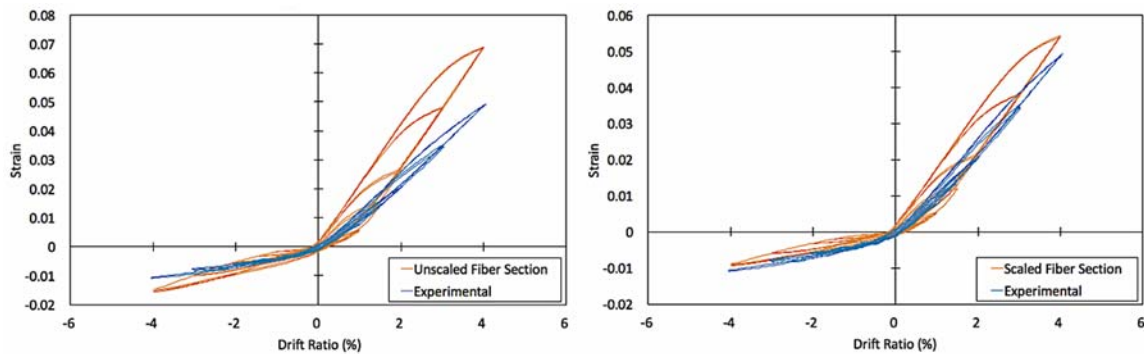
FIGURE 4-34: COMPARISON OF A TYPICAL MEASURED CYCLIC STRAIN IN THE CONCRETE SURFACE OF CH100 VS. CORRESPONDING UNSCALED AND SCALED RESULTS FROM FIBER-SECTION

4.6 Summary and Conclusions

A behavioral model is proposed to scale strain estimates obtained from a calibrated force-formulation fiber-section computational element to achieve desired representative strain estimates. The framework is calibrated using 12 cyclic experimental tests conducted on concrete columns and beams that were cycled to large damage states and in some cases bar fracture. The resulting computational framework is capable of matching the global

153

deformation behavior of reinforced concrete members through the fiber-section element, and provides reliable strain demands in the longitudinal bars and surrounding concrete through the full range of expected inelastic deformations. It was found that:

- Tension strains in longitudinal bars depend on the axial load ratio, shear stress, and tensile-to-yield-strength ratio of the steel.
- Compression strains in bars depend on the axial load ratio
- Tension strains in the concrete surface within the plastic hinge region depend on axial load ratio
- No clear correlation was found between test parameters and the ratio of concrete surface compression strains to strains from analysis.

The accurate estimate of strains in the longitudinal bars and surrounding concrete at the point of maximum demands provides reliable estimates of material damage and strength degradation, particularly for applications considering longitudinal bar fracture and buckling.

4.7 Limitations and recommendation for future work

It was the purpose of this study to use results from well-controlled and instrumented lateral load tests of concrete members incorporating different grades and types of reinforcement. As such, a limited number of tests were available. As more tests on concrete members with different grades and types of steel are carried, future work should focus on increasing the accuracy in strain demand prediction, by calibrating and validating the framework to a larger dataset. Also, it may be useful to distinguish strain models for bars with a rounded stress-strain relation (e.g., ASTM A1035) and those with a distinct yield point (e.g., ASTM A706).

154

5 BUCKLING AND FRACTURE OF HSRB IN SPECIAL MOMENT FRAME MEMBERS

Special Moment Frame (SMF) members undergoing typical flexural degradation under seismic loads are subjected to longitudinal bar yielding, concrete crushing, longitudinal bar buckling and/or fracture. While longitudinal bar fracture has typically not been of major concern in concrete members of SMF, it is gaining more attention as higher strength reinforcing bars (HSRB) with lower fracture elongation and low-cycle fatigue life are introduced to the market. A methodology for predicting longitudinal bar buckling initiation and fracture in SMF members is proposed. The methodology is based on estimates of local strain demands in longitudinal bars of SMF members. A buckling initiation model is proposed that accounts for the mechanical properties of the reinforcing bars, as well as the loading history the bars and surrounding concrete experience prior to buckling. Material specific bar fatigue relations calibrated through material test results are used to predict the number of half-cycle to bar fracture based on accumulation of strain demands prior and after buckling, if it occurs.

5.1 Introduction

Special Moment Frame (SMF) members undergoing typical flexural degradation under seismic loads are subjected to longitudinal bar yielding, concrete crushing, longitudinal bar buckling and/or fracture. While longitudinal bar fracture has typically not been of concern in concrete members of SMF, it is gaining more attention as higher strength reinforcing bars (HSRB) with lower fracture elongation and low-cycle fatigue life are introduced to the U.S. market. A methodology for predicting longitudinal bar buckling initiation and fracture in SMF members is proposed. The methodology is based on estimates of local strain demands in longitudinal bars of SMF members and accounts for member properties and loading conditions, as well as the mechanical properties of reinforcing bars.

The proposed methodology is intended for use with reinforced concrete beams and columns that satisfy ACI 318-14 Special Moment Frame requirements. For this reason, it is assumed that one or both of the following strength degradation mechanisms occur (Figure 5-1):

1. The strain history demand at the point of maximum moment leads to the longitudinal bars fracturing at that location (typically at member end).
2. Longitudinal bars buckle between hoops (typically between the first and second hoops from member ends), which generates strain concentrations within the buckled length and eventually lead to bar fracturing within the buckled length, typically at a distance equal to spacing of the ties from the end of the member.
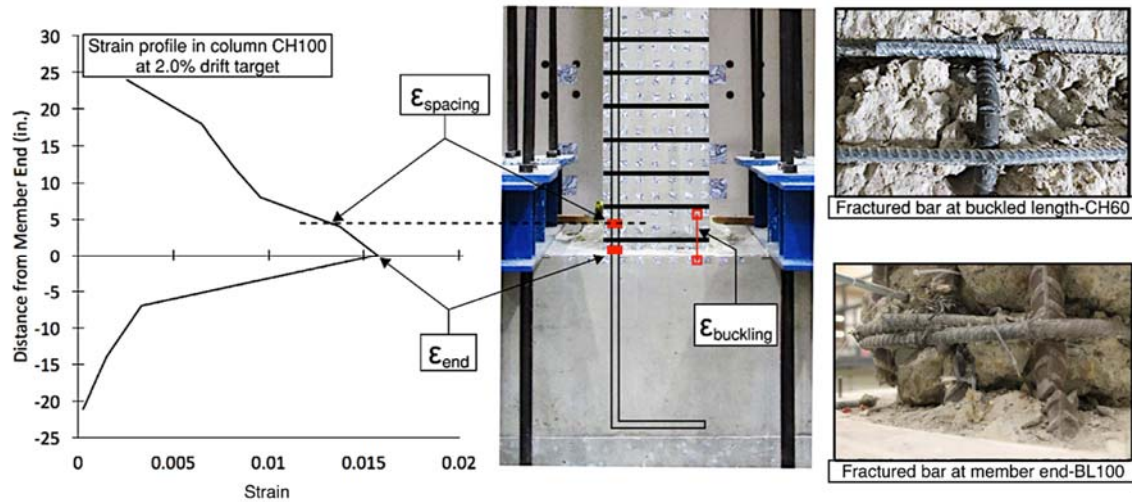
FIGURE 5-1: TYPES OF REPRESENTATIVE STRAINS AND BAR FRACTURE LOCATIONS

The sequence of the two listed possible events is tracked in the proposed methodology in order to determine if and which occurs first, as illustrated in the flow chart in Figure 5-2. The starting point for the methodology is estimating the deformation or strain histories of frame members during a simulated seismic event. If the frame members are modeled using lumped plasticity elements in the structural simulation, then a fiber-section representation of each member is generated and run through the deformation and loading history of the member. The framework introduced in Chapter 3 for deriving accurate strain demands is then used to scale fiber-section strains to obtain representative longitudinal bar strain histories at the section of maximum moment and at mid-span of the potential bar-buckled shape (i.e., half way between the first two hoops from member end), as well as longitudinal strain histories for the concrete around the potential bar buckling region. Alternatively, if the structural model is constructed directly using fiber-section elements in accordance with recommendations in Chapter 3, then representative bar and concrete

157

strains could be obtained by directly scaling the fiber-section element strains per Chapter 3. The strain scaling procedure is described in more detail in Section 5.3.

At the location of maximum moment, bar buckling cannot occur (Figure 5-1). Therefore, strain histories at that location are used to estimate bar damage due to fatigue using a Coffin-Manson (Manson 1953, Coffin 1954) type relation that was calibrated using fatigue tests on essentially unbuckled bars (Ghannoum and Slavin 2016, Hogsett 2017). If the damage index calculated using the fatigue model reaches a value of 1.0 during an earthquake scenario, then bars are deemed to fracture at the member end during that scenario, unless bar fracture occurs at the bar buckle first.
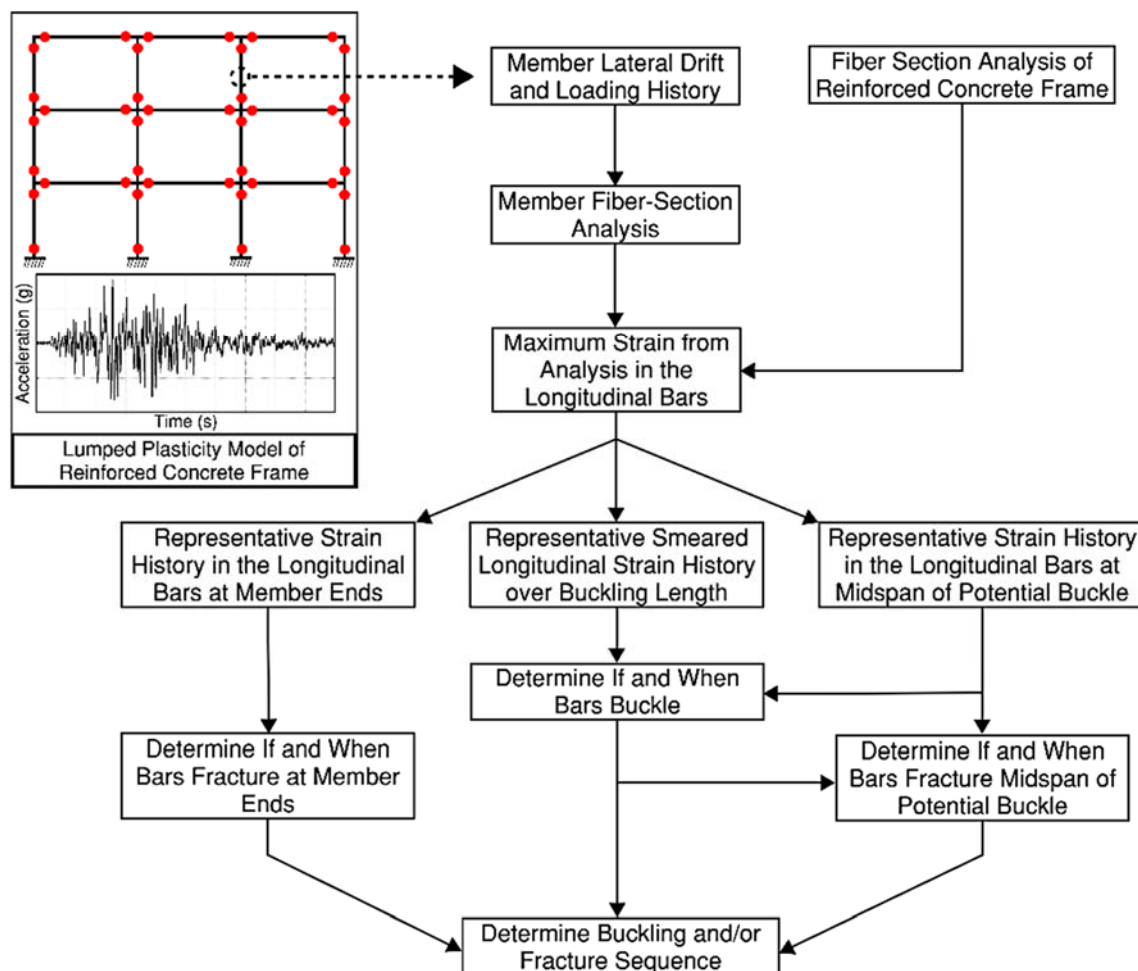
FIGURE 5-2: FLOW-CHART FOR PREDICTING BAR FRACTURE IN SMF MEMBERS

At mid-span of the potential buckled shape, however, strain demands in the longitudinal bar are lower than those at the section of maximum moment until bar buckling occurs (Figure 5-1). Therefore, fracture at that location cannot materialize if bar buckling does not occur. Once bar buckling occurs, curvature demands tend to localize at that weakened location, while strain concentrations increase in the bars due to the buckled shape (Figure 5-3). Therefore, after buckling, strain demands in the longitudinal bars within

the buckled length can outpace those at the section of maximum moment, forcing the damage index to exceed 1.0 and bars to fracture at the buckled location. The proposed methodology requires tracking the damage index due to pre and post buckling strain demands at both potential locations of fracture to determine if and where bar fracture will occur during an earthquake scenario (Figure 5-2). A buckling initiation model is also proposed to determine if and when bar buckling occurs during an earthquake scenario.
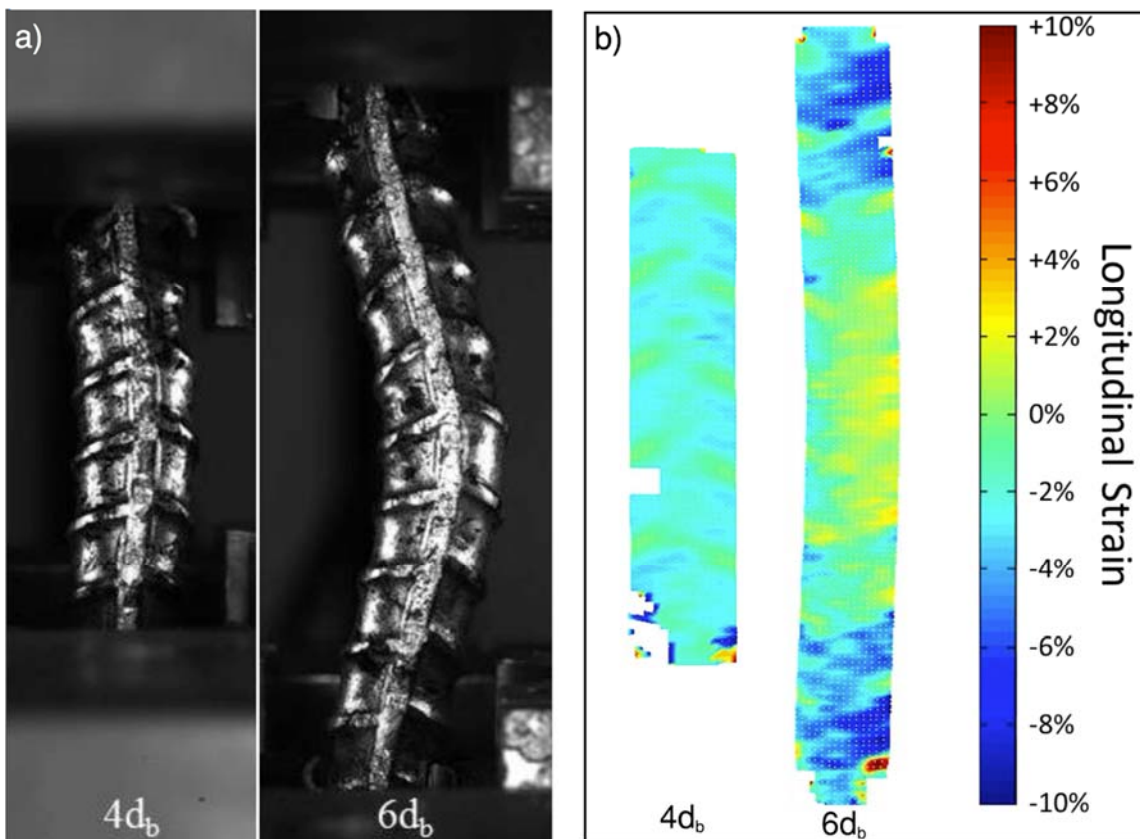
FIGURE 5-3: LOW CYCLE FATIGUE TESTS OF BARS GRIPPED AT SPANS OF 4 AND 6 BAR DIAMETER: A) PICTURES OF GRADE 100 BARS DURING TESTING B) MEASURED LONGITUDINAL STRAINS IN GRADE 80 BARS DURING TESTING (ADOPTED FROM GHANNOUM AND SLAVIN 2016)

5.2 Experimental Data

The experimental data used to calibrate the proposed buckling initiation model and validate the bar fracture methodology was extracted from four series of tests carried on twelve reinforced-concrete beams and columns having various reinforcing steel grades and stress-strain properties.

- Series 1 reversed cyclic tests were conducted on moderately confined columns sustaining shear and axial failure (Leborgne, 2012). The two columns in Series 1 (2L06, 2H06) were nominally identical in design and detailing. Both were reinforced with grade 60 ASTM A615 bars. In this publication, grade refers to the specified yield strength of steel bars. Columns were loaded under the same lateral cyclic protocol but a different axial load was applied to each. Series 1 columns sustained significant flexural yielding prior to shear and axial failures. Bar buckling was not observed in these columns prior to shear failure.

- Series 2 tests (CS60, CS80) investigated the ability of high-strength transverse reinforcement in maintaining confinement integrity and the shear strength of concrete columns during inelastic demands (Sokoli 2014, Sokoli and Ghannoum 2016). These two columns were designed to have equivalent moment strength and constructed using different grades of reinforcement: grade 60 ASTM A706 bars for CS60, and grade 80 ASTM A706 bars for CS80. Hoop spacing varied between the columns. Series 2 columns were well confined and satisfied ACI 318-14 Special Moment Frame provisions. Columns CS60 and CS80 sustained flexural yielding prior to shear and axial failures. Bar buckling was not observed in these columns prior to shear failure.

- Series 3 tests (CH100, CL100, CM100, CH60) investigated the effects of varying stress-strain relations of the longitudinal bars on the plasticity spread and deformation capacity of concrete columns (Sokoli et al. 2017). All columns were

geometrically identical, reinforced with the same longitudinal bar layout and size. Three of these columns were reinforced with grade 100 steel sourced from different steel manufacturing processes, which led to different post-yield stress-strain curves. Column CH60 was reinforced with grade 60 A706 bars. Hoop spacing was tighter for the columns with grade 100 steel than for the column with grade 60 steel to mitigate the higher buckling propensity of higher strength bars. The four specimens sustained a flexural mode of degradation characterized by concrete crushing, varying degrees of longitudinal bar buckling, and eventually longitudinal bar fracture. Column CM100 reinforced with ASTM A1035 steel exhibited almost no bar buckling prior to bar fracture at column end where moment demands were largest. All other columns sustained longitudinal bar fracture with the buckled length after significant buckling.

- Series 4 tests were conducted on four beams (BH100, BL100, BM100, BH60) reinforced with the same steel as Series 3 columns (To and Moehle 2017). The beams had nominally identically dimensions and concrete material properties, but were designed to maintain the same nominal moment strength across bar grades. Hoop spacing was also tighter in this series for beams with grade 100 bars than for the beam with grade 60 reinforcement. All members failed at relatively high lateral deformation demands due to bar fracture or global instability. Limited buckling of longitudinal bars was observed in the beam tests.

Relevant structural parameters for each specimen are summarized in Table 4-1, and observed failure modes in Table 5-2 and Table 4-2. Additional information about the design, material properties, and loading protocol of each specimen is presented in Sokoli et al. (2017).

TABLE 5-1: STRUCTURAL PARAMETERS FOR EACH SPECIMEN

Member	Section Effective Depth $(d)^1$ (in.)	Concrete Comp. Strength (ksi)	Axial Load Ratio[2]	Shear Stress[3] ($\sqrt{f_c'}$ psi)	Shear Span to Section Depth Ratio	Long. Bar Dia. (in.)	Long. Reinf. Ratio[3]	Long. Bar Yield Strength (ksi)	T/Y^4 Strength Ratio	Hoop Spacing / Long. Bar Dia.
2L06	13.50	3.13	0.19	4.46	4.00	1.00	0.025	65.5	1.64	6.0
2H06	13.50	3.34	0.41	4.74	4.00	1.00	0.025	65.5	1.64	6.0
CS60	15.27	3.83	0.30	10.55	2.75	1.25	0.047	67.3	1.41	4.4
CS80	15.44	4.29	0.27	9.86	2.72	1.13	0.037	79.1	1.35	4.9
CH100	16.13	5.16	0.15	4.00	3.60	0.75	0.011	84.6	1.27	4.7
CM100	16.13	5580	0.15	4.55	3.60	0.75	0.011	124.2	1.27	4.7
CH60	16.13	4.57	0.15	3.15	3.60	0.75	0.011	68.5	1.45	6.0
BH100	21.75	5.00	0.00	3.13	4.31	1.00	0.007	102.1	1.25	5.0
BL100	21.75	5.10	0.00	2.91	4.31	1.00	0.007	105.7	1.17	5.0
BH60	21.70	5.34	0.00	3.69	4.31	1.13	0.011	65.1	1.47	4.4
BM100	21.75	5.47	0.00	3.82	4.31	1.00	0.007	100.4	1.63	5.0

[1] The section effective depth (d) is taken as the distance measured from the extreme compression fiber to the centroid of the outermost layer of longitudinal tension reinforcement.
[2] Axial load ratio is taken as the applied axial load divided by the gross sectional area and the measured concrete compressive strength at the day of column testing
[3] Longitudinal reinforcement ratio taken as the area of longitudinal steel divided by gross sectional area for column members, and tension layer of reinforcement divided by gross sectional area for beam members.
[4] T/Y = Tensile-to-yield strength ratio of the longitudinal reinforcement

Test members are divided in two groups in Table 5-2 and Table 4-2, based on their failure modes. Members listed in Table 5-2 failed due to bar buckling and/or bar fracture and were used to calibrate the buckling initiation model and to verify the fracture prediction methodology. Members listed in Table 5-2 failed in shear, axial, and/or global instability and were used to validate the buckling and fracture models. Members reinforced using ASTM A1035 were not included at this stage as their material tests needed to obtain fatigue and mechanical properties of those bars were not available at the time of writing.

TABLE 5-2: DRIFT RATIOS AT BEHAVIORAL MILESTONES FOR MEMBERS THAT SUSTAINED BAR BUCKLING/FRACTURE

Specimen	D1[1]			D2[1]		
	Mode	Drift Target Event[2] (%)	Half-Cycle to Drift Target	Mode	Drift Target Event[2] (%)	Half-Cycle to Drift Target
CH100	BB[3]	5.5	2	BF[4]	5.5	4
CL100	BB	5.5	3	BF	7.0	1
CH60	BB	5.5	2	BF	5.5	3
BL100	BF	4.9	2	BF	6.5	2

[1] D1 = First damage mode; D2 = Second damage mode
[2] Drift target towards which the damage mode took place
[3] Bar buckling from observation
[4] Bar fracture

TABLE 5-3: DRIFT RATIOS AT BEHAVIORAL MILESTONES FOR MEMBERS WHICH DID NOT SUSTAIN BAR BUCKLING/FRACTURE

Specimen	D1[1]		D2	
	Maximum Drift Ratio Prior to D1[2] (%)	Mode	Maximum Drift Ratio Prior to Event[2] (%)	Mode
2L06	4.0	SH[3]	7.6	A[4]
2H06	3.4	SH	3.4	A
CS60	5.5	SH	5.5	A
CS80	7.0	SH	7.0	A
BH100	6.5	GI[5]	-	-
BH60	4.9	GI	-	-

[1] D1 = First damage mode; D2 = Second damage mode
[2] Member completed the half-cycle to that drift ratio prior to damage mode
[3] Shear failure = initiation of lateral strength loss due to shear strength degradation
[4] Axial failure = member was not able to sustain the prescribed axial load
[5] Global instability due to buckling over several ties, or torsional instability.

5.3 From Fiber-Section Strains to Representative strains

As mentioned previously, this work utilizes the fiber-section based computational approach proposed in Chapter 3 to obtain longitudinal strain demands that are representative of experimentally measured strains on longitudinal bars at member ends and in the surrounding concrete within the plastic hinge region. This methodology is further expanded in this work to deliver strain demands in the longitudinal bars at the mid-span location of potential bar buckling (Figure 5-1), or approximately one hoop spacing from member end.

The force-formulation fiber section model proposed in Chapter 3 provides longitudinal strain estimates for longitudinal bars and the surrounding concrete at member end, which partially reflect axial loads and material properties. As demonstrated in Chapter 3 however, additional empirical scaling is then required to obtain strains that are representative of experimentally measured values at the locations of interest (Figure 5-1), namely:

- Representative strain histories in longitudinal bars at member end, ε_{end}
- Representative smeared longitudinal strain histories in the concrete or longitudinal bars over the span of a potential bar buckle, $\varepsilon_{buckling}$. This region tends to concentrate curvature and longitudinal strains after bar buckling, as will be demonstrated later.
- Representative strain histories in longitudinal bars at mid-span of a potential bar buckle, or approximately at a distance equal to one hoop spacing from member end, $\varepsilon_{spacing}$.

5.3.1 Representative strain histories in longitudinal bars at member ends

To obtain the representative cyclic strain histories for longitudinal bars at the critical moment sections (ε_{end}) of frame members, the Compression Scale Factor (*CSF*) and the Tension Scale Factor (*TSF*) are applied to the compression and tension strain history outputs at member ends from fiber-section analysis ($\varepsilon_{analysis}$). The scaling relations and their effects on fiber-section longitudinal bar strains in column CH100 are presented in Figure 5-4. For this member, CSF was equal to 0.12 and TSF equal to 0.56.

$$TSF = \frac{9}{10} - \frac{2}{3}\frac{P_o}{A_g f_c'} - \frac{1}{30}\frac{V_o}{bd\sqrt{f_c'}} - \frac{2}{5}\left(\frac{T}{Y}-1\right)$$

$$CSF = \frac{\epsilon_{EC}}{\epsilon_{CA3}}; \quad \epsilon_{EC} = \frac{P_o}{100\,A_g\,f_c'}$$
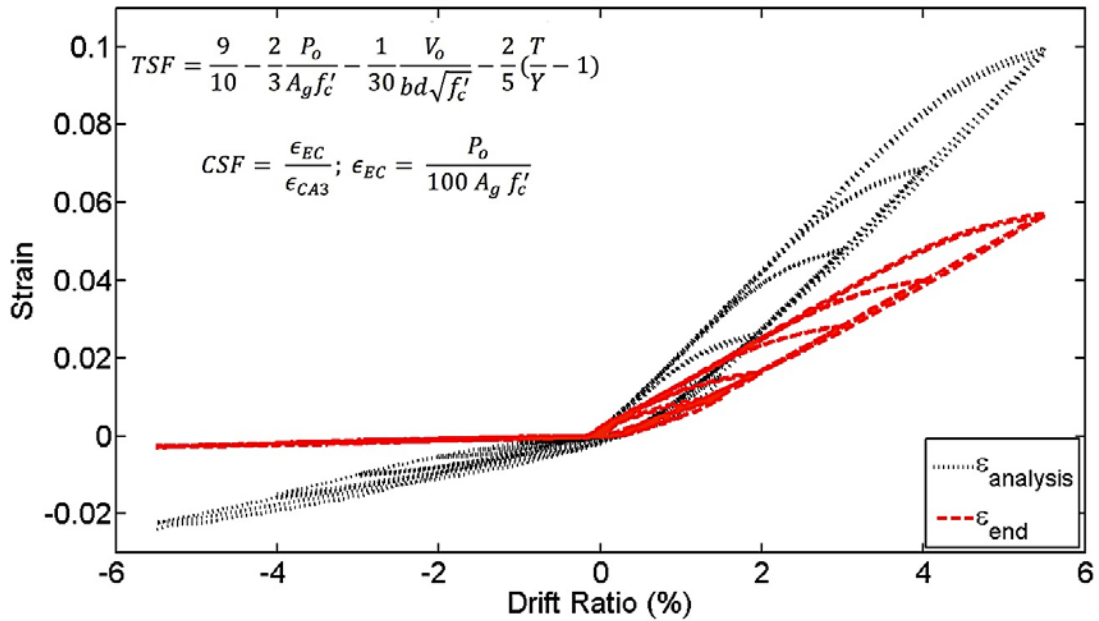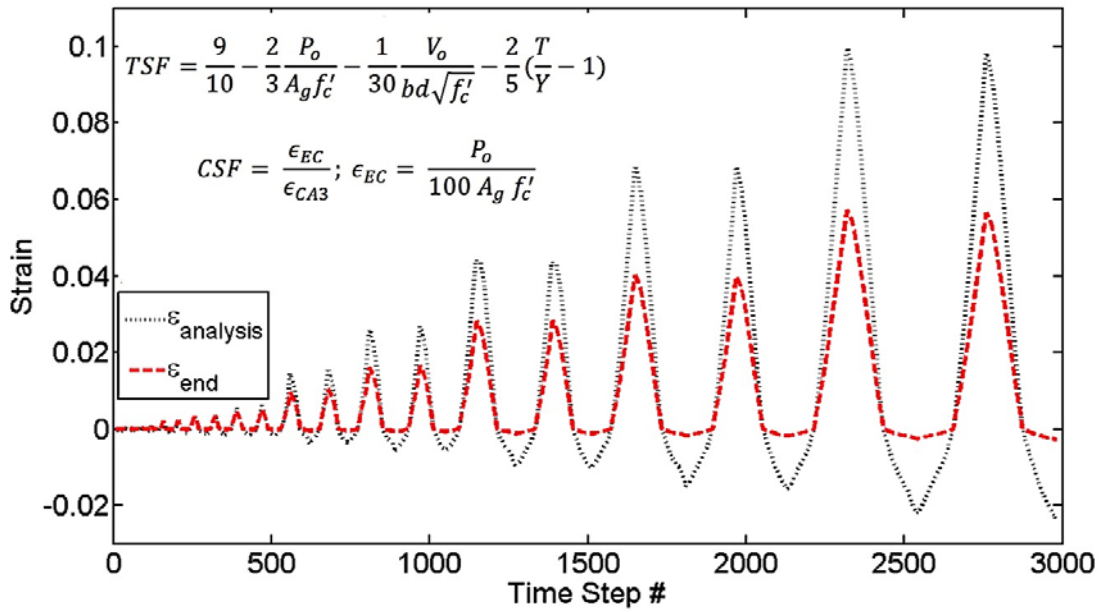
NOTE: TSF is the Tensile Strain Factor used to get the representative tensile strains over at the member end from strains from analysis; CSF is the Compression Strain Factor used to get the representative compression strains over at the member end from strains from analysis; P_o is the applied axial load (in lb, positive in compression); A_g the gross sectional area (in.^{2}); f_c' is the concrete compressive strength (in psi); V_o the maximum expected shear demand and can be obtained from fiber-section analysis (in lb); b and d are the cross-sectional width and effective depth in inches, respectively; and T/Y is the tensile to yield strength ratio for the longitudinal reinforcement, ϵ_{CA3} is the compression strain from fiber-section analysis taken at a drift ratio of 3%.

FIGURE 5-4: REPRESENTATIVE STRAIN HISTORY IN LONGITUDINAL BARS AT MEMBER ENDS SCALED FROM STRAIN FROM ANALYSIS

5.3.2 Representative smeared longitudinal strain histories over buckling length

To obtain the representative smeared longitudinal strain histories in the concrete or steel bars over the span of bar buckling, ($\varepsilon_{buckling}$), the Surface Compression Scale Factor (*SCSF*) and the Surface Tension Scale Factor (*STSF*) are applied to the compression and tension strain history outputs at member ends from fiber-section analysis ($\varepsilon_{analysis}$). These scaling factors were calibrated from surface strain measurements on test members at the location illustrated in Figure 5-1. The scaling for column CH100 is presented in Figure 5-5.
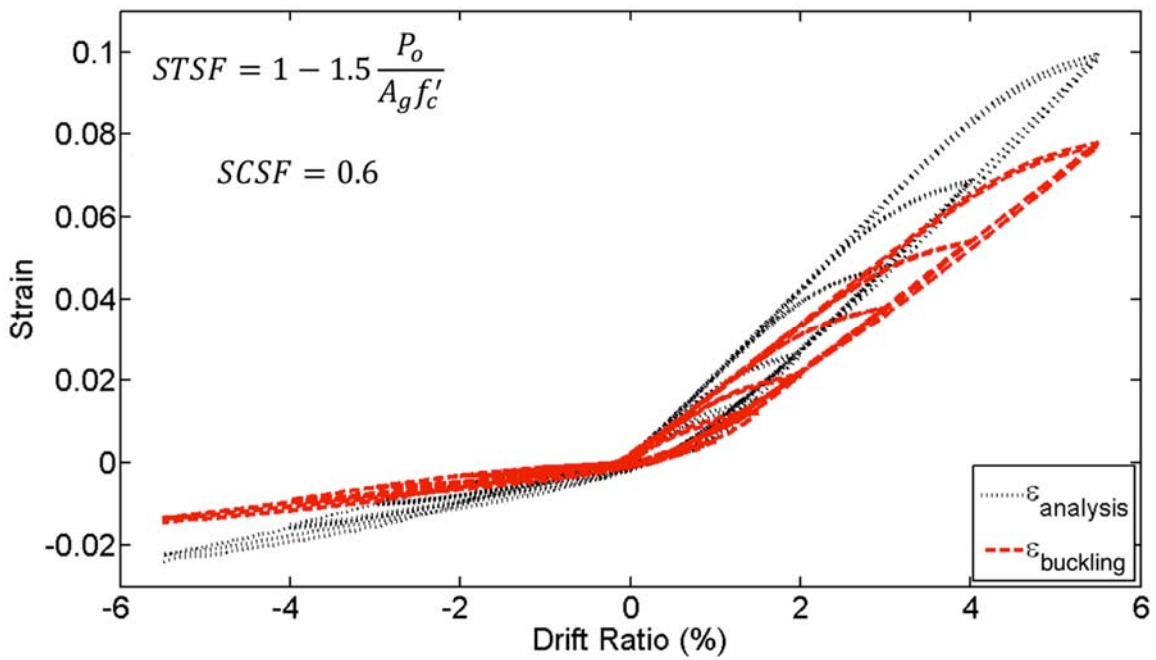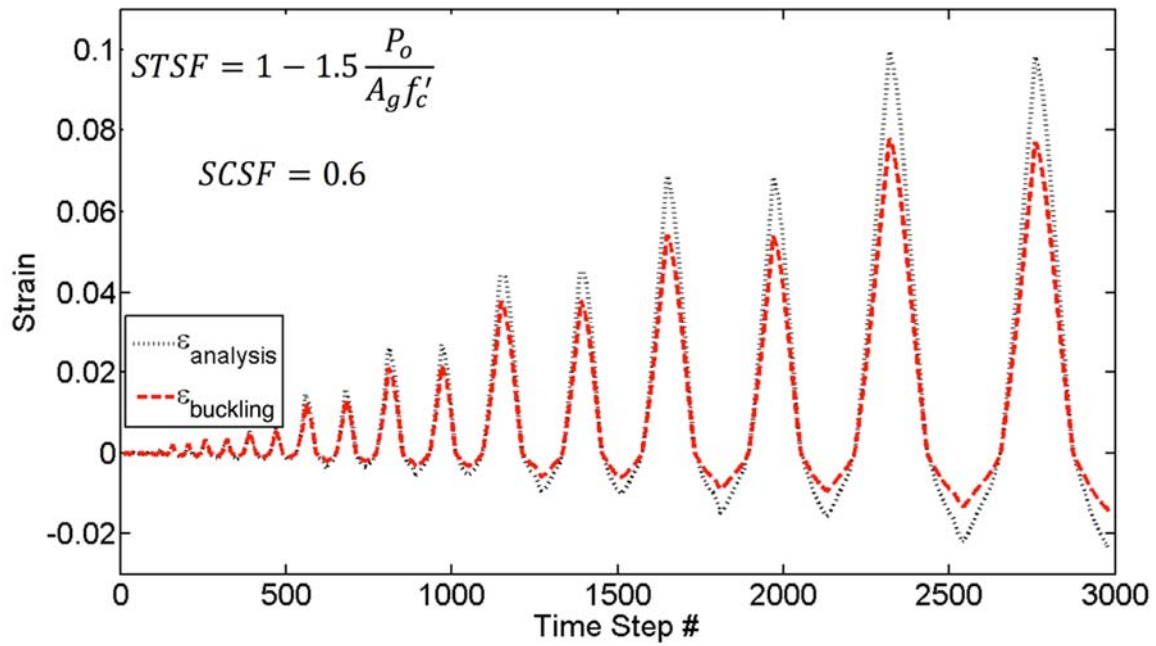
NOTE: STSF is the Tensile Strain Factor used to get the representative tensile strains over the buckling length from strains from analysis; SCSF is the Compression Strain Factor used to get the representative compression strains over the buckling length from strains from analysis.

FIGURE 5-5: REPRESENTATIVE STRAIN HISTORY IN CONCRETE SURFACE VS. STRAIN FROM ANALYSIS

169

Figure 5-6 shows the measured surface strain readings with and without bar-slip deformations for column CH100. The point at which bar buckling initiated is highlighted on the figure. Significant differences between strain measurements with and without bar-slip deformations can be seen in Figure 5-6 up to the initiation of bar buckling. This is particularly true for tension strain measurements. However, once bar buckling initiates, both readings become similar, which indicates that the bar-slip component reduces substantially and strains, or conversely curvatures, concentrate within the buckling length. For this reason, the longitudinal bar strain demands over the buckled length can be assumed after buckling to be approximately the same as the representative smeared longitudinal strains measured over the concrete surface including the bar slip region, $\varepsilon_{buckling}$.
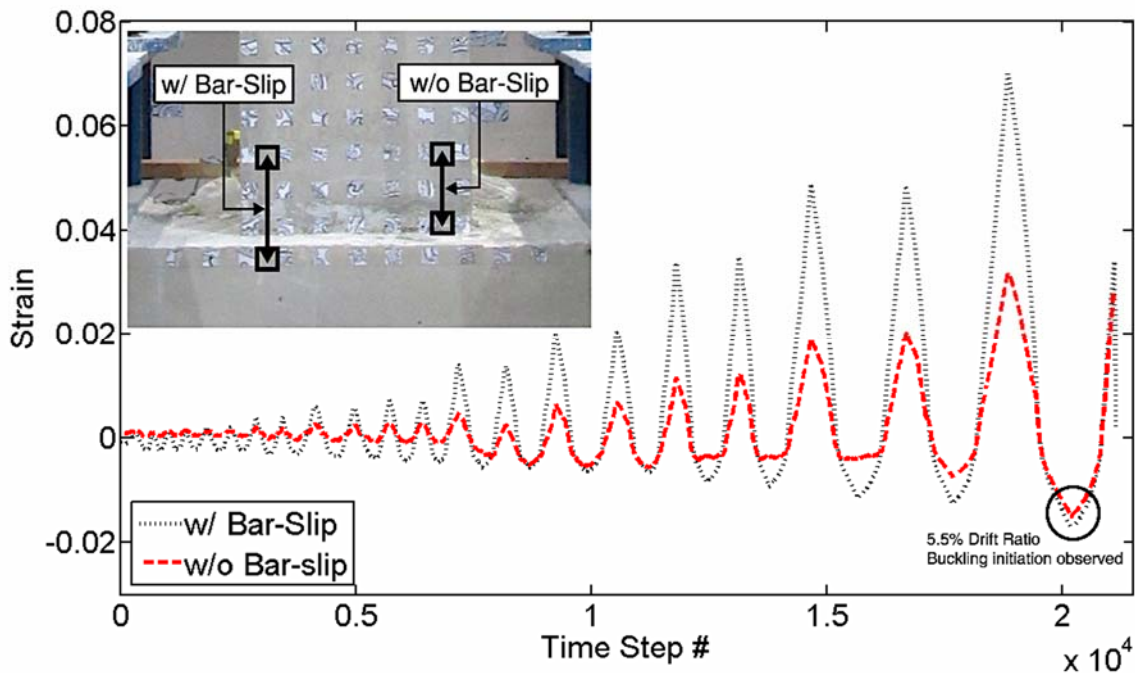
FIGURE 5-6: MEASURED SURFACE STRAINS FROM EXPERIMENT IN COLUMN CH100 WITH AND WITHOUT BAR-SLIP DEFORMATION

5.3.3 Representative strain histories in longitudinal bars at hoop-spacing distance from member ends

The procedure to scale strain in the longitudinal bars from analysis to get the representative strain history in longitudinal bars at mid-span of a potential bar buckle or approximately at a hoop-spacing distance from member ends ($\varepsilon_{spacing}$) is discussed in this section. This strain measure is not included in Chapter 3. Six of the specimens had available and reliable strain gauge data for strains along the length of the longitudinal bars, namely CH100, CL100, CH60, BH100, BL100, and BH60.

A schematic representation of the strain profile over the plastic hinge length is illustrated in Figure 5-7 and is assumed to be linear from the section of maximum moment

171

until the strain drops to the yield strain. The linear profile assumption is in agreement with experimental data as shown in Figure 5-1.

The length over which inelastic tension strains spread away from the section of maximum demand was identified from experiments at the first cycle to each drift target (h_p). It is noteworthy that measured bar strains were slightly lower in the following cycles to the same drift level. h_p was taken as the mean distance from member end to the section the strain in instrumented bars went down to a value equal to the yield strain (ε_y). Bar yield strains were obtained from material tension testing.
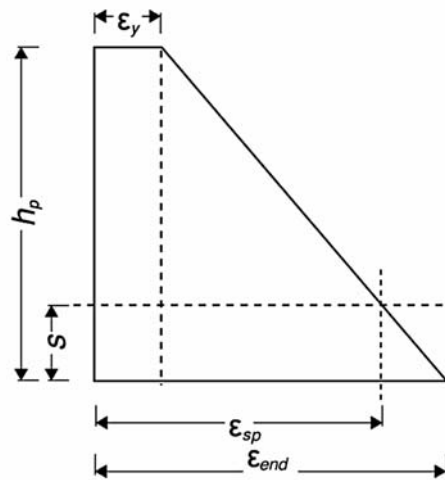
FIGURE 5-7: SCHEMATIC OF CALCULATING STRAIN AT A DISTANCE SPACING FROM BASE

Based on experimental values of h_p, the strains at a hoop spacing from member end ($\varepsilon_{spacing}$) could be obtained using Equation 5-1:

EQUATION 5-1: ESTIMATING STRAIN AT A DISTANCE SPACING FROM BASE

$$\varepsilon_{spacing} = \varepsilon_y + (\varepsilon_{end} - \varepsilon_y)(\frac{h_p - s}{h_p})$$

172

The Spacing Strain Factor (*SSF*) was then calculated for each member and at various drift targets as $\frac{\varepsilon_{end}}{\varepsilon_{spacing}}$. Results for *SSF* at different lateral drift ratio targets are given in Figure 5-8. For the specimens under consideration, the values of *SSF* varied from 0.74 to 0.99 at a drift ratio target of 1%. At higher drift ratios, the range of *SSF* narrowed to about 0.81 to 0.88. At a drift ratio of 3%, the mean value for the *SSF* was 0.85, with a standard deviation of 0.03. For simplicity, this constant scale factor of 0.85 is proposed to convert from tension strains at the section of maximum moment to tension strains at a hoop-spacing distance member end as defined in Equation 5-2. Compression strains were assumed to remain the same at a hoop-spacing distance from the member ends and member ends, based on the limited available test data (Equation 5-2).
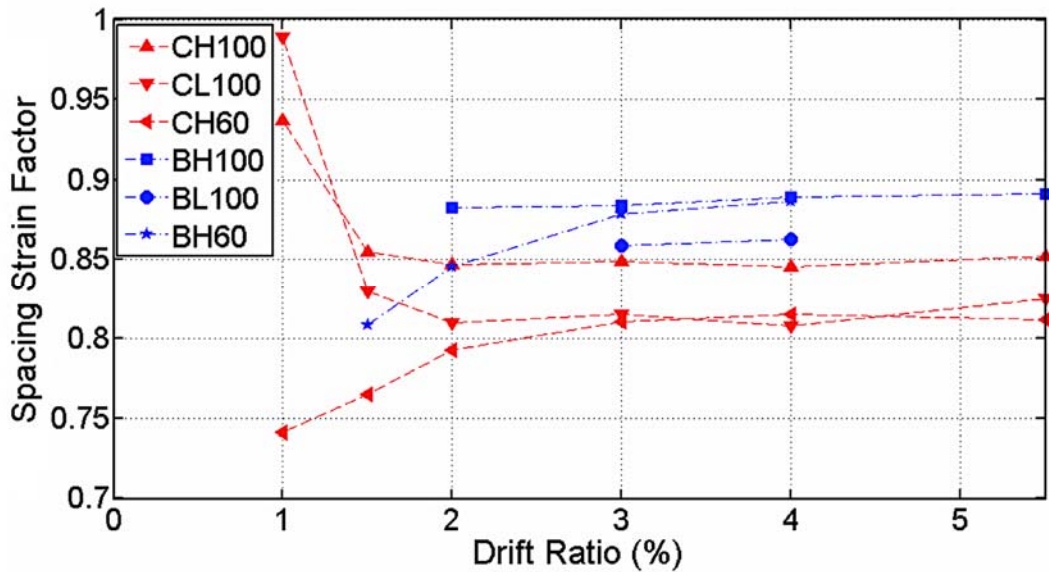
FIGURE 5-8: SSF – STRAIN SPACING FACTOR AT VARIOUS TARGET DRIFT RATIOS

EQUATION 5-2: TENSILE STRAINS AT A DISTANCE SPACING FROM BASE

$$\varepsilon_{i-spacing} = 0.85\, \varepsilon_{i-end} \quad for\ \varepsilon_{i-end} > 0$$

$$\varepsilon_{i-spacing} = \varepsilon_{i-end} \quad\quad for\ \varepsilon_{i-end} < 0$$

5.4 Buckling initiation model

5.4.1 Prior Buckling Initiation Models

Buckling of longitudinal bars in reinforced concrete columns subjected to gravity loads only has been attributed to compression strains in the plastic hinge region, while the magnitude of the compression strain required to trigger buckling has been related to the geometric configuration of both the longitudinal and transverse reinforcement (Bresler 1961, Scribler 1986, Papia et. al 1988, Papia and Russo 1989, Pantazopoulou 1998). The primary focus in those studies has been to set an adequate spacing of stirrups to prevent bar buckling. Additionally, Papia et. al (1988) concluded that compression strains experienced in longitudinal bars of uniaxially loaded members at the onset of buckling can be higher than the compression yield strain, depending on the provided spacing of transverse reinforcement.

Differences between bar buckling under monotonic lateral loads and buckling under cyclic loading have been recognized in experimental studies and summarized by Brown et. al (2007). First, strains in the compressed bars subjected to monotonic loading are relatively small, and therefore buckling is unlikely to take place because the concrete carries most of the compression demand. When subjected to cyclic loads, a large flexural crack may be present, which in the next consecutive cycle may lead the bar to buckle before the crack closes (Wang and Restrepo 1996, Brown et. al 2007, Goodnight et al. 2012). Second, the cyclic nature of loading may change the local stress-strain properties of the

steel due to the Bauschinger effect, leading to a lower tangent modulus of the material which in return reduces the inelastic buckling load of the bar. [SEP]

Additionally, the influence of the maximum experienced tensile strain on the buckling initiation of reinforcing bars has been corroborated by various authors (Wang and Restrepo 1996, Rodriguez et. al. 1999, Moyer and Kowalsky 2003, Brown et. al 2007, Goodnight et al. 2012, Feng et. al 2014). Rodriguez et. al. (1999) concluded through monotonic and cyclic axial tests on bars that reinforcing bars are more susceptible to buckling upon reversal from cycles of significant tension strains. They cited that the onset of buckling of steel bars could occur in the tensile region of the hysteresis cycle. Moyer and Kowalsky (2003) and Feng et. al (2014) supported the idea behind the influence of the loading history of the bars and especially that of the tensile strains on the onset of bar buckling, and proposed a tension-based buckling mechanism in circular bridge columns. Additionally, they argued on the importance of quantifying the compression load capacity associated with bar buckling, since bar buckling occurs under compression.

Dhakal and Maekawa (2002) related buckling initiation to the compression strain demand in core concrete coupled with the buckling tendency of the longitudinal bars at such demands lead to cover spalling. Therefore, the inherent assumption that spalling is caused due to buckling. The authors recognized the importance of considering the loading history and the tensile strains the bar may have experienced, however the compression strain at spalling was calibrate for monotonic cases only.

Berry and Eberhardt (2005) established a statistical drift-based bar buckling initiation model. The model includes the effect of the confinement ratio, axial-load ratio, aspect ratio, and longitudinal bar diameter on the required lateral deformation for bar buckling. The dataset to which the empirical equation was calibrated did not contain bars with yield strength higher than 75 ksi.

Tension-based models were primarily calibrated with results from circular bridge piers with spiral reinforcement. These members have typically high confinement and are subjected to low axial loads. The design parameters in such members are significantly different from concrete members of SMF and therefore could not upon verification capture buckling initiation in the members part of this study. Additionally, the effect of higher-strength reinforcing bars was not treated in any of the above-mentioned references. Therefore, a buckling initiation model is proposed here that accounts for the mechanical properties of the reinforcing bars, as well as the tension and compression loading histories experienced by the bars and surrounding confining concrete prior to buckling.

5.4.2 Proposed Buckling Initiation Model

A model is proposed to predict the point in a loading history at which longitudinal bar buckling initiates. The proposed buckling initiation model assumes that the restraint provided by hoops is sufficient to prevent the longitudinal reinforcing bars from buckling across multiple hoops or prior to compression yield. The model accounts for the mechanical properties of the reinforcing bars, as well as the loading history the bars and surrounding confining concrete experience prior to buckling. The proposed model takes on the form of the Euler's buckling equation for critical buckling stress, but modified through

176

factors α and β to account for the cyclic nature of seismic loading and the associated damage progression (Equation 5-3). Factors α and β degrade the critical buckling stress by reducing the effective restrained length of the bar as the concrete surrounding the bar reaches higher levels of compressive and tensile strains, respectively. Whenever the stress in a longitudinal bar reaches the degrading critical buckling stress evaluated using Equation 5-3 then buckling is deemed to initiate.

EQUATION 5-3: CRITICAL STRENGTH OF THE BAR AT BUCKLING INITIATION

$$f_{cr} = \frac{\pi^2 E_{tp}}{(\alpha\beta\frac{L}{r})^2}$$

where f_{cr} is the critical stress at which a longitudinal bar is expected to buckle; E_{tp} is the tangent modulus of elasticity of the bar at a given strain demand, and is calculated as described in Section 5.4.3; L is the effective buckled length, which based on experimental tests is taken as 1.25 times the center-to-center spacing between the seismic hoops (Figure 5-9); r is the radius of gyration taken as $d_b/4$ with d_b being the diameter of the bar; and α and β are factors calibrated to account for the loading history experienced by the concrete surrounding the bar prior to buckling, and are discussed in more detail in Section 5.4.4.
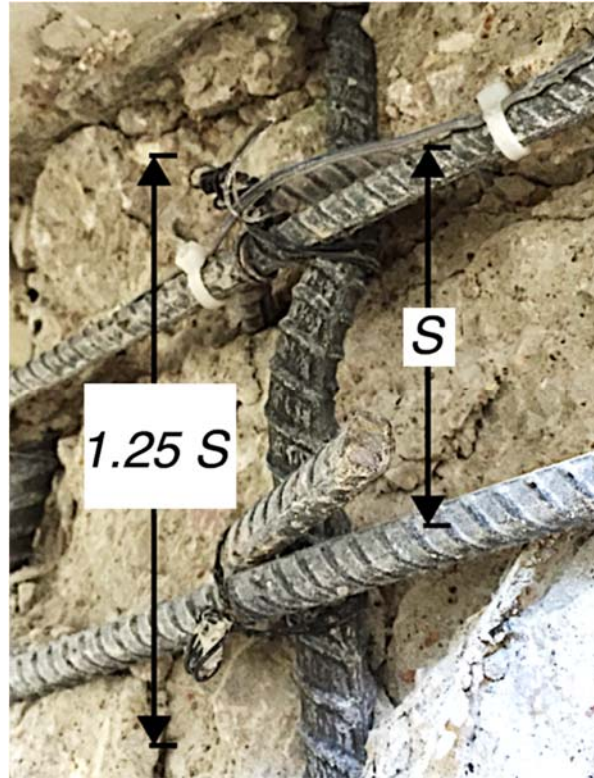
FIGURE 5-9: EFFECTIVE LENGTH OF BUCKLED BAR

The stress history of a longitudinal bar can be obtained from the fiber-section analysis of the member and that value compared with the degrading critical buckling stress to determine if and when a bar will buckle. However, given that bar stresses vary within the inelastic range of behavior between the yield stress (f_y) and the ultimate stress (f_u), the stress in a bar at buckling initiation (f_{ub}) can be simply estimated as the average of the tensile and ultimate stress as per (Equation 5-4) with limited loss in resolution.

EQUATION 5-4: ASSUMED STRESS IN THE BAR AT BUCKLING INITIATION

$$f_{ub} = \frac{f_u + f_y}{2}$$

Using the proposed model, buckling in well confined frame members satisfying the ACI 318-14 Special Moment Frame provisions is therefore triggered by the following mechanisms:

- Increased compressive strains that cause loss of confinement, damage in the core concrete after spalling, and opening of 90-degree crossties captured by the α factor
- Increased peak tensile strains experienced by the longitudinal bar in the previous cycles, which increases flexural crack widths and bar instability, and is captured by the β factor
- Increased differential between the tensile and compressive strains experienced by the bar and surrounding concrete, which increases concrete damage and bar instability, and is captured by the product of α and β

5.4.3 Reinforcing Bar Tangent Modulus of Elasticity

An empirical relation was derived for the tangent modulus of elasticity of the reinforcing bars subjected to compression strains in the inelastic range of behavior. Data from low-cycle fatigue tests on #8 Grade 60 and 100 bars sourced from two different manufacturers were used to calibrate the tangent modulus model (Ghannoum and Slavin 2016, Slavin 2015). Manufacturer 1 (M1) high-strength bars were produced using the micro-alloying process, while Manufacture 2 (M2) bars were produced using the quenching and tempering process (Ghannoum and Slavin 2016). The bars for which cyclic stress-strain data was used to calibrate the tangent modulus model were sourced from the same manufacturers as the bars used in the concrete members considered in this study, except those reinforced with ASTM A1035 bars. The grade 60 and 100 bars selected had tensile-to-yield-strength ratios varying from 1.18 to 1.68, and monotonic tangent moduli at

initiation of strain hardening ranging from 661 to 1452 ksi. Properties of the bars selected for the calibration process are listed in Table 5-4.

Stress-strain results were taken for calibration from a loading protocol cycling between strains of -1% in compression to 4% in tension (Figure 5-10). This strain range was the most representative of strains observed in the reinforcement of the concrete beams and columns around the point at which bar buckling occurred (Chapter 3). The cyclic fatigue tests considered were performed in a universal test machine with a spacing between the grips of 4 bar diameters or 4 inches, which lead to bars sustaining practically no buckling in compression.

TABLE 5-4: PROPERTIES OF BARS TESTED IN LOW CYCLE FATIGUE

	G60M1	G100M1	G60M2	G100M2
	Manufacturer 1		Manufacturer 2	
	Grade 60	Grade 100	Grade 60	Grade 100
f_y (ksi)	63.2	101.5	61.5	104.6
f_u ksi)	93.7	128.5	103.1	123.8
T/Y	1.48	1.27	1.68	1.18
ε_y	0.0026	0.0038	0.0026	0.0040
ε_u	0.1	0.081	0.095	0.062
E_s (ksi)	26900	30100	25800	31400
E_{sh} (ksi)	315	350	449	331
E_{tm} (ksi)	861	945	1452	661

[1] *f_y is the yield strength of the bars in tension, f_u is the tensile strength of the bars, T/Y is the ratio of the tensile-to-yield strength, ε_y is the yield strain of bars, ε_u is the uniform elongation measured per ASTM E8 procedures, E_{sh} is the inelastic secant modulus estimated as $(f_u - f_y)/(\varepsilon_u - \varepsilon_y)$, and E_{tm} is the tangent modulus of the bars tested in tension taken at the beginning of the strain hardening region.*

The tangent modulus (E_{tp}) of the bars cycled to inelastic strains was taken as the slope of the stress-strain curve in the second cycle to the compression target strain during the fatigue test (Figure 5-10).
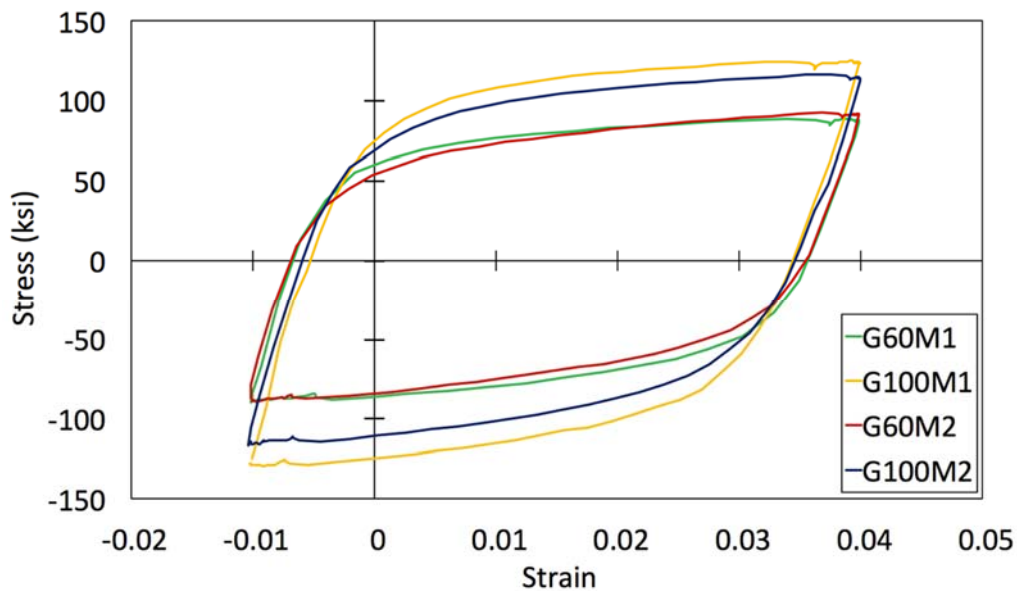
FIGURE 5-10: STRESS-STRAIN CURVE OF BARS IN THE SECOND LOADING CYCLE

In Figure 5-11, the tangent modulus E_{tp} is plotted versus the strain increment from the peak tensile strain at which the cyclic protocol reversed direction ($\Delta\varepsilon$). The curves in Figure 5-11 represent average values from at least three successful tests per bar type. As can be seen in the figure, the tangent modulus is higher for reinforcing bars with higher yield strength in the initial strain range after load reversal. This can be attributed to the lower yield strain of grade 60 bars, which leads the stress-strain curve of these bars to soften at a lower strain level as compared to grade 100 bars. In the higher inelastic strain range after load reversal, the tangent moduli were found to converge at similar values for all grades (Figure 5-11).

181
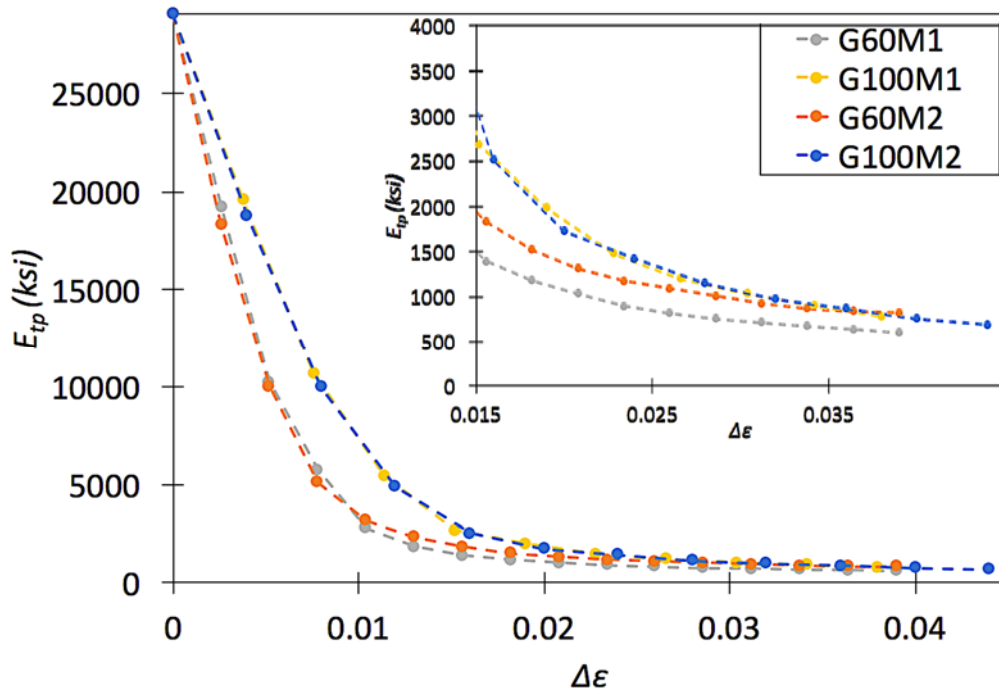
FIGURE 5-11: TANGENT MODULUS VS. STRAIN INCREMENT FROM LOAD REVERSAL

The strain reversal values were normalized to the yield strain (ε_y) in Figure 5-12. This led to the lines converging throughout the monitored strain range, with differences becoming pronounce at high strain values. The grade 60 bars from Manufacturer 2, G60M2, displayed the higher modulus values in the normalized plot, whereas the grade 100 from Manufacturer 2, G100M2, had the lowest values. This corresponds with their inelastic properties from monotonic tension tests, with G60M2 having the highest *T/Y* ratio and E_{sh} values, and G100M2 having the lowest values (Table 5-4).
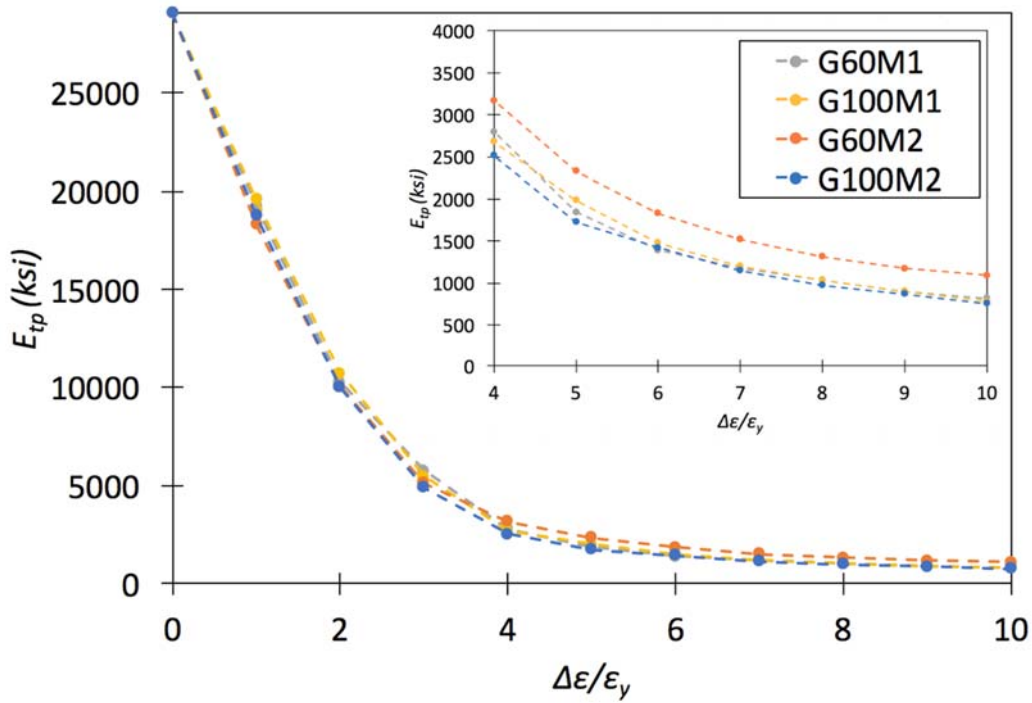
FIGURE 5-12: TANGENT MODULUS VS. NORMALIZED STRAIN INCREMENT FROM LOAD REVERSAL
TO YIELD STRAIN

Equation 5-5 was derived through nonlinear regression analysis to estimate the
tangent modulus of reinforcing bars subjected to inelastic strains. The model captures the
effects of varying bar strength, as well as bar inelastic properties, such as the T/Y ratio and
E_{sh}. Using both these properties in the equation was found to increase the accuracy of
estimates, as opposed to using only the secant modulus, E_{sh} or the tangent modulus, E_{tm}.

EQUATION 5-5: TANGENT MODULUS AT INELASTIC STRAINS

$$E_{tp} = (E_{sh} \times \frac{f_u}{f_y}) + \frac{E_s - (E_{sh} \times \frac{f_u}{f_y})}{1 + (\frac{5}{7}\frac{\Delta\varepsilon}{\varepsilon_y})^{2.3}}$$

183

In Figure 5-13, the tangent modulus values from material testing are compared to the tangent modulus estimates using Equation 5-5 for G60M2 and G100M2 bars, which respectively represent the highest and the lowest T/Y ratio and E_{sh} values. The mean error ratio of the 4 bar types calculated as the ratio of the estimated tangent modulus from Equation 5-5 over the tangent modulus taken from the material testing at $\frac{\Delta\epsilon}{\epsilon_y}$ of 1 to 10 was 1.04. The standard deviation was 0.07.
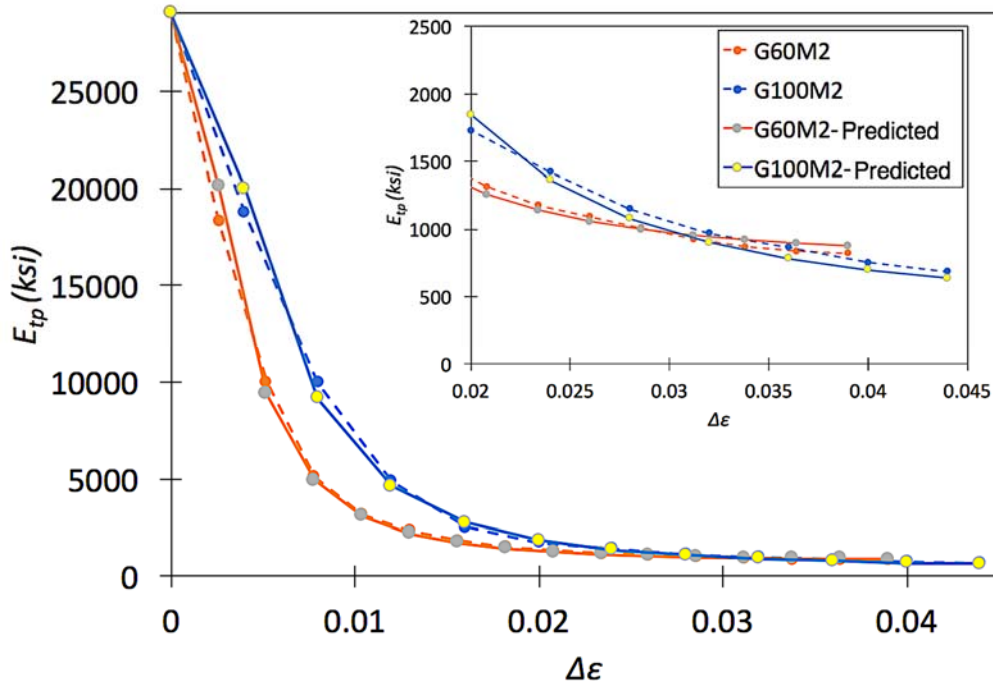
FIGURE 5-13: TANGENT MODULUS FROM MATERIAL TESTING COMPARED TO PREDICTION FROM EQUATION 5-5

5.4.4 Alpha and Beta Factors

Members CH100, CL100, and CH60 exhibited buckling of longitudinal bars between two consecutive ties at relatively large lateral deformation demands. Buckling was

observed well after the bars had yielded in compression. As the members were cycled to higher lateral deformation demands, the damage in the concrete cover and core increased. It is postulated that this concrete damage reduced the effective bracing of the longitudinal bars leading to bar buckling once the damage was severe enough. Additionally, at high compressive demands in the longitudinal bars the 90-degree crossties are prone to opening up leading to increased unsupported length.

The mechanics of such degradation in the plastic hinge region is captured by factors α and β in Equation 5-3. The variation of factors α and β with longitudinal strain demands on the concrete around the longitudinal bars in the plastic hinge region are presented in Figure 5-14. The values were calibrated such that Equation 5-3 captures buckling in members CH100, CL100 and CH60, and no buckling is predicted up to the end of the loading protocol for the rest of the members.

Factor α accounts for the loss of lateral support due to damage and spalling caused by compressive strain demands, and was calibrated using the smeared longitudinal strain histories in the concrete over the span of bar buckling, $\varepsilon_{buckling}$. Factor α was determined to vary from 0.2 to 1.0 as $\varepsilon_{buckling}$ goes from 0 to -0.03. Beyond a compression strain of -0.03 the factor remains at 1.0. Maximum damage is therefore assumed to occur at a compression strain of -0.03 as that value constitutes an upper bound on the compressive strain achievable by concrete in a well confined core prior to significant strength loss (Moehle 2015).

Factor β accounts for the peak tensile strain experienced by the longitudinal bar in the previous cycles, which can contribute to bar instability (Wang and Restrepo 1996,

185

Rodriguez et. al. 1999, Moyer and Kowalsky 2003, Brown et. al 2007, Goodnight et al. 2012, Feng et. al 2014). β was calibrated using the tensile strain demands in the bar at mid-span of a potential buckle or a distance equal to spacing of hoops from the member ends, $\varepsilon_{spacing}$. Factor β was determined to vary from 0.2 to 1, as the tensile strain demand, $\varepsilon_{spacing}$, goes from 0 to a maximum of 0.1. A tensile strain of 10% was chosen for maximum damage as that values is representative of the uniform or fracture elongations of the reinforcing bars considered in this study. Therefore, tension strain demands in bars could not exceed this threshold without a high risk of bar fracture.

The calculations carried to predict buckling initiation based on the proposed model are presented in Table 5-5. It is noted that the α factor is evaluated continuously during a cyclic loading protocol whereas the β factor is updated only if the peak tension strain experienced by a bar exceeds the prior recoded peak. The model was able to predict buckling accurately for all members, i.e., buckling was predicted to occur in members CH100, CL100 and CH60 at the correct peak drift excursion, and no buckling was predicted in the other members up to the end of their loading protocols. For members CH100 and CL100 buckling is predicted to occur at the end of the first cycle to a drift ratio of 5.5%. For member CH60, buckling initiation is predicted earlier, at the first excursion to the first half-cycle to +5.5% drift, meaning that the maximum tensile strain the bar experienced when the member was cycled at 4% drift ratio combined with compression strain the bar experienced at 5.5% drift ratio resulted in large enough product of α and β that triggered buckling. During the experimental testing of these members, buckling was

observed at the end of the first cycle to 5.5% drift ratio for members CH100 and CH60, and at the third half-cycle excursion of the second cycle for CL100.

The proposed buckling initiation model is intended to capture the fundamentals of the mechanisms and parameters leading to buckling of longitudinal bars in the well confined concrete frame members. It was however calibrated to a limited dataset, as few tests were conducted using bars of various strengths and mechanical properties. This model should be further validated or adjusted when additional data becomes available.
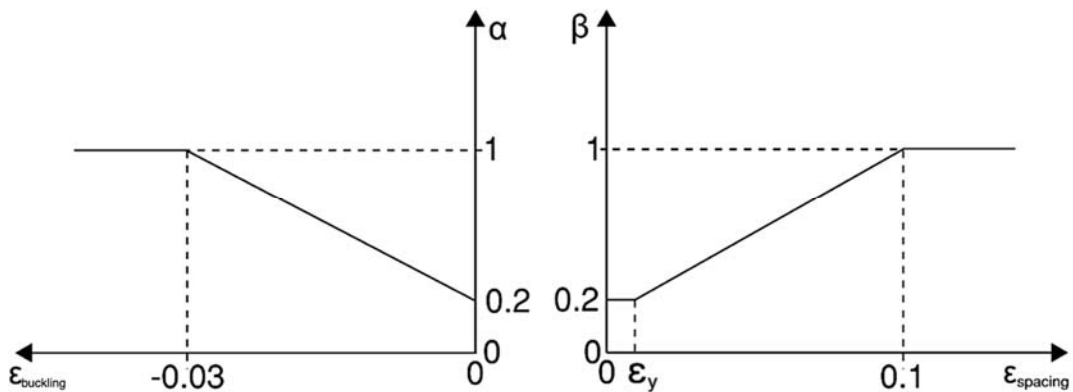
FIGURE 5-14: VARIATION OF FACTOR α AND β WITH STRAIN DEMAND (NEGATIVE VALUES REPRESENT COMPRESSION STRAINS)

TABLE 5-5: BUCKLING INITIATION PREDICTION CALCULATIONS FOR ALL MEMBERS

	Drift Ratio*	$\varepsilon_{buckling}$	$\varepsilon_{spacing}$	$\Delta\varepsilon/\varepsilon_y$	E_{tp}	f_y (ksi)	f_u (ksi)	ε_y	T/Y	E_{sh} (ksi)	s (in)	d_b (in)	α	β	$\alpha\beta$	Eq. 1-3: f_{cr}	Eq. 1-4: $(f_y+f_u)/2$	Check** $(f_y+f_u)/2/f_{cr}$
CH100	4.0%	0.051	0.034															
	-4.0%	-0.009	-0.002	10	758	100	127.0	0.0034	1.27	375	3.5	0.75	0.451	0.454	0.205	327.5	113.5	0.3
	5.5%	0.075	0.049	11	742								0.557	0.454	0.253	209.8		0.5
	-5.5%	-0.013	-0.003	15	601								0.557	0.574	0.320	106.2		1.1
CL100	4.0%	0.055	0.037															
	-4.0%	-0.009	-0.002	11	513	106.4	123.4	0.0037	1.16	210	3.5	0.75	0.453	0.478	0.217	198.3	114.9	0.6
	5.5%	0.079	0.052	11	499								0.569	0.478	0.272	122.0		0.9
	-5.5%	-0.014	-0.003	15	365								0.569	0.606	0.345	55.6		2.1
CH60	4.0%	0.060	0.033															
	-4.0%	-0.011	-0.002	16	488	64.4	93.4	0.0022	1.45	260	4.5	0.75	0.487	0.445	0.217	114.0	78.9	0.7
	5.5%	0.085	0.049	16	482								0.602	0.445	0.268	73.6		1.1
	-5.5%	-0.015	-0.003	23	422								0.602	0.575	0.346	38.6		2.0
2L06	5.5%	0.040	0.019	10	1015	65.5	107.4	0.0023	1.64	450	6	1	0.733	0.325	0.238	195.6	86.5	0.4
	-5.5%	-0.020	-0.005															
2H06	4.0%	0.016	0.008	8	1246	65.5	107.4	0.0023	1.64	450	6	1	1.000	0.238	0.238	240.8	86.5	0.4
	-4.0%	-0.035	-0.010															
CS60	5.5%	0.048	0.015	9	808	67.3	94.9	0.0023	1.41	315	5.5	1.25	1.000	0.296	0.296	187.8	81.1	0.4
	-5.5%	-0.032	-0.007															
CS80	7.0%	0.065	0.020	10	763	79.1	106.8	0.0027	1.35	320	5.5	1.13	1.000	0.337	0.337	111.5	92.9	0.8
	-7.0%	-0.045	-0.006															
BH100	6.5%	0.073	0.044	12	535	102.1	127.6	0.0035	1.25	280	5	1	0.200	0.536	0.107	734.1	114.9	0.2
	-6.5%	0.000	0.000															
BL100	6.5%	0.076	0.048	13	504	105.7	123.7	0.0036	1.17	290	5	1	0.200	0.569	0.114	612.8	114.7	0.2
	-6.5%	0.000	0.000															
BH60	4.9%	0.082	0.042	19	478	65.1	95.7	0.0022	1.47	275	5	1.13	0.200	0.518	0.104	897.9	80.4	0.1
	-4.9%	0.000	0.000															

*Negative values represent compression

**Values greated than 1.0 indicate Eq. 1-3 predicted buckling

■ Buckling observed in experimental test

■ Eq. 1-3 predicts buckling

■ Eq. 1-3 does not predict buckling

5.5 Damage Accumulation Index and Fracture

5.5.1 Fatigue Fracture Models

The low-cycle fatigue life and the accumulated strain demand of reinforcing bars have been related in models by many authors (Mander et al. 1994, Brown and Kunnath 2004, Hawileh et al. 2010, Slavin 2015, Ghannoum and Slavin 2016). However, the work presented by Slavin et. al. (2015), Slavin (2015), Ghannoum and Slavin (2016) and Hogsett (2017) are the only studies that capture the effect of HSRB currently in production in the U.S. Moreover, the types of bars tested by Slavin et. al. (2015) were sourced from the same manufacturers as the bars used to reinforce concrete members considered in this study (Table 5-6).

Slavin et. al. (2015) used a power function of the form described in Equation 5-6, with coefficients "c" and "d" calibrated per the material properties to relate the number of half-cycles to fracture, $2N_f$, to the total strain range over which bars are cycled, ε_a. Values of coefficients "c" and "d" for different manufacturers, grades, and clear spans between machine grips are presented in Table 5-6. The parameters were calibrated using results from #8 bars tested in low-cycle fatigue up to fracture. These bars were cycled to total strain ranges of 4% and 5%, which are representative of the peak strain range experienced by the longitudinal bars in the concrete members considered.

In this study, the fatigue model coefficients "c" and "d" used to represent the fatigue life of bars prior to buckling were those from $4d_b$ clear span tests, as bars did not experience significant buckling at that test clear span. After a bar is deemed to have buckled based on the buckling initiation model, coefficients "c" and "d" are taken from $5d_b$, $6d_b$, or $8d_b$, based

on the 1.25 times the spacing of the transverse reinforcement in the concrete member. Because data was not available for tests on grade 60 bars tested at $8d_b$, the value was interpolated linearly from $4d_b$ and $6d_b$ values. Linear interpolation was also used for an assumed buckled length in between the reported clear testing spans. It is noteworthy that the fatigue life of bars decreased as the clear span in testing increased due to increased strain concentrations caused by the buckled shape (Figure 5-3). By taking the fatigue model coefficients corresponding to the buckled length of a bar in a concrete member, the effects of the strain concentration due to buckling are captured indirectly by the reduced fatigue life estimated by the adjusted "c" and "d" coefficients.

EQUATION 5-6: RELATION OF STRAIN RANGE TO THE NUMBER OF HALF-CYCLES TO FAILURE

$$2N_f = c \times \varepsilon_a{}^d$$

TABLE 5-6: SUMMARY OF MATERIAL COEFFICIENTS FOR FATIGUE LIFE EQUATION

Manufacturer	Grade	Member	Clear Span	c	d
1	60	CH60, CS60, BH60	$4d_b$	5.14E-03	-2.87
			$6d_b$	7.92E-03	-2.59
	80	CS80	$4d_b$	2.48E-03	-2.97
			$6d_b$	6.60E-03	-2.43
	100	CH100, BH100	$4d_b$	2.40E-05	-4.62
			$6d_b$	1.49E-06	-3.03
2	100	CL100, BL100	$4d_b$	1.90E-06	-5.42
			$6d_b$	1.65E-05	-4.46

Based on the work by Miner (1945), Equation 5-7 is used to calculate the accumulation of damage index, a model that assumes a linear summation of damage as a function of the number of half-cycle the bar is loaded at a certain deformation amplitude.

A bar is assumed to fracture when the damage index factor D in Equation 5-7 reaches a value of 1.0 in a tensile half-cycle.

<div align="center">EQUATION 5-7: COFFIN-MANSON CUMULATIVE DAMAGE INDEX</div>

$$D = \sum D_i = \sum_{i=1}^{N} \frac{n_i}{2N_{fi}}$$

where n_i is the number of half cycles a bar is cycled to a certain total strain range of ε_a, $2N_{fi}$ is the number of half cycles to fracture to the same strain range of ε_a.

5.5.2 Predicting Fracture

Predicting the fracture of longitudinal bars in frame members using the proposed methodology requires tracking the damage indices of the longitudinal bars at the locations of expected highest moments (typically at member ends) and about one hoop spacing from member ends, which corresponds to the mid-span of the bar buckled shape. Damage index calculations should therefore typically be performed at four sections in frame members and for all longitudinal bars at those sections. The four sections to consider are: both member ends and at one hoop spacing away from both member ends. All these checks may be necessary because it is not always evident which member end will experience the largest rotation demands during a seismic event or which longitudinal bars will experience the highest damage index at a particular section. For the sections at a hoop spacing from member ends, the damage index ($D_{spacing}$) is incremented for each bar at each loading step using $\varepsilon_{spacing}$ and the unbuckled fatigue model parameters "c" and "d". At the same time, the buckling initiation check is performed at each loading step. For a given bar, if buckling is not predicted at any point in the loading history, then this location will not govern and

fracture can only occur at the section of maximum moment. If buckling is predicted, then after buckling the damage index ($D_{spacing}$) is incremented using $\varepsilon_{buckling}$ and the bar fatigue model parameters "c" and "d" corresponding to the expected buckled shape. At the same time, the damage index for longitudinal bars at the sections of highest moment demands (D_{end}) is incremented at each loading step using ε_{end} and the unbuckled fatigue model parameters "c" and "d". Fracture will occur at the bar and location at which the damage index exceeds 1.0 first.

The methodology predicted buckling of the outermost longitudinal bars in member CH100 at the end of the first cycle to a drift ratio of 5.5% (Table 5-5), followed by fracture at the same location two half cycles later. Estimated representative strain demands in the outermost longitudinal bars of member CH100 at a hoop spacing away from the end are given through the loading history in Figure 5-15. Up to buckling initiation, $\varepsilon_{spacing}$ is used at a hoop spacing from member end. After buckling initiation is triggered, the smeared longitudinal strain in the concrete or steel bars over the span of bar buckling, $\varepsilon_{buckling}$, is used. The strain demands ε_{end} at the critical moment section are also given in Figure 5-15 for the outermost longitudinal bars.

The cumulative damage indices $D_{spacing}$ and D_{end} in the longitudinal bars of member CH100 are plotted against the number of half cycles in Figure 5-16. D_{end} shown in Figure 5-16 reaches a maximum of 0.30 at the point where $D_{spacing}$ reaches 1.0. The cumulative damage index $D_{spacing}$ exceeds the value of 1.0 at the last half cycle to a drift ratio of 5.5% (i.e. the end of the second cycle to 5.5% drift ratio). This concurs with the

recorded fracture during experimental testing, at the end of the second cycle to 5.5% drift ratio.

The methodology predicts that about 80% of the damage leading to fracture at a hoop spacing from member end is induced after buckling takes place. A similar high damage value is predicted after buckling initiates for members CL100 and CH100. This is a plausible scenario because all these three members during testing sustained fracture of the longitudinal bars at similar drift ratios of about 5.5%, although the mechanical properties and the strain demands in the bars were significantly different.
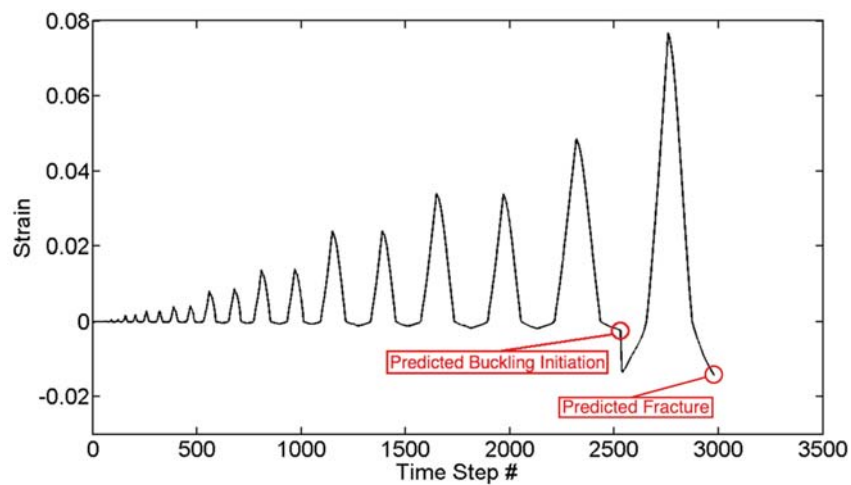
FIGURE 5-15: REPRESENTATIVE STRAIN DEMANDS IN THE LONGITUDINAL BARS OF MEMBER CH100 THROUGH THE LOADING HISTORY
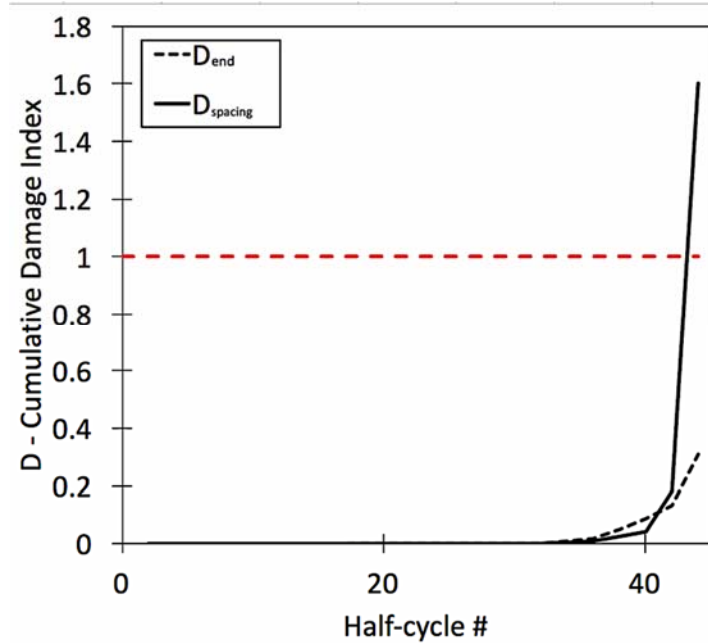
FIGURE 5-16: ACCUMULATION OF DAMAGE INDEX IN THE LONGITUDINAL BARS OF CH100 AS THE COLUMN IS CYCLED LATERALLY

The methodology predicted that bar fracture in member BL100 takes place at the end of the first excursion to a drift ratio of 6.5% (Table 5-7). Fracture was observed in the experimental testing at the end of the first cycle to 4.9% drift ratio. Additionally, fracture of the longitudinal bars at the member ends was predicted at the same point in the loading protocol in member BH100, and no fracture was observed in the experiments. However, at this drift, member BH100 sustained global buckling.

TABLE 5-7: SUMMARY OF EXPERIMENTALLY OBSERVED AND PREDICTED BUCKLING AND FRACTURE

	Experimnetal Observed Buckling		Methodology Predicted Buckling		Experimental Observed Fracture			Methodology Predicted Fracture		
	Drift Target Towards which Buckling Observed (%)	Half Cycle #	Drift Target Towards which Buckling Predicted (%)	Half Cycle #	Drift Target Towards which Fracture Observed (%)	Half Cycle #	Location	Drift Target Towards which Fracture Predicted (%)	Half Cycle #	Location
CH100	5.5	2	5.5	2	5.5	4	At Buckle	5.5	4	At Buckle
CL100	5.5	3	5.5	2	5.5**	5	At Buckle	5.5	4	At Buckle
CH60	5.5	2	5.5	1	5.5	3	At Buckle	5.5	4	At Buckle
BL100	Did Not Buckle		Did Not Buckle		4.9	2	At End	6.5	1	At End
2L06	Did Not Buckle		Did Not Buckle		Did Not Fracture			Did Not Fracture		
2H06	Did Not Buckle		Did Not Buckle		Did Not Fracture			Did Not Fracture		
CS60	Did Not Buckle		Did Not Buckle		Did Not Fracture			Did Not Fracture		
CS80	Did Not Buckle		Did Not Buckle		Did Not Fracture			Did Not Fracture		
BH100	Did Not Buckle		Did Not Buckle		Did Not Fracture			6.50%	1	At End
BH60	Did Not Buckle		Did Not Buckle		Did Not Fracture			Did Not Fracture		

End of loading protocol assumed in order to compare dammage index

**Fracture was observed at a drift ratio of 5.5% as the member was being pushed towards the first half-cycle to 7.0% drift target*

5.6 Summary and Conclusions

A methodology for predicting longitudinal bar buckling initiation and fracture in SMF members is proposed. The methodology is based on estimates of local strain demands in longitudinal bars of SMF members. A buckling initiation model is proposed that accounts for the mechanical properties of the reinforcing bars, as well as the loading history the bars and surrounding concrete experience prior to buckling. Material specific bar fatigue relations calibrated through material test results are used to predict the number of half-cycles to bar fracture for buckled and un-buckled bars based on accumulation of strain demands prior and after buckling, if it occurs.

Conclusions and contributions also include:

- The proposed methodology predicted both buckling initiation and fracture of the longitudinal bars within a half-cycle of loading compared to the bar buckling initiation and fracture observed in the tests. The proposed buckling initiation model accounts for both bar properties and member design properties: decrease in steel tangent modulus with increase in compression strain demand, hoop spacing, axial load demand, local loading history of the bar and the surrounding concrete.
- Local deformation measurements of longitudinal strains around the buckled bars indicate that curvatures concentrate within this region after bar buckling. Once buckling is initiated, bar-slip deformations are reduced.
- An empirical relation was derived for the tangent modulus of elasticity of grade 60 to 100 reinforcing bars subjected to compression strains in the inelastic range of behavior. This relation was found to be dependent on the yield strength of the longitudinal bars, as well as bar inelastic properties, such as the T/Y ratio and secant modulus, E_{sh}. At low inelastic compressive

strain demands, the tangent modulus of elasticity of grade 60 bars was lower than that of the higher strength bars. This can be attributed to the lower yield strain of the grade 60 bars, which results in the stress-strain curve of these bars softening at a lower strain level compared to grade 100 bars. At high compression strains, the tangent modulus was found to converge to a value of about $E_{sh} \times \frac{f_u}{f_y}$ for all bar grades and types considered.

The proposed methodology indicates that curvature and bar-strain concentrations after bar buckling can increase fatigue damage in longitudinal bars leading to bar fracture shortly after bar buckling.

5.7 Limitations and recommendation for future work

It was the purpose of this study to use results from well-controlled and instrumented cyclic load tests of concrete members incorporating different grades and types of reinforcement. As such, a limited number of tests were available. As more tests on concrete members with different grades and types of steel are carried, future work should focus on increasing the accuracy in buckling initiation demand prediction, by calibrating parameters α and β to a larger dataset. Additionally, as steel mills get closer to a final product for grade 80 and100 bars, the Coffin-Manson equation parameters could be re-evaluated to remain representative of bar production in the U.S.

6   SUMMARY AND CONCLUSIONS

The project described in this report is part of a larger national effort aimed at quantifying changes in the seismic collapse risk of concrete structures associated with switching from conventional grade 60 reinforcing bars to HSRB. The objective of this project in particular is to provide the necessary experimental data and behavioral models to identify when longitudinal bars in seismically detailed frame members reach fracture during seismic events across all types of bars and grades in production or under development in the U.S. Three tasks were undertaken to achieve project objectives: 1) a low-cycle fatigue-capacity model was calibrated to cyclic tests conducted on bars of different grades and mechanical properties; 2) a mechanics-based model was developed and calibrated to experimental data from the literature to correlate member global deformations with strain demands that govern the fatigue behavior of longitudinal bars in concrete members; and 3) based outcomes from tasks 1) and 2), a methodology was proposed to estimate the point during a seismic loading history at which longitudinal bars fracture in seismically detailed concrete frame members. Cyclic tests were performed on reinforcing bars to bolster available fatigue data and included bars of varying grades of steel, manufacturing techniques, clear lateral bracing spans, and strain amplitudes.

6.1 Bar Fatigue-Life Observations and Models

Three series of fatigue tests were compiled in this study, with Series 2 low-cycle fatigue tests being conducted within the scope of this project. In all, 526 low-cycle fatigue tests were compiled and the following observations were made based on the data:

1. A linear relation was observed in log-log space between the numbers of half-cycles to fracture (NHF) and total strain amplitude experienced by the bars within a range of 1.5% to 6% strain. This confirms prior study results.

2. The clear unbraced span at which the bars were gripped in the testing machine governed the degree of buckling the bars experienced and therefore the maximum curvature and associated strain concentrations in the bars. At a clear span of $4d_b$ or less, practically no buckling could be observed, while increasing the clear span increased the level of buckling. As the clear span increased the number of half-cycles to fracture decreased substantially and appeared to level off at a clear span of $8d_b$. The relation between clear span and half-cycles to fracture therefore followed a power law.

3. Substantial gains in the NHF were observed when minimum radii at the base of bar deformations changed from about 1 to 2 times the deformation height. A bar deformation base radius to deformation height of at least 1.5 is advised to improve fatigue life of reinforcing bars.

4. Bars having additional longitudinal ribs used to designate bar grade were tested. These bars experience up to seven times fewer NHF than comparable bars without the longitudinal ribs. It is strongly advised not to use bars with additional longitudinal ribs in seismic applications.

5. Bars from the main three manufacturing processes used in the U.S. were tested in this study; namely micro-alloying (M1), quenching and tempering (M2) and the patented MMFX process (M3). Significant differences in the fatigue life of bars were observed

between the various production methods. Separate fatigue models were produced for each manufacturing process to capture those differences.

6. Fatigue models were developed for each manufacturing process to estimate the NHF for bars based on strain amplitude, clear unbraced length, bar yield strength and bar fracture strain measured in monotonic tension tests. It is important to note that the proposed fatigue relations were calibrated within the range of parameters of bar tests used. Particularly, except for a limited number of bars from earlier manufacturing process 2 batches, bars tested in this study had relatively smooth deformation radii, generally exceeding a ratio of deformation base radius to deformation height (R_{min}/H) of 1.5. As demonstrated in this report, sharper deformation radii or other deformation patterns such as additional ribs used to mark bar grade can reduce the fatigue life of bars substantially. Bar deformation radii to deformation height below 1.5 are not advised for bars used in seismic applications.

7. The proposed fatigue life relations highlight that manufacturing process 2 (M2, quenching and tempering) produced in general larger numbers of half-cycles to fracture than manufacturing processes 1 and 3. As noted from experimental results, the hardened outer shell of bars treated using quenching and tempering appeared to hinder the progress of fatigue cracks that formed at the base of bar deformations. This behavior may have contributed to the improved fatigue life measured in number of half cycles to fracture (NHF) for those bars.

8. The fatigue life of bars produced using the quenching and tempering process (M2) appear to be more sensitive to clear unbraced length, which is related to buckling

amplitude, than those of bars produced using process M1. Buckling tends to increase strain demands more at the outer surface of bars than within the barrel, due to curvatures associated with buckling. Since M2 bars have a hardened shell that appeared to hinder fatigue crack propagation in tests, concentrating strains due to buckling within that layer may cause such bars to see larger decreases in fatigue life as buckling amplitudes increase, compared to bars that have more homogenous micro-structure distributions.

9. For manufacturing process 2, the fatigue life between grades is estimated to be similar across the strain amplitude ranges of interested for concrete members subjected to seismic excitation (i.e., 1% to 8% strain amplitudes). For manufacturing process 1, higher fatigue life is estimated for grade 80 and 100 bars compared with grade 60 bars at smaller strain amplitudes of 1 to 3%. However, lower fatigue life for higher strength bars is predicted at higher strain amplitudes exceeding 4%. This cross-over may be attributed in part to the smaller fracture elongations of higher strength bars.

6.2 Predicting Bar Fracture in Frame Members

The behavior of Special Moment Frame (SMF) members with high-strength reinforcing bars (HSRB) subjected to large inelastic demands was investigated through test da and computational investigations. Test data from concrete columns and beams with seismic detailing and varying grades of reinforcing bars ranging from grade 60 to grade 100 and from various manufacturing processes were considered in this study.

In the analytical examination, a computational framework based on fiber-section elements and mechanics-based behavioral models is proposed to accurately estimate both member-level deformations and strain demands in longitudinal bars and the concrete surrounding them within the plastic hinge regions of frame members. Strain demands derived through the proposed analytical framework were used to track the damage progress of longitudinal bars up to buckling and fracture. Tensile strain demands in the longitudinal bars were found correlate with the tensile-to-yield strength ratio (T/Y) of the bars, the axial load ratio on the member, and shear stresses on the member. Compression strain in the bars were found to correlate with the axial load ratio applied to a member.

A methodology for predicting longitudinal bar buckling initiation and fracture in SMF members is proposed. The methodology is based on estimates of local strain demands in longitudinal bars of SMF members. A buckling initiation model is proposed that accounts for the mechanical properties of the reinforcing bars, as well as the loading history the bars and surrounding concrete experience prior to buckling. Material specific bar fatigue relations calibrated through material test results are used to predict the number of

half-cycles to bar fracture for buckled and un-buckled bars based on accumulation of strain demands prior and after buckling, if it occurs.

Conclusions and contributions also include:

- The proposed methodology predicted both buckling initiation and fracture of the longitudinal bars within a half-cycle of loading compared to the bar buckling initiation and fracture observed in the tests. The proposed buckling initiation model accounts for both bar properties and member properties including a decrease in steel tangent modulus with increase in compression strain demand, hoop spacing, axial load demand, and local loading history of the bar and the surrounding concrete.

- Local deformation measurements of longitudinal strains around the buckled bars indicate that curvatures concentrate within this region after bar buckling. This phenomenon coupled with an increase in strain concentrations due increased curvatures in buckled bars accelerated the rate of damage accumulation in bars drastically after buckling initiation from the rate of damage accumulation prior to bar buckling.

- An empirical relation was derived for the tangent modulus of elasticity of grade 60 to 100 reinforcing bars subjected to compression strains in the inelastic range of behavior. This relation was found to be dependent on the yield strength of the longitudinal bars, as well as bar inelastic properties, such as the T/Y ratio and secant modulus, E_{sh}. At low inelastic compressive strain demands, the tangent modulus of elasticity of grade 60 bars was lower than that of the higher strength bars. This can be attributed to the lower yield strain of the grade 60 bars, which results in the stress-strain curve of these bars softening at a lower strain level compared to grade 100 bars. At high compression strains, the tangent modulus was found to converge to a value of about $E_{sh} \times \frac{f_u}{f_y}$ for all bar grades and types considered.

The proposed methodology indicates that concentrations of member curvatures around buckled bars and bar-strain concentrations after bar buckling can increase fatigue damage in longitudinal bars leading to bar fracture shortly after bar buckling.

7 LIST OF REFERENCES

ACI Committee 318, "Building Code Requirements for Structural Concrete (ACI 318-14) and Commentary (ACI 318R-14)," American Concrete Institute, Farmington Hills, MI, 2014, 519 pp.

ACI Committee 369, "Standard Requirements for Seismic Evaluation and Retrofit of Existing Concrete Buildings (ACI369-17)," American Concrete Institute, Farmington Hills, MI, 2017, 110 pp.

Addessi, D and Ciampi, V., "A regularized force-based beam element with a damage-plastic section constitutive law," *International Journal for Numerical Methods in Engineering,* V. 70, No. 5, 2007, pp. 610–629.

Aoyama, H., 2001, "Design of Modern Highrise Reinforced Concrete Structures," Imperial College Press, London, United Kingdom.

ASCE/SEI 41-17, "Seismic Rehabilitation of Existing Buildings," ASCE/SEI Standard 41-17, American Society of Civil Engineering, Reston, VA, 2017.

ASTM A1035 / A1035M-16b, Standard Specification for Deformed and Plain, Low-Carbon, Chromium, Steel Bars for Concrete Reinforcement, ASTM International, West Conshohocken, PA, 2016, www.astm.org.

ASTM A370-17a, "Standard Test Methods and Definitions for Mechanical Testing of Steel Products," ASTM International, West Conshohocken, PA, 2017, 50 pp.

ASTM A706 / A706M-16, Standard Specification for Deformed and Plain Low-Alloy Steel Bars for Concrete Reinforcement, ASTM International, West Conshohocken, PA, 2016, www.astm.org.

ASTM C39/C39M-18, "Standard Test Method for Compressive Strength of Cylindrical Concrete Specimens," ASTM International, West Conshohocken, PA, 2018, 8 pp., www.astm.org.

ASTM E8 / E8M-16a, Standard Test Methods for Tension Testing of Metallic Materials, ASTM International, West Conshohocken, PA, 2016, www.astm.org.

ATC-115 "Roadmap for the Use of High-Strength Reinforcement in Reinforced Concrete Design,", Applied Technology Council, 2015, 197 pp.

Benzoni, G.; Ohtaki, T.; Priestley, M. J. N.; and Seible, F., "Seismic Performance of Circular Reinforced Concrete Columns under Varying Axial Load," SSRP 96/04, Structural Systems Research, University of California-San Diego, La Jolla, CA, 1996.

Berry, M. P., and Eberhard, M. O., "Practical Performance Model for Bar Buckling," *Journal of Structural Engineering, ASCE*, V. 131, No. 7, 2005, pp. 1060–1970.

Berry, M. P., and Eberhard, M. O., "Performance Modeling Strategies for Modern Reinforced Concrete Bridge Columns," PEER-2007/07, Pacific Earthquake Engineering Research Center, University of California-Berkeley, Berkeley, CA, 2007, 213 pp.

Brown, W. A., Lehman, D. E., and Stanton, J. F., "Bar Buckling in Reinforced Concrete Bridge Columns," PEER-2007/11, Pacific Earthquake Engineering Research Center, University of California-Berkeley, Berkeley, CA, 2007, 138 pp.

Bresler, B., and Gilbert, P. H., "Tie Requirements for Reinforced Concrete Columns," *ACI Structural Journal*, V. 58, No. 5, 555–570.

Coleman, J., and Spacone, E., "Localization Issues in Force-Based Frame Elements," *ASCE Journal of Structural Engineering*, V. 127, No. 11, 2001, pp. 1257–1265.

Dhakal, R., and Maekawa, K., "Reinforcement Stability and Fracture of Cover Concrete in Reinforced Concrete Members," *Journal of Structural Engineering,* ASCE, V. 128, No. 10, 2002, 1253–1262.

Elwood, K. J. and Eberhard, M.O., "Effective Stiffness of Reinforced Concrete Columns," *ACI Structural Journal*, V. 106, No. 4, 2009.

Federal Emergency Management Agency (FEMA), "Interim Testing Protocols for Determining the Seismic Performance Characteristics of Structural and Nonstructural Components." FEMA-461, Federal Emergency Management Agency, Washington, DC, 2007, 138 pp.

Feng, Y., Kowalsky M. J., Nau, J. M., "Finite-Element Method to Predict Reinforcing Bar Buckling in RC Structures," *Journal of Structural Engineering*, ASCE, V. 141, No. 5, 2015.

Ghannoum, W. M., and Moehle, J. P., "Shake-Table Tests of a Concrete Frame Sustaining Column Axial Failures," *ACI Structural Journal*, V. 109, No. 3, May-June 2012, pp. 393-402.

Ghannoum, W.M. and Slavin, C.M., "Low-Cycle Fatigue Performance of High-Strength Steel Reinforcing Bars," *ACI Material Journal*, 113 (6), 2016.

Hoggsett, G. S., "Defining Structurally Acceptable Properties of High-Strength Reinforcing Bars through Low-Cycle Fatigue Testing," master's thesis, University of Texas at Austin, Austin, TX, 2017, 118 pp.

Huq, M. S., Weber-Kamin, A. S., Ameen, S., Lequesne D. R., and Lepage, A., "High-Strength Steel Bars in Reinforced Concrete Walls: Influence of Steel Mechanical Properties on Deformation Capacity," (04-14), Charles Pankow Foundation, 2017, pp. 311. http://www.pankowfoundation.org/download.cfm?ID=319

Karsan, I. D., and Jirsa, J. O. (1969). "Behavior of Concrete Under Compressive Loading," *Journal of Structural Division,* ASCE, V. 95, No. 12, 2543-2563.

Kent, D. C., and Park, R., "Flexural Members with Confined Concrete," *Journal of Structural Division,* ASCE, V. 97, No. 7, 1971, pp. 1969–1990.

Kwon, Jinhan, "Strength, Stiffness, and Damage of Reinforced Concrete Buildings Subjected to Seismic Motions," Ph.D. Dissertation, The University of Texas at Austin, Austin, Texas, May 2016.

LeBorgne, M.R., "Modeling the Post Shear Failure Behavior of Reinforced Concrete Columns," Ph.D. Dissertation, The University of Texas at Austin, Austin, Texas, May 2012.

Limantono, A. A., "Modeling Strain Demands in Longitudinal Steel Bars of Concrete Columns," master's thesis, University of Texas at Austin, Austin, TX, 2016, pp. 178.

Macchi, G., Pinto, P.E. and Sanpaolesi, L., "Ductility Requirements for Reinforcement Under Eurocodes," *Structural Engineering International*, 6.4, 1996, pp. 249-54.

Mander. J. B., Priestley, M. J. N., Park, R., "Theoretical Stress-Strain Model for Confined Concrete," *Journal of Structural Engineering*, Vol. 114, No. 8, 1988, pp. 1804-1826.

McKenna, F., Fenves, G.L., Scott, M.H., and Jeremie, B., 2000, *Open System for Earthquake Engineering Simulation*, Open System for Earthquake Engineering Simulation (OpenSEES), University of California, Berkeley.

Menegotto M., Pinto P.E., "Method of Analysis for Cyclically Loaded R.C. Frames Including Changes in Geometry and Non-Elastic Behavior of Elements Under Combined Normal Force and Bending," Istituto di Scienza e Tecnica delle Costruzioni, University of Rome, Report 32, October 1972.

MMFX Technologies Corporation, "Material Properties and Design Considerations MMFX2 (ASTM A1035/AASHTO MP18)," MMFX Product Information, December 2012, 36 pp.

Moyer, M. J., and Kowalsky, G., "Influence of Tension Strain on Buckling of Reinforcement in Concrete Columns," *ACI Structural Journal*, V. 100, No. 1, Jan.-Feb. 2003, pp. 78-85.

Neuenhofer, A., and Filippou, F. C., "Evaluation of Nonlinear Frame Finite-Element Models," *Journal of Structural Engineering*, ASCE, V. 123 No. 7, 1997, pp. 958–966.

NIST, "Use of High-Strength Reinforcement in Earthquake-Resistant Concrete Structures (GCR 14-917-30)," NEHRP Consultants Joint Venture, National Institute of Standards and Technology, Gaithersburg, MD, 2014, 231 pp.

OpenSees, Version 2.4.5, http://opensees.berkeley.edu, accessed May. 13, 2015.

Pantazopoulou, S. J., "Detailing for Reinforcement Stability in Reinforced Concrete Members," *Journal of Structural Engineering,* ASCE, V. 124, No. 6, 1998, 623–632.

Papia, M.; Russo, G.; and Zingone, G., "Instability of Longitudinal Bars in RC Columns," *Journal of Structural Engineering*, ASCE, V. 114, No. 2, 1988, pp. 445-461.

Papia, M., and Russo, G., "Compressive Concrete Strain at Buckling of Longitudinal Reinforcement," *Journal of Structural Engineering*, V. 115, No. 2, 1989, 382–397.

Park, R. and Paulay, T., Reinforced Concrete Structures, Wiley, 1975.

Puranam, A. and Pujol, S., "Minimum Flexural Reinforcement in Reinforced Concrete Walls," 16th World Conference on Earthquake Engineering, 16WCEE, Chile, 2017.

Qi, X. and Moehle, J. P. "Displacement Design Approach for Reinforced Concrete Structures Subjected to Earthquakes," Earthquake Engineering Research Center, University of California, Berkeley, CA, UCB/EERC-91/02, January 1991, 186 pp.

Rodriguez, M., Botero, J., and Villa, J. 1999. "Cyclic Stress-Strain Behavior of Reinforcing Steel Including Effect of Buckling," *Journal of Structural Engineering,* ASCE, V. 125, No. 6, 605–612.

Scott, M. H., and Fenves G. L., "Plastic Hinge Integration Methods for Force-Based Beam–Column Elements," *Journal of Structural Engineering*, ASCE, V. 132, No. 2, 2006, pp. 244-252.

Scribner, C. F. "Reinforcement Buckling in Reinforced Concrete Flexural Members" *ACI Structural Journal*, V. 83 No. 6, 1986, pp. 966–973.

Slavin, C. M., "Defining Structurally Acceptable Properties of High-Strength Steel Bars through Material Testing," master's thesis, University of Texas at Austin, Austin, TX, 2015, 136 pp.

Slavin, C.M. and Ghannoum, W.M., "Defining Structurally Acceptable Properties of High- Strength Steel Bars through Material and Column Testing, PART I: MATERIAL TESTING REPORT," (05-14), Charles Pankow Foundation, August 2015, pp. 135. http://www.pankowfoundation.org/download.cfm?ID=282

Sokoli, D., Shekarchi, W., Buenrostro, E. and Ghannoum, W. M., "Advancing Behavioral Understanding and Damage Evaluation of Concrete Members Using High-Resolution Digital Image Correlation Data," Earthquakes and Structures, V. 7, No. 5, 2014, pp. 609-626. doi: 10.12989/eas.2014.7.5.609

Sokoli, D., "Seismic Performance of Concrete Columns Reinforced with High-strength Steel," master's thesis, University of Texas at Austin, Austin, TX, 2014, 166 pp. Sokoli, D. and Ghannoum, W.M., "High-strength Reinforcement in Columns under High Shear Stresses," *ACI Structural Journal*, V. 113, No. 3, 2016.

Sokoli, D., "Fracture of High-Strength Bars in Concrete Frame Members under Earthquake Loads," Ph.D. Dissertation, The University of Texas at Austin, Austin, Texas, August 2018.

Sokoli, D. Limantono, and A., Ghannoum, W. M., "Defining Structurally Acceptable Properties of High- Strength Steel Bars through Material and Column Testing, PART II: COLUMN TESTING REPORT," (05-14), Charles Pankow Foundation, August 2017, pp. 219. http://www.pankowfoundation.org/grants.cfm?prodonly=1

Spacone, E., Filippou, F. C., and Taucer, F. F. ''Fibre beam-column model for nonlinear analysis of R/C frames. I: Formulation,'' *Earthquake Engineering and Structural Dynamics*, V. 25, No. 7, 1996, pp. 711–725.

To, D. V. and Moehle, J. P., "Seismic Performance Characterization of Beams with High-Strength Reinforcement," (06-14), Charles Pankow Foundation, 2017, pp. 140.

Wang, Y. C., and Restrepo, J. I., "Strength Enhancement of Concentrically Loaded Reinforced Concrete Columns Using TYFO S Fiber-Wrap Jackets." Res. Rep. 96-12, Dept. of Civil Engineering, Univ. of Canterbury, Christchurch, New Zealand, 1996.

Zhao, D.S. and Ghannoum, W.M., "Setting Bar-Bending Requirements for High-Strength Steel Bars," (01-15), Charles Pankow Foundation, 2016, pp. 92. http://www.pankowfoundation.org/download.cfm?ID=297